University of Alberta

The Effects of Substrate Heterogeneity on Colloid Deposition

by

Jeffrey A. L. Kemps

A thesis submitted to the Faculty of Graduate Studies and Research
in partial fulfillment of the requirements for the degree of

Doctor of Philosophy

Department of Mechanical Engineering

Spring 2010
Edmonton, Alberta

Examining Committee

Subir Bhattacharjee, Mechanical Engineering

Larry Kostiuk, Mechanical Engineering

Tian Tang, Mechanical Engineering

Michael Lipsett, Mechanical Engineering

Anthony Yeung, Chemical Engineering

Nathalie Tufenkji, Chemical Engineering, McGill University

To my family...

My parents, Leonce and Audrey,

My sister Caroline, my brother-in-law Ron and my nieces Alexis and Hannah,

And my wife Nana.

Abstract

Heterogeneity of surfaces is often included in mathematical treatments of colloid transport and deposition as an afterthought, if at all. Most previous models of colloid transport and deposition have employed idealizations and simplifications such as assuming smooth collector surfaces with uniform chemical properties. This research proposes a new heterogeneous interaction model (HIM) to account for colloidal forces between particles and heterogeneous substrates. Extending the approach employed with the HIM, the inclusion of convection and diffusion in the model leads to a Lagrangian particle tracking model (PTM) for predicting colloid transport and deposition on a planar substrate containing one or more protruding asperities in the presence of shear flow. An important part of the PTM is an accurate rendering of the fluid flow field around the model substrate, which is obtained from a numerical solution of the Stokes equations. A simple approximation of the particle-substrate hydrodynamic interactions was developed for the PTM based on the universal hydrodynamic correction functions. This model was employed to quantitatively predict how presence of asperities on a collector can influence the deposition of particles on the substrate in shear flow. Flow field modifications due to the substrate's physical heterogeneity – coupled with hydrodynamic interactions – and the lateral migration (colloidal) forces near chemically heterogeneous

substrates yield remarkably diverse deposition probabilities and deposit morphologies. The general approach of this research, which involves the use of the HIM in conjunction with the Brownian PTM, results in the first simulation tool of its kind to attempt to quantify deposition on heterogeneous substrates.

Acknowledgements

Many people played roles, major or minor, in the completion of my work on this thesis. Looking back, I have so much gratitude for these extraordinary individuals, whose contributions run the gamut from uttering a single phrase of remarkable clarity to lengthy, routine interactions leading to small increments of progress.

First of all, I would like to thank my supervisor, Dr. Subir Bhattacharjee, for his support and guidance in matters both central and peripheral to my research, as well as on life as an academic and other personal and philosophical issues. On several occasions, he applied the necessary balance of deadline pressure and attention to detail that prevented me from languishing in some distant corner of the vast field of research I explored. His tremendous enthusiasm for the pursuit of scientific knowledge permeated our discussions, which often strengthened my resolve. His clear aptitude with theory and zeal for working with numerical models inspired me to seek out unique approaches to the work. I am particularly appreciative of his lessons on improving presentation skills during our lab group meetings, highlighting the power of a well-crafted message.

During the course of my studies, I had the fortune of receiving feedback from exceptional researchers involved in a broad range of disciplines. Drs. Warren Finlay and Kumar Nandakumar provided valuable advice and suggestions in the early stages of my research and for my candidacy examination. I am very grateful to Drs. Larry Kostiuk and Tian Tang for assuming the roles of my supervisory committee in the latter part of my studies. I would also like to thank the other members of my examining committee for lending

their keen insights to my research: Drs. Michael Lipsett, Nathalie Tufenkji, and Anthony Yeung. For their words of encouragement, I would also like to show my gratitude to Mr. Mark Ackerman and Drs. Eric M.V. Hoek, Donald Raboud and Sharon Walker.

I have special thanks for the office staff and IT personnel in the Mechanical Engineering department, who helped me with countless aspects of my life and work at the University; at many times, I felt like I had a whole team assisting me in this endeavour. The financial support of NSERC and the Queen Elizabeth II Doctoral Scholarship, as well as scholarships from Petro-Canada and the Canadian Heavy Oil Association, are also greatly appreciated.

I would like to acknowledge the moral support of many friends, and initially take exception to three in particular: Darek Kominek, for our philosophical discussions about a wide variety of topics, his unwavering support, and his raucous humor that has resulted in many outbursts of laughter; Anton Brereton, for his particular brand of humor that I cherish, and for continually reminding me that I am an artistic, as well as rational, soul; and Jay Easaw, for being a supportive coach, for empathizing with my academic struggles, and for inspiring me to run this marathon and show what I am truly capable of. I regard myself as very fortunate to have worked along side many talented researchers in the CCF lab. I am profoundly grateful to Farshid Mostowfi, Neda Nazemifard, Shahnawaz Molla and Noor Al-Quddus for their advice and friendship over the years, and I am especially thankful to my dear friend and research "twin" Tania Rizwan for being so supportive and the best sounding board I could ever ask for.

The completion of this thesis would not have been possible without the patience and support of my family. Although my father Leonce is no longer with us in body, I can see from my experiences with this work that his spirit lives on in some way through me; his words of wisdom from many years ago guided me on this journey. For my mother Audrey, I am so grateful for her love and persistence in standing by me, and the completion of this degree is perhaps my biggest gift to her. My sister Caroline, my brother-in-law Ron, and

my nieces Alexis and Hannah were four bright stars that guided me through the darkest nights of my life, providing the means to navigate when I lost my bearings. And of course, I am deeply thankful for having my sweet wife Nana by my side now. Her love, her words of encouragement, and her balanced perspective on life propel me forward with hope and faith.

Contents

List of Tables

List of Figures

List of Symbols

a_c	radius of spherical collector
a_i	radius of subunit i in heterogeneous substrate
a_p	radius of approaching spherical particle
A_a	area of semi-circular window from which particles are released near single spherical asperity
A_L	fraction of area A_a from which released particles are intercepted by single spherical asperity
A_{ip}	effective Hamaker constant between particle and subunit i
$A_{H,0}$	effective Hamaker constant between base subunit and particle
$A_{H,patch}$	effective Hamaker constant between patch subunit and particle
$A_{H,pa}$	effective Hamaker constant between particle and asperity
$A_{H,ps}$	effective Hamaker constant between particle and flat portion of heterogeneous substrate
b	half-height of channel, or radius of spherical fluid shell in Happel's cell model
d	surface-to-surface distance of closest proximity between particle and subunit of planar substrate
dV_i	differential volume element in subunit i
D_{ip}	distance between atom in subunit i and centroid of particle
D_∞	Stokes-Einstein (bulk) diffusivity of particle ($= k_B T/6\pi\mu a_p$)
e	fundamental electron charge
$\mathbf{e}_u$	unit vector in direction of $\mathbf{u}$
$\mathbf{e}_v$	unit vector in direction of $\mathbf{v}$

f_1, f_2, f_3, f_4	universal correction functions of hydrodynamic interaction (between sphere and flat plate)
$\mathbf{F}$	total DLVO interaction force vector acting on particle (for Chapter 3)
$\sum_i \mathbf{F}_i$	net external force vector acting on particle
$\mathbf{F}^{Br}(t)$	randomly fluctuating Brownian force vector acting on particle
$\mathbf{F}_{net}^{det}$	net deterministic force vector acting on particle
$\mathbf{F}^{DLVO}$	total DLVO interaction force vector acting on particle
$\mathbf{F}^{DLVO*}$	scaled total DLVO force vector acting on particle ($= \mathbf{F}^{DLVO} a_p / k_B T$)
$\mathbf{F}_{ps}^{DLVO}$	DLVO force vector acting on particle due to flat portion of composite substrate only
$\mathbf{F}_{pa}^{DLVO}$	DLVO force vector acting on particle due to asperity of composite substrate only
$\mathbf{F}^{EK}$	net electrokinetic force vector acting on particle
$\mathbf{F}_{fluid}^{drag}$	fluid drag force vector acting on particle due to fluid motion
$\mathbf{F}^{g}$	gravitational force vector acting on particle
F_x, F_y	resultant forces acting on particle in $x-$ and $y-$ directions, respectively
F_L	resultant lateral force acting on particle in $x-y$ plane
F_L^*	scaled lateral force acting on particle ($= F_L a_p / k_B T$)
F_z	resultant normal force acting on particle in $z-$ direction
F_z^*	scaled normal force acting on particle ($= F_z a_p / k_B T$)
F_L / F_z	ratio of total lateral force over total normal force acting on particle
h	separation distance between heterogeneous substrate and particle
h_{min}	separation distance between particle and closest feature of composite substrate
H	scaled separation distance ($= h / a_p$)
H_a	scaled separation distance between particle and closest asperity of composite substrate

H_s	scaled separation distance between particle and flat portion of composite substrate
H_{min}	scaled separation distance between particle and closest feature of composite substrate ($= h_{min}/a_p$)
I	molar concentration of electrolyte (*i.e.*, solution ionic strength)
k_B	Boltzmann's constant
m	mass of particle
$\mathbf{m}$	vector of two normally distributed random numbers
$n(x,t)$	number of particles per unit volume at distance x and time t
$\mathbf{n}$	unit normal vector with respect to distance of closest approach to composite substrate
$\mathbf{n}_f$	unit vector for direction of net DLVO force vector
$\mathbf{n}_s$	substrate surface normal vector for point of closest approach to composite substrate
$\mathbf{n}_{PAP}$	unit normal vector for PAP
$\mathbf{n}_{PSP}$	unit normal vector for PSP
N	number of released particles
N_A	Avogadro's number
N_S	number of subunits in planar substrate
p	pressure of the dispersing medium (*i.e.*, fluid)
p^*	scaled pressure of the dispersing medium ($= a_p p/\mu U_{avg}$)
Pe	particle Peclet number ($= U a_p/D_\infty$)
r^*	scaled radial position with respect to center of asperity
$\mathbf{r}$	position vector
$\mathbf{r}^*$	scaled position vector ($= \mathbf{r}/a_p$)
$\mathbf{R}$	total displacement vector of particle over time step Δt
$\mathbf{R}^*$	scaled total displacement vector of particle over time step Δt
$\mathbf{R}^{Br}$	random Brownian displacement vector of particle over time step Δt
$\mathbf{R}^{det}$	net deterministic displacement vector of particle over time step Δt

R_H	Hamaker constant ratio
Re, Re_{ch}	bulk Reynolds number
Re_p	Reynolds number for flow near channel wall's surface
s	surface-to-surface separation distance between two asperities (on the $x-$ axis)
St	Stokes number ($= 2\rho_p U a_p/9\mu$)
t	time elapsed
t^*	scaled time elapsed ($= t(D_\infty/a_p^2)$)
$\mathbf{t}$	unit tangential vector with respect to distance of closest approach to composite substrate
Δt	time step
T	temperature of dispersion medium
$\mathbf{u}$	undisturbed fluid velocity vector
u_n, u_t	normal and tangential components of $\mathbf{u}$
$\mathbf{u}^*$	scaled undisturbed fluid velocity vector ($= \mathbf{u}/U_{avg}$)
u_x^*, u_y^*, u_z^*	Cartesian components of $\mathbf{u}^*$
$u_{x,flat}^*$	scaled undisturbed fluid velocity in $x-$ direction for smooth, flat substrate
$\lvert\delta u_x^*\rvert$	absolute error in $x-$ component of $\mathbf{u}^*$
$\lvert\delta u_y^*\rvert$	absolute error in $y-$ component of $\mathbf{u}^*$
$\lvert\delta u_z^*\rvert$	absolute error in $z-$ component of $\mathbf{u}^*$
U	characteristic fluid velocity
U_{avg}	average fluid velocity in channel (from parabolic Poiseuille flow)
U_∞	approach velocity of fluid
U_{ip}^{vdW}	vdW interaction energy between subunit i and particle
U_{fp}^{vdW}	total vdW interaction energy between planar substrate and particle
U_{ip}^{EDL}	EDL interaction energy between subunit i and particle
U_{fp}^{EDL}	total EDL interaction energy between planar substrate and particle

U_{fp}^{DLVO}	total DLVO interaction energy between planar substrate and particle
$\mathbf{v}$	particle velocity vector due to fluid flow only
v_x, v_y, v_z	Cartesian components of $\mathbf{v}$
v_n, v_t	normal and tangential components of $\mathbf{v}$
$\mathbf{v}_{net}^{det}$	net deterministic velocity vector of particle
w	width of channel
(x, y, z)	Cartesian coordinates in the $\mathbf{i}$, $\mathbf{j}$, and $\mathbf{k}$ directions
$\mathcal{A}, \mathcal{B}, \mathcal{C}$	hydrodynamic interaction tensors
$\mathcal{I}$	unit tensor
$\mathcal{Z}$	zero tensor

Greek Symbols:

α	angle between unit vectors $\mathbf{n}_f$ and $\mathbf{n}_s$
β	angle between unit vectors $\mathbf{e}_u$ and $\mathbf{e}_v$
β_{ip}	Lifshitz-van der Waals energy constant for interaction between atom in subunit i and atom in approaching particle
$\dot{\gamma}$	shear rate
$\dot{\gamma}^*$	scaled shear rate
Γ_a	no-slip boundary of asperity (or asperities) in Ω
Γ_s	no-slip boundary of flat surface in Ω
Γ_{in}	far-field inlet boundary where simple shear flow is applied to Ω
Γ_{out}	oultet/normal boundary of Ω
Γ_{sym}	slip-symmetry boundary (*i.e.*, $x-z$ plane of symmetry) of Ω
δ_{ij}	Kronecker delta
$\delta(t_2 - t_1)$	Dirac delta function
ϵ	permittivity of dispersing medium at temperature T
ζ	frictional coefficient of particle ($= 6\pi\mu a_p$ in this study)
η	total initial collection efficiency of single spherical collector

η_I	initial collection efficiency of single spherical collector due to interception only
θ	angle around top half of the asperity, measured from front stagnation point
κ	inverse Debye length
λ	asperity-to-particle size ratio ($= a_a/a_p$)
μ	absolute viscosity of dispersing medium at temperature T
ν	valency of electrolyte
ν_i	total charge number on subunit i of planar substrate
ν_p	total charge number on particle
ρ_f	density of dispersing medium (*i.e.*, fluid density)
ρ_i	number of atoms per unit volume in subunit i
ρ_p	number of atoms per unit volume in particle, or density of particle
σ^*	scaled hydrodynamic stress tensor
σ_R	square root of mean squared displacement of particle
τ^{Br}	particle's momentum relaxation time ($= m/6\pi\mu a_p$)
τ^{det}	upper limit of time step for non-accelerating particle motion
ϕ_a	deposition probability for asperity (or asperities)
ϕ_T	total deposition probability for entire composite substrate
ϕ_{flat}	deposition probability for flat substrate
ψ_i	surface potential of base subunit i
$\psi_{i,patch}$	surface potential of subunit i of heterogeneous patch
ψ_p	surface potential of particle
ψ_a	surface potential of asperity on heterogeneous substrate
ψ_s	surface potential of flat portion of heterogeneous substrate
ψ_{avg}	mean-field (based on surface area average) surface potential of heterogeneous substrate
Ψ_L	limiting particle trajectory
χ	porosity of porous medium
Ω	computational domain for undisturbed hydrodynamic field

Abbreviations:

ALE	arbitrary Lagrangian Eulerian method
$DLVO$	Derjaguin-Landau-Verwey-Overbeek
EDL	Electrostatic Double Layer
HHF	Hogg-Healy-Fuerstenau (often referred to as Hogg *et al.*)
HIM	Heterogeneous Interaction Model
PAP	particle-asperity proximity
PSP	particle-flat surface proximity
PTM	Particle Tracking Model
RSA	Random Sequential Adsorption
SEI	Surface Element Integration technique
UCF	universal correction function (*i.e.*, f_1 to f_4)
vdW	van der Waals

Chapter 1

Introduction

1.1 Background and Overview

The deposition of particles onto solid surfaces is relevant to many fields of endeavour in industry and research. There are situations in which deposition is desirable, including the filtration of pollutants from water (*i.e.*, with particles depositing on collectors, such as filter grains or fibres) and various manufacturing processes that require a coating of particles to be formed on a surface. For some other situations, the goal is to prevent deposition, such as with the fouling of heat exchangers, the formation of biofilms harbouring bacteria, and mineral processing. With the growing number of applications of microfluidics and the advent of nanotechnology, there is increasing interest in a deeper practical understanding of the deposition of nanoscale particles to improve the efficiency and throughput of many processes in biomedical, environmental, forensic and materials sciences and engineering.

Deposition involves the transport of particles to a large surface, or collector, where they are adsorbed (*i.e.*, become attached, as shown schematically in Figure 1.1). This thesis is aimed toward elucidating the processes and mechanisms of a particle traversing the fluid and attaching itself to the surface. During the transport stage, particles are brought closer to the collector by Brownian motion, fluid motion, and/or field forces such as gravity over comparatively large (with respect to particle size) distances. Once the particles are very close to the collector, then colloidal interactions contribute signifi-

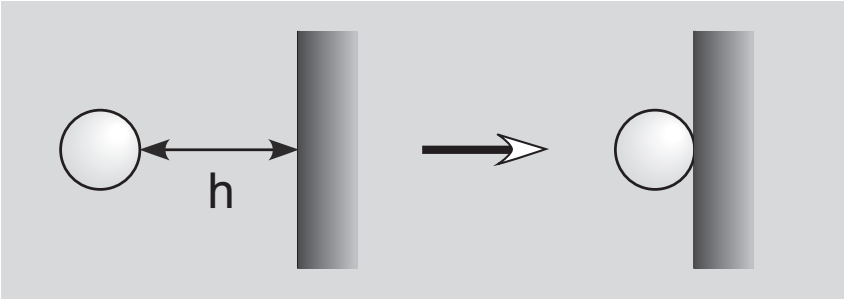

Figure 1.1: Schematic representation of the deposition process. The left side depicts the transport stage of the process, with the two entities separated by a distance h, and the right side shows the adsorption stage, when the two entities collide and remain attached.

cantly to particle transport. In studies of colloid deposition (*i.e.*, for particles in the size range of 10^{-9} m $< a_p < 10^{-5}$ m, where a_p is the particle radius), colloidal interactions are often modeled using the classic DLVO (Derjaguin-Landau-Verwey-Overbeek) theory [DL41, VO48], which states that the total interaction energy or force between two colloidal bodies is a function of their separation distance h. As the sample relationships of Figure 1.2 demonstrate, the DLVO interaction energy or force can be attractive or repulsive depending on h. The theory also suggests that the attraction or repulsion is determined by, among other factors, the chemical and physical properties of the surfaces of both the particles and the collector.

Given the complexity and lack of sufficient detail available with real scenarios involving deposition, models (mathematical and experimental) and simulations of the process are typically constructed with simplifying assumptions, such as uniformly spherical particles, smooth collector surfaces, constant surface-chemical conditions and laminar flow [EGJW95]. The mechanisms of particle transport in models of deposition are divided into three categories: (i) convection, (ii) diffusion, and (iii) migration. These mechanisms are often handled independently and then added together to depict the deposition process. Convection, which is sometimes referred to as advection in this context, is a deterministic mechanism by which hydrodynamic forces such as viscous drag carry the particle along with the fluid flow. It can be the dominant

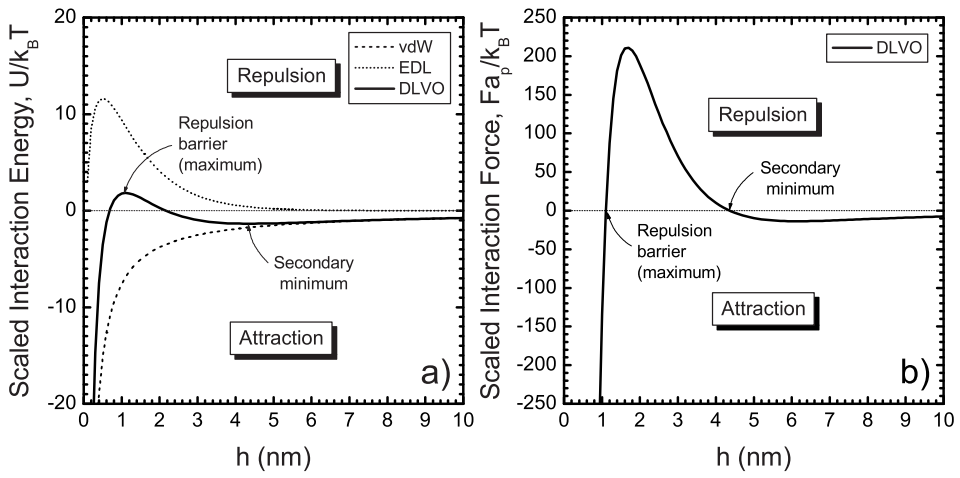

Figure 1.2: Sample relationships of (a) interaction energy and (b) interaction force between a flat plate and a sphere with separation distance, h, in accordance with the DLVO theory.

transport mechanism when the particle is far from any surface if the magnitude of the bulk flow is substantial [RSS89, vdV89]. Diffusion is due to the random, Brownian motion of the particle in the fluid, and the rate of this stochastic transport mechanism increases with increased system temperature and decreased particle size [Ada06]. Migration is also a deterministic mechanism with force components that can – depending on the properties of the colloidal system – be involved in particle transport at all separation distances. These migrational forces can include those of colloidal interactions (close to the substrate), as well as gravitational force (far from the surface; leading to sedimentation) and forces from externally-applied electric or magnetic fields.

Particles move in response to the motion of the viscous fluid they are immersed in, but their motion also affects the fluid's flow over long ranges. If the fluid motion is in the Stokesian regime (*i.e.*, slow, laminar flow, also referred to as low Reynolds number hydrodynamics; $Re \ll 1$), then viscous damping is more significant than inertia. The steady state Navier-Stokes equations for depicting the velocity field $\mathbf{u}$ can be simplified in this flow regime to the Stokes

equation [CW75, D§9, KK05],

$$0 = -\nabla p + \mu \nabla^2 \mathbf{u} + \mathbf{f}_b, \tag{1.1}$$

for which μ is the fluid's absolute viscosity, p is the local pressure, and $\mathbf{f}_b$ is the external body force per unit volume. From the solution of Eq. (1.1) and the continuity equation (*i.e.*, conservation of mass) with a single, small sphere in an unbounded fluid, there is a linear relationship between the hydrodynamic force applied to the spherical particle by the fluid and the flow disturbance it produces at some distance away from itself, and *vice versa* [RSS89, KK05]. This reciprocal relationship, in which particles both react and contribute to the fluid's local velocity, can profoundly affect the way they hydrodynamically interact with each other and the walls of their container. Whether the fluid is at rest or in motion, these dissipative hydrodynamic interactions must be accounted for, reducing the velocities at which colloidal particles immersed in the fluid can approach each other and any collector's surface.

Hydrodynamic interactions (also known as hydrodynamic retardation) are the result of the fluid's molecules pushing against the approaching surfaces to resist their approach as the fluid is squeezed out of the shrinking space between them [KK05, Ada06]. Due to the linearity of the representative equations, hydrodynamic retardation for a given particle can be represented by a resistance tensor (the inverse of which is the particle's mobility tensor). From this resistance tensor, the diffusion coefficients of the particle can be derived and subsequently determine the mass transfer rate of particles in a given system [Ada06]. Hydrodynamic retardation affects all three particle transport mechanisms (convection, diffusion, migration), though each at different rates, which are represented as functions of separation distance for simple systems. With their widespread applicability in studies of deposition, the understanding of hydrodynamic interactions in various scenarios continues to be a topic of research. However, to this author's knowledge, there is no prior study concerning the hydrodynamic interactions between "real" surfaces containing physical heterogeneity in the sub-micrometre scale.

1.2 Problem Statement

Nearly all surfaces, including those that appear to be smooth to the naked eye, have some roughness at submicron ($< 10^{-6}$ m) or even molecular ($\approx 10^{-9}$ m) length scales. There is considerable interest in how such roughness, and variations in chemical composition at those scales, may influence the trajectories of colloidal particles near fluid-solid interfaces and the subsequent deposition of the particles onto the solid substrate. Efforts of many researchers have provided a comprehensive understanding of the mechanisms of particle deposition. Some research has attempted to determine how the physical and/or chemical properties of a surface can be altered to encourage the deposition of colloidal entities at particular locations [DD08, SZSR09, CDS09]. Nevertheless, various aspects of particle deposition phenomena are still persistently debated, and the level of sophistication of the models of the systems is often the source of debate.

In this thesis, the primary goal is to examine how the presence of chemical and/or physical heterogeneity on a substrate affects the deposition of spherical, Brownian particles on it when the system is immersed in a Stokesian (Newtonian with $Re \ll 1$) fluid with all solid surfaces fully-wetted. This general type of system has been used to model a variety of applications and phenomena, both natural and artificial, such as the filtration of pollutants from water, the adhesion of microorganisms to surfaces or the site-specific delivery of drugs to mitigate side effects. Some questions that have been posed with such a system include: Can the location where a particle contacts the surface be predicted with a high probability? How can the physical and chemical properties of the system be changed to encourage or discourage the deposition of a particle on the surface? At what scale (relative to particle size) of surface roughness do particle deposition phenomena begin to change from what is observed with a flat, smooth surface? Finally, deposition models and simulations also typically consider ideal flows (*e.g.* one-dimensional shear flow or radial stagnation flow). However, when particles are interacting with the collector surface, sur-

face roughness of a substantial scale can produce modifications to the ideal representation of the fluid flow near the substrate, thereby altering convective particle transport in this region. In light of this, another question that has rarely been asked before is whether or not hydrodynamic disturbances induced by surface roughness can modify particle transport during deposition.

1.3 Objectives and Scope

1.3.1 Objectives of the Present Study

To confront the preceding questions and issues, this research has the following major objectives:

1. Show how the colloidal interactions between a spherical particle and a collector can be affected when the collector surface – often considered smooth and chemically uniform – has features of physical and/or chemical heterogeneity.

2. Demonstrate the value and significance of rendering undisturbed (*i.e.*, without particles in the fluid) flow fields near substrates with nanoscale roughness as accurately as possible.

3. Develop a particle transport simulation tool that approximates the effect of hydrodynamic retardation on a Brownian particle as it approaches a physically and/or chemically heterogeneous substrate.

4. Using this simulation tool, explore scenarios involving Brownian particles that reveal how the presence of physical and/or chemical heterogeneity on a substrate can affect the deposition probability and rate, and subsequent morphology, of the deposit on such a substrate.

1.3.2 Scope of the Present Study

For many previous studies of deposition, the assumption of smooth, chemically-uniform surfaces for all interacting bodies greatly simplified the calculations

for all three particle transport mechanisms (*i.e.*, convection, diffusion and migration), but at the expense of representing the system realistically. When the model collector (or substrate) is rendered with features of heterogeneity on a scale similar to the particle size, this added realism also entails challenges in depicting particle transport near the collector surface. Thus far, no rigorous mathematical model of deposition has been developed that precisely depicts particle transport at all separation distances from a collector surface of arbitrary heterogeneity. Even if such a rigorous model existed, its inclusion in a simulation tool for particle transport and deposition would constitute a heavy computational burden, increasing run times considerably and thereby limiting the tool's usage. In order to grapple with the complexities that accompany any heterogeneity of the collector, the models in the present study employ a few assumptions and approximate techniques to calculate hydrodynamic and colloidal interactions. In doing so, these models furnish a means to bridge the gap between real systems and their idealized, homogeneous representations.

Conceptually, the general approach presented in this study can be applied to an arbitrarily rough substrate. However, to demonstrate the applicability of the approach, and to compare the developed model against existing approaches, a simpler geometry has been devised to represent a rough substrate. The model geometry consists of one or more spherical asperities attached to a smooth flat plate. The objectives of this thesis are to systematically address how the presence of these asperities modifies the hydrodynamics and colloidal interactions of the system, which consequently influence particle convection, diffusion and migration (due to colloidal interactions) near the substrate. In place of a broad scan of the parameter space that the models from this approach can explore, this investigation includes a selection of particular cases of interest. These cases explore different configurations of physical (through size and spatial distribution of asperities) and/or chemical (through colloidal interaction parameters) heterogeneity to reveal and discuss their general effects on deposition phenomena.

1.4 Organization of the Thesis

In this chapter, a brief overview of the process of deposition has been presented, followed by a description of the objectives and scope of the present study.

Chapter 2 is a detailed review of previous research efforts into particle deposition, starting with established models and then following their evolution (*i.e.*, incorporating heterogeneity in various ways).

In Chapter 3, the Heterogeneous Interaction Model is proposed and used to examine the colloidal interactions between a particle and a planar substrate with regions (*i.e.*, patches) of chemical heterogeneity. The same model is then employed to look at the effects of physical heterogeneity on colloidal interactions using a chemically-uniform substrate with a single, spherical asperity on it. The fluid is always at rest with this model.

A Lagrangian particle tracking model that accounts for convection, diffusion and migration (colloidal interaction) forces, as well as hydrodynamic interactions, near a "rough" substrate is described in Chapter 4. The hydrodynamic field used with this model is numerically determined by solving the Stokes equations for the specified substrate topography. The substrate can also be rendered chemically heterogeneous.

After establishing the limits of the parameter space explored in this study, validations of various aspects of the particle tracking model presented in Chapter 4 are made in Chapter 5. These validations include those for testing the accuracy of the hydrodynamic field, Brownian motion, and comparisons with the results from earlier studies using the classic Happel cell model for deposition on a single spherical collector.

Chapter 6 presents the results of simulations for scenarios, starting with a single asperity on a planar substrate and then with multiple asperities in a variety of configurations. Some simulations are with only deterministic forces acting on the particle, and the others are full simulations that also include Brownian displacements. The results from a variety of noteworthy scenarios are discussed in this chapter.

Lastly, conclusions from the present study and suggestions for potential avenues of future work stemming from this investigation are given in Chapter 7.

Chapter 2

Literature Review

2.1 Introduction

Research into colloid deposition phenomena is rich and diverse, spanning many fields of endeavour for more than a century. More specifically, particle deposition is an extensively studied subject, relevant to filtration, fouling of flow channel walls and membranes, chromatographic separations, colloid transport in groundwater, and numerous other natural and engineered processes. Some of these investigations have concentrated on only colloidal interactions, while others have tried to depict the kinetics of deposition from far-field transport to adsorption on the surface. This review of previous literature in this field is divided into two major parts, with the first part delving into research on colloidal interactions and the second part on models of particle transport and deposition. The common direction in both parts is from studies of homogeneous systems to those with some form of heterogeneity.

2.2 Colloidal Interactions

2.2.1 Validity of the Classical DLVO Theory

In the deposition process, colloidal interactions are manifested over the shortest range of distances. The phenomena associated with the interactions of colloidal particles with surfaces have been studied for decades in innumerable ways, and the DLVO interaction model has often been the mainstay of these

studies. The merits of using DLVO theory to assess colloidal phenomena in real systems have also been debated a great deal over the past six decades. However, as Ninham [Nin99] stated:

> *The genius of DLVO lies not in complicated models that add more and more parameters, but in its extraction of the essential physics of the problem of lyophobic colloid stability.*

Basically, the DLVO theory is a tool with which to interpret the qualitative characteristics of complex colloidal phenomena engendered by Lifshitz-van der Waals forces and electrostatic interactions.

Albeit approximate, the theory tends to capture the underlying physics of colloidal interactions quite well for some clearly defined systems [Nin99]. The experiments of Israelachvili [Isr92] sought to determine the interaction forces between two molecularly-smooth mica surfaces and the results showed remarkable agreement with the DLVO model. Nonetheless, the DLVO theory remains controversial, as many individuals subscribe to it wholesale while others reject it in part or in its totality. Criticisms have been raised through comparisons with ample experimental evidence [Nin99, Isr92, KN01], whereby the DLVO theory has been shown to falter when applied to many real systems, including biological ones. It is unclear whether or not the characteristics of the systems tested in these experiments violated any of the key assumptions that the DLVO theory is based upon, which include the following:

- The solvent (*i.e.*, dispersing medium) is treated as a continuum;
- The ions in the solvent are treated as points (*i.e.*, no volume) and are from indifferent electrolytes (*i.e.*, no specific ion interactions, possibly leading to chemical reactions, etc.); and
- The interacting colloidal bodies have smooth surfaces and simple geometric forms, such as cylinders, spheres and planes.

Some researchers have sought to bridge the gap between theory and experiment by adding new forces to compensate, leading to an extended DLVO

interaction model. The most frequently added force is the solvation force, which is attributed to the layered structure of solvent molecules very close to solid-liquid interfaces. Current theory explains that as two such solid surfaces approach each other, layer after layer of solvent molecules are pushed out of the closing gap [LHLS07]. The chemical nature of the surfaces determines if the force is repulsive, attractive or even oscillatory [CL06, LHLS07]. If the surfaces contain non-polar groups, then the polar molecules like water would prefer to escape the gap, generating an attractive force referred to as hydrophobic attraction. When the surfaces contain polar or charged groups, a repulsive hydration force emerges [IW96, RK02, vOG04] because energy is required to remove polar solvent molecules from polar surface groups [CL06]. An investigation of hydration forces between silica surfaces by Valle-Delgado *et al.* [VDMBGG$^+$05] used many prominent models – from the phenomenological model of Marčelja and Radić [MR76] to the Ruckenstein and Manciu model [MR04] – for comparison with their experimental results. Each of these models proposes a unique mechanism to explain the microscopic nature of the hydration force, but it was acknowledged that the origin of the force may differ depending on the system (mica, lipid bilayers, silica, proteins, *etc.*) [VDMBGG$^+$05]. They concluded from their data that formation and breaking of hydrogen bonds was the main contributor to the force, perhaps combined with one or more other mechanisms. Nonetheless, these solvation forces are expected to act over very short separation distances ($<$ 1-2 nm), and therefore, they are only significant for modeling the adsorption stage of the deposition process.

Some other types of interactions and forces that have been proposed include depletion forces [AO54, WS94, VHRMC07], steric interactions [Isr92, LHLS07] and specific ion effects [BWN01, MR04, CL06], all of which are complicated and their respective theories continue to evolve. Naturally, most types of forces added to describe colloidal phenomena are manifestations of factors that were ignored in the original DLVO model. Specific ion effects, for instance, are concerned with ion types and their affinities for water and other ions in the

system [CL06], but the DLVO model assumes electrolyte ions to be indifferent, charged point masses. Looking back at the tremendous developments in the general subject of colloidal interactions, one is faced with a fundamental question concerning the application of these compensatory forces: since the interactions between atoms are primarily dictated by van der Waals and Coulombic (*i.e.*, electromagnetic) forces, how can other types of forces manifest themselves in colloidal systems? The present study attempts to address this question by modeling a planar surface in a manner that is as realistic as possible while adhering to the assumptions of the DLVO theory stated above.

In this context, the fundamental assumptions in the DLVO interaction model, such as, continuum solvent, point charge ions obeying the Boltzmann distribution, pairwise summation of attractive dispersion interactions between two macro-bodies, are consistently shown to be fairly robust for many colloidal systems. For instance, the granularity of the solvent and ions do not manifest themselves substantially unless two charged surfaces are brought to sub-nanometer separations [RSS89]. Similarly, the ion correlations are usually governed by the Boltzmann distribution in the Debye-Hückel limit (salt concentrations < 0.5 M) [TV79, TV80, JWH80]. Another significant factor to consider in these colloidal systems is whether or not all of the interacting surfaces are fully wetted. In a recent study using a colloidal polystyrene particle mounted on an AFM (Atomic Force Microscope) cantilever tip, Thormann *et al.* [TSHM08] discovered that the interaction forces between the particle and a hydrophilic (*i.e.*, fully wetted) surface exhibited DLVO-like characteristics. When the same surface was hydrophobic, the measured interaction forces were very different from DLVO theory, and this was attributed to the formation of air bubbles between the particle and the surface [TSHM08]. The presence of air bubbles would alter the dispersing medium's characteristics (such as its dielectric constant) in the gap between the surfaces, and hence a dramatic change in interaction would be expected. On the basis of this evidence, it seems plausible that the leading cause of failure of the DLVO model at reasonable separations between two charged colloidal objects (separations $>$ 1-2 nm)

is an inadequate resolution of the interacting surfaces with respect to their physical and chemical properties. Traditionally, one recasts a real colloidal system in terms of geometrically regular and chemically homogeneous objects, and applies the DLVO interaction model to this simplified system.

2.2.2 Introducing Heterogeneity to the DLVO Model

The accuracy of the DLVO theory has often been questioned in the context of its ability to describe interactions between heterogeneous colloidal objects. Physical and/or chemical heterogeneity in real colloidal systems have been considered as the key factors leading to the inadequacy of the DLVO model [Don02, WRE04]. In spite of this, many theoretical and experimental studies of colloidal interactions persist in considering all bodies to be physically and chemically homogeneous. On the other hand, there have been studies involving real cell membranes with their inherent heterogeneity that have reported generally useful information concerning colloidal interactions. An investigation of microbial adhesion by Dorobantu *et al.* [DBFG08] mapped surface heterogeneities of two bacterial species immersed in an aqueous buffer using AFM and discovered a direct correlation between their spatial heterogeneity and differences in adhesion forces determined from retraction force curves. Interaction forces with both species were also found to vary when the chemically-functionalized AFM tips were changed from hydrophilic and hydrophobic. In light of the above discussion, it would be of interest to explore avenues of modeling real colloidal interfaces and particles as collections of nanoscale subunits. Such DLVO interaction models can be applied to describe the interactions between the subunits while allowing greater flexibility of incorporating nanoscale physical and chemical heterogeneities of the surface.

An important aspect of incorporating such a model in the framework of the DLVO theory is to establish the three-dimensional nature of the resulting interaction forces. Even when heterogeneity is present in the model, nearly all studies thus far have disclosed data on interaction energies and forces acting normally between the interacting surfaces. Although lateral forces have

been mentioned in studies on surface roughness [Cza86, CW87, Wal98], there has been little substantive effort to quantify these forces on physically and chemically heterogeneous substrates in terms of DLVO interactions. When considering the three-dimensional nature of the interaction forces, it is pertinent to explore the influence of lateral forces caused by heterogeneities on colloidal phenomena, such as the attraction or repulsion of particles to/from particular regions of a surface. An investigation by Busscher *et al.* [BPB98] concluded that lateral DLVO interaction energies arising from minor chemical or structural heterogeneities and leading to the adhesion of two surfaces are one order of magnitude smaller than the perpendicular interaction energies between them. However, there is no explicit determination of the DLVO interaction forces, lateral or perpendicular, in their study. The work of Ma *et al.* [MSH$^+$07] is one exception, for which lateral forces were estimated to be as strong as 3×10^{-7} dynes (3×10^{-12} N) for the electrostatically-guided placement gold nanoparticles in a CMOS (Complementary Metal Oxide Semiconductor) fabrication process.

2.2.3 Interaction Models with Physical and/or Chemical Heterogeneity

With the objective to produce a more sophisticated and realistic model, there have been both theoretical and experimental studies in the past three decades that have included some type of physical and/or chemical heterogeneity in their systems. The following examples include studies of physical heterogeneity in the form of surface roughness [Wal98, HBE03], and studies of chemical heterogeneity in the form of variations of electrical surface charge or potential and/or variations in material composition leading to altered van der Waals interactions [CHG03].

Physical Heterogeneity

Czarnecki and Dąbroś [CD80] were among the first to construct models that included surface roughness, calculating the van der Waals (vdW) interaction

energy between a rough particle and the smooth surface of a semi-infinite medium. Various particle sizes, thicknesses of roughness and separation values were compared, and their efforts yielded a simple correction factor to estimate the influence of surface roughness on the vdW interaction energy. Czarnecki continued to explore this subject with rough unequal-sized colloidal spheres, and concluded that surface irregularities have significant effects on the vdW energy only at very close separation distances between the bodies [Cza86]. These irregularities were "smoothed out" at larger distances, where the volumes of the bodies were more prominent in determining the interaction energy [Cza86]. In another paper with Warsynski [CW87], the estimated tangential (with respect to the line of approach between the spheres) vdW forces were compared with the corresponding hydrodynamic drag forces acting on the spheres and found to be of similar magnitudes, therefore possibly playing a role in particle immobilization in some deposition scenarios. Herman and Papadopoulos determined how spherical and conical asperities [HP90] and depressions [HP91] in two parallel plates affect the van der Waals and double layer interactions between them. Although physical heterogeneity of both a convex and concave nature were explored in these two studies, again only interaction energies were calculated and interactions with colloidal particles were not considered.

While investigating the effect of particle size on collision efficiency, Elimelech and O'Melia [EO90b] created a model to simulate the interaction energy between a smooth particle and a flat plate with a single, hemispherical asperity. Assuming low surface potentials and applying the Derjaguin approximation [Der34, Whi83], the energy barrier to deposition for rough surfaces was found to be lower than for smooth surfaces. This result was echoed when Suresh and Walz [SW96] investigated how roughness on a colloidal particle's surface would affect its DLVO interaction energy with a smooth plate. They found that at close separations, an increase in vdW attraction energy lowered the height of the repulsive energy barrier. Again, physical heterogeneity was used to explain why capture rates observed in experiments were higher than what was predicted with DLVO theory for smooth surfaces.

In an effort to incorporate the exact topographies of interacting surfaces into models of colloidal interactions, the surface element integration (SEI) technique was devised [BE97, BKE98]. This technique numerically integrates the interaction energy per unit area between directly opposing differential planar elements over the entire surfaces of the two colloidal bodies to obtain the total interaction energy [ZBC$^+$08]. Whether the interaction originates from the particle's volume (as with Hamaker's approach to vdW interactions) or from its surface (as with EDL interactions), the equivalence of surface and volume integrals through Gauss' divergence theorem allows SEI to accommodate surface and body forces in its calculations [BE97]. The SEI technique has been included in the models of various studies to account for surface roughness. To name a few, Hoek and Agarwal [HA06] applied SEI to an extended DLVO model for membrane applications, Martines *et al.* [MCM$^+$08] pondered the benefits of patterning surfaces with regular features at the nanoscale that are much smaller than a particle interacting with them, and Zhao *et al.* [ZBC$^+$08] explored the influence of particle surface roughness on the stability of clay suspensions.

The repulsive energy barrier is perhaps the most crucial element in ascertaining the stability of a colloidal system, which depends on the electrostatic double layer force (EDL). Das and Bhattacharjee [DB05] determined the EDL force on a spherical particle approaching the center of a flat substrate with four previously deposited particles placed at the vertices of a square. The previously deposited particles imparted a physical heterogeneity to the otherwise chemically homogeneous substrate (*i.e.*, uniform, constant surface potential for all components). The force, in the normal direction, was calculated for several different interaction ranges (*i.e.*, screening or inverse Debye lengths, which are based on electrolyte concentration of the fluid) and separation distances. Two different approaches were used to determine the force: first, by solving the nonlinear Poisson-Boltzmann equation with appropriate boundary conditions for the three-dimensional geometry; and second, by a pairwise additive approach, summing the interaction forces between the free particle and each previously

deposited particle and the flat plate. Both approaches showed that the repulsive EDL force on the approaching particle was markedly lower for this physically heterogeneous, many-body scenario than for a smooth sphere-plate interaction, and the reduction in force was more pronounced when the screening length is close to the particle radius [DB05]. The pairwise additive approach to determining the EDL force also overestimated its magnitude for such scenarios. These results are very similar to those found by Phillips [Phi95], who used a singularity method with the linearized Poisson-Boltzmann equation for three previously deposited, spherical particles positioned at the vertices of an equilateral triangle.

As useful as these models have been, they have some limitations and disadvantages in common. None of them accounted for chemical heterogeneity in the system, they are incapable of dynamically (with time) altering the topography of the interacting entities, and typically only the net normal force component between the entities was calculated with them. Comprehensive models of physical heterogeneity like SEI and fractals also do not integrate well with colloid transport models, mainly due to the intensive computations required for only the colloidal interactions at each time step.

Chemical Heterogeneity

Research into chemically heterogeneous colloidal systems has been frequently aimed at sphere-sphere and plate-plate interactions, (*i.e.*, aggregation) but less often at sphere-plate interactions (*i.e.*, deposition), especially with the DLVO theory included in the model. With two interacting flat surfaces modeled as periodic lattices of arbitrary configuration, Miklavic *et al.* [MCWH94] looked at two scenarios for EDL interactions between them. For the first scenario, one surface had non-uniform, but net neutral, charge while the other had uniform charge. In this case, the interaction energy was either attractive or repulsive depending on whether the surfaces were constrained with constant charges or constant potentials. When both surfaces had non-uniform surface charges, the attraction or repulsion of the surfaces depended on whether or

not regions of like and unlike charge were directly opposite from one another. Holt and Chan [HC97] applied the periodic patchy model of Miklavic *et al.* to two charge-heterogeneous spheres. They found substantial free attractive energies when the lattices of the spheres were misaligned, and large restraining torques even at significant separation distances (like the secondary DLVO energy minimum; refer to Figure 1.2). However, the size of the particles in this study was large relative to the screening length of the EDL interactions (*i.e.*, thin electrostatic double layers), and for a uniformly charged system with the parameters used, a highly attractive secondary minimum would be present anyway according to DLVO theory. An analytical model by Velegol and Thwar [VT01] estimated the mean EDL force between two plates, and then two spheres, with random, non-uniform surface charge distributions. Although the paper did not provide firm conclusions regarding the effects of charge non-uniformity on hydrophobic phenomena and colloidal stability, the model predicted the potential of the mean EDL force at any practical gap distance that is experimentally measurable. The systems observed with this model also had thin double layers [VT01].

Chemical heterogeneity through surface charge or potential non-uniformity is often achieved experimentally by preparing surfaces with coatings of functionalized molecules such as alkanethiols. Chun *et al.* [CHG03] created surfaces with nanoscale, patchwise distributions of two types of alkanethiols (with hydrophilic methyl and hydrophobic carboxylic acid sites) that interact differently with a polyacrylic acid polymer in an aqueous solution. At a certain concentration of heterogeneous sites, significant quantities of polymers adsorbed on the surface, and they concluded that the amount of polymer adsorbed was dependent on the fraction of heterogeneous sites present [CHG03]. From a different experimental perspective, Taboada-Serrano *et al.* [TSVYT05] employed force-volume-mode AFM to map interaction forces on a flat, silica surface and relate them to surface charge heterogeneities. Copper ions were adsorbed onto select regions of the silica surface to modify local surface charge and produce charge reversal, and local differences in both the magnitude and direction of

surface forces were measured in the vicinity of these regions. Thus far, chemical heterogeneity remains a challenge to create experimentally, especially in a spatially-ordered manner on the micro- or nano- scale. Using a soft lithographic technique, Rizwan and Bhattacharjee [RB09] produced self-assembled monolayers of the carboxyl- and amine-terminated alkanethiols in striped patterns to study the deposit morphologies of polystyrene particles on the charge-heterogeneous surfaces. Comparisons of the experimental results with the results from Monte Carlo RSA (Random Sequential Adsorption) [Fed80, ST89] simulations showed good agreement, adequately predicting the periodicity of the patterns on the substrate. More specifically, it was found that the particles preferred to deposit at the edges of the attractive stripes, and this was controlled by the stripe width relative to the particle size [RB09].

Models that explicitly consider the effects of chemical heterogeneity on planar substrates on colloidal interaction forces in two or three dimensions have only recently emerged. An investigation by Kemps and Bhattacharjee [KB05], which is discussed in greater detail in Chapter 3, had the specific aim to model chemically heterogeneous colloidal systems in three dimensions using a homogeneous, spherical particle near a planar substrate that had regions with different chemical compositions and electric surface potentials. Using a scheme referred to as "electrostatic funneling", the study by Ma *et al.* [MSH$^+$07] mentioned earlier produced alternately charged lines of about 100 nm width to achieve a precision of 6 nm in gold nanoparticle placement. The long range interactions observed in their experiments were in good agreement with their "semiquantitative" calculations based on DLVO theory, which looked only at two dimensions.

Physical and Chemical Heterogeneity

Although it is prudent to explore the effects of physical and chemical heterogeneity separately, real colloidal systems usually possess both at the same time and place. Duval *et al.* [DLvL04] presented a theoretical formalism for electrostatic interactions between two heterogeneous surfaces. Their approach

accounted for the effects of surface roughness and non-uniform surface charge density, as well as specific interactions between ions in the intervening electrolyte and the surfaces themselves. Unfortunately, their model and its heterogeneity were only two-dimensional, but it is a rare example that considers physical and chemical heterogeneity concurrently.

One of the cornerstones of the SEI technique [BE97] is its use of the Derjaguin approximation [Der34, Whi83], which is only valid for short separation distances between interacting bodies. An exploration of the validity of this approximation for physically and chemically heterogeneous colloidal particles was undertaken by Rentsch *et al.* [RPCPB06]. Bare silica spheres of different sizes were used for observing the effects of physical heterogeneity, and then for chemical heterogeneity, positively-charged poly (amido amine) (PAMAM) dendrimers were adsorbed on the spheres in monolayers with low surface coverage, producing local charge reversal for the negatively-charged silica surfaces. Of course, the screening lengths of the EDL interactions in this study were small compared to the particle sizes used (*i.e.*, thin double layers). Using an AFM to measure the forces between the spheres, the Derjaguin approximation was found to be valid for heterogeneous substrates down to separation distances that compared with the characteristic sizes of the surface heterogeneities (*e.g.* attractive forces emerged at 10 nm distances, roughly equal to the expected inter-dendrimer spacing) [RPCPB06]. This conclusion supports the findings of the theoretical works by Miklavic *et al.* [MCWH94] and Stankovich and Carnie [SC99]. The authors also stated that the approximation would likely result in some deviations for systems with "highly pronounced lateral heterogeneities" [RPCPB06], but a threshold at which significant deviations would emerge was not presented.

2.3 Particle Transport and Deposition

2.3.1 Established Models of Particle Deposition

As stated earlier in Section 2.2.2, the majority of the previous studies of deposition phenomena, both theoretical and experimental, have been based on systems with no physical or chemical heterogeneity. These studies have modeled particle transport and deposition using one or both of two general approaches: Eulerian and Lagrangian. The Eulerian approach provides a macroscopic perspective of the deposition process, describing particles in terms of their concentration distribution, or probability density, in time and space [EGJW95]. The Lagrangian approach is from a microscopic perspective, following the trajectories of individual particles as they move in time in accordance with Newton's Second law of motion [EGJW95]. Both of these approaches have yielded particle transport equations for analytical and numerical models with ideal collectors, including rotating discs [Lev62, DA79, PL80], impinging jet flows [DvdV83, CR85a, CR85b, AZSC86, DvdV87], and parallel plate channels [BLE76, BE79, AvdV81, SB89, SB90]. Assuming all of the interacting surfaces are smooth, experimental data has been accumulated and analyzed to derive semi-empirical collection efficiency equations for surfaces in a number of scenarios. One such scenario that has gained prominence in several fields of research is the packed bed of spherical collectors, which has been used to simulate particle transport and deposition in granular porous media [YHO71, PRT74, RT76, TE04] like sub-surface soils and water filtration systems. Among the established models for packed beds, such as Brinkman [Bri47], Happel [Hap58], and Kuwabara [Kuw59], Happel's sphere-in-cell model is the most commonly used, and it has laid much of the groundwork for Colloid Filtration Theory (CFT).

The Lagrangian approach of trajectory analysis has been used extensively to describe the capture of non-Brownian particles with the Happel cell model, since their trajectories are deterministic and can be expressed analytically [EGJW95]. Trajectories of Brownian particles can also be determined with

this approach [vdV89], although it has been argued that the incorporation of Brownian motion requires time-consuming integration of the stochastic equation of motion over time [EGJW95]. Fortunately, a careful selection of time step length on the basis of particle size removes this impediment from the simulations [NG05, KB09].

When considering CFT for porous media, the physical heterogeneity of the system is typically modeled on the scale of collector grain size [RPW01], which is considerably larger than the scale that is explored in the present study. As Figure 2.1(a) shows, Happel's model depicts a porous medium as an assemblage of identical spherical collectors, each enveloped in a fluid shell, and therefore, having no contact with other collectors. Despite its physical isolation, the flow field around each spherical collector is affected by the presence of neighbouring collectors. The thickness of the fluid shell, labeled as b in Figure 2.1(b), is a function of overall porosity of the medium, which is based on the volume fraction of the collectors in the packed bed. This overall porosity factor is used to modify the fluid velocity distribution around a single, isolated spherical collector [PRT74]. Happel's cell model considers only the interactions between a particle moving through the fluid and this single collector that is "nearest" to it. The phenomena observed with this single collector is subsequently applied to the entire packed bed, thereby determining general effective parameters like filtration efficiency for the whole system.

For any given deposition scenario, a numerical solution of the Eulerian convection-diffusion-migration equation or the Lagrangian trajectory model is not easily acquired or readily available for use [TE04]. To provide a convenient alternative, some researchers have devised semi-empirical approaches to predict the filtration efficiency of a packed bed filter. The first water filtration model based on Happel's cell was presented by Yao *et al.* [YHO71], which proposed a closed-form correlation equation for the initial collection efficiency η (vs. particle radius a_p) of a single collector grain in a deep-bed filter. The resulting equation is a function of several dimensionless parameters governing particle filtration, including the aspect ratio N_R (particle size over

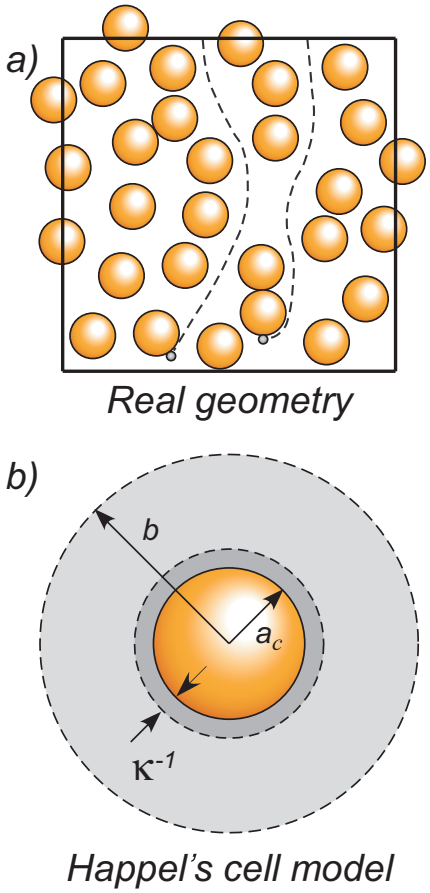

Figure 2.1: Pictorial representation of Happel's cell model of a porous medium. (a) The complexity of the real system is simplified by modeling the medium as a number of spherical collectors. (b) Each cell contains one collector surrounded by a spherical fluid shell. The radius of the shell, b, is a function of the volume fraction of the collector grains in the porous medium.

collector size), the Peclet number N_{Pe} (convective transport over diffusional transport), and the gravitation number N_G (Stokes particle settling velocity over fluid approach velocity). However, this model (sometimes called Yao-Habibian [LJA+95]) did not consider the effects of hydrodynamic interactions and the attractive van der Waals interactions on filtration efficiency for any particle size.

Several years later, Rajagopalan and Tien [RT76] considered these interactions explicitly, although only for non-Brownian particles. They employed trajectory analyses, comparisons with earlier experimental findings and dimensional analysis to formulate their correlation equation for the initial collection

efficiency η. With several dimensionless parameters added to account for more factors, the Rajagopalan-Tien correlation became a standard for comparison in many studies of deposition. One such study was that of Tufenkji and Elimelech [TE04], who sought to improve upon Rajagopalan and Tien's equation by including the influence of hydrodynamic retardation and van der Waals interactions on the deposition of particles in the diffusion-dominated regime. Their process of formulating a new correlation equation for η was based on the numerical solution of a non-dimensionalized convection-diffusion-migration equation with boundary conditions commonly used in previous studies. Multiple linear regression analyses of several dimensionless parameters, including those mentioned above, determined the values of coefficients and exponents in their correlation. The η vs. a_p curves for the correlations of Rajagopalan-Tien and Tufenkji-Elimelech are qualitatively very similar, with significant differences only emerging around the lowest value of η (*i.e.*, at $a_p \approx 1$ μm in [TE04]). The reasons for this difference have been debated [RT05, TE05a]. Nevertheless, the correlation equations of both Rajagopalan-Tien and Tufenkji-Elimelech continue to be utilized in discussions of results for numerous studies to the present day, with a recent example from Long and Hilpert [LH09].

2.3.2 Evolution of Established Models

In real systems, the collector grains – perhaps of various sizes – of a granular porous medium would be in contact with some of their neighbours, held in place by packing constraints and physicochemical interactions. The surfaces of these collectors would not be perfectly smooth either, having asperities of different sizes protruding into the fluid. Solving the Navier-Stokes equations with the no-slip boundary condition at the surfaces of these collectors, the resulting fluid velocity distribution in the near-field around these collectors would differ from that of the isolated spherical collector in Happel's cell model. This highlights the significance of capturing the fluid velocity distribution, or flow field, around these collectors as accurately as possible, and numerically solving the Navier-Stokes equations for such a geometry is an effective approach to this.

Torkzaban *et al.* [TBW07] used finite element software to determine the flow field around a single spherical collector with greater accuracy than the typical Happel cell model, but again the collector's surface was smooth.

Models of deposition based on ideal collectors do not accurately predict deposition rates on real surfaces. The discrepancy between theoretical predictions and experimentally-observed deposition rates or deposit morphologies have generally been ascribed to physical and chemical heterogeneity of the interacting surfaces. Consider, for instance, the deposition of particles onto a planar substrate in the presence of a shear flow. The ideal model portrays the substrate as smooth (Figure 2.2a), and a straightforward analytical expression depicts the flow across its surface. A more realistic model will have some roughness, with asperities generating local effects that forbid analytical expressions for steady state fluid velocity profiles near the surface (Figure 2.2b). Presence of roughness on the substrate gives rise to two major sources of discrepancy between theoretical predictions and experimental observations of deposition rates or deposit morphologies. First, roughness modifies the colloidal interactions between the depositing particle and the substrate, thereby affecting the migration-based particle transport. Second, collector surface roughness alters both the local flow field and particle-collector hydrodynamic interactions, which directly influences convection and indirectly influences diffusion and migration. If the asperities are large enough relative to the particle size, they can affect the trajectories of particles that come close to the surface, and ultimately contribute to deposition phenomena in some way.

The effects of physical heterogeneity on particle deposition in porous media have been explored with techniques evolved from the original cell models, including the array of spheres (AOS) model [SS66]. When depicting the hydrodynamic field within the medium, some newer techniques have explicitly considered the pore structure formed by contact points between collector grains [CL98,LZLJ05,TJ06,JLY07] as well as zones of flow stagnation [JLY07]. A recent study by Ma *et al.* employed Lagrangian particle trajectory analysis with numerically-determined flow fields in the vicinity of grain-to-grain

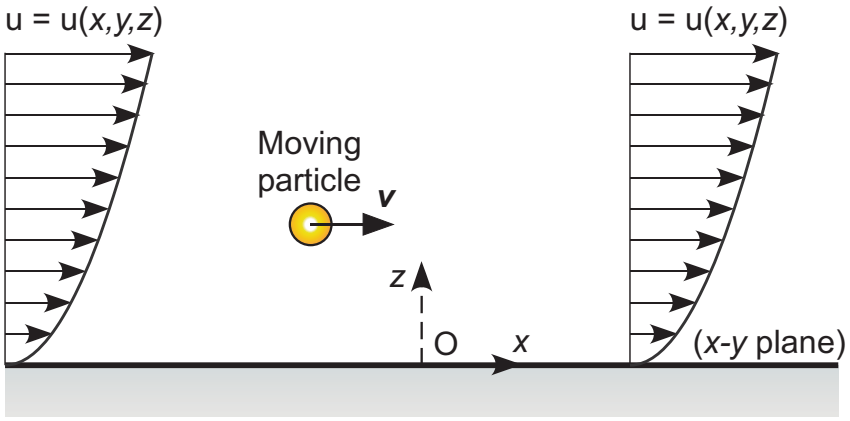

a) Classic Approximation - Smooth Surface
(No Asperities Present)

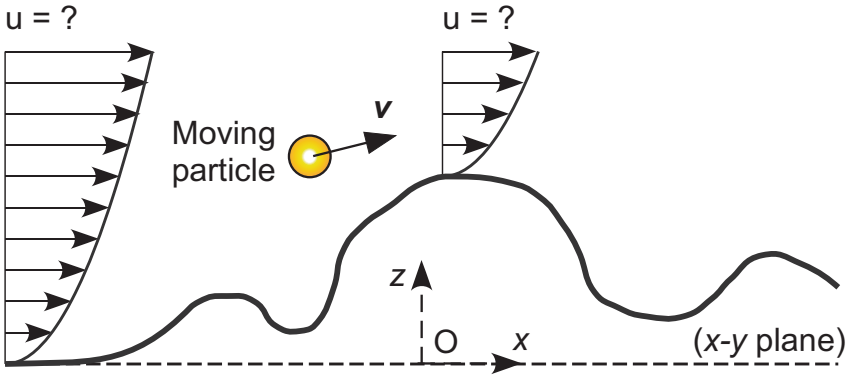

b) More Realistic - Rough Surface
(Asperities Present)

Figure 2.2: Local hydrodynamic fields near model collector surfaces. (a) The classic approximation of a smooth surface allows the fluid velocity profile to be represented as an analytical expression. (b) With a more realistic depiction of the surface, physical roughness (*i.e.*, presence of asperities) can significantly alter the velocity profile, requiring a numerical solution for the entire flow field and affecting particle transport near the surface.

contact points, providing a mechanistic model of particle deposition in such systems [MPFJ09]. Other flow fields in complex geometries have been calculated to assess colloid transport in porous media, such as the constricted tube model [CCL03, CDCC04, CCC08]. In spite of this level of model refinement, these and many other similar studies (some other recent examples include [BSB$^+$05, BT07, BTW07]) were concerned with a scale of physical heterogeneity that was much larger than the particles in the fluid, and the collector grains had perfectly smooth surfaces (*i.e.*, Classic Approximation: Figure 2.2a).

From a strictly Eulerian perspective, physical and chemical heterogeneity in porous media have also been modeled in terms of effective medium parameters such as specific deposit, hydraulic conductivity and "heterogeneity parameter" [BT00,SESR01,LBRE03]. For example, Abdel-Salam and Chrysikopoulos modeled the effects of physical heterogeneity on colloid transport in a fractured rock medium [ASC95,CAS97], using an Eulerian description of the matrix with apertures of varying size, but these models were in two dimensions only representing a fracture plane. Although the use of effective medium parameters can give valuable information concerning the broad picture, particle-collector interactions are lost in a "smeared-out" view of the deposition process. Random walk particle tracking (RWPT) models, which use both the Eulerian and Lagrangian trajectory approaches in a complementary fashion, have also been applied to simulate colloid transport in porous media [DAD05, SFGGH06]. However, these random walk models have been applied to larger systems (*i.e.*, heterogeneity on the macroscale, not microscale [PBBK08]) that are typically two-dimensional. Only convective- (advective-) and diffusion-based transport have been explicitly included in these models, sometimes with hydrodynamic interactions represented with a retardation factor that is a function of concentration, not the proximity of individual particles to other bodies [WK96, DAD05, ADK09].

2.3.3 Physical Heterogeneity and Near-Field Hydrodynamics

Models for particle transport and deposition, either Eulerian or Lagrangian, commonly consider convection, diffusion (Brownian motion), and migration due to colloidal interactions as the mechanisms of transport. The convective component of particle transport is computed by first determining the undisturbed hydrodynamic field near a model collector, followed by the application of corrections for the particle-collector hydrodynamic interactions. The hydrodynamic corrections are also employed to modify the diffusivity of the particles near the collector surface. These corrections are generally obtained from analytical expressions based on fluid flow over a smooth, flat surface. Such an approach may be inadequate for the following situations:

(i) Deposition of a few particles can alter the topography of an initially smooth substrate. Such immobilized particles can modify the local fluid flow, and therefore, subsequent particle convection [LBRE03, KBE00, Ada03]. Prediction of particle deposition rates beyond initial (clean substrate) deposition might require continual update of the hydrodynamics to account for the effects of the immobilized particles.

(ii) Many surfaces that are macroscopically planar can have substantial roughness. Depending on the scale of roughness, the near-field hydrodynamics on such rough surfaces can be significantly misrepresented by expressions for shear flow past a smooth flat plate. In context of colloid transport and deposition, such misrepresentations can have consequences when considering deposition of nanoparticles onto surfaces containing large asperities (larger than the nanoparticles) [RB07, RPW01].

(iii) Numerous applications with nanoengineered surfaces containing regular arrays of bumps, posts, and corrugations are being proposed. Such surfaces have already been shown to produce remarkable effects on friction losses during fluid flow [WUU99, CK06, CUK$^+$06, CDC07]. To assess how colloid transport and deposition will be influenced by such textured substrates, one needs to consider the flow fields and particle convection near such surfaces accurately.

In the above mentioned situations, physical (topographical) heterogeneity of a macroscopically planar surface is expected to influence particle deposition by modifying the hydrodynamics. Many studies have considered the effects of surface roughness on colloidal interactions [Len94, SW96, BKE98, HBE03], thereby affecting migration-based particle transport. Studies elucidating the influence of surface roughness on the flow field [Hig85,Poz97], and consequently on convective and migrational particle transport [MDvdV86,D89,DvdV92], are more scarce in deposition literature.

Suspended colloidal particles also modify the undisturbed fluid velocity field. These hydrodynamic interactions are typically accounted for by the appropriate hydrodynamic correction functions in colloid transport models. On the other hand, there are more rigorous and very accurate approaches to numerically determine the full flow field and comprehensively account for the hydrodynamic interactions between bodies. One such approach is Stokesian Dynamics (SD) [DBB87, BB88], which relates the forces and torques acting on N spheres to their velocities through a grand mobility matrix set up to a particular order of accuracy, depending on the version used. These versions can include only two-body force - translational velocity interactions (*i.e.*, F version), two body force/torque - translational/rotational velocity interactions (*i.e.*, F-T version), or two-body force/torque/stresslet - translational velocity/rotational velocity/rate of strain interactions (*i.e.*, F-T-S version). Another approach involves the use of arbitrary Lagrangian-Eulerian (ALE) [HLZ81, Hu96, AQMB08] type models with finite element programs, allowing the mesh to follow moving boundaries such as particles' surfaces while maintaining element shape [SZ01]. Unfortunately, both of these approaches are computationally intensive and generally compute the flow fields assuming smooth solid surfaces with no-slip condition. Detailed calculation of a flow field that resolves the surface roughness of the collectors in conjunction with either of these techniques is computationally prohibitive.

Hydrodynamic retardation has been thoroughly investigated for sphere-plate interactions [Bre61, GCB67a, GCB67b, GO71, Dah74, KK05], which is the

case when the particle is much larger than the roughness features (*i.e.*, posts, attached spheres, etc.) on the collector, or when those features are much larger than the particle itself. The intermediate cases of hydrodynamic interactions for unequally-sized spheres have also been investigated in a number of scenarios [JO84, KK05], but the spheres were located in the bulk, far away from any collector surfaces. However, research into the hydrodynamic interactions between a spherical particle and a collector surface with topographical features that simulate roughness of a scale close to the particle size is far less common. The study by Bafaluy *et al.* [BSVS93] observed the diffusional motion of a single Brownian particle near a Brownian particle of equal size attached to a planar surface using Brownian Dynamics simulations. Anekal and Bevan [AB06] employed Monte Carlo methods and Stokesian Dynamics to compute the self-diffusion of a dilute, dynamic monolayer of equally-sized colloidal particles coating a planar wall. Although both of these models comprehensively accounted for hydrodynamic interactions between bodies, neither of them considered a system with the fluid flowing past the wall. Thus far, there have been no investigations of particle deposition that include all three transport mechanisms – convection, diffusion and migration – and hydrodynamic retardation for particles approaching a physically heterogeneous substrate with asperities or roughness features of similar size to the particles themselves.

2.3.4 Chemical Heterogeneity and Near-Field Transport

It has only been in recent years that the effects of chemical heterogeneity on near-field transport and deposition have been explored. One of the long standing mysteries in deposition phenomena is how surfaces that are expected to be unfavourable to deposition can have some particles still deposit on them. In an attempt to resolve this issue among others, the experimental study of Elimelech *et al.* [ECK03] and the numerical simulations of Nazemifard *et al.* [NMB06a, NMB06b] chose a radial stagnation-point flow cell with micropatterned, concentric circular stripes of alternating charge to observe

the resulting phenomena of such chemical heterogeneity when particles are released into the flow. These studies revealed a relationship between the hydrodynamics and the electrostatic double layer interactions of the system, otherwise called the "Hydrodynamic Bump" effect by Elimelech *et al.*. When a small fraction of the collector surface was covered with favourably charged stripes amidst the predominantly unfavourably charged, the observed deposition rate of micron-sized particles increased substantially. Similar findings have been made for systems with one-dimensional shear flow across a flat surface with 11 nm disks [DD07, DD08] and 30 nm patches [SK07, KS08]. It is the presence of surface charge heterogeneity (of a particular character) that leads to this, affecting the motion of the particles near the surface and ultimately promoting the adsorption of some of them. With this in mind, Kline *et al.* [KCW08] devised an experimental apparatus with transparent microelectrodes to vary electric surface potential in order to control particle deposition in a parallel-plate chamber through chemical heterogeneity. Their experimental results agreed with those of the previously mentioned patch model (*i.e.* favourable and unfavourable stripes) when a negative potential was applied. However, discrepancies were observed for applied potentials of 0.0 and +0.2 V, which led the authors to conclude that future modeling should account for the coupling of hydrodynamic and colloidal interaction forces.

2.4 Overview of Limitations of Previous Studies

The preceding literature review has uncovered several gaps in the knowledge of particle deposition onto heterogeneous surfaces that remain largely unexplored in previous studies. Many previous studies of particle transport and deposition have employed the Eulerian approach. Greater computational efficiency and the ease with which Brownian motion is incorporated relative to the Lagrangian approach are two common reasons for this choice [Nel04]. In fact, Eulerian models have been used sometimes to assess the accuracy of

Lagrangian trajectory analyses [NMB06a]. Trajectory models are limited in that they simulate the motion of one particle at a time near a "clean" collector surface (*i.e.*, no particle-particle interactions). This precludes any explicit analysis of long term deposition behaviour with such models, since particle concentrations in the fluid and the effects of previously deposited particles are not considered.

However, there is a need to provide a "direct mechanistic description of particle transport" [Nel04] near heterogeneous collector surfaces with features of comparable size to the particles that Eulerian models cannot provide. Such a description is required to discern the relevant mechanisms for deposition on more realistic representations of collector surfaces than those of smooth, flat plates. As this thesis proposes, a Lagrangian trajectory model that includes convection, diffusion and migration – with hydrodynamic retardation influencing all of these transport mechanisms – can furnish this. Trajectory models are more intuitive than their Eulerian counterparts, following a particle's path as different forces change magnitude and direction to guide its motion through the fluid. They also provide a reliable means of testing the validity of different assumptions for deposition scenarios [Nel04].

Within the limits of the Lagrangian approach, the objectives of this research seek to address the most prominent gaps of knowledge of particle deposition onto heterogeneous collectors. These gaps are as follows:

1. When convective, diffusional and migrational forces were included in the models of previous studies, the surfaces of both the particle and the collector were smooth and featureless (*i.e.*, no physical or chemical heterogeneity). For these simple geometries, the methods employed to account for hydrodynamic retardation were originally based on, or readily compared with, the correction factors for sphere-plate interactions [Bre61, GCB67a, GCB67b, GO71, Dah74]. Unfortunately, the lack of heterogeneity in these idealized models makes them inappropriate for meeting the objectives of this research.

2. If heterogeneity was embodied in the model, it was typically of a characteristic scale that was much larger or much smaller than the particles themselves, and sometimes limited to only two-dimensional fields (like for RWPT models). When the features were much smaller than the particles (about 100 times smaller in [DD07, SZSR09]), it was safely assumed that such physical heterogeneity did not appreciably modify the undisturbed flow field around the collector, so convective particle transport was left unaltered in these scenarios. On the other hand, studies like those of Johnson *et al.* [TJ06, JLY07] regarded pore structures from periodic arrays of spherical collector grains in contact with each other to be a form of physical heterogeneity in porous media. The flow fields in these models reflected the modifications from uniform flow due to the grains, but the grains were 200 to 6000 times larger than the particles and their surfaces were assumed to be smooth.

3. For the rare occasions when the characteristic scale of the collector's heterogeneity was similar to the particle, the [trajectory] model was missing one or two transport mechanisms. The numerical models of Dąbroś and van de Ven involved physical heterogeneity in the form of a single, previously deposited particle [MDvdV86, D§9, DvdV92]. Brownian motion of the moving particles in these studies was suppressed, and hence their trajectories were entirely deterministic (*i.e.*, included only convection and sometimes migration due to gravity and/or colloidal interactions). From another perspective, the works of Bafaluy *et al.* [BSVS93] and Anekal and Bevan [AB06] focused on diffusion and migration with hydrodynamic interactions, but the fluid itself was at rest so no convective particle transport was considered.

These gaps leave an intermediate realm in the scale of collector heterogeneity, and its subsequent effects on all three particle transport mechanisms, to be investigated. As of yet, there have been no models of Brownian particle deposition onto physically and chemically heterogeneous (on a scale close

to particle size) substrates that account for the effect of hydrodynamic retardation on convection-, diffusion- and migration-based transport. Perhaps the main reason for this is the formidable challenge in developing a technique for explicitly determining the hydrodynamic interactions between a spherical particle and a substrate with a given configuration of heterogeneity of similar scale to the particle size.

2.5 Summary

Despite extensive research into colloid transport and deposition over many decades, there remains an intermediate realm that has not been fully explored. The extent to which a collector's physical and/or chemical heterogeneity – on length scales comparable to the sizes of approaching particles – can influence particle transport and deposition is not apparent from existing studies in the field. One of the specific objectives of this investigation is to determine how presence of surface roughness on a collector can modify near-field hydrodynamics and ultimately capture particles under situations where conventional deposition models that assume geometrically smooth surfaces will predict no particle attachment. The next chapter introduces a model in which the planar substrate is divided into subunits, and hence the substrate can be rendered physically and chemically heterogeneous simultaneously. A number of salient scenarios are explored with this model, providing some unique insights into the influence of both types of heterogeneity on deposition phenomena.

Chapter 3

Colloidal Interactions between a Particle and a Heterogeneous Substrate

3.1 Introduction

This chapter concentrates on how chemical and physical heterogeneity on a substrate can affect its colloidal interactions with a nearby Brownian particle.[1] The general methodology used in this study to impart chemical heterogeneity to a macroscopically planar surface is described in the first part of this chapter. This approach considers a substrate as comprised of a large number of subunits with individual physical (*i.e.*, size and shape) and chemical properties assigned to each of them. The technique for evaluating the interaction energy and force between a neighbouring spherical particle and the heterogeneous substrate is then presented. The entire mathematical formulation for evaluating the interaction force is based on the DLVO (Derjaguin-Landau-Verwey-Overbeek) theory [DL41, VO48]. This involves representing the total interaction force as the sum of the van der Waals and electrostatic double layer interaction forces, with the assumption that pairwise additivity of interaction energies and forces holds. This particular model can also be used to render a substrate physically heterogeneous.

[1] A version of this chapter has been published. Kemps and Bhattacharjee, 2005, *Langmuir*, 21(25):11710-11721.

3.2 Formulation of the Heterogeneous Interaction Model

3.2.1 Imparting Heterogeneity to a Model Planar Substrate

Thin, chemically heterogeneous structures – such as cell membranes – have complex molecular architectures. Representing such a structure as a planar film is an idealized approximation that smears out all of the chemical heterogeneity present in the structure. On the other hand, describing a large expanse of such a heterogeneous surface in terms of its exact molecular structure, as is done with most molecular modeling approaches, is cumbersome. A reasonable compromise between these two approaches might be to represent the complex heterogeneous films as an assemblage of nanoscale subunits. Each subunit in such an assemblage can possess different properties, such as chemical composition and surface potential, and may even be assigned different translational and orientational degrees of freedom. This procedure provides a fairly accurate representation of the chemical heterogeneity and geometrical flexibility of the system, albeit on a somewhat coarser length scale when compared with molecular simulations (including coarse-grained ones [NLSK04,BS06,KFT08]). The advantage to such coarsening of the molecular architecture of a chemical structure is that it facilitates the modeling of considerably larger systems than what is possible using a completely atomistic description of the system.

In this study, the approach described above is adopted to represent a macroscopically planar surface as an assemblage of nanoscale subunits, and compute the interaction forces between a neighbouring spherical particle and the model surface. A general geometrical representation of the interaction between a neighbouring spherical particle and a model chemically heterogeneous surface is shown in Figure 3.1. Here, the cross section of the surface is depicted as an assemblage of spherical subunits. The properties of the individual subunits can vary, as indicated by the different shades. Even the presence of gaps in the substrate, as well as surface roughness, can be modeled in this manner. The

objective of using such a model is to render the substrate chemically heterogeneous in the lateral directions by assigning different interaction parameters to each subunit. This enables the computation of the lateral forces acting on the neighbouring probe particle. It should, however, be noted at the outset, that using spherical subunits also imparts a nanoscale "roughness" to the substrate.

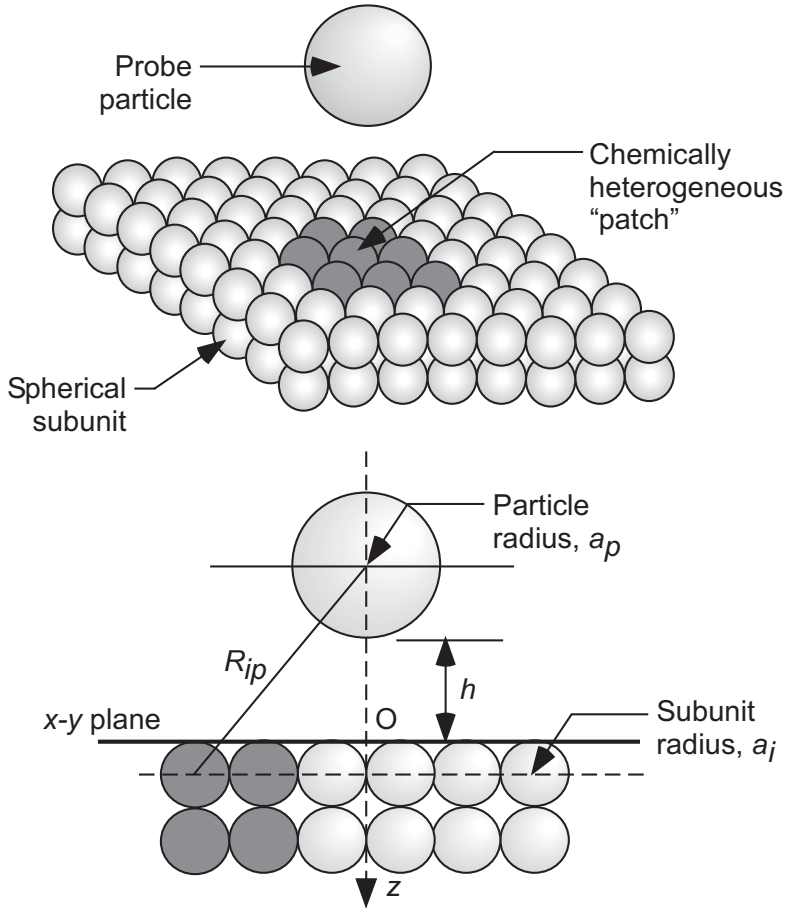

Figure 3.1: Pictorial and schematic representations of the mathematical model, showing the planar surface as a planar array of spheres. The spheres within the heterogeneous region are shaded to distinguish them from the other base spheres in the array. The Cartesian coordinate system used in the simulations is also shown.

3.2.2 DLVO Interaction Energy and Force

Within the framework of the DLVO theory [DL41, VO48], the total interaction energy between the neighbouring probe particle and the macroscopically

planar substrate, U_{fp}^{DLVO}, can be represented as

$$U_{fp}^{DLVO} = U_{fp}^{vdW} + U_{fp}^{EDL}. \tag{3.1}$$

with U_{fp}^{vdW} as the total van der Waals interaction energy and U_{fp}^{EDL} as the total electrostatic double layer interaction energy. The total DLVO interaction force experienced by the probe particle due to the heterogeneous planar substrate can be determined from the above DLVO interaction energy as

$$\mathbf{F} = -\nabla U_{fp}^{DLVO} = -\frac{\partial U_{fp}^{DLVO}}{\partial x}\mathbf{i} - \frac{\partial U_{fp}^{DLVO}}{\partial y}\mathbf{j} - \frac{\partial U_{fp}^{DLVO}}{\partial z}\mathbf{k}. \tag{3.2}$$

This expression divides the total DLVO interaction force vector $\mathbf{F}$ into its three Cartesian components, with $\mathbf{i}$ in the $x-$ direction, $\mathbf{j}$ in the $y-$ direction, and $\mathbf{k}$ in the $z-$ direction. In the same manner, the van der Waals or electrostatic double layer interaction force between the particle and the heterogeneous planar substrate can also be determined by substituting the notation "DLVO" with "vdW" or "EDL", respectively, in Eq. (3.2). In subsequent discussions, the total DLVO interaction force, or a component of it, will sometimes be referred to in scaled form. For example, the scaled normal force is expressed as $F_z^* = F_z a_p / k_B T$.

It is important to note that Eq. (3.2) resolves the DLVO force into its components acting laterally and perpendicular to the substrate. Usually for homogeneous surfaces, one only considers the normal component of the force. The resolution of the DLVO force into both its lateral and normal components represents a key departure of the present approach from the existing methodologies. It is expected that the lateral forces will be manifested strongly near the edges of the chemical heterogeneities on the substrate.

3.2.3 Unretarded van der Waals (vdW) Interactions

To evaluate the unretarded van der Waals component of the DLVO interaction, Hamaker's approach was used between a spherical probe particle and a macroscopically planar surface rendered as an assemblage of spherical subunits as described previously. The approach is illustrated with the simple geometry

depicted in Figure 3.1. Here, a macroscopically planar film is represented as an array of spherical subunits arranged in a tight planar lattice. Each spherical subunit can be characterized with a specific Hamaker constant for its interaction with the probe particle. Each spherical subunit has a radius a_i, while the approaching particle has a radius a_p. The Cartesian coordinate system has its origin located on the planar surface with the $z-$ axis passing through the center of the probe particle. The distance of closest approach between the particle's surface and the planar substrate is h (along the $z-$ axis).

The van der Waals interaction energy between an atom in one of the spherical subunits constituting the planar surface and the spherical probe particle can be represented in terms of a 9-3 potential [Hun01,Isr92]. This 9-3 potential is obtained by integrating the 12-6 Lennard-Jones interaction potential over the volume of the probe particle. The resulting expression for the attractive component (the component with the exponent 3) is [Ham37]

$$E_{ip}^{vdW}(D_{ip}) = -\frac{4}{3}\pi\rho_p\beta_{ip}\frac{a_p^3}{(D_{ip}^2 - a_p^2)^3} \tag{3.3}$$

where D_{ip} is the distance between the atom in the subunit i and the center of the particle, ρ_p is the number of atoms per unit volume in the particle, β_{ip} is the Lifshitz-van der Waals energy constant for the interaction between an atom in subunit i and an atom in the particle, and a_p is the radius of the probe particle. Referring to the geometry shown in Figure 3.1, the interaction potential between a differential volume element, dV_i, in a spherical subunit of the planar substrate and the probe particle will be

$$dU_{ip}^{vdW} = E_{ip}^{vdW}(D_{ip})(\rho_i dV_i) \tag{3.4}$$

where ρ_i is the number of atoms per unit volume in the spherical subunit i and $dV_i = dxdydz$ is the volume of a differential element in the subunit. Integrating Eq. (3.4) over the entire volume of the spherical subunit yields

$$U_{ip}^{vdW} = -\rho_i \int_{V_i} E_{ip}^{vdW}(D_{ip})dV_i. \tag{3.5}$$

Substituting Eq.(3.3) into Eq.(3.5) provides,

$$U_{ip}^{vdW} = -\frac{4A_{ip}}{3\pi}a_p^3 \int_{V_i} \frac{dxdydz}{(D_{ip}^2 - a_p^2)^3}. \tag{3.6}$$

In Eq. (3.6), $A_{ip} = \pi^2 \rho_i \rho_p \beta_{ip}$ is the effective Hamaker constant for the van der Waals interaction between the probe particle and the spherical subunit i. The length parameter D_{ip} can be expressed in terms of the centroid-to-centroid distance between the probe particle and a differential element of a subunit in the planar surface. The integrand in Eq. (3.6) is resolved into an expression of purely Cartesian components and constants,

$$D_{ip} = \sqrt{x^2 + y^2 + (a_p + h + z)^2} \tag{3.7}$$

where (x, y, z) represents the coordinates of the centroid of the differential volume element dV_i in each subunit. The total van der Waals interaction energy between the probe particle and the flat substrate, the latter being a planar array of spherical subunits, can be written as a sum of the pairwise interactions between individual subunits and the probe particle. This will take the form

$$U_{fp}^{vdW} = \sum_{i=1}^{N_s} U_{ip}^{vdW}, \tag{3.8}$$

where U_{fp}^{vdW} represents the total van der Waals interaction energy between the probe particle and the planar surface, and N_s is the number of subunits in the planar surface.

The above formulation is quite general, and allows the use of any geometrical shape for the subunits, provided that the volume integrations in Eq. (3.6) are performed numerically. The flexibility of this provides the opportunity to alter the packing density, roughness and general distribution of mass in the planar surface, leading to a remarkable variety of surface morphologies that can be investigated. However, when considering spherical subunits, the integrations for obtaining the interaction energy between the probe particle and each subunit can be performed analytically [MN76, EGJW95]. The resulting van der Waals interaction between the probe particle and the model planar surface can be expressed as a summation of the interaction energies over all

the subunits, given by

$$U_{fp}^{vdW} = \sum_{i=1}^{N_s} -\frac{A_{ip}}{6}\left[\frac{2a_ia_p}{R_{ip}^2-(a_i+a_p)^2}+\frac{2a_ia_p}{R_{ip}^2-(a_i+a_p)^2+4a_ia_p} + \ln\left(\frac{R_{ip}^2-(a_i+a_p)^2}{R_{ip}^2-(a_i+a_p)^2+4a_ia_p}\right)\right], \tag{3.9}$$

with R_{ip} as the centroid-to-centroid distance between the probe particle and the spherical subunit i as shown in Figure 3.1.

The effective Hamaker constant, A_{ip}, can be used to impart chemical heterogeneity to a planar surface by noting that each subunit can be assigned a different Hamaker constant. In other words, this constant can be used to depict chemically heterogeneous patches on a surface by assigning a particular Hamaker constant value to a cluster of subunits, which is different from the Hamaker constant of the remaining subunits. For this purpose, a quantity, R_H – which can be named the Hamaker constant ratio – is defined as

$$R_H = \frac{A_{H,patch}}{A_{H,0}}, \tag{3.10}$$

with $A_{H,patch}$ as the effective Hamaker constant between a heterogeneous patch and the probe particle, and $A_{H,0}$ as the effective Hamaker constant between the region of the surface surrounding the patch and the probe particle. When $R_H > 1.0$, the patch has a greater interaction energy with the particle than does the surrounding volume. Note that the value of R_H itself does not influence whether the van der Waals interaction energy is attractive or repulsive. However, for this study, the van der Waals interaction energy between the probe particle and any region of the surface is always assumed to be attractive.

3.2.4 Electric Double Layer (EDL) Interactions

The electric double layer (EDL) interaction is the second component of the total DLVO interaction. Typically, the electrostatic interaction energy between a subunit of the substrate and the probe spherical particle can be described

using a screened Coulomb interaction [VP92, BKE99]. The screened Coulomb interaction is given by

$$U_{ip}^{EDL} = \frac{\nu_p \nu_i e^2}{4\pi\epsilon} \frac{\exp[-\kappa(R_{ip} - a_i - a_p)]}{R_{ip}[1 + \kappa(a_i + a_p)/2]^2} \tag{3.11}$$

where e is the magnitude of the fundamental electron charge, R_{ip} is the center-to-center distance between the probe particle and the subunit i, ϵ is the permittivity of the dispersing medium and κ is the inverse Debye length. The total charge number on the probe particle (ν_p) and that on the subunit (ν_i) can provide a fairly accurate description of the electrostatic double layer interaction energy. In the context of colloidal systems, one limitation of such a screened Coulomb interaction is that it becomes inaccurate for particles with different surface charges. It is well known that two colloidal particles, one with a finite surface potential and another with a zero surface potential, will have a finite EDL interaction in an electrolyte solution. However, according to Eq. (3.11), the interaction energy predicted for such a situation will be zero. Consequently, in this study, the EDL interaction energy is calculated using the analytical expression derived by Hogg *et al.* [HHF66] for two spheres of unequal radii and constant but dissimilar surface potentials given by

$$U_{ip}^{EDL} = \frac{\pi\epsilon a_i a_p}{(a_i + a_p)} \left[2\psi_i \psi_p \ln\left(\frac{1 + \exp(-\kappa d)}{1 - \exp(-\kappa d)} \right) + (\psi_i^2 + \psi_p^2) \ln[1 - \exp(-2\kappa d)] \right]. \tag{3.12}$$

In Eq. (3.12), ψ_i is the surface potential of the subunit i in the planar surface, ψ_p is the surface potential of the probe particle, and $d = R_{ip} - a_i - a_p$ is the surface-to-surface distance of closest proximity between the probe particle and the spherical subunit. For a symmetric ($\nu : \nu$) electrolyte, the inverse Debye length is given by

$$\kappa = \sqrt{\frac{2000 e^2 \nu^2 N_A I}{\epsilon k_B T}} = (3.286 \times 10^9) \nu \sqrt{I}, \tag{3.13}$$

in which I is the molar concentration of the electrolyte (in mol/L). For this study, the system temperature is assumed to be $T = 298.15$ K, and the permittivity of water at this temperature is $\epsilon = 6.95 \times 10^{-10}$ C^2/N m^2. The

remaining constants in the expression for the inverse Debye length are the Boltzmann constant, $k_B = 1.381 \times 10^{-23}$J/K, the fundamental electron charge, $e = 1.602 \times 10^{-19}$ C, and Avogadro's number, $N_A = 6.022 \times 10^{23}$/mol.

Eq. (3.12) is applicable for particles with low surface potentials suspended in a symmetric electrolyte solution. Furthermore, since Eq. (3.12) is based on Derjaguin approximation, it is restricted to $\kappa a_i \geq 10$ and $d \ll a_i$. Such a limitation imposes a lower bound to the subunit size that can be employed in the simulations of this study. For monovalent salt concentrations of about 10^{-1} M, the lowest subunit size that should be used is about 10 nm.

As with the van der Waals interaction energy, the total EDL interaction energy between the probe particle and the flat substrate, the latter being represented as a planar array of spherical subunits, can be written as a sum of the pairwise interactions between individual subunits and the probe particle. This will take the form

$$U_{fp}^{EDL} = \sum_{i=1}^{N_s} U_{ip}^{EDL}, \tag{3.14}$$

where U_{fp}^{EDL} represents the total EDL interaction energy between the probe sphere and the planar surface, and N_s is the number of subunits in the planar surface.

At this point, it is pertinent to note that the pairwise summation of the EDL interaction between every subunit (even the subunits residing in the "bulk" of the substrate) and the probe particle using the Hogg *et al.* expression, Eq. (3.12), might seem unrealistic. Such an approach will inherently assume that the subunits in the bulk will have a surface potential, whereas in context of colloidal systems, and certainly in context of Eq. (3.12), only the true surface should bear an electric potential. One should note, however, that in strictly adhering to the limits of the Derjaguin approximation, the main contribution to the total EDL interaction energy determined with Eq. (3.14) will be from the regions of closest approach between the probe particle and the substrate. Although the bulk subunit contributions are added up in a pairwise manner when Eq. (3.14) is used to calculate the total EDL interac-

tion, the contribution of these subunits to the total interaction are negligible. One should also note that the screened Coulomb interaction, Eq. (3.11), is generally used in a pairwise additive manner to calculate the many-body electrostatic interactions in concentrated colloidal systems [VP92, BKE99]. In the next section, the implications of the pairwise summation approach applied to Eq. (3.12) will be discussed, following a comparison of the Hogg *et al.* and the screened Coulomb interactions.

3.3 Validation of the Heterogeneous Interaction Model

The approach of determining the total interaction energy and force between a colloidal particle and a large chemically heterogeneous substrate is comprised of two steps. The first step involves a judicious representation of a large substrate as a collection of nanoscale subunits. This is followed by determination of the overall interaction between the substrate and a neighbouring probe particle by pairwise summation of the interactions between the particle and the individual subunits. Considering a substrate of homogeneous chemical composition, it is demonstrated that the approach does not constitute a departure from the existing norms of computing the interaction energy between colloidal objects. To validate this approach, the van der Waals interaction between a spherical particle and an infinite planar surface of finite thickness is considered, for which an analytical expression is available [Tad01].

To accurately represent a macroscopically planar surface of a finite thickness, one needs to consider cubic subunits. The validation model considers a sphere of radius a_p placed at different separation distances from the center of a finite slab of homogeneous composition measuring $6a_p \times 6a_p \times 2a_p$. For the computation of the interaction, the slab was divided into $3000 \times 3000 \times 1000$ cubic subunits, and the normal van der Waals interaction force was determined using a numerical integration scheme based on Simpson's rule, all of which was done in FORTRAN computer code. The analytical expression for

Table 3.1: Comparison of results from the present, Heterogeneous Interaction Model and the analytical solution by Tadmor [Tad01] for the scaled van der Waals normal force, F_z^{vdW*}, between a sphere of radius a_p and a finite slab measuring $6a_p \times 6a_p \times 2a_p$ at several scaled separation distances, $H = h/a_p$.

Separation Distance H	van der Waals Normal Force, F_z^{vdW*}		
	Present Model	**Tadmor Solution**	**Percent Difference**
0.01	−1651.036	−1650.114	0.056
0.02	−408.452	−408.447	0.001
0.03	−179.739	−179.742	0.002

the normal vdW interaction force was derived by taking the expression for the corresponding interaction energy from Tadmor [Tad01] and differentiating it with respect to the separation distance, h. Table 3.1 shows a comparison of the numerical results of the Heterogeneous Interaction Model with the analytical results of Tadmor for three separation distances. Only very close separation distances are considered, since the magnitude of the van der Waals interaction is the largest at close separations. Furthermore, since the analytical expression applies to an infinite plate while the length and width of the plate in the numerical model are finite, good agreement between the two approaches can be expected only at close separations. The comparison of the two results in Table 3.1 reveals excellent agreement between the forces obtained numerically and analytically. In all cases, the agreement between the two results was well within a percent.

It is commonly recognized that the pairwise summation principle cannot be rigorously applied to EDL interactions in many-body systems. To assess the validity of pairwise summation for the EDL interactions in the Heterogeneous Interaction Model, a few characteristics of the Hogg *et al.* [HHF66] expression, Eq. (3.12), need to be considered. The Hogg *et al.* expression was derived by first solving the linearized Poisson-Boltzmann equation to determine the EDL interaction energy per unit area between two infinite planar

surfaces. Following this, Derjaguin approximation was employed to arrive at Eq. (3.12). The use of Derjaguin approximation means that the interaction energy calculation is based on the local radii of curvature of the interacting surfaces in the vicinity of the distance of closest approach. This approach can be extended through the surface element integration (SEI) technique to incorporate the exact geometries of the interacting surfaces [BE97, BKE98]. Using this technique to determine the total interaction energy between a sphere and an infinite planar substrate, it was shown for large κa (> 10) that results of pairwise summation of the EDL interaction energies per unit area for this geometry are in excellent agreement with the exact interaction energies obtained by solving of the linearized Poisson-Boltzmann equation. If the subunit size is chosen to be sufficiently large compared to the range of interaction, the main contribution to the EDL interaction energy predicted by pairwise summation with the Hogg *et al.* expression will be from a few subunits of the substrate that are the closest to the probe particle's surface. Ordinarily, one considers the Hogg *et al.* expression to be fairly accurate for surface potentials $< 60 - 75$ mV, and $\kappa a > 10$, where a is the radius of the smaller interacting entity. There is, however, considerable evidence that the Hogg *et al.* expression provides remarkably good predictions of the EDL interaction energy for $\kappa a > 2$, particularly for low surface potentials [CC83, Phi95, DB05].

The screened Coulomb interaction, Eq. (3.11), has been used frequently to compute many-body interactions in colloidal systems [VP92, BKE99]. Such an approach essentially constitutes pairwise summation of the EDL interactions over all of the interacting entities, and this is identical to the approach of this study. In Figure 3.2, a comparison is made between the scaled EDL interaction force calculated using both the screened Coulomb and the Hogg *et al.* expressions (*i.e.*, Eq. 3.11 and Eq. 3.12, respectively) for a spherical particle (of radius $a_p = 100$ nm) near a chemically homogeneous, planar substrate, represented as a $10 \times 10 \times 2$ planar array of spherical subunits. In this comparison, the centroid of the probe particle was positioned directly above the center of the substrate. The surface potential of each of the subunits and the probe particle

was -25 mV, and the electrolyte concentration for the system was 10^{-1} M. Each subunit had a radius of $0.25a_p$ (*i.e.*, $\kappa a_i \approx 25$) or $0.10a_p$ (*i.e.*, $\kappa a_i \approx 10$), where a_p represents the radius of the probe particle. The remaining parameters are identical to those listed in Table 3.2. It is evident from Figure 3.2 that the two expressions provide similar interaction forces over the range of separation distances shown. Appreciable differences between the two curves arise only with the smaller subunit size (*i.e.*, $\kappa a_i \approx 10$, or $a_i = 10$ nm), for which the curves diverge as h decreases below 1.5 nm. For larger separations, and particularly for $\kappa a_i > 10$, the pairwise summation of the screened Coulomb as well as the Hogg *et al.* expressions provides virtually identical EDL forces. This establishes the fact that using the Hogg *et al.* expression (henceforth denoted as the HHF expression) in a pairwise additive manner does not constitute a major departure from existing methodologies for computing many-body EDL interactions using the screened Coulomb expression.

Table 3.2: Parameters for the Heterogeneous Interaction Model simulations.

Quantity	**Symbol**	**Value**	**Units**
Particle radius	a_p	100	nm
Substrate subunit radius	a_i	10 or 25	nm
Thickness of substrate ($= 2a_p$)	$-$	200	nm
Base subunit Hamaker constant	$A_{ip,0}$	k_BT	J
Patch subunit Hamaker constant	$A_{ip,patch}$	$5.0(k_BT)$	J
Particle surface potential	ψ_p	-25	mV
Base subunit surface potential	ψ_i	-25	mV
Patch subunit surface potential	$\psi_{i,patch}$	-75	mV
System temperature	T	298.15	K
Permittivity of medium (water @ T)	ϵ	6.95×10^{-10}	$C^2/N\cdot m^2$
Valency of electrolyte in medium	ν	1	$-$

From the above arguments, it is discernible that the pairwise summation of the EDL interactions, although approximate, is reasonable if the subunit sizes on the substrate are chosen judiciously. Furthermore, the Hogg *et al.* expression is only one of the possible expressions that can be employed in

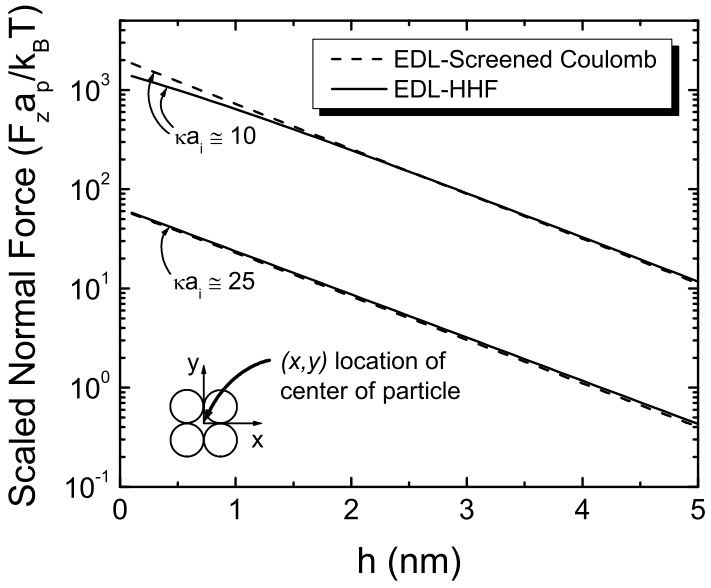

Figure 3.2: Comparison of scaled normal EDL interaction force calculated using the screened Coulomb expression and the Hogg *et al.* (HHF) expression. For this comparison, the planar substrate was chemically homogeneous, spanning $10 \times 10 \times 2$ spherical subunits of $0.25a_p$ (*i.e.*, $\kappa a_i \approx 25$) or $0.10a_p$ (*i.e.*, $\kappa a_i \approx 10$) size. The particle was positioned at various separation distances h from the center of the substrate in the $x-y$ plane. The electrolyte concentration is 10^{-1} M, and other parameters for this simulation are listed in Table 3.2. Note that the center of the particle is situated directly above the origin of the coordinate system, which is located between the four subunits nearest to the center of the planar array (as depicted in the schematic in this figure).

the computation of the EDL interactions. The use of the screened Coulomb interaction, Eq. (3.11), in a pairwise additive manner for computing many-body interactions is more common [VP92, BKE99], and can substitute the Hogg *et al.* expression for the present problem as well.

Based on the evidence discussed above, it is clear that the approach of the Heterogeneous Interaction Model can be used with sufficient confidence to determine the total DLVO interaction energies and forces between a spherical particle and a planar array of subunits.

3.4 Forces on a Particle Near a Heterogeneous Substrate

In this section, the effects of chemical and of physical substrate heterogeneity will be explored from the perspective of the colloidal (DLVO) forces acting on a particle in the substrate's vicinity. The chemical heterogeneity is applied to a macroscopically planar substrate in the form of "patches" that have different chemical characteristics from their surrounding regions. The physical heterogeneity of the substrate is in the form of a spherical asperity, which is modeled as a sphere attached to the planar surface.

3.4.1 Chemically Heterogeneous "Patches"

First of all, the interaction forces experienced by a spherical probe particle near a chemically heterogeneous substrate are investigated. Figure 3.3 schematically depicts the pertinent geometry, where the substrate is divided into two regions shown by the unshaded and gray spherical subunits. The macroscopically planar substrate is comprised of two types of spherical subunits with different properties that dictate the intensity of the interactions; the unshaded subunits are referred to as the base subunits, while the shaded ones represent the heterogeneity. In this case, a probe particle (shown as a dashed circle) is observed at various separation distances above the edge of the heterogeneity. Table 3.2 shows the parameters used for all of the simulations in this study, including the values that are assigned to the subunits inside and outside of the heterogeneous patch.

As the schematic in Figure 3.3 depicts, the centroid of the probe particle was positioned directly above the origin of the coordinate system. The subunit size was chosen to be $0.25a_p$, where a_p represents the radius of the probe particle. This implies that the particle's center was offset a distance of $0.25a_p$ in the $x-$ direction from the edge of the heterogeneous patch. For the subunits within the patch, the Hamaker constant ratio R_H was set to be 5.0 (*i.e.*, five times more attractive than the subunits in the region outside of the patch)

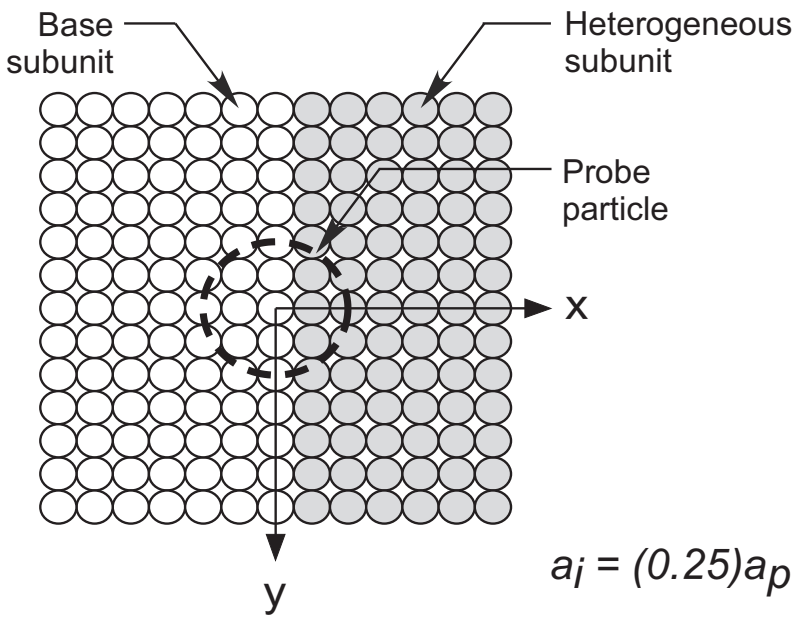

Figure 3.3: Schematic of a simple heterogeneous substrate model. The substrate is composed of a planar array of $13 \times 13 \times 4$ spherical subunits of $0.25a_p$ radius. The probe particle, shown with a thick, dashed line, is situated directly above the origin of the coordinate system. The viewpoint is from above the planar substrate, with the $z-$ axis pointing into the page.

and the electric surface potential was set at -75 mV. The surface potential of the base subunits outside of the patch was -25 mV.

For the model described above, the graphs in Figure 3.4 show the absolute values of the lateral and normal forces (*i.e.*, F_L and F_z, respectively), as well as the force ratio F_L/F_z acting between the surface and the probe particle for separation distances of up to 100 nm. The lateral interaction force is the magnitude of the two interaction force components tangential to the planar surface, F_x and F_y, and it is computed as

$$F_L = \sqrt{(F_x)^2 + (F_y)^2}. \tag{3.15}$$

The figure depicts the absolute values of the forces, or magnitudes, and ignores the sign, or direction. The forces are computed for two different molar concentrations, namely, 10^{-3} M and 10^{-1} M of a symmetric $(1:1)$ electrolyte. These calculations reveal the effects of electrolyte concentration on the total DLVO interaction forces when the particle is near the edge of a heterogeneity

on the substrate.

This investigation first focuses on the lateral forces (Figures 3.4a and b) and the normal forces (Figures 3.4c and d) predicted for the model geometry. Each graph depicts the vdW, the EDL and the total DLVO force. The most prominent features of these graphs are the asymptotic behaviours (spikes) displayed at specific separation distances. These spikes occur in the DLVO force profiles when the DLVO interaction force approaches zero (*i.e.*, spikes pointing down). The spikes coincide with the points where the vdW and EDL force lines intersect, as seen in Figures 3.4(a), (c), and (d). For the 10^{-3} M ionic concentration, the lateral force exhibits one such spike over the range of separation distances shown, while for the 10^{-1} M concentration, the lateral force is monotonic. Furthermore, at this higher salt concentration, the van der Waals interaction is the dominant contributor to the lateral interactions. The normal DLVO force (Figures 3.4c and d) exhibits two spikes for the 10^{-3} M concentration and a single spike for the 10^{-1} M concentration. These spikes in the normal force represent the separation distance from the substrate (along $z-$) where the normal DLVO force becomes zero. The normal forces are generally dominated by the EDL interactions for separations > 1 nm until the crossover point at the secondary minimum. Figure 3.4(d) depicts that the EDL interaction is slightly greater than the vdW interaction for the normal component of the total DLVO force for 1 nm $< h <$ 4 nm, but when $h > 5$ nm, the vdW interaction dominates again.

The force ratios F_L/F_z depicted in Figures 3.4(e) and (f), obtained by combining the results of Figures 3.4(a) to (d), indicate how the lateral force behaves relative to the normal force when the particle is at various separation distances from the substrate along the $z-$ axis. The force ratio exhibits an upward spike at small separations, while for 10^{-3} M salt concentration, there is an additional spike showing a hyperbolic behaviour at a larger separation. The upward spike in the force ratio occurs when the magnitude of the lateral DLVO force becomes larger than the normal DLVO force. The location of the spike coincides with the location of the zero normal force.

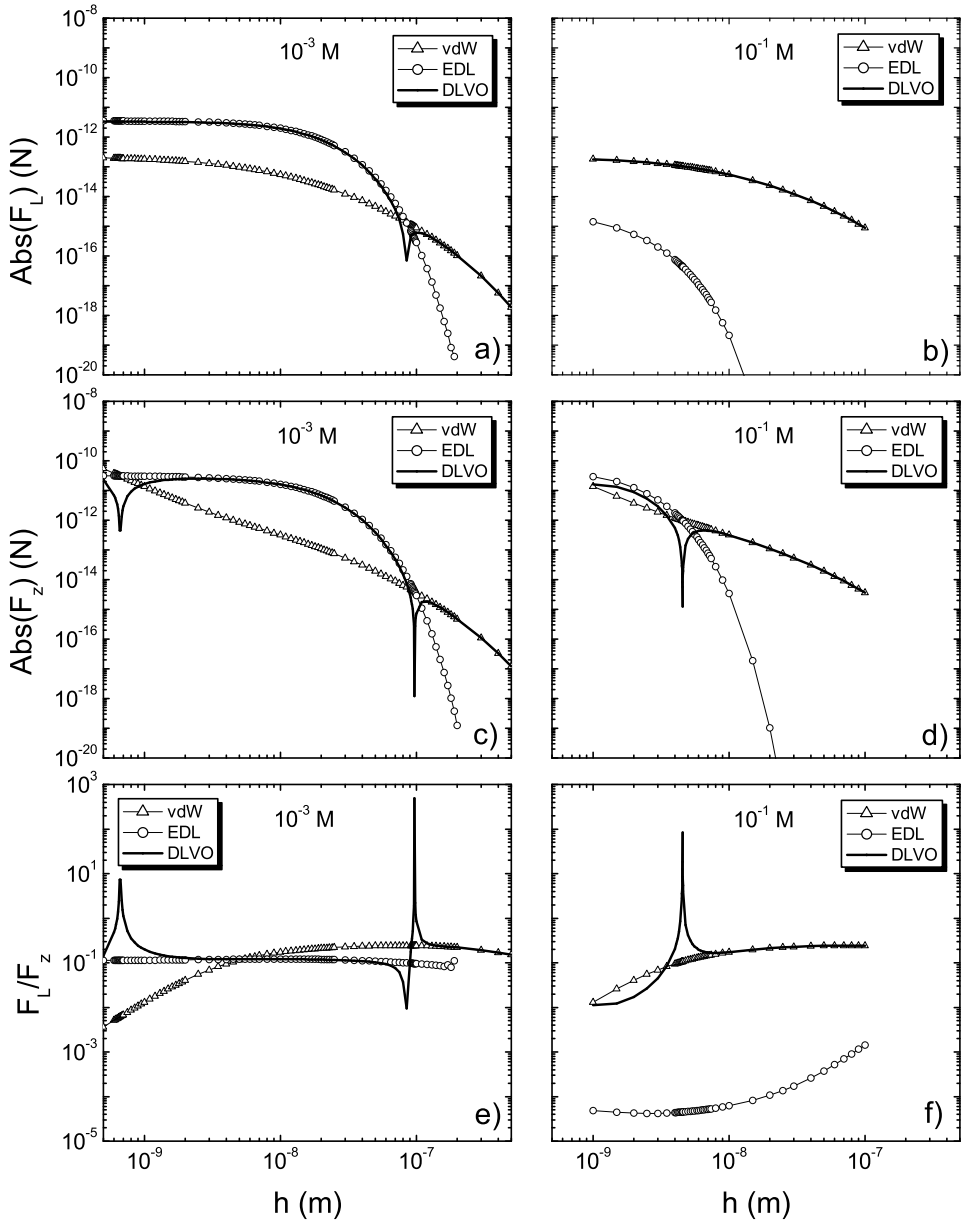

Figure 3.4: Effects of electrolyte concentration on lateral and normal forces, as well as force ratios, acting between the model heterogeneous substrate of Figure 3.3 and a probe particle at various separation distances h. The graphs on the left (a, c, and e) are for a 10^{-3} M concentration, the graphs on the right (b, d, and f) are for a 10^{-1} M concentration. Other parameters for these simulations are listed in Table 3.2.

For the case of 10^{-1} M salt concentration (Figures 3.4b, d and f), it is observed that the lateral force becomes the dominant force in the 4 to 5 nm range. Since the normal vdW and EDL interactions cancel each other out in the 4 to 5 nm separation distance range (evident with the downward spike in Figure 3.4(d) while the lateral vdW force does not vanish, the force ratio in Figure 3.4(f) approaches a large value. This implies that for separation distances between 4 and 5 nm, there are significant net lateral forces acting on the particle, pulling it laterally into the heterogeneous region or patch. In other words, at some point during its approach to the surface, the particle will move laterally over the surface toward the more attractive region of it.

Now, the range of distances over which the lateral force can be felt by a probe particle are explored. Figure 3.5 depicts a new model of the surface that was used to investigate how the DLVO force ratio changes not only with the separation distance, h, normal to the substrate (along $z-$), but also with radial distance away from the center of the heterogeneous patch. For this model of the substrate, its overall size in the $x-y$ plane was increased from $6a_p \times 6a_p$ in Figure 3.3 to $14a_p \times 14a_p$. The heterogeneous region was transformed into a circular patch of radius $2a_p$ centered at the origin of the coordinate system. The ionic concentration was maintained at 10^{-1} M, but the spherical subunit size was reduced to $0.10a_p$. The remaining parameters used here are the same as those used to obtain the results shown in Figure 3.4.

Figure 3.6 depicts the variation of the lateral and normal DLVO forces, as well as the DLVO force ratio, F_L/F_z, with the normal separation distance h between the particle and the substrate. Figure 3.6(a) shows the variations of the lateral and normal forces with separation distance h when the probe particle is positioned directly above the edge of the heterogeneous patch (*i.e.*, radial distance, $r = 200$ nm). It is evident that over a small range of normal separation distance between $3.5 < h < 4$ nm, shown by the hatched band in Figure 3.6(a), the scaled lateral force remains virtually unchanged at a value of about -5, while the normal force changes sharply from a negative to a positive value. Within this narrow band, the lateral force is comparable to or

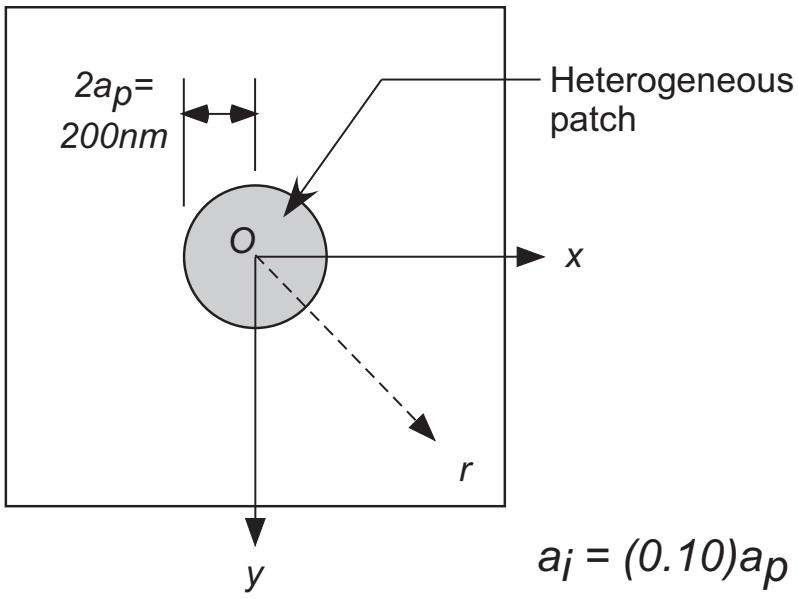

Figure 3.5: Schematic of a model heterogeneous substrate with a single circular heterogeneous patch of 200 nm radius centered at the origin. The substrate is composed of a planar array of $71 \times 71 \times 10$ spherical subunits of $0.10a_p$ radius. The probe particle is situated at various positions along the r axis shown. The viewpoint is from above the planar substrate, with the $z-$ axis pointing into the page.

larger than the normal force. Within this range of dominating lateral force, indicated by the hatched region in Figure 3.6(a), the lateral to normal force ratio, F_L/F_z, goes to infinity at a specific separation distance, corresponding to the location where the normal force becomes zero. In Figure 3.6(b), this phenomenon is depicted for different radial positions of the probe particle as upward spikes in the force ratios. The different lines in Figure 3.6(b) were obtained by changing the lateral (radial) distance of the probe particle from the center of the heterogeneous patch (*cf.* Figure 3.5). It is interesting to note that near an upward spike in the force ratio, the lateral force is generally one to two orders of magnitude greater than the normal force. Furthermore, the separation distance at which the spike appears depends on the radial position of the probe particle relative to the center of the heterogeneous patch. From

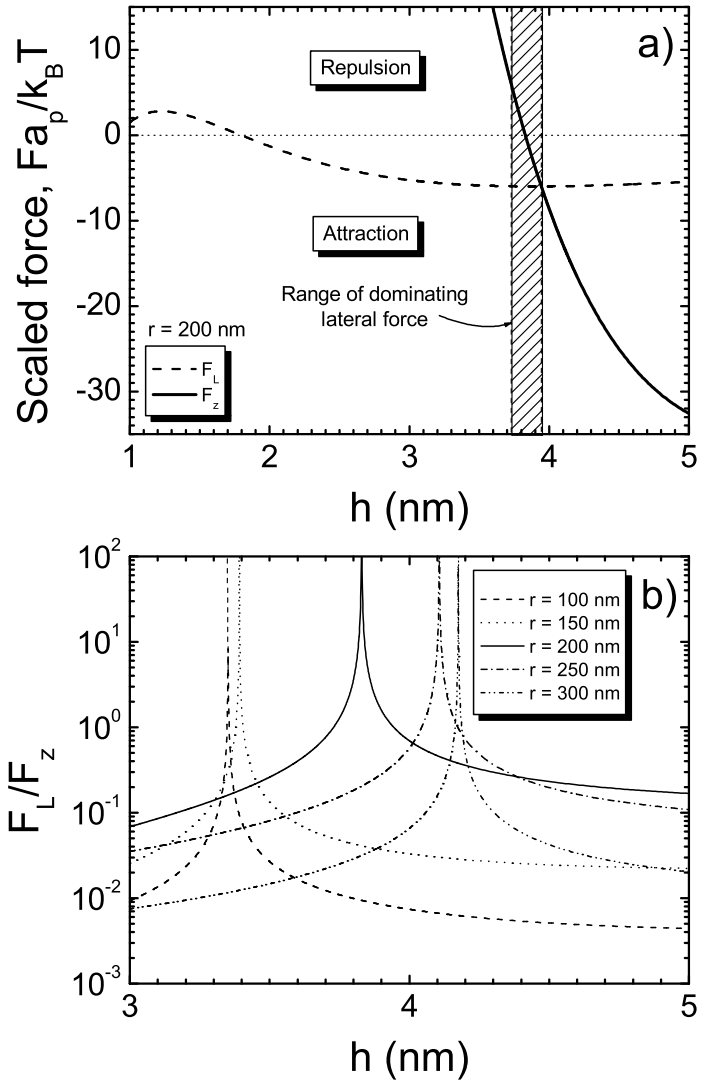

Figure 3.6: Force ratios with changes in separation distance h for interactions between the model heterogeneous substrate of Figure 3.5 and a probe particle positioned at various radial distances (r) away from the center of the heterogeneous patch. (a) Lateral and normal force curves for $r = 200$ nm; (b) Force ratio curves for several radial positions. The electrolyte concentration here is 10^{-1} M. Other parameters for these simulations are listed in Table 3.2.

these observations, it appears that the asymptotic spike in the force ratio marks the separation distance h at which a substantial lateral force can be found while the normal force vanishes. This prevents the particle from moving closer to the substrate in the normal direction, although the lateral forces can continue to displace the particle laterally.

The location of the lateral force spike changes for different radial positions of the particle relative to the center of the heterogeneous patch. Figure 3.6(b) shows that as the radial position r of the particle decreases, the separation distance h at which the upward spike occurs decreases as well. A key observation from this figure is that for radial positions near the edge of the patch (*i.e.*, $r = 200$ nm, 250 nm), the force ratio remains above 0.1 (10%) for $h \leq 5$ nm. However, for all of the other radial positions (*i.e.*, $r = 100$ nm, 150 nm, 300 nm), the force ratio drops off quickly, falling to 0.02 (2%) or less for $h = 5$ nm. This implies that the most significant lateral forces act on the probe particle when it is within the vicinity of the edge of the patch.

3.4.2 Chemical Heterogeneity - Force Mapping

The effects of the presence of a single heterogeneous patch were explored in the preceding subsection. Now, phenomena arising from presence of several heterogeneous patches are studied, with the patches simultaneously influencing the forces acting on the particle. For this purpose, the normal and lateral DLVO interaction forces acting on the particle were mapped as it sampled different lateral locations above the surface, keeping a fixed normal separation distance from a model heterogeneous substrate. The model of the surface used in the preceding section was further enlarged to a square array of spherical subunits measuring $20a_p \times 20a_p$ in the $x - y$ plane with the origin of the coordinate system located at its center. The subunits in this array remained at one-tenth particle size (*i.e.*, $a_i = 0.10a_p$), therefore creating a planar array of $200 \times 200 \times 10$ spherical subunits. The schematic of this model in Figure 3.7 shows the surface with three circular heterogeneous patches of equal radii ($= 2a_p$) with their centers located at $(-2a_p, -4a_p)$, $(-2a_p, +4a_p)$ and

$(+4a_p, 0)$. The probe particle was then positioned at different $x - y$ locations within a region measuring $8a_p \times 8a_p$ of the substrate, indicated by the dashed square in the schematic. The overall interaction force acting on the particle was computed considering the entire area of the square array ($20a_p \times 20a_p$). The remaining parameters for this investigation are identical to those used in producing the results of Figures 3.4 and 3.6.

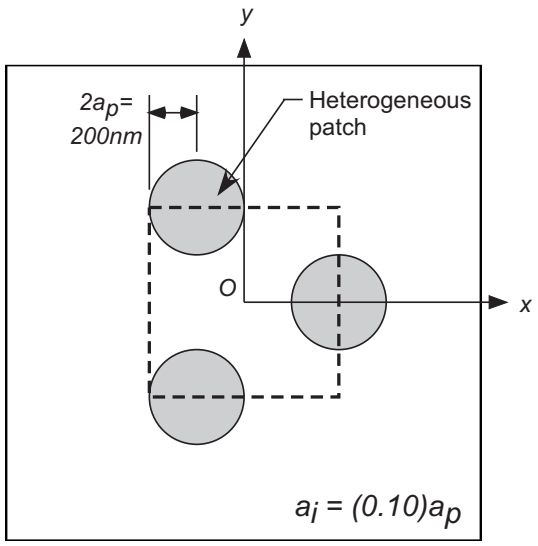

Figure 3.7: Schematic of a model heterogeneous substrate with three circular heterogeneous patches of $2a_p$ radius centered at the origin. The substrate is composed of a planar array of $201 \times 201 \times 10$ spherical subunits of $0.10a_p$ radius. The viewpoint is from above the planar substrate, with the $z-$ axis pointing into the page.

Figure 3.8 depicts several contour plots showing the normal DLVO force (Figures 3.8a, c, e and g) and the lateral-to-normal force ratio F_L/F_z (Figures 3.8b, d, f and h) mapped over the square region delimited by the dashed line in Figure 3.7, wherein the patches lie. For these plots, the dimensions in the $x - y$ plane and the normal separation distance, h, are scaled with respect to the particle radius, while the DLVO forces are scaled with respect to a_p/k_BT. The normal force plots indicate the direction of the force as well as its magnitude, with positive values (darker shades) representing attraction between the particle and the surface, and negative values (lighter shades) representing repulsion. The force ratio plots, however, are displayed in absolute

values and do not distinguish between attractive and repulsive values. All of these force maps are intended to show the regions where the normal and lateral interaction forces become dominant, and in some cases whether they are attractive or repulsive, when the particle is at a particular scaled separation distance H (*i.e.*, $= h/a_p$) from the model heterogeneous surface.

Based on the insights gained from Figures 3.4 and 3.6, the focus is drawn to a range of separation distances of 3 nm to 5 nm ($0.03 < H < 0.05$) for an electrolyte concentration of 10^{-1} M. When $H = 0.05$, Figure 3.8(a) shows that the normal force between the particle and the surface is entirely attractive throughout the field, with greater attractiveness toward the heterogeneous patches. The corresponding force ratio map of Figure 3.8(b) shows that the regions around the edges of the patches are beginning to develop significant lateral forces relative to the normal forces. When $H = 0.04$, the normal force still remains mostly attractive throughout the field in Figure 3.8(c), but Figure 3.8(d) reveals a thin dark band at about $0.5a_p$ outside the edges of the patches where the lateral forces are remarkably high compared to the normal forces. Within this dark band, the force ratios approach infinity, signifying that the lateral force between the particle and the center of a patch is much greater than the normal force. From another perspective, it is within these dark bands that the normal force vanishes, quickly changing direction from repulsion to attraction as one crosses the band to reach the inside of the patch. Figure 3.8(e) shows that for $H = 0.035$, the normal force throughout the field has become more repulsive, with only the regions of the patches themselves remaining attractive. However, the dark bands previously mentioned have become more numerous in Figure 3.8(f), and they have moved slightly closer to the centers of the patches. These dark bands enclose the regions of the substrate where the normal force remains attractive. Once $H = 0.03$ is reached, the entire field is exhibiting repulsive normal forces of varying intensity, with particularly strong repulsive regions along the edges of the patches as shown in Figure 3.8(g). Figure 3.8(h) bears a similar appearance to Figure 3.8(b), with shaded regions around the patch edges indicating where the lateral forces

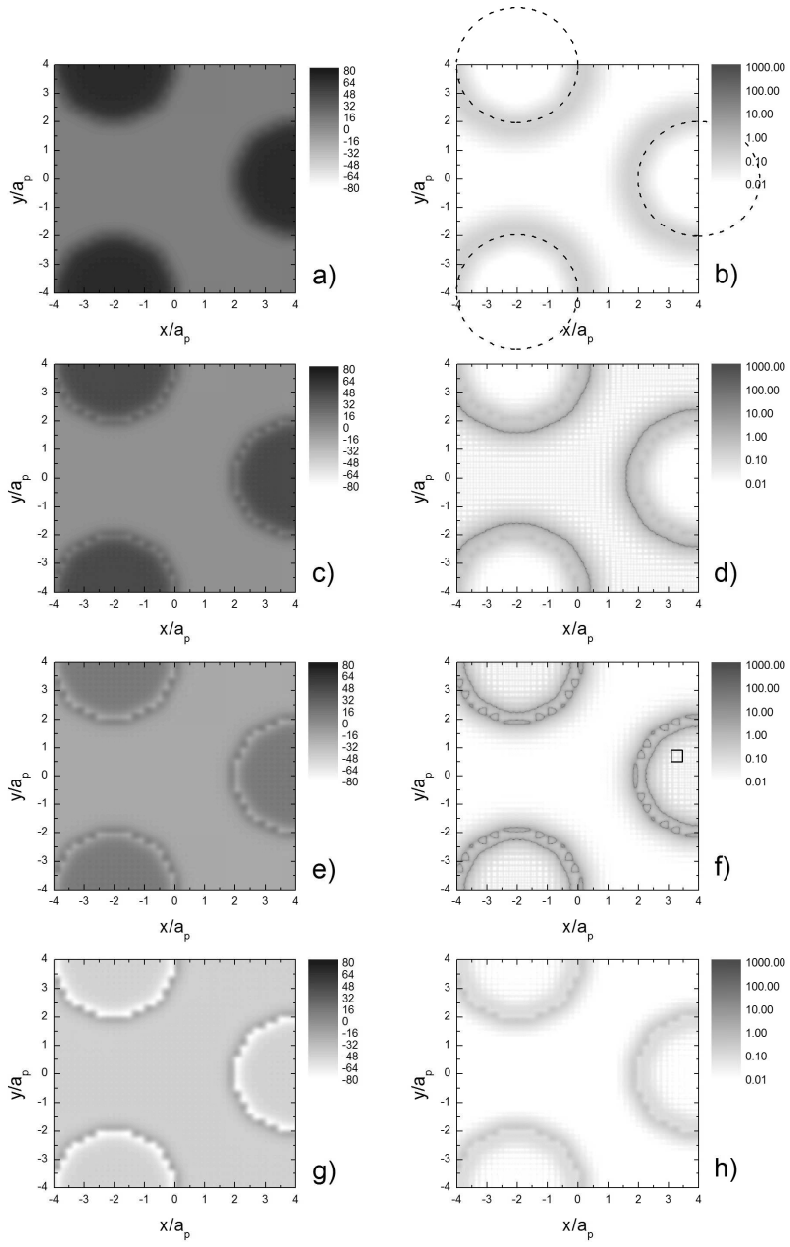

Figure 3.8: Force maps showing the variations in total normal DLVO force and force ratio between a spherical particle and the model heterogeneous substrate of Figure 3.7. The limits of the view field shown in these maps is shown with the dashed line box in Figure 3.7. Each pair of graphs represents the force maps for the particle held at a particular separation distance from the substrate: (a) and (b) $H = 0.05$; (c) and (d) $H = 0.04$; (e) and (f) $H = 0.035$; (g) and (h) $H = 0.03$. The electrolyte concentration is 10^{-1} M for all values of H. All other simulation parameters are provided in Table 3.2. Note: The box with the patch on the right side of (f) is a smaller view field comprised of four subunits, which is shown in Figure 3.9.

remain more pronounced than the normal forces.

Although the lateral to normal force ratio maps in Figure 3.8 provide an impression regarding the relative magnitudes of these forces, the directions of the lateral forces are not resolved in these figures. In this context, referring back to Figure 3.6, one notes that the magnitude of the lateral force becomes considerably larger than the normal force near the asymptotic spikes in the DLVO force ratio. But as Figure 3.6(a) indicated, the direction of lateral force is always attractive toward the center of the patch for all separation distances greater than the separation distance at which the force ratio goes to infinity. Consequently, the dark bands seen in the force ratio maps of Figure 3.8 correspond to the locations of the asymptotic spikes observed in Figure 3.6. Therefore, one can conclude that the lateral forces are most significant in the regions of the dark bands, located at the periphery of the patches. Particles located near the regions of the dark bands will tend to move laterally toward the center of the patch under the influence of this lateral DLVO force.

A closer inspection of the force ratio maps reveals a very fine, checkered pattern adjacent to the patch edges. These checkered patterns move from outside to inside the patches as the separation distance becomes smaller. Such patterns are an outcome of the representation of the substrate as a regular array of spherical subunits. Figure 3.9 provides a close-up view of the lateral-to-normal force ratios over a region of the substrate spanning four subunits (shown as dashed line circles) when the separation distance $H = 0.035$, or $h = 3.5$ nm. The size and position of this smaller region is indicated as a box within the heterogeneous patch on the right side of the view field in Figure 3.8(f). It is evident from Figure 3.9 that a coupled influence of the geometry of the surface and its heterogeneity has given rise to a local variation of the interaction forces. Key features of this convolution of roughness with chemical heterogeneity are the locations in the force ratio map of Figure 3.9 where the lateral force vanishes (*i.e.*, $F_L/F_z \to 0$). When a particle reaches one of these locations, it ceases to move any further toward the center of the patch, or in any lateral direction at all. If this location coincides with a position of

insignificant normal force acting on the particle, then the location marks a point of net DLVO force balance or equilibrium. Here, the particle will no longer move due to DLVO interactions with the heterogeneous substrate.

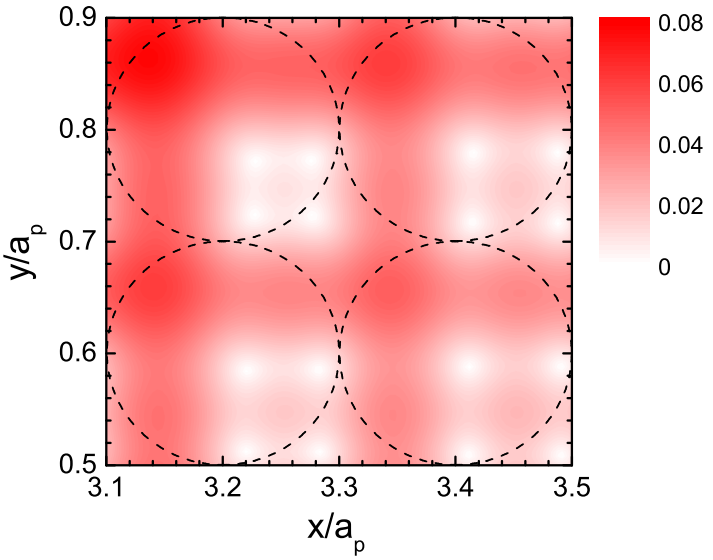

Figure 3.9: Closer view of force map showing the variations in total DLVO force ratio between a spherical particle and the model heterogeneous substrate of Figure 3.7 when their separation distance is $H = 0.035$. Limits of the view field of this map are shown with the solid line box in Figure 3.8(f). The electrolyte concentration is 10^{-1} M, and all other simulation parameters are provided in Table 3.2.

One should note that the analysis presented here does not consider any force other than the DLVO interaction force acting on the particle. Incorporation of hydrodynamic and Brownian forces on the particle can provide further insight regarding the interplay of various physico-chemical interactions on the trajectory of the particle when it is near a chemically heterogeneous surface. Nevertheless, the present simulations bring forth the tremendous influence of lateral forces in dictating the optimal location of closest approach of the particle over a chemically heterogeneous substrate. The modeling approach presented here also imparts roughness to the substrate (owing to the use of spherical subunits). Therefore, these results can be considered as a

manifestation of the combined effects of the surface roughness and chemical heterogeneity.

It is also of interest to note that the influence of the lateral forces become most pronounced at high salt concentrations (*i.e.*, 10^{-1} M), which is highly relevant for biological systems. For lower salt concentrations, as previously shown in Figure 3.4(e), the spikes in the force ratio are pushed further away from the surface where the interaction forces are quite insignificant. Consequently, the influence of lateral DLVO forces are expected to be quite significant for biological systems where the DLVO interactions are highly screened.

3.4.3 Physical Heterogeneity - Force Mapping

Thus far, the focus has been on chemical heterogeneity on a macroscopically planar substrate. The following graphs of force magnitude and direction maps are concerned with the use of the Heterogeneous Interaction Model for substrates with physical heterogeneity. Although the spherical subunits of the model lend some physical heterogeneity to a planar substrate, the scale of roughness is at least an order of magnitude smaller than the particle size. It is of great interest to explore scenarios where the physical heterogeneity is of the same size or larger than the particle near the surface. Such explorations are a means to study many aspects of deposition phenomena, including random sequential adsorption (RSA) [Fed80, ST89, KBE00, Ada06], formation of monolayers [Ada06], and deposition on "textured" surfaces [KBB$^+$00, KH02].

A particular case of physical heterogeneity is the presence of previously deposited particles on an initially flat substrate, which undoubtedly affects the rate at which subsequent particles will deposit on those surfaces over time [Ada06]. One such previously deposited spherical particle can be seen in Figure 3.10, which can also be regarded as a single spherical asperity of radius a_a extending from the flat substrate into the surrounding fluid. Colloidal interactions between previously deposited particles and a probe particle have been explored [Phi95, DB05], but these investigations did not specifically address the magnitudes of lateral DLVO forces.

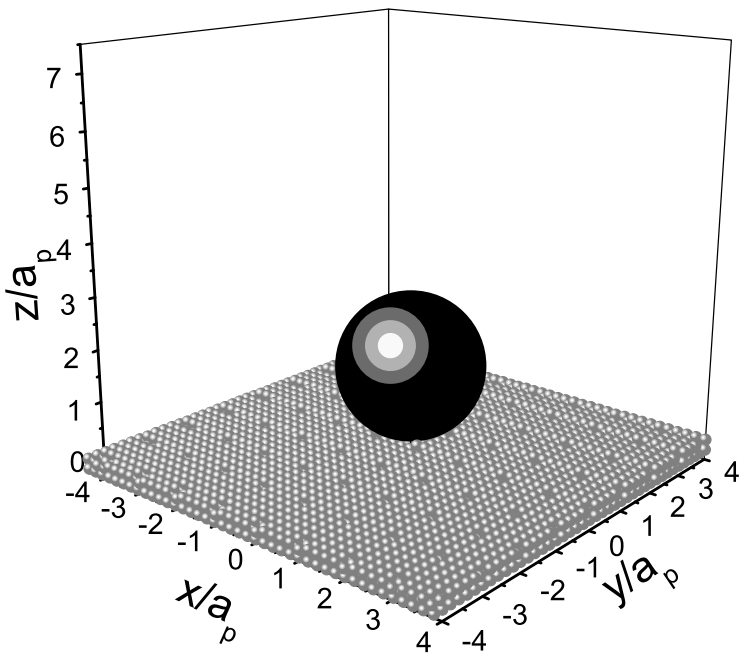

Figure 3.10: Schematic of a model heterogeneous substrate with a single spherical asperity of radius a_a protruding from the flat surface, centered at the origin. In this example, the asperity has a radius equal to that of the probe particle ($a_a = a_p$).

Similar to the approach used for a chemically heterogeneous substrate in Figures 3.8 and 3.9, Figure 3.11(a) is a DLVO force magnitude map of the region near the spherical asperity in Figure 3.10 in the $x - z$ plane. This map is for the case of a 10^{-2} M symmetric (1:1) electrolyte concentration with the same system parameters as those listed in Table 3.2, showing the DLVO force magnitude acting on the particle when its center is located at a given position. The spherical asperity, with its outline represented as a dashed circle, is of equal size to the particle (*i.e.*, $a_a = a_p$), centered directly above the origin of the Cartesian coordinate system. The white region of the map indicates locations where the particle's center cannot be positioned because the particle would physically overlap some portion of the substrate. In this plane, there

are only two DLVO force components, F_x and F_z, so the total DLVO force magnitude at a given location is computed as

$$F_{x-z} = \sqrt{(F_x)^2 + (F_z)^2}. \tag{3.16}$$

All forces are scaled with respect to the Brownian force parameter a_p/k_BT. For this single spherical asperity scenario, the particle radius is 100 nm (= a_p), and all parameters for the associated graphs are the same as those in Table 3.2. Since the composite substrate is chemically homogeneous in this case, the surface potentials of the particle, the asperity and the flat substrate subunits are all -25 mV and the Hamaker constant between the particle and all parts of the substrate, A_{ip}, is k_BT.

Although the force magnitudes on the particle can be much higher or drop down to zero at various positions within the field of view of Figure 3.11(a), a logarithmic colour scale between 0.01 and 100 is sufficient to show the variations of the DLVO force with respect to Brownian force (k_BT/a_p). Since the magnitude does not reveal the direction (attractive or repulsive) of the force, one needs to carefully interpret how the DLVO force changes direction in Figure 3.11(a). In this respect, one can consider the behaviour of the DLVO force profile for a probe particle approaching the composite substrate from an infinite distance along the line of the unit vector $\mathbf{n}_s$ that is normal (perpendicular) to the surface of the spherical asperity in Figure 3.11(a). The DLVO force at larger distances is slightly attractive owing to the long-range van der Waals interactions. This attraction increases as the particle comes closer to the substrate. At around ($x/a_p = 1.6$; $z/a_p = 2.6$) – where a thin, white line emerges – the force becomes zero. This is the location of the secondary DLVO energy minimum. At closer separations, the interaction force becomes repulsive due to the dominance of the repulsive EDL interaction. Before reaching contact with the substrate, the force on the particle crosses a second zero value, which is not distinguishable from adjacent areas of Figure 3.11(a) because it is located at a very short separation distance between the particle and the substrate. This zero corresponds to the DLVO repulsive energy barrier maximum. Below this

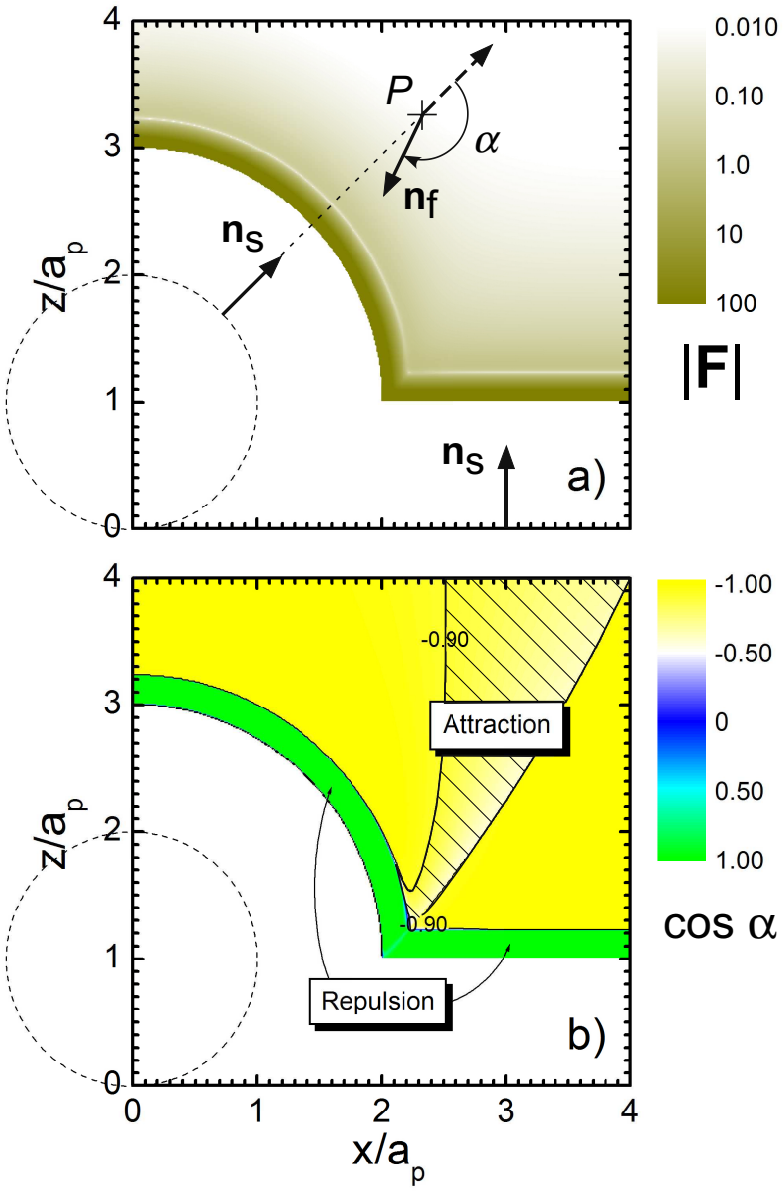

Figure 3.11: Net DLVO force magnitude (a) and direction (b) maps in the $x - z$ plane for a particle in the region immediately surrounding the spherical asperity in Figure 3.10. The radius of both the particle ($= a_p$) and the asperity ($= a_a$) is 100 nm and the (1:1) electrolyte concentration is 10^{-2} M. Positions in the colour map of (b) depict the angular deviation of the net DLVO force vector ($\mathbf{n}_f$) from the substrate surface normal vector ($\mathbf{n}_s$) at the point of closest approach between the particle and the substrate. The colour scale in (b) is based on the dot product of the two vectors, yielding the cosine of the angle between them, α.

separation distance, the particle gets attracted to the primary DLVO energy minimum.

Figure 3.11(b) is a DLVO force direction map, showing how much the direction of the net DLVO force vector ($\mathbf{n}_f$) deviates from the direction of the unit vector normal to the portion of the substrate's surface ($\mathbf{n}_s$) that a given point (*i.e.*, particle's center), such as P in Figure 3.11(a), is closest to. This angular deviation is determined by taking the dot product of these two unit vectors, which yields the scalar cosine of the angle between them, α (*i.e.*, $\mathbf{n}_s \cdot \mathbf{n}_f = \cos\alpha$). These vectors are pointing in the same direction (*i.e.*, repulsion) when their dot product is equal to 1.0, pointing in opposite directions (*i.e.*, attraction) when their dot product is -1.0, and perpendicular to each other when the product is 0.0. A positive value for the dot product means $0° \leq \alpha < 90°$, while a negative value indicates that $90° < \alpha \leq 180°$. In both the green (repulsive) and yellow (attractive) regions of Figure 3.11(b), the net DLVO force and nearest surface normal vectors are essentially parallel to each other. The greatest angular deviation of $\mathbf{n}_f$ from pointing normal to the nearest surface occurs in the hatched region of Figure 3.11(b) where the colour is changing to white and then to blue. In this region, which is bounded by the two contour lines for $\cos\alpha = -0.90$, the particle encounters a transition in the direction of $\mathbf{n}_f$. However, most of this region is located far from the surface of the composite substrate, where colloidal forces are much weaker than the Brownian force ($k_B T/a_p = 4.117 \times 10^{-14}$ N). At such positions for this scenario, particle transport would be dominated by convection and/or diffusion instead of the migrational DLVO force. This region also encompasses only a very small fraction of the area near the substrate.

As Figure 3.12 demonstrates, an increase in the size of the spherical asperity to five times the particle radius ($a_a = 5a_p$) yields similar results to those of Figure 3.11. Aside from asperity size, the simulation parameters for the results in Figure 3.12 are identical to those used for Figure 3.11. Again, the net DLVO force acting on the particle is directed along the distance of closest approach to the substrate for much of the area around the asperity. Figure 3.12(b) shows

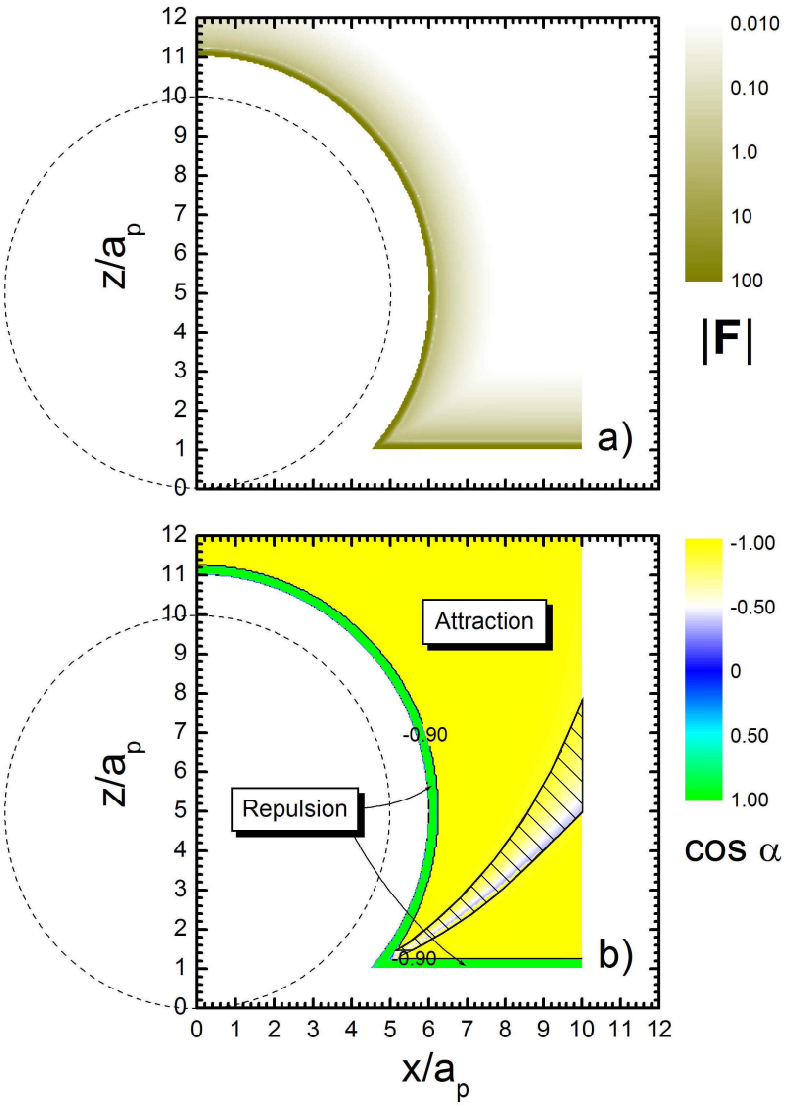

Figure 3.12: Net DLVO force magnitude (a) and direction (b) maps in the $x - z$ plane for a particle in the region immediately surrounding the large spherical asperity. The particle radius ($= a_p$) is 100 nm, the radius of the asperity is five times larger than the particle's radius ($a_a = 5a_p$) and the (1:1) electrolyte concentration is 10^{-2} M. Positions in the colour map of (b) depict the angular deviation of the net DLVO force vector ($\mathbf{n}_f$) from the substrate surface normal vector ($\mathbf{n}_s$) at the point of closest approach between the particle and the substrate. The colour scale in (b) is based on the dot product of the two vectors, yielding the cosine of the angle between them, α.

the repulsive green region remains along the entire surface of the composite substrate, and the area encompassed by the attractive, yellow region is also increased. This increased yellow area can be attributed to the larger asperity size, which makes the top half of the asperity even more disconnected from the flat portion of the substrate than the asperity in Figure 3.11. Consequently, the hatched region (bounded by the contour lines for $\cos\alpha = -0.90$) where the DLVO force vector $\mathbf{n}_f$ is substantially deviated from the normal to the nearest surface $\mathbf{n}_s$ is significantly reduced for a larger asperity. The results in Figures 3.11 and 3.12 reveal that for $a_a \geq a_p$, the size of the spherical asperity makes little difference in the direction of the net DLVO force vector when the magnitude of its force is significant.

When the substrate is physically heterogeneous but chemically homogeneous, the DLVO force on the particle is typically pointing normal to the nearest point on the substrate's surface. There is no appreciable lateral force until chemical heterogeneity is introduced to the substrate. As previously discussed in this chapter, substantial (relative to the Brownian force) lateral forces do not arise until the particle reaches separation distances around the secondary DLVO energy minimum, with the particle positioned over the edge where the two regions of differing chemical characteristics meet (as depicted in Figures 3.4, 3.6 and 3.8). Such separation distances are certainly in the near-field ($h \ll a_p$) for the range of electrolyte concentrations considered in this study (10^{-3} M to 10^{-1} M).

3.5 Summary

This chapter discusses characteristics of the colloidal (DLVO) interactions between a spherical particle and a substrate with chemical or physical heterogeneity. In nearly all locations where colloidal forces are substantial (relative to Brownian force), the net DLVO force acting on the particle is directed along the distance of closest approach to the substrate. Physical heterogeneity by itself does not give rise to significant forces that are lateral (tangential) to the

region of closest approach to the substrate. Nonetheless, consideration of the lateral component of the DLVO force over a heterogeneous substrate – which is generally neglected in most studies involving the DLVO theory – sheds some light on the three-dimensional nature of the DLVO interactions for chemically heterogeneous substrates. Even with a highly simplified model involving the use of the Hamaker approach to evaluate the unretarded van der Waals interactions and the Hogg *et al.* expression for the electrostatic double layer interactions, the lateral forces seem to be a distinct phenomenon for chemically heterogeneous surfaces, and cannot be disregarded at close (near-field) separations corresponding to the secondary minimum of the DLVO interaction potential. These lateral forces act relative to the distance of closest approach between the two bodies. Therefore, lateral forces are indicators of chemical heterogeneity near the point of closest approach between entities, regardless of their topography.

The colloidal force investigated here is only one of the forces acting on a Brownian particle while it is transported near a surface immersed in a viscous fluid. In Chapter 4, a particle tracking model is proposed that includes these forces with those of convection and diffusion to simulate the motion of colloidal particles near surfaces with physical as well as chemical heterogeneity.

Chapter 4

Particle Tracking Model: Problem Formulation

4.1 Overview

In this chapter, a comprehensive description is provided of the Particle Tracking Model (PTM) that simulates the motion of Brownian particles near surfaces with asperities projecting into the fluid.[1] This PTM accounts for van der Waals, electrostatic, hydrodynamic, and Brownian forces acting on the moving particle. The mathematical formulation for evaluating the dispersion and electrostatic interaction forces between any two bodies is based on the DLVO theory [DL41, VO48]. The hydrodynamic field around the asperity is determined numerically by solving the Stokes equations for the system geometry. A detailed description of the geometry, the mathematical formulation including equations of motion, and the boundary conditions of the problem are presented in this chapter, as well as the numerical solution methods employed in the PTM.

[1] A version of this chapter has been published. Kemps and Bhattacharjee, 2009, *Langmuir*, 25(12):6887-6897.

4.2 Mathematical Model

4.2.1 Computational Domain

A schematic representation of the system is shown in Figure 4.1. It consists of a planar surface containing several immobilized spherical asperities (which could be previously deposited particles, roughness features, or engineered bumps). The colloidal suspension in contact with this model "rough" surface experiences a simple one-dimensional shear flow along the $x-$ direction of the Cartesian coordinate system, applied at one end of the domain. This inflow condition is applied at a substantial distance upstream from any asperities. In subsequent discussions, the particle and asperity radii will be denoted as a_p and a_a, respectively. Within this domain, the main intent is to compute the trajectories of individual colloidal particles in the suspension and predict the probability of deposition of these particles onto the model substrate. The Particle Tracking Model (PTM) considers convection, Brownian motion and migration (due to colloidal forces).

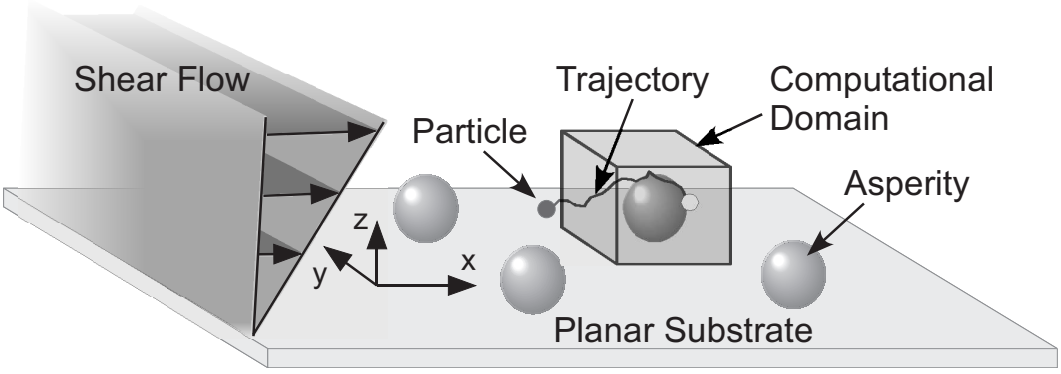

Figure 4.1: Conceptual model of particle deposition onto a planar substrate containing protruding spherical asperities in presence of a shear flow. The transparent box represents the simplified system consisting of a single spherical asperity on a planar substrate. A sample particle trajectory is also shown.

The transparent cubic volume circumscribing a spherical asperity (denoted as the computational domain) in Figure 4.1 depicts the limiting case of particle deposition onto a planar substrate containing a single spherical asperity. Such a system may be considered as a unit cubic cell representing some ordered

geometrical arrays of asperities. It should be noted that even this simple geometry requires a three-dimensional analysis due to a lack of symmetry, and hence, is computationally labourious.

4.2.2 Undisturbed Hydrodynamic Field

The undisturbed (particle-free) hydrodynamic field over the domain of interest is obtained by numerically solving the continuity and Stokes equations for shear flow past the model rough surface employing finite element analysis. As previously indicated, a three-dimensional Cartesian coordinate system is used. The no-slip boundary condition is applied to all of the solid surfaces. The far-field boundary conditions included specified flow (such as shear in the $x-$ direction), pressure, and the appropriate hydrodynamic stress-neutrality conditions.

As depicted in Figure 4.2, the computational domain for the flow field is denoted by Ω, while Γ_s is the no-slip boundary of the flat surface, Γ_a is the no-slip boundary of the asperity, Γ_{in} is the far-field boundary where the simple shear flow regime is applied, Γ_{out} is the outlet/normal flow boundary of Ω, and Γ_{sym} is the slip-symmetry boundary that bisects the flow field along its $x-z$ plane of symmetry. For the scenario shown in this figure, there is a single asperity that is five times larger than the particles in the fluid (*i.e.*, $a_a = 5a_p$) and the computational domain measures $200a_p \times 100a_p \times 100a_p$, where a_p is the particle radius. With the outer boundaries at large distances ($\approx 20a_a$) away from the asperity, the presence of the asperity has a negligible effect on the fluid velocity profile there (refer to validation in Section 5.3.1). Therefore, the fluid velocity at the outer boundary Γ_{in} can be represented as parallel plate channel flow. The undisturbed fluid velocity at Γ_{in} would be expressed as

$$\mathbf{u} = \frac{3}{2} U_{avg} \frac{z}{b} \left(2 - \frac{z}{b}\right) \mathbf{i} \qquad \text{on } \Gamma_{in}, \tag{4.1}$$

where U_{avg} is the average fluid velocity in this parabolic Poiseuille flow, b is the half-height of the channel, z is the vertical position, and $\mathbf{i}$ is the unit vector in the $x-$ direction. Since the scenarios investigated in this study are concerned

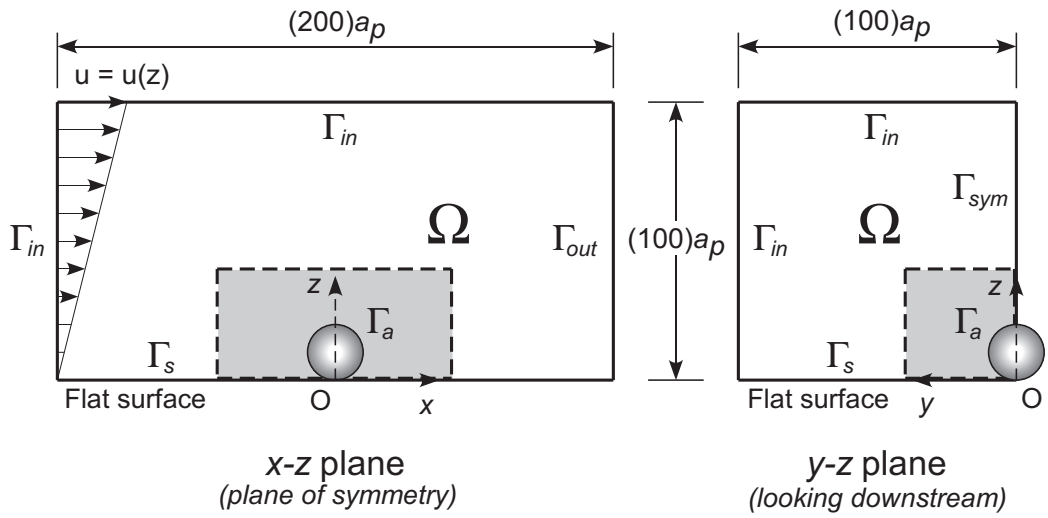

Figure 4.2: Schematic of the fluid domain Ω and its boundaries for determination of hydrodynamic field around a single asperity using COMSOL. For this system, the fluid domain measures $200a_p \times 100a_p \times 100a_p$, keeping its outer limits at a large distance away from the asperity ($a_a = 5a_p$) itself, which is centered on top of the origin of the Cartesian coordinate system. The $x-z$ plane view shows the one-dimensional shear flow starting upstream from the asperity. The $y-z$ plane view looking downstream toward the asperity. The shaded sub-domain enclosed with the dashed line shows the extents of the fluid velocity grid used by the PTM (not-to-scale).

with particle motion near the channel wall (*i.e.*, $z \ll b$),

$$\mathbf{u} = 3U_{avg}\left(\frac{z}{b}\right)\mathbf{i} \qquad \text{on } \Gamma_{in}, \tag{4.2}$$

with $b = 1000a_p$ for all of the PTM simulations.

The particle radius a_p and the average fluid velocity in the channel U_{avg} are used to scale length and velocity, respectively. Letting $\mathbf{r} = a_p\mathbf{r}^*$, where $\mathbf{r}$ is the position vector, $\mathbf{u} = U_{avg}\mathbf{u}^*$ and $p = (\mu U_{avg}/a_p)p^*$, where p is the pressure and μ is the viscosity, the scaled (*i.e.*, non-dimensionalized) forms of the continuity and Stokes equations are, neglecting other body forces,

$$\nabla^* \cdot \mathbf{u}^* = 0 \qquad \text{in } \Omega, \tag{4.3}$$

and

$$\nabla^{*2}\mathbf{u}^* - \nabla^* p^* = 0 \qquad \text{in } \Omega. \tag{4.4}$$

respectively. The boundary conditions, also in scaled form, are

$$\mathbf{u}^* = 0 \qquad \text{on } \Gamma_s, \Gamma_a, \tag{4.5}$$

$$\mathbf{u}^* = 3\left(\frac{a_p}{b}\right) z^* \qquad \text{on } \Gamma_{in}, \tag{4.6}$$

$$\mathbf{n} \cdot \mathbf{u}^* = 0, \qquad \text{on } \Gamma_{sym}, \tag{4.7}$$

$$\mathbf{t} \cdot \mathbf{u}^* = 0, \quad \sigma^* = \frac{\mu U_{avg}}{a_p}\Big(- p^* \mathcal{I} + \left[(\nabla^* \mathbf{u}^*) + (\nabla^* \mathbf{u}^*)^T \right] \Big) = \mathcal{Z}, \qquad \text{on } \Gamma_{out}, \tag{4.8}$$

in which σ^* is the scaled hydrodynamic stress tensor, $\mathcal{I}$ is the unit tensor and $\mathcal{Z}$ is the zero tensor. The numerical approach to solving for the undisturbed flow field is comprehensively described in Appendix A.3, and the manner in which the PTM utilizes this flow field in its simulations is part of the PTM's algorithm in Section 4.3.

4.2.3 Particle Trajectory Equations

The generalized PTM employed in this study considers both deterministic and Brownian movement. The derivation of this model begins with the application of Newton's Second law of motion to a Brownian particle suspended in a viscous, Newtonian fluid, otherwise known as the Langevin equation [RSS89, vdV89],

$$m\frac{d^2\mathbf{r}}{dt^2} + 6\pi\mu a_p \frac{d\mathbf{r}}{dt} = \sum_i \mathbf{F}_i, \tag{4.9}$$

for which m is the mass of the particle, a_p is its radius, $\mathbf{r} = (\mathbf{x}, \mathbf{y}, \mathbf{z})$ is the position vector of the particle's center, t is the time, μ is the absolute fluid viscosity, and $\sum_i \mathbf{F}_i$ represents components of the net external force acting on the particle. The particle's inertia and viscous drag on the left hand side of the equation are balanced against all external forces acting on the particle. These external forces include deterministic forces such as those of fluid drag ($\mathbf{F}^{drag}_{fluid}$), net DLVO interaction ($\mathbf{F}^{DLVO}$), gravity ($\mathbf{F}^{g}$) and electrokinetic effects ($\mathbf{F}^{EK}$), as well as the randomly fluctuating Brownian force, $\mathbf{F}^{Br}(t)$, that varies with time.

The relative magnitudes of each of the terms in Eq. (4.9) can be observed by non-dimensionalizing them, letting $\mathbf{r} = a_p\mathbf{r}^*$, $t = (a_p t^*/U)$ where U is the characteristic fluid velocity, and $\mathbf{F}_i = (\mathbf{F}_i^*)(k_B T/a_p)$. The resulting scaled Langevin equation is

$$(St)\frac{d^2\mathbf{r}^*}{dt^{*2}} + \frac{d\mathbf{r}^*}{dt^*} = \frac{1}{Pe}\left[\sum_i \mathbf{F}_i^*\right], \tag{4.10}$$

which now includes the Stokes number St $(= 2\rho_p U a_p/9\mu)$ and the particle Peclet number Pe $(= Ua_p/D_\infty)$, with ρ_p as the particle's density and D_∞ as its Stokes-Einstein (bulk) diffusivity. For the simulations in this study, the particle is assumed to be neutrally buoyant (*i.e.*, $\rho_p \approx \rho_f$, ρ_f is the fluid density), therefore the force due to gravity is considered to be insignificant $(\mathbf{F}^g \approx 0)$. Due to its extremely small mass, it is reasonable to assume that the particle's inertia is negligible as well, so there is no acceleration in the particle's motion during a given time step (as long as the time step is sufficiently short). This is achieved by ensuring the Stokes number is below approximately 10^{-5} for all simulations $(St \leq 10^{-5})$, and the consequences of this are discussed with regard to the PTM's parameter space in Chapter 5.

For the parameter space explored in this study, thereby neglecting gravity as well as any electrokinetic effects (*i.e.*, $\mathbf{F}^{EK} \approx 0$), the net deterministic force on the particle is the sum of the fluid drag and DLVO forces,

$$\mathbf{F}_{net}^{det} = \mathbf{F}_{fluid}^{drag} + \mathbf{F}^{DLVO}, \tag{4.11}$$

excluding any factors that represent the effect of hydrodynamic interactions between bodies as of yet. Also neglecting rigid body rotation and ignoring the acceleration term, Eq. (4.9) becomes a first order stochastic differential equation because the uncorrelated Brownian force $\mathbf{F}^{Br}(t)$ is taken from a random distribution:

$$\begin{aligned} 6\pi\mu a_p \frac{d\mathbf{r}}{dt} &= \mathbf{F}_{net}^{det} + \mathbf{F}^{Br}(t) \\ d\mathbf{r} &= \left[\frac{\mathbf{F}_{net}^{det}}{6\pi\mu a_p}\right] dt + \left(\frac{1}{6\pi\mu a_p}\right)\mathbf{F}^{Br}(t)\, dt. \end{aligned} \tag{4.12}$$

This new form of the equation demarcates the deterministic and random Brownian parts of the particle's motion. Eq. (4.12) can be solved for by forward integration once with respect to time, subsequently leading to the particle trajectory equation for the PTM. With the use of sufficiently short time steps, the net deterministic force is purely a function of the particle's position and therefore assumed to remain constant over time, so time integration of the deterministic part of Eq. (4.12) is straightforward.

In contrast, the random, probabilistic nature of the Brownian force term calls for more effort to determine its time evolution. Ermak and McCammon [EM78] devised an approach to Brownian Dynamics simulations based on the Langevin equation, taking the time average of Eq. (4.9) over a time step that is much longer than the particle's momentum relaxation time (refer to Section 4.3.7). For a spatially homogeneous system, the Brownian force is described by a normal (Gaussian) distribution [Ein05,RSS89] with the mean and covariance

$$\langle \mathbf{F}^{Br}(t) \rangle = \mathbf{0} \tag{4.13}$$

$$\langle \mathbf{F}_i^{Br}(t_1) \mathbf{F}_j^{Br}(t_2) \rangle = 2k_B T \zeta \delta_{ij} \delta(t_2 - t_1) \delta \tag{4.14}$$

where k_B is Boltzmann's constant, T is the absolute system temperature, ζ ($= 6\pi\mu a_p$) is the particle's frictional coefficient, δ_{ij} is the Kronecker delta, $\delta(t_2 - t_1)$ is the Dirac delta function, and δ is a unit second-order tensor. Eqs. (4.12) to (4.14) are equivalent to the Fokker-Planck equation's interpretation of diffusion (Section 9.7 of [Yip05]), which describes the time evolution of the probability density function of the position of a particle [Kad00].

Eqs. (4.12) to (4.14) also satisfy the fluctuation-dissipation theorem, which states that fluctuations of a system at thermal equilibrium are directly related to the system's linear response to applied perturbations (assuming they are weak enough so that relaxation rates remain constant). In the case of Brownian motion, the amplitude of the fluctuation forces is balanced by the frictional coefficient ζ on the basis of system temperature, and this relationship yields the Stokes-Einstein diffusion coefficient D_∞ (its significance discussed further in Sections 4.2.3 and 5.4). Setting aside the deterministic force term (*i.e.*, drift)

in the Fokker-Planck equation leaves what is known as the Einstein Diffusion equation (for a spatially homogeneous system of non-interacting particles with no external forces present). By calculating the time-averaged mean square displacement of a given particle with this equation, the result is a function of the diffusion coefficient D_∞ and the time elapsed t. Therefore, the approach of Ermak and McCammon has transformed the Brownian force term into a time-averaged Brownian displacement term, and a detailed description of this result is shown from the Eulerian perspective in Section 5.4.

Many independent trajectories should be averaged together to obtain the time evolution of an ensemble-averaged property such as position (Section 9.7 of [Yip05]). Fortunately, when the system is given a long enough period of time to evolve, ergodic theory can be employed to calculate a steady-state property through a time-average of a single trajectory (refer to Section 5.4). The resulting particle trajectory equation in the overdamped Langevin limit (*i.e.*, neglecting particle inertia) [EM78, Dho96, Pro03] can be written as

$$\mathbf{R} = \mathbf{r}(t+\Delta t) - \mathbf{r}(t) = \left[\frac{\mathbf{F}_{net}^{det}}{6\pi\mu a_p}\right](\Delta t) + \mathbf{R}^{Br} = \left[\mathbf{v}_{net}^{det}\right](\Delta t) + \mathbf{R}^{Br} \qquad (4.15)$$

where $\mathbf{v}_{net}^{det}$ is the net deterministic velocity of the particle. The position vector of the particle's center $\mathbf{r}$ at the beginning of any given time step is the basis for calculating all forces causing the particle's subsequent motion during the time step. The equation above simply states that the overall displacement of the particle, $\mathbf{R} = \mathbf{r}(t+\Delta t) - \mathbf{r}(t)$, over a time step Δt is comprised of a deterministic component dictated by the systematic forces and a random Brownian displacement, $\mathbf{R}^{Br}$. The methodologies for obtaining the deterministic and Brownian components of the overall displacement vector are presented in detail later in Section 4.2.3, after a description of how hydrodynamic interactions are represented in the PTM simulations.

Hydrodynamic Interactions

Depictions of hydrodynamic retardation in a robust manner are possible through techniques such as arbitrary Lagrangian Eulerian (ALE) methods [HLZ81,

AQMB08]. Unfortunately, combining such calculations with the PTM can be computationally difficult. As an alternative, the PTM utilizes the conventional approach of accounting for hydrodynamic retardation effects through the universal correction functions (UCFs) of hydrodynamic interactions (*i.e.*, f_1 to f_4) [Bre61, GCB67a, GCB67b, GO71, Dah74], albeit in a slightly modified manner. For creeping flow near a flat surface, components of the particle's velocity due to fluid flow only ($\mathbf{v}$) are related to the corresponding undisturbed fluid velocity ($\mathbf{u}$) components by:

$$v_{\perp} = f_1(H) f_2(H) u_{\perp}, \tag{4.16}$$

$$v_{\parallel} = f_3(H) u_{\parallel}, \tag{4.17}$$

with $\perp$ and $\parallel$ denoting the normal (perpendicular) and tangential (parallel) velocity components respectively (both relative to the flat substrate), and f_1 to f_3 being functions of the scaled separation distance between the particle and the substrate, H $(= h/a_p)$.

For the PTM, the force and velocity vectors are represented in a normal-tangential ($\mathbf{n}$,$\mathbf{t}$) reference frame relative to the particle's distance of closest approach to the composite substrate. This is the same reference frame that was shown to be effective (using the Heterogeneous Interaction Model) for colloidal interactions with physically heterogeneous substrates in Section 3.4.3. Figure 4.3 depicts the methodology employed for this representation. The shortest distance, H_{min} $(= h_{min}/a_p)$, between the suspended particle and the closest approaching feature of the substrate is determined first. Depending on the particle's position, the planar region of the substrate (particle-surface proximity, PSP) or a spherical asperity (particle-asperity proximity, PAP) could be the closest feature. This closest separation distance is the basis for calculation of the unit vectors in the principal normal and tangential directions. Such a representation renders all the vectors two-dimensional, as the original Cartesian components are resolved into the two principal directions.

For example, the following procedure describes the conversion of the undisturbed fluid velocity $\mathbf{u}$ to a normal-tangential $(\mathbf{n}, \mathbf{t})$ reference frame with re-

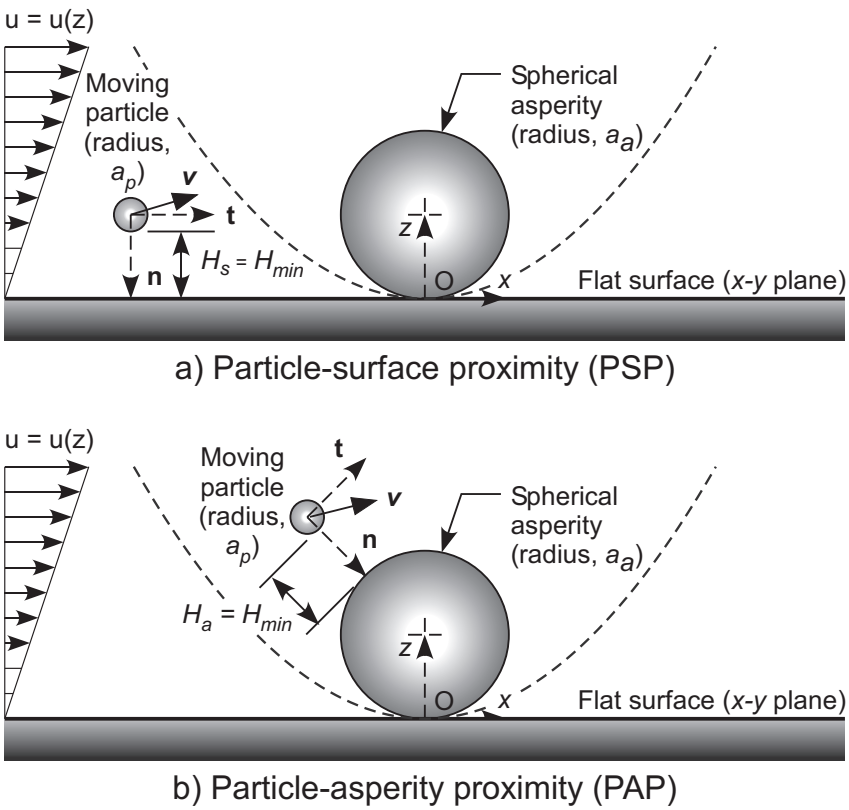

Figure 4.3: Schematic depiction of two different scenarios of collector surface proximity that the moving particle experiences within the fluid domain: (a) Particle-surface proximity (PSP), in which the particle is closest to the flat portion of the substrate, and (b) Particle-asperity proximity (PAP), in which the particle is closest to the spherical asperity. A one-dimensional shear flow, varying only in the $z-$ direction, is applied to the fluid at the inlet boundaries of the system. The Cartesian coordinate system and the corresponding ($\mathbf{n}$,$\mathbf{t}$) coordinate system for each scenario are also shown.

spect to the closest feature of the composite substrate (refer to Figure 4.3). Using the particle's position $\mathbf{r}$, it is first determined whether the planar substrate or the spherical asperity of the composite collector is closest to the particle. Once the closest separation distance H_{min} is found, the associated unit normal vector $\mathbf{n}$ between the particle and the closest approaching surface of the composite collector is calculated using directional cosines. This normal vector then provides the means to transform the velocity vector $\mathbf{u}$ at $\mathbf{r}$ into its normal and tangential (with respect to the nearest approaching surface of the

Table 4.1: Curve fit expressions for the universal correction functions of hydrodynamic interaction (UCFs), taken from Chapter 13 of Masliyah and Bhattacharjee [MB06].

i	a_i	b_i	c_i	d_i	e_i
1	+0.9267	−0.3990	+0.1487	−0.6010	+1.2020
2	+0.5695	+1.3550	+1.3600	+0.8750	+0.5250
3	+0.1500	−0.3750	+3.9060	−0.6250	+3.1050
4	+1.2600	−2.6760	+0.3581	+1.9990	+0.2320

$$f_i = 1.0 + b_i \exp(-c_i H_{min}) + d_i \exp(-e_i H_{min}^{a_i})$$

composite substrate) components, giving

$$u_\perp = \mathbf{u} \cdot \mathbf{n}, \tag{4.18}$$

$$\mathbf{u}_\parallel = (\mathcal{I} - \mathbf{nn}) \cdot \mathbf{u}, \tag{4.19}$$

$$\mathbf{t} = \frac{\mathbf{u}_\parallel}{u_\parallel}, \tag{4.20}$$

in which $\mathcal{I}$ is the unit tensor, $\mathbf{nn}$ is a dyadic tensor, $\mathbf{t}$ is the unit tangential vector, and $u_\perp$ and $u_\parallel$ are the magnitudes of the normal and tangential fluid velocity vectors, respectively.

The dashed parabola in Figure 4.3 represents the loci of positions that are equidistant to the surfaces of both the asperity and the planar substrate. This parabola represents a section of the surface of a paraboloid cradling the asperity. For particle locations outside and inside this paraboloid, the UCFs are computed assuming PSP and PAP, respectively. Switching from PSP to PAP in Figure 4.3 depicts how the $(\mathbf{n}, \mathbf{t})$ reference frame reorients with respect to the asperity as the particle enters the paraboloid. The effects of this abrupt reorientation will be discussed in Section 5.5.

In the ($\mathbf{n}$,$\mathbf{t}$) reference frame described above, the UCFs (f_1 to f_4) are computed on the basis of the distance of closest approach, H_{min}, between the particle and the composite collector employing the curve fit expressions available in Masliyah and Bhattacharjee [MB06]. Table 4.1 presents the generic

form of these expressions, together with their term coefficients. To improve the curve fit for function f_4, the Masliyah/Bhattacharjee expression is replaced with a new expression that more closely fits the exact values calculated in the original paper by Goldman, Cox and Brenner [GCB67b]:

$$f_4 = 1.0 + b_4 \exp(-c_4 H_{min}^{a_{4a}}) + d_4 \exp(-e_4 H_{min}^{a_{4b}}), \tag{4.21}$$

with $a_{4a} = +0.7300$, $a_{4b} = +0.5850$, $b_4 = -0.2750$, $c_4 = +3.7500$, $d_4 = -0.4850$, and $e_4 = +0.6200$.

This approach considerably simplifies the calculation of hydrodynamic interactions. It should be noted that this method provides the upper bound of the hydrodynamic retardation effect when the particle is positioned around the top half of the asperities of the rough substrate, since it assumes that the asperities are analogous to infinite flat surfaces. This maximum hydrodynamic retardation will result in the lowest probability of particle deposition on the asperity. The lower bound of the hydrodynamic retardation effect can be obtained by simply setting the UCFs to 1 (*i.e.*, completely ignoring hydrodynamic retardation). Real deposition behaviour on any finite radius asperity will lie somewhere between these two limiting situations. However, an exception to this occurs if the particle ventures near the wedge between the lower hemisphere of an asperity and the planar surface, where the drag force on the particle will be modified by both surfaces simultaneously, most likely exceeding the upper bound. To the author's knowledge, there is a lack of data concerning retardation in this wedge region to directly compare against results from the PTM's approach, and so this study focuses mainly on deposition on the top half of the asperities. Furthermore, the approximation employed here to compute these functions will become more accurate as the asperity-to-particle size ratio λ $(= a_a/a_p)$ increases.

The technique used here to determine f_1 to f_4 is similar in principle to that used in most colloid deposition studies, where these functions are computed on the basis of the distance of closest approach to a collector [PRT74, RT76, EGJW95, TE04, NG05]. The only modification here pertains to the manner

in which the distance is computed for a composite geometry. In the following sections, descriptions are given of how the UCFs – based on the nearest feature of the composite substrate – are used in the $(\mathbf{n}, \mathbf{t})$ reference frame to modify the deterministic (hydrodynamic and colloidal) and Brownian forces on the particle as it approaches the composite collector. Accordingly, components of the force and displacement vectors in the following discussion are expressed in the $(\mathbf{n}, \mathbf{t})$ reference frame. After all of the calculations are completed for a given time step, the vector components along the axes of the global Cartesian coordinate system (x, y, z) are obtained.

Deterministic Motion

Including the effect of hydrodynamic retardation, the total deterministic force on the particle during a given time step Δt can be written as

$$\begin{aligned} \mathbf{F}_{net}^{det} &= \mathbf{F}_{fluid}^{drag} + \mathcal{B} \cdot \mathbf{F}^{DLVO} \\ &= 6\pi\mu a_p \mathbf{v} + \mathcal{B} \cdot \mathbf{F}^{DLVO} \\ &= (6\pi\mu a_p)\, \mathcal{A} \cdot \mathbf{u} + \mathcal{B} \cdot \mathbf{F}^{DLVO} \end{aligned} \tag{4.22}$$

in which $\mathbf{F}^{DLVO} = (F_{\perp}^{DLVO}, F_{\parallel}^{DLVO})$, $\mathbf{v} = (v_{\perp}, v_{\parallel})$ and $\mathbf{u} = (u_{\perp}, u_{\parallel})$ are the vectors for net DLVO force, particle velocity due to fluid flow only and undisturbed fluid velocity, respectively, with their components projected onto the ($\mathbf{n}$,$\mathbf{t}$) reference frame. The term $6\pi\mu a_p \mathbf{v}$ equals the fluid drag on a spherical particle in a Stokesian flow field. The tensors $\mathcal{A}$ and $\mathcal{B}$, which incorporate the hydrodynamic interactions between the particle and the composite substrate, are entirely functions of the UCFs and given by:

$$\mathcal{A} = \begin{pmatrix} f_1 f_2 & 0 \\ 0 & f_3 \end{pmatrix} \qquad\qquad \mathcal{B} = \begin{pmatrix} f_1 & 0 \\ 0 & f_3 \end{pmatrix}$$

Substituting Eq. (4.22) into Eq. (4.15) results in

$$\mathbf{R} = \left[\mathcal{A} \cdot \mathbf{u} + \frac{\mathcal{B} \cdot \mathbf{F}^{DLVO}}{6\pi\mu a_p} \right] (\Delta t) + \mathbf{R}^{Br} = \mathbf{R}^{det} + \mathbf{R}^{Br} \tag{4.23}$$

where $\mathbf{R}^{det}$ is the deterministic displacement. For the deterministic simulations, Eq. (4.23) is used with $\mathbf{R}^{Br} = 0$.

Brownian Motion

To account for Brownian motion of the particle, the PTM employs a modified version of the method used in a recent study by Nelson and Ginn [NG05], which also conforms to the standard approach to Brownian Dynamics simulations [EM78]. The particle displacement due to stochastic forces is given by

$$\mathbf{R}^{Br} = \mathbf{m}\sigma_R, \tag{4.24}$$

where $\mathbf{m} = (m_\perp, m_\parallel)$ is a vector of two normally distributed random numbers, and σ_R is the square root of the mean-square displacement [RSS89] of the particle. For the normal and tangential components of the Brownian displacement during the time step, one can write

$$R_\perp^{Br} = m_\perp \sigma_{R\perp} = m_\perp \sqrt{2D_\perp \Delta t}, \tag{4.25}$$

$$R_\parallel^{Br} = m_\parallel \sigma_{R\parallel} = m_\parallel \sqrt{2D_\parallel \Delta t}, \tag{4.26}$$

with $D_\perp$ and $D_\parallel$ representing the diffusivity of mass for the particle in the normal and tangential directions respectively. Accounting for the hydrodynamic retardation effect in the Brownian motion of the particle, $D_\perp$ and $D_\parallel$ are written as [Bre61, GCB67b]:

$$D_\perp = f_1(H) D_\infty, \tag{4.27}$$

$$D_\parallel = f_4(H) D_\infty, \tag{4.28}$$

where $D_\infty (= k_B T / 6\pi\mu a_p)$ is the Stokes-Einstein diffusivity and H is the separation distance between the particle and the nearest approaching region of the collector (H_{min}). This approach leads to the Brownian displacement vector being expressed as:

$$\mathbf{R}^{Br} = \left(\sqrt{2D_\infty \Delta t}\right) \, \mathcal{C} \cdot \mathbf{m}, \tag{4.29}$$

with the tensor $\mathcal{C}$ imparting the hydrodynamic retardation effect on the particle's diffusivity, given by

$$\mathcal{C} = \begin{pmatrix} \sqrt{f_1} & 0 \\ 0 & \sqrt{f_4} \end{pmatrix}$$

Total Displacement

The total displacement of the particle during a given time step is obtained by substituting Eqs. (4.22) and (4.29) into Eq. (4.15), giving

$$\mathbf{R} = \left[\mathcal{A}\cdot\mathbf{u} + \frac{\mathcal{B}\cdot\mathbf{F}^{DLVO}}{6\pi\mu a_p}\right](\Delta t) + \left(\sqrt{2D_\infty \Delta t}\right)\,\mathcal{C}\cdot\mathbf{m} \tag{4.30}$$

The PTM employs a scaled version of the total displacement vector, $\mathbf{R}^* = (R^*_\perp, R^*_\parallel)$. By letting $\mathbf{r} = a_p\mathbf{r}^*$, $\mathbf{u} = U_{avg}\mathbf{u}^*$, $\Delta t = (\Delta t^*)a_p/U_{avg}$, and $\mathbf{F}^{DLVO} = (\mathbf{F}^{DLVO*})(k_BT/a_p)$, the scaled form of the total displacement vector is

$$\mathbf{R}^* = \left[\mathcal{A}\cdot\mathbf{u}^* + \left(\frac{D_\infty}{a_pU_{avg}}\right)\,\mathcal{B}\cdot\mathbf{F}^{DLVO*}\right](\Delta t^*) + \left(\sqrt{\frac{2D_\infty\Delta t^*}{a_pU_{avg}}}\right)\,\mathcal{C}\cdot\mathbf{m}. \tag{4.31}$$

4.2.4 DLVO Interactions

The colloidal interactions between the particle and the composite substrate are calculated as a summation of the DLVO force between the particle and the planar substrate (ps) and that between the particle and the asperity (pa). The net DLVO force is given by,

$$\mathbf{F}^{DLVO} = \mathbf{F}^{DLVO}_{ps} + \sum \mathbf{F}^{DLVO}_{pa}. \tag{4.32}$$

The summation sign indicates that the force is added over all the asperities. The expressions used for the unretarded (in terms of dispersion only, not hydrodynamic) van der Waals (vdW) [Ham37] and electric double layer (EDL) [HHF66] forces of the DLVO interaction are, respectively,

$$\mathbf{F}^{vdW}_{pi} = -\frac{32A_{H,pi}}{3a_p}\left[\frac{\lambda^3(H_i+1+\lambda)}{(H_i^2+2H_i+2\lambda H_i)^2(H_i^2+2H_i+2\lambda H_i+4\lambda)^2}\right]\mathbf{n}, \tag{4.33}$$

$$\mathbf{F}^{EDL}_{pi} = \frac{4\pi\epsilon\kappa a_p\psi_p\psi_i\lambda}{(1+\lambda)}\left[\frac{\exp(-\kappa H_i a_p)}{1+\exp(-\kappa H_i a_p)} - \frac{(\psi_i-\psi_p)^2}{2\psi_p\psi_i}\left(\frac{\exp(-2\kappa H_i a_p)}{1-\exp(-2\kappa H_i a_p)}\right)\right]\mathbf{n}, \tag{4.34}$$

where $A_{H,pi}$ is the effective Hamaker constant for the van der Waals interaction between the particle and the feature of the composite substrate (*i.e.*, asperity or planar substrate, represented by the index $i = a, s$ respectively), $H_i =$

h_i/a_p is the scaled separation distance between the particle and the feature, ϵ is the permittivity of the medium, κ is the inverse Debye length of the system, ψ_i is the surface potential of the feature, ψ_p is the surface potential of the particle, and $\lambda = a_i/a_p$ is the ratio of the radii of the feature and the particle. For the planar substrate, $\lambda \to \infty$. In this study, the vdW interaction force between the particle and any feature is always attractive. As a sign convention, attractive forces acting on the particle point from the particle's center toward the composite substrate along the vector $\mathbf{n}$ (see Figure 4.3). The above expressions can emulate attractive (favourable deposition, denoted by F) or repulsive (unfavourable deposition, denoted by U) interactions between the particle and the composite substrate with appropriately selected parameters.

The above expressions are by no means rigorous representations of colloidal interactions in real systems. Retardation effects have been neglected in computing the vdW interactions, whereas the EDL interactions are obtained from a solution of the linearized Poisson-Boltzmann equation with the Derjaguin approximation, rendering such an expression valid only for low surface potentials and large κa_p.

Calculation of the DLVO force between the particle and a spherical asperity in the PTM is very similar to the technique used in the Heterogeneous Interaction Model for the DLVO force between a particle and a spherical subunit in the substrate. Consequently, the PTM can also be applied to systems containing substrates with various configurations of heterogeneity through specific placement of, and assignment of chemical characteristics to, spherical subunits. These subunits can also vary in size to form irregular, non-periodic substrate topographies.

4.3 Numerical Solution Methodology

The numerical solution of the particle trajectory equations is implemented with a FORTRAN program, using an explicit time marching scheme otherwise referred to as the forward Euler method. The PTM algorithm – displayed as a

flowchart in Figure 4.4 – starts with the initial conditions and a starting position of the first particle, for which the undisturbed fluid velocity components at the particle center and the particle-substrate DLVO forces are computed. Following this, the distance of closest approach (H_{min}) and the corresponding ($\mathbf{n}$,$\mathbf{t}$) reference frame are determined employing the technique outlined in Section 4.2.3. The UCFs are calculated on the basis of these parameters, subsequently filling the matrices $\mathcal{A}$, $\mathcal{B}$ and $\mathcal{C}$ and leading to the evaluation of the particle's deterministic and Brownian displacements over the time step. For the Brownian displacement, the normally distributed random numbers in the vector $\mathbf{m}$ are generated using a random number generator [PTVF92]. The particle position is then updated for the beginning of the next time step using Eq. (4.30). Only very dilute particle suspensions are considered in the simulations of this study, with essentially one particle released at a time. The following sections explain particular details of the steps in the PTM's algorithm.

4.3.1 Initial Conditions

Among the system parameters at the beginning of the PTM's program `MAIN` (*i.e.*, "System Parameters" in Figure 4.4), `ISCEN` is an index number for choosing if the simulation will include only deterministic forces (= 0) or deterministic and Brownian forces (= 1). The `IFLOW` parameter distinguishes between simulations with no fluid flow (= 0) or some finite fluid velocity (= 1). `IFLOW` changes the value of the average fluid velocity `UAVG` (U_{avg}), which is used to scale quantities in the PTM such as fluid velocity $\mathbf{u}$ and time t. To avoid division by zero for scaling in the case of no fluid flow, the diffusion time scale a_p^2/D_∞ is employed and results in $U_{avg} = D_\infty/a_p$; otherwise, U_{avg} is provided by the user.

In order to set up the initial system configuration for the PTM, the substrate's geometry and the properties of all system components need to be identified and readily accessible in the FORTRAN program. The properties of the system's fluid, including the average fluid velocity U_{avg} and electrolyte

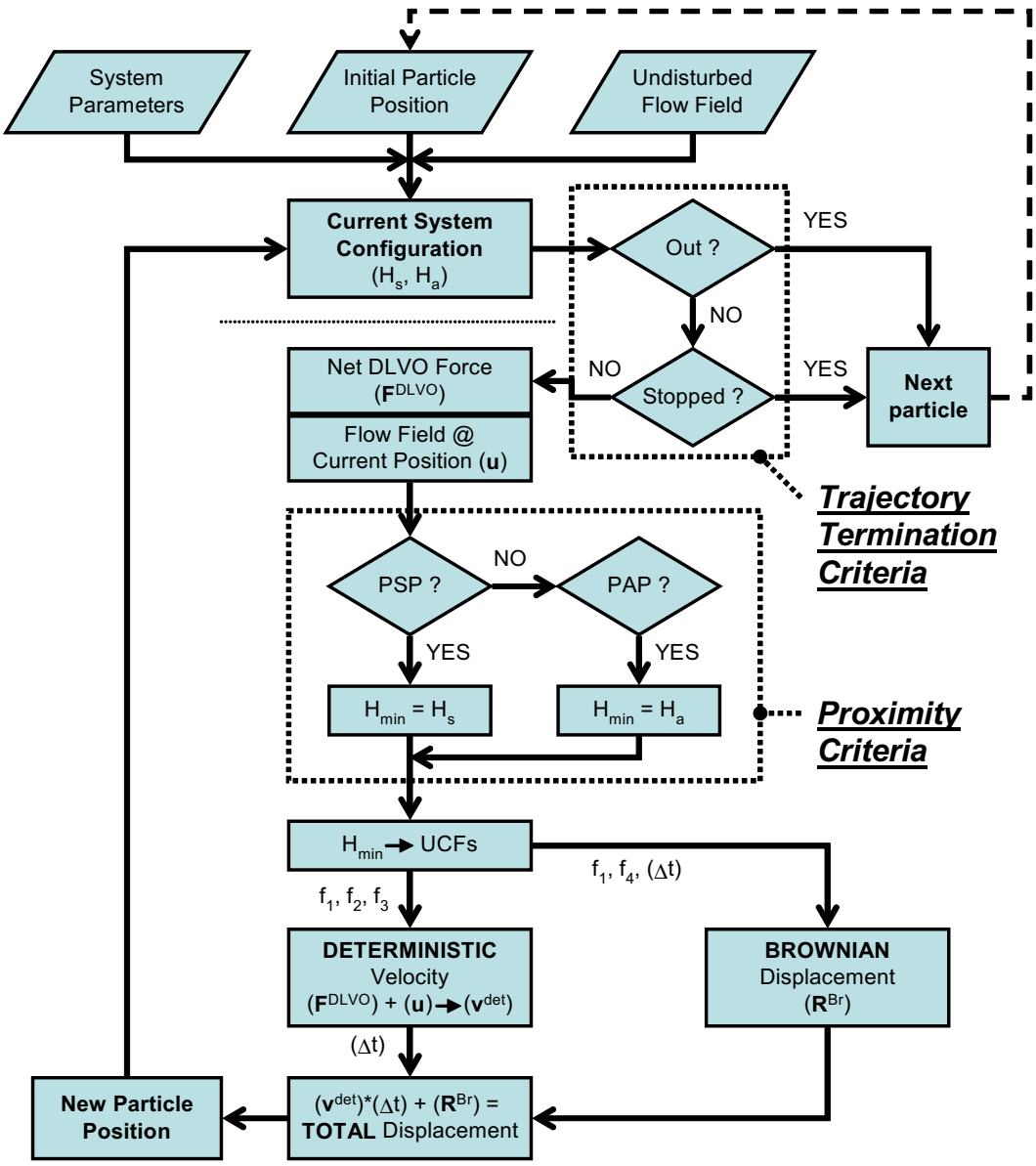

Figure 4.4: Flowchart for the algorithm of the Particle Tracking Model (PTM).

concentration, are stored in the array F() in the subroutine FLUID. Parameter NSA specifies the number of spherical asperities present in the scenario, and subroutine SUBSTRATE establishes the positions and properties of those spherical asperities on the flat surface in the array S(). These properties include asperity size, mass density, surface potential and scaled Hamaker constant. Also, in cases of irregular physical and/or chemical heterogeneity, SUBSTRATE can include the positions and properties of substrate subunits ($a_i < a_p$, identical to those of the Heterogeneous Interaction Model in Chapter 3). Only subunits that lie within the cut-off distance RCUT (refer to Section 4.3.4) from the particle's center would be considered in calculating DLVO interactions, reducing computational time and effort for such cases.

With the substrate clearly defined, the model substrate can be formed in finite element software to numerically solve for the undisturbed hydrodynamic field in its vicinity (*i.e.*, "Undisturbed Flow Field" in Figure 4.4; refer to Section 4.3.3 for more background). Before this undisturbed hydrodynamic field can be properly entered into the FORTRAN program, the values of NX, NY and NZ (*i.e.*, number of grid node positions in the $x-$, $y-$ and $z-$ directions for the sub-domain of interest, shown with a shaded box in Figure 4.2 and the enlarged schematic in Figure 4.5a) must be set in the program MAIN. These values must match the corresponding values used to create the sub-domain grid for the given scenario in the first place. NX, NY and NZ are functions of the scaled dimensions of the sub-domain and the chosen grid resolution, RES (to be discussed further in Section 4.3.3).

The subroutine PARTICLES provides another major component of the initial system configuration, storing the initial particle positions (or release points within the sub-domain) and their properties in the array P(). These release points are distributed in a pseudo-random manner using a random number generator (refer to Section 4.3.2). They are kept away from the edge of the sub-domain for full Brownian simulations as the particle could be quickly ejected from the sub-domain by Brownian motion, thereby ending the particle's trajectory prematurely. Typical starting positions are at least two to five particle

radii away from any of the sub-domain's outer boundaries. The number of particles released for a single simulation run is specified with the parameter `NP`.

4.3.2 Random Number Generation

Random numbers serve two functions in the PTM simulations: (i) random initial placement of `NP` particles in the computational sub-domain for a single simulation run (*i.e.*, "Initial Particle Position" in Figure 4.4), and (ii) determination of the magnitudes of Brownian displacement in the $(\mathbf{n}, \mathbf{t})$ directions experienced by the particle at each time step (*i.e.*, "BROWNIAN Displacement" in Figure 4.4). For each simulation run, the starting positions of the particles are distributed throughout a prescribed area or volume in the sub-domain using `RAN2`. `RAN2` is a random number generator subroutine by L'Ecuyer (found in Chapter 7 of Numerical Recipes for FORTRAN [PTVF92]) that returns a pseudo-random value between 0 and 1 (not including 0 or 1) (*i.e.*, uniform deviate). Although it has a relatively longer execution time when compared with several other random number generators [PTVF92], `RAN2` has an extremely long period ($> 2 \times 10^{18}$ executions) before repeating. This is very effective when some of the PTM simulation runs in this study involve as many as 10^9 calls for random numbers. For this study, the particles are typically released from an area in the $y - z$ plane at some distance upstream from any asperity in the sub-domain. With the $x-$ position fixed at some value, the $y-$ and $z-$ positions are set between limits, and a uniform deviate obtained from `RAN2` modulates the position in each direction. Magnitudes of the two components of the vector m (*i.e.*, part of the Brownian displacement vector $\mathbf{R}^{Br}$) are determined with the subroutine `GAUSS` (also from Chapter 7 of Numerical Recipes for FORTRAN [PTVF92]). This subroutine transforms a uniform deviate that it calls for with `RAN2` into a normally distributed deviate with zero mean and unit variance.

In order to initialize subroutine `RAN2`, an initial seed number that is a negative integer is required. Near the beginning of the program `MAIN`, the

subroutine `HMS_CURRENT_HMS` (modified from a FORTRAN90 version written by John Burkhardt [Bur05]) outputs a three digit integer for thousandths of a second from the current time. This integer is subtracted from another negative integer `INIT` to produce a seed number `IC` that changes for each time a group of PTM simulation runs are started. Subsequent calls of `RAN2` then use a new value of IC derived from the execution of `RAN2` to continue generating random numbers.

4.3.3 Undisturbed Hydrodynamic Field

For this study, the numerical solution of the Stokes equation to determine the fluid velocity field around the model rough surface was achieved with a commercially available finite element software package, COMSOL Multiphysics 3.3 (Comsol Inc.; Burlington, MA). To reduce computational effort in the numerical solution of the flow field, symmetry in the $x - z$ plane is utilized to cut the field in half, as depicted in Figure 4.3. This half-field enables the full flow field to be rendered perfectly symmetric. The velocity data is exported from the finite element program and then input into the PTM in the form of a three-dimensional Cartesian grid of predetermined resolution (*i.e.*, "Undisturbed Flow Field" in Figure 4.4). As noted earlier, the limits of this grid are smaller than the overall computational domain, which is shown (not-to-scale) with a shaded sub-domain in Figure 4.2. A detailed procedure of how the undisturbed hydrodynamic field is created for use by the PTM can be found in Appendix A.

Despite the validity of using linear superposition with Stokes flow scenarios, there are no closed form analytical solutions for velocity fields around spherical asperities on a flat surface in a shear flow. The works of Higdon [Hig85], Dąbroś [Dąb89], van de Ven [MDvdV86, DvdV92], and Pozrikidis [Poz94, Poz97, Poz99], to name a few, have applied boundary integral and/or singularity methods to the Stokes equations and generated very good results for Stokesian flow fields around obstacles on flat surfaces. Results of the finite element technique applied to the single spherical asperity were compared against a boundary

integral solution given by Pozrikidis [Poz97], with $< 2\%$ deviation between the two approaches (refer to Section 5.3.1 for details concerning this validation). The PTM's numerical approach to determining such Stokesian flow fields is clearly more computationally demanding than the approaches of the earlier works. However, this approach has the flexibility of rendering a hydrodynamic field over a surface of irregular topography (*i.e.*, physical heterogeneity or roughness), incorporating the full Navier-Stokes formulation, and including additional body forces (such as electrical forces).

4.3.4 DLVO Interactions and Undisturbed Fluid Velocity

After testing for trajectory termination criteria (explained later in Section 4.3), the particle's current position (*i.e.*, "Current System Configuration" in Figure 4.4) is used to calculate the net DLVO force acting on it at that given moment (*i.e.*, "Net DLVO Force" in Figure 4.4). Its position is also used to determine the undisturbed fluid velocity at the center of the particle, as if the particle is not there to disturb the steady Stokes flow over the substrate (*i.e.*, "Flow Field @ Current Position" in Figure 4.4).

At the beginning of each time step, the DLVO interaction between the particle and each component of the composite substrate (*i.e.*, asperity, subunit, and flat portion) is computed in the subroutine `TOTAL_DLVO`. Within `TOTAL_DLVO`, a section handling sphere-sphere interactions has the subroutine `SEPARATION`, which sets up the array `DIF()` to temporarily store the information regarding the separation between the particle and any spherical component of the composite substrate. This includes the (center-to-center) position difference vector (calculated using the SLATEC library subroutine `DAXPY` for adding/subtracting vectors), and subsequently, the unit normal vector `UN()` pointing along the separation distance between the two bodies. Unit vector `UN()` is determined using the position difference vector and its magnitude in `DIF()` with the SLATEC library subroutine `DSCAL` for scaling vectors. For each pairwise interaction, the separation distance is compared with the previously-

stored minimum value to see if a new minimum is found. If so, the new minimum separation distance and its associated unit vector are stored as HOMIN and UNO() respectively. When applicable, this procedure is also used in a separate section of TOTAL_DLVO for previously deposited particles on the substrate, with its minimum separation distance and associated unit vector stored as HPMIN and UNP() respectively. These separation distances and unit vectors are used later in another subroutine concerned with the particle's closest proximity to the composite substrate (refer to Section 4.3.5).

Using the information in DIF(), each call of subroutine FORCE_DLVO calculates the DLVO force between the particle and a spherical asperity or subunit in the substrate, and subroutine EDL_HHF_SS within it is called to determine the EDL portion of the force. There is also a section of subroutine TOTAL_DLVO that calculates the DLVO force between the particle and the flat portion of the substrate based on a simple sphere-plate separation distance HS, with subroutine EDL_HHF_SP computing the EDL component. Only pairwise interactions that are within a specified scaled cut-off distance RCUTD are computed for the net DLVO force on the particle; DLVO interactions between bodies separated by more than RCUTD are not calculated, and hence, neglected. For the PTM simulations in this study, RCUTD has been set to 3.0 (*i.e.*, three times the particle radius). The summation of all of the individual DLVO force vectors to obtain the particle's net DLVO force vector is accomplished with the SLATEC library subroutine DAXPY in the PTM subroutine TOTAL_DLVO.

The subroutine HYDROVEL is a hunting-and-interpolation scheme that determines the Cartesian components of the undisturbed fluid velocity at the current position of the particle's center anywhere within the sub-domain that the particle may occupy. This subroutine calls for the arrays for the sub-domain grid node positions GRX, GRY and GRZ as the basis to hunt for the particle's position within the grid. For each Cartesian direction, the subroutine HUNT (acquired from Chapter 3 of Numerical Recipes for FORTRAN [PTVF92]) searches for the two grid nodes that the particle's position currently resides between, then outputs the index number of the grid node that is lower (*i.e.*,

ILO for $x-$, JLO for $y-$, KLO for $z-$). These index numbers correspond with the indices of the three undisturbed fluid velocity arrays (*i.e.*, UUX(), UUY() and UUZ(), in the $x-$, $y-$ and $z-$ directions, respectively) exported from COMSOL into data files that can be read by the FORTRAN program. From ILO, JLO and KLO, the eight nodes of the sub-domain grid subunit (labeled with numbers 1 to 8 in Figure 4.5b) that the particle presently resides in are identified and used to extract the associated undisturbed fluid velocity data for each of the eight nodes from the data files originating from the finite element solution (by COMSOL in this study) of the flow field near the composite substrate.

Now, the position of the particle with respect to the eight adjacent grid nodes and the undisturbed fluid velocity at each of those nodes is known. This information is required to perform trilinear interpolation [Tod03] using the subroutine INTERPOLATE in all three Cartesian directions, which determines the undisturbed fluid velocity vector $\mathbf{u}$ at the location of the particle's center. The use of trilinear interpolation assumes that there are linear changes in $\mathbf{u}$ over the volume of any given grid subunit that the particle's center may lie within. This is a reasonable assumption when considering that the flow fields in the PTM simulations are Stokesian (and therefore, solved as a linear system). The validity of this assumption is tested in Section 5.3.2.

4.3.5 Proximity Criteria and Hydrodynamic Interactions

With the net DLVO force acting on the particle $\mathbf{F}^{DLVO}$ and the undisturbed fluid velocity vector $\mathbf{u}$ calculated, the next step in the PTM program is to determine which region of the substrate that the particle is closest to. The stored information concerning the closest approach to any spherical asperity (or spherical subunit), the flat surface and any previously deposited particle (when applicable) is accessed in the subroutine CLOSEST. Within this subroutine, a comparison of these separation distances is made, resulting in a declaration of the minimum separation distance HMIN (H_{min}) along with its associated unit vector UNMIN() (*i.e.*, "Proximity Criteria" in Figure 4.4). The

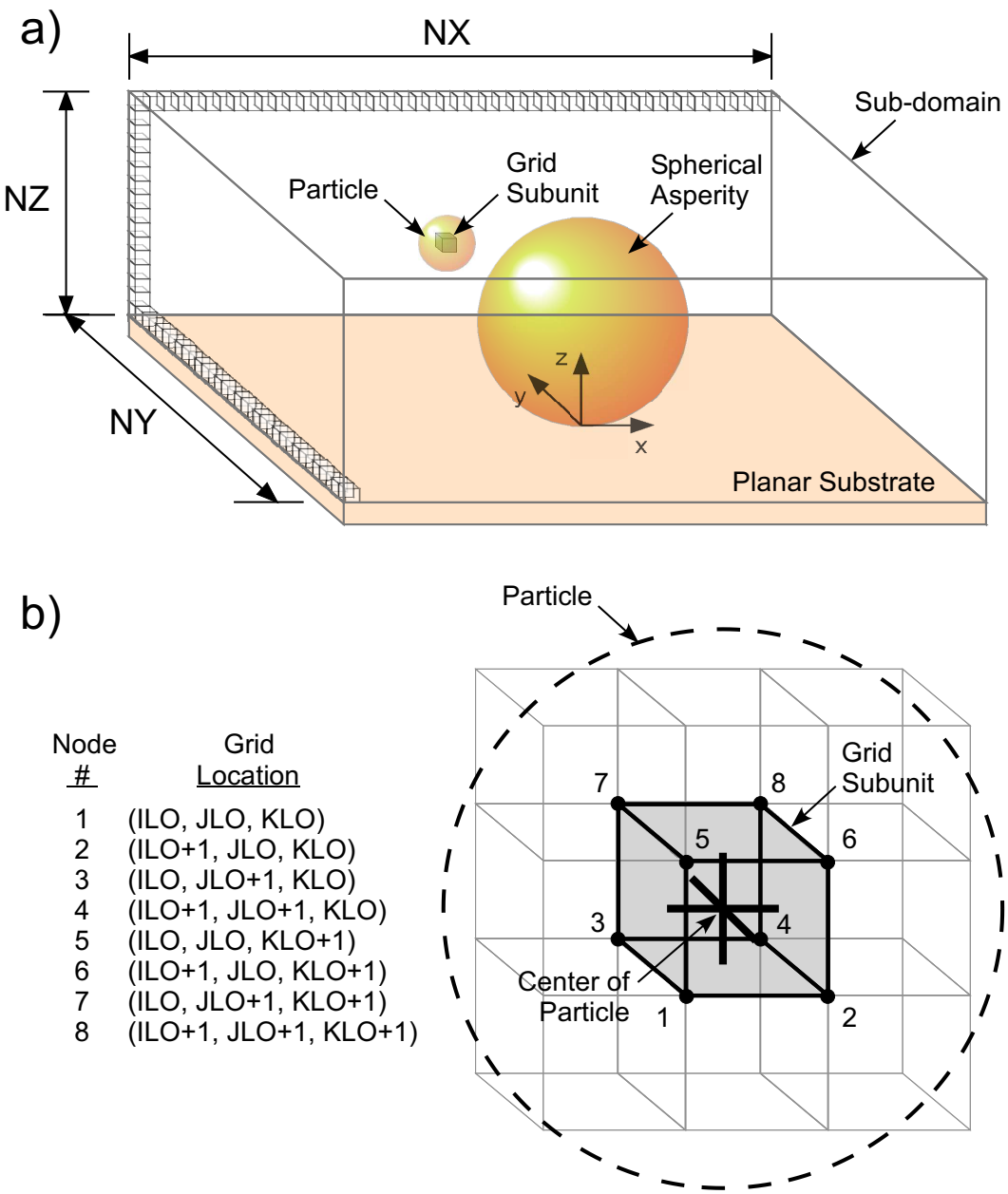

Figure 4.5: Grid search in the $x-$, $y-$ and $z-$ directions for the position of the particle's center by the subroutine `HUNT`. (a) Schematic representation of the Cartesian grid in the sub-domain (*i.e.*, shaded region of Figure 4.2) used to export undisturbed fluid velocity data from the region of interest in the numerically-determined computational domain around the model substrate (not-to-scale). (b) Schematic of the grid subunit that the particle's center currently resides in. The index numbers of the eight adjacent grid nodes are shown, and the grid resolution in all three directions is $0.5a_p$.

unit vector UNMIN() will be the normal direction of the relative (**n**,**t**) coordinate system described in Section 4.2.3.

Hydrodynamic interactions between the particle and the closest approaching surface of the substrate can now be accounted for. The UCFs (f_1 to f_4) are calculated on the basis of HMIN in the subroutine HYDRO_CORRECTION, and temporarily stored in the array UCF() (*i.e.*, "$H_{min} \rightarrow UCFs$" in Figure 4.4). The UCF() array will be used in the subroutines DETERMINISTIC and BROWNIAN to calculate the particle's deterministic velocity and Brownian displacement vectors (DVEL() and B(), respectively) over the next time step. The values in UCF() are the constituents of the 2×2 tensors $\mathcal{A}$ to $\mathcal{C}$ found in Eq. (4.31).

4.3.6 Deterministic Particle Velocity

The deterministic particle velocity in the PTM is a function of not only the net DLVO force $\mathbf{F}^{DLVO}$ and the undisturbed fluid velocity **u** at the particle's center, but also hydrodynamic retardation via the particle's distance of closest approach to the substrate (*i.e.*, "DETERMINISTIC Velocity" in Figure 4.4). Accounting for hydrodynamic interactions is all done in the (**n**,**t**) reference frame, but as of yet the direction of the tangential component of this reference frame with respect to the global Cartesian coordinate system has not been determined. Both the normal and tangential components of hydrodynamically-retarded velocities and displacements must be converted back into the global Cartesian coordinate system before the particle is moved during the next time step Δt (refer to Eq. 4.31).

In subroutine DETERMINISTIC, the deterministic particle velocity is not calculated (for scenarios with some finite flow) until the unit tangential vector has been determined by calling the subroutine TANGENT. In TANGENT, a projection tensor PRJ() (*i.e.*, its mathematical equivalent shown in Eq. 4.19) is formed using the unit normal vector UNMIN(). Employing the SLATEC library subroutine DGEMV for general matrix-vector operations in double precision, the product of this tensor and the current undisturbed fluid velocity vector U() (**u**) yields the undisturbed fluid velocity vector projected on a plane

tangential to the point of closest approach on the substrate surface, labeled `UTEMP()`. The SLATEC library subroutine `DSCAL` is used here again, taking the reciprocal of the magnitude of `UTEMP()` as the scaling factor for `UTEMP()` itself to obtain the unit tangential vector for the closest approach distance, `UTMIN()`. Both `UNMIN()` and `UTMIN()` are subsequently used in subroutines `DETERMINISTIC` and `BROWNIAN` to: (i) project the Cartesian fluid velocity and Brownian force vectors onto the relative ($\mathbf{n}$,$\mathbf{t}$) reference frame using SLATEC subroutine `DDOT` for taking dot products, and (ii) transform the deterministic velocity and Brownian displacement vectors from the ($\mathbf{n}$,$\mathbf{t}$) reference frame to the global Cartesian one.

In no flow scenarios (`IFLOW=0`), the unit tangential vector is a zero vector since all deterministic motion will be due to the DLVO force acting on the particle in the direction normal to the point of closest approach to the substrate.

4.3.7 Time Step and Brownian Displacement

For purely deterministic motion, it is evident that the smaller the time step, the more accurately the particle's motion can be portrayed with the PTM simulations. However, smaller time steps with the explicit, forward Euler method of solving the trajectory equations would result in longer simulation run times for the PTM. The inclusion of Brownian motion also necessitates the optimization of the time step. The time step used in the PTM is dictated by the particle size through the Brownian displacement vector $\mathbf{R}^{Br}$ (which is calculated as `B()` in the subroutine `BROWNIAN`) and the particle's momentum relaxation time scale $\tau^{Br}(= m/6\pi\mu a_p$, where m is the mass of the particle) [KET83]. Brownian motion can be represented as an uncorrelated random process only when the time step is larger than the Brownian particle's momentum relaxation time, *i.e.*, $\Delta t \gg \tau^{Br}$. With the relaxation time as the lower bound, the time step must reside within the limits $\tau^{Br} \ll \Delta t < \tau^{det}$, where τ^{det} is the time increment for which the particle's velocity $\mathbf{v}$ is considered constant (*i.e.*, non-accelerating) [NG05]. For a neutrally buoyant, 100 nm radius particle in water,

$\tau^{Br} = 2.22$ ns. In the full PTM simulations (*i.e.*, including deterministic and Brownian forces), $\Delta t = 100$ ns is used for 100 nm particles, as prior investigations revealed that it is sufficiently small to satisfy the limits while minimizing simulation run times. For the deterministic PTM simulations with 100 nm particles, $\Delta t = 1$ μs is satisfactory and further reduces overall run times.

4.3.8 Trajectory Termination Criteria

After the deterministic and Brownian displacements have been imparted to the particle (*i.e.*, "TOTAL Displacement", followed by "New Particle Position" in Figure 4.4), the `STATUS` subroutine is then called to determine if the particle has exited the computational sub-domain or if it has stopped for some reason (*i.e.*, "Trajectory Termination Criteria" in Figure 4.4). The trajectory termination criteria for the particle stopping need some elaboration. For favourable deposition, it is straightforward to postulate an equilibrium approach distance resembling a primary adhesion minimum, which provides a deterministic end point for the trajectories. Accordingly, particles approaching within a cut-off distance of 0.3 nm [Isr92] from the collector surface are assumed to be irreversibly attached, and the trajectory is terminated. However, particles may also be immobilized in the system without specifically attaching to the substrate. For instance, with unfavourable deposition, the particles never approach the primary adhesion minimum. Consequently, in deterministic simulations involving unfavourable deposition, the trajectories simply terminate at the stagnation points in the flow field where the net sum of colloidal and hydrodynamic forces on the particle becomes zero, leaving the particle immobile. In these PTM simulations, the trajectory is terminated when the scaled deterministic displacement becomes less than a preset tolerance (10^{-8}), and the particles are deemed to be immobilized, implying that they are not deposited in the conventional sense (at a primary minimum). One might consider this to be analogous to deposition at a secondary DLVO minimum [RWE04, HAO04, TE05b, KE07]. In Brownian simulations of unfavourable deposition, however, the random excursion of these immobilized

particles can either re-release them into the flow, or capture them in the primary adhesion minimum. For these simulations, the termination criterion is modified as follows: if the particle experiences an average displacement of 0.3 nm or less in the $x-$, $y-$ and $z-$ directions over the previous 100 time steps, then it is assumed that the particle is immobilized, thereby terminating the simulation. The last 100 positions are stored in the arrays `XPOS()`, `YPOS()` and `ZPOS()` which are updated on a rotating basis. The standard deviation of each array is calculated in subroutine `MOMENT` (from Chapter 14 of Numerical Recipes for FORTRAN [PTVF92]). With the PTM simulations involving unfavourable deposition, there are virtually no immobilized particles trapped in the secondary minimum when Brownian motion is considered. For all cases that the particle's trajectory has been terminated, the PTM proceeds with starting the next particle's trajectory (*i.e.*, "Next Particle" in Figure 4.4).

4.4 Summary

In this chapter, the general mathematical formulation of the PTM for a shear flow field over a substrate with complex geometry has been developed. Using the PTM to calculate a particle's trajectory, it is necessary to obtain the undisturbed (*i.e.*, particle-free) fluid velocity vector, $\mathbf{u}$, near the composite substrate, the hydrodynamic interaction tensors $\mathcal{A}$ to $\mathcal{C}$, and the net DLVO force between the particle and the composite substrate. Numerical solution methods for the governing transport equations have also been presented. In Chapter 5, the use of these equations is demonstrated for some conventional colloid transport and deposition scenarios, providing a validation of the approach. In the following chapter, the limits of the parameter space to which the PTM can be applied will be laid out.

Chapter 5

Particle Tracking Model: Parameter Space and Validations

5.1 Overview

Now that the components of the Particle Tracking Model (PTM) have been described in detail, there remains the issue of validating the PTM for the types of systems that it is applied to. In this chapter, the effectiveness of several aspects of the PTM will be explored using some conventional scenarios in fluid dynamics, colloid transport and deposition. These aspects of the PTM include: its use of the (numerically-determined) undisturbed hydrodynamic flow field, its simulation of Brownian motion, its depiction of hydrodynamic interactions over a range of separation distances, and its application to classic deposition scenarios such as the collection efficiency of a single spherical collector.[1]

5.2 Parameter Space

In Chapter 4, the scaled Langevin equation (4.10) was simplified to the PTM's particle trajectory equation of Eq. (4.15) by neglecting particle inertia. This assumption can only be valid if the Stokes number St ($= 2\rho_p U a_p/9\mu$) is very small ($St \ll 1$), thereby implying that the particle will follow fluid streamlines

[1] A version of this chapter has been published. Kemps and Bhattacharjee, 2009, *Langmuir*, 25(12):6887-6897.

Table 5.1: Parameters (fluid and particle properties) for the PTM simulations.

Quantity	Symbol	Value	Units
System temperature	T	298.15	K
Particle density	ρ_p	1000	kg/m^3
Density of medium (water @ T)	ρ_f	1000	kg/m^3
Permittivity of medium (water @ T)	ϵ	6.95×10^{-10}	C^2/N·m^2
Viscosity of medium (water @ T)	μ	10^{-3}	Pa·s

closely and not experience any significant acceleration during each time step. Another dimensionless group that appears in Eq. (4.10) is the particle Peclet number, Pe ($= 6\pi\mu a_p^2 U/k_B T$), which relates convective forces to those of diffusion (Brownian motion). To arrive at Eq. (4.15), the values of both St and Pe must be as low as possible, with $St \leq 10^{-5}$. For a given set of system parameters, these two dimensionless groups are proportional to the characteristic fluid velocity U and the particle size a_p, with $St \propto U a_p$ while $Pe \propto U a_p^2$.

If Pe is sufficiently high, then the force term on the right side of Eq. (4.10) could be of the same order of magnitude as St. In such cases for the parameters of this study (refer to Table 5.1), particle inertia cannot be neglected as this would mean the external forces ($\sum_i \mathbf{F}_i^*$, such as DLVO and the fluctuating Brownian force) should be neglected as well. This would reduce Eq. (4.10) to the trivial case of zero particle velocity, which is certainly not appropriate for a system of high Pe, and hence, high convection. An example of this can be seen in Table 5.2 when $a_p = 1000$ nm and $U = 10^{-3}$ m/s.

Consequently, for a given particle size, the selection of a valid range of values for the average fluid velocity in the channel U_{avg} is necessary. However, the computational sub-domain in which the particle's motion is tracked by the PTM is close to the substrate's surface, where the characteristic fluid velocity is much lower ($U \ll U_{avg}$). For instance, with the channel half-height b held constant at $1000a_p$ for this study, a particle in the sub-domain is at an average

Table 5.2: Stokes and particle Peclet numbers in relation to particle size a_p and characteristic fluid velocity U for the parameters of this study (listed in Table 5.1).

a_p (nm)		$U = 10^{-5}$ (m/s)	$U = 10^{-4}$ (m/s)	$U = 10^{-3}$ (m/s)
10	St	2.2×10^{-8}	2.2×10^{-7}	2.2×10^{-6}
	Pe	4.6×10^{-3}	4.6×10^{-2}	4.6×10^{-1}
20	St	4.4×10^{-8}	4.4×10^{-7}	4.4×10^{-6}
	Pe	1.8×10^{-2}	1.8×10^{-1}	1.8×10^{0}
50	St	1.1×10^{-7}	1.1×10^{-6}	1.1×10^{-5}
	Pe	1.1×10^{-1}	1.1×10^{0}	$1.1 \times 10^{+1}$
100	St	2.2×10^{-7}	2.2×10^{-6}	2.2×10^{-5}
	Pe	4.6×10^{-1}	4.6×10^{0}	$4.6 \times 10^{+1}$
200	St	4.4×10^{-7}	4.4×10^{-6}	4.4×10^{-5}
	Pe	1.8×10^{0}	$1.8 \times 10^{+1}$	$1.8 \times 10^{+2}$
500	St	1.1×10^{-6}	1.1×10^{-5}	1.1×10^{-4}
	Pe	$1.1 \times 10^{+1}$	$1.1 \times 10^{+2}$	$1.1 \times 10^{+3}$
1000	St	2.2×10^{-6}	2.2×10^{-5}	2.2×10^{-4}
	Pe	$4.6 \times 10^{+1}$	$4.6 \times 10^{+2}$	$4.6 \times 10^{+3}$

height of about $10a_p$ above the flat portion of the substrate. With a simple shear flow profile near the channel's surface at the inlet boundary of the full computational domain, the particle will encounter fluid velocities that are $\approx 0.01U_{avg}$. In other words, an average fluid velocity range of $10^{-3} \leq U_{avg} \leq 10^{-1}$ m/s will mean a particle in the PTM simulation is experiencing fluid velocities in the range of about $10^{-5} \leq U \leq 10^{-3}$ m/s near the substrate.

The values of U and U_{avg} are parts of two more hydrodynamic limiting criteria for the PTM simulations: the particle Reynolds number, $Re_p = \rho_f U a_p/\mu$ and the channel Reynolds number, $Re_{ch} = \rho_f U_{avg} d_h/\mu$, where $d_h = 4 \times area/perimeter$ is the hydraulic diameter of the channel. As the channel's width w is assumed to be much larger than its full height in this study (*i.e.*, $w \gg 2b$), then $d_h = 4 \times 2bw/(4b + 2w) \approx 4b$, so $Re_{ch} = \rho_f U_{avg}(4b)/\mu =$

$4000\rho_f U_{avg} a_p/\mu$. It is important to distinguish these two Reynolds numbers, as Re_p is for the flow near the surface of the channel while Re_{ch} is for the bulk flow in the channel. For Stokes flow, the particle Reynolds number should be considerably less than unity ($Re_p \ll 1$) [RSS89, vdV89], and the channel Reynolds number marks the transition to turbulence at $Re_{ch} \approx 2000$ [PMM08]. Both of these conditions are met for the parameters in Table 5.1 and all of the Brownian particle sizes listed in Table 5.2 (*i.e.*, $a_p \leq 1000$ nm) when $U_{avg} \leq 0.5$ m/s, which corresponds to fluid velocities of $U \leq 3 \times 10^{-2}$ m/s at a height of $10a_p$ above the substrate.

On the basis of the PTM's limitations with dimensionless groups St, Pe, Re_p and Re_{ch}, the upper limit for the average fluid velocity in the channel for Brownian particles considered in this study (*i.e.*, $a_p \leq 100$ nm) is 1 m/s. With regard to colloidal interactions, the PTM inherits the limitations of the HHF approach to calculating the EDL force, which were discussed at length in Section 3.3. To reiterate, these limitations for the particle and all components of the composite substrate (*i.e.*, asperities, subunits and planar surfaces) include surface potentials (ψ) < 75 mV and $\kappa a > 2$ (especially for low surface potentials), where κ is the inverse Debye length and a is the radius of the smaller interacting entity.

5.3 Undisturbed Hydrodynamic Field

5.3.1 Flow Over a Sphere on a Flat Plate - Comparison with Pozrikidis (1997)

A key element of the PTM's simulation of hydrodynamics is the undisturbed hydrodynamic field in the vicinity of the physically heterogeneous substrate. In this study, this field is obtained using the finite element software COMSOL, which numerically solves the Stokes equations for steady state, simple shear flow across the field's computational domain. Appendix A provides a comprehensive description of the procedure used to create the undisturbed hydrodynamic field for a given substrate, including the particular system parameters

used in the finite element software to generate the numerical solution. For this part of the procedure, an evaluation of how well COMSOL renders such flow fields is necessary. Unfortunately, there are no analytical solutions available for the case of a sphere touching a plane wall, so a comparison with another numerical solution method is required. A numerical approach by Pozrikidis [Poz97] calculates the three-dimensional Stokes flow over an axisymmetric shape projecting from a plane wall using a boundary integral method. More specifically, Pozrikidis' approach can determine the effect that a single sphere resting on a flat surface will have on a simple shear flow field moving across it.

With the boundary integral solution of Pozrikidis, the fluid velocity $\mathbf{u}$ is the sum of the incident shear flow velocity across the substrate and a flow velocity modification due to the asperity that vanishes at infinity. This flow modification is depicted with hydrodynamic potentials using the free-space Green's function of the Stokes flow equations for the velocity and stress [RSS89, EGJW95, KK05]. For the COMSOL solution of the flow field, the size of the computational domain is important. If the domain is too small, the Dirichlet condition of simple shear at the inlet boundaries (Γ_{in} in Figure 4.2) will result in higher flow velocities throughout the field and understating the asperity's modification of the shear flow in the far-field. If the domain is too large, the finite element matrix of the system will be exceedingly sparse, so the numerical solution will take longer to determine and potentially lead to out-of-memory errors or gross inaccuracies in some regions of the solution if the local mesh resolution is too coarse. Consequently, the domain size must be optimized.

Figure 5.1 looks at the scaled fluid velocity around the asperity in the prevailing direction of flow, u_x^* (Figure 5.1a), and in the $z-$ direction, u_z^* (Figure 5.1b), at five different scaled (with respect to asperity size a_a) heights in the domain's $x-z$ plane. The shaded circle in the middle of Figures 5.1(a) and (b) represents the spherical asperity, appropriately sized with respect to the $x-$ axis scale. In the context of the PTM's scaling parameters, the scaled shear rate ($\dot{\gamma}^*$) in this comparison is 1 and the asperity-to-particle size ratio (λ) is also 1 (*i.e.*, $a_a = a_p$).

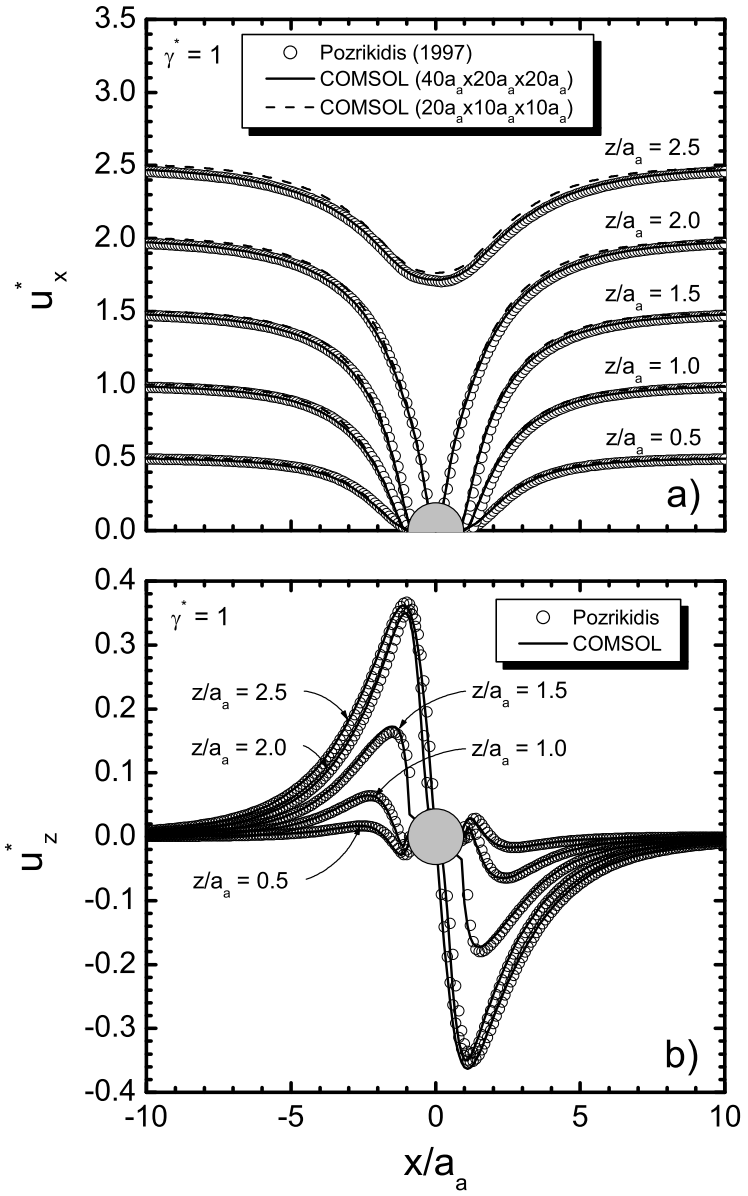

Figure 5.1: Validation of the undisturbed hydrodynamic field (around a single spherical asperity on a flat surface) determined using COMSOL, based on comparison with the numerical solution by Pozrikidis [Poz97]. Comparisons are made for scaled fluid velocities in the (a) $x-$ and (b) $z-$ directions at five scaled heights above the flat surface in the $x-z$ plane. For this system, the scaled shear $\dot{\gamma}^*$ is 1. In (a), two sizes of the computational (half-field) domain for the COMSOL solution approach are included for comparison. In (b), only the COMSOL solution for the larger domain ($40a_a \times 20a_a \times 20a_a$) is included.

For comparison with the results of Pozrikidis' approach in Figure 5.1(a), two sizes of the half-field domain were solved for in COMSOL: a large one measuring $40a_a \times 20a_a \times 20a_a$ and a smaller one measuring $20a_a \times 10a_a \times 10a_a$. The system and solver parameters for the solutions of these two field sizes were identical, and the total number of mesh elements was within about 3% of each other (35541 for the smaller one, 36674 for the large one). The finite element meshes for both domains were created automatically by the COMSOL software using the parameters provided in Appendix A. In close proximity to the asperity, the solid and dashed lines coincide in Figure 5.1(a). This indicates that the size of the computational domain makes no difference in the accuracy of the fluid velocity in the near-field of the asperity. Far away from the asperity (at $x/a_a = \pm 10$), the larger domain is in closer agreement with Pozrikidis' solution than the smaller one. This is expected since the finite inlet boundaries (Γ_{in} from Figure 4.2) of the COMSOL domain are assigned the Dirichlet condition of one-dimensional shear flow, and COMSOL solves the flow field to attain that boundary condition. With the larger field, the inlet boundary is further away and the COMSOL solution extends the modification of the flow due to the asperity over a larger volume. COMSOL cannot extend the boundaries to infinity in order to mimic Pozrikidis' solution, but the larger domain with nearly 37000 elements effectively portrays the flow modification caused by the asperity's presence, which can also be seen in Figure 5.1(b) for fluid velocity in the $z-$ direction. Using Pozrikidis' solution as the standard, Table 5.3 lists the relative percentage errors in the $x-$ and $z-$ fluid velocities at three positions near the asperity in COMSOL's solution of the larger ($40a_a \times 20a_a \times 20a_a$) computational domain, all of which are less than 2%. From this validation, it is concluded that when the outer boundaries of the computational domain are a distance of approximately $20a_a$ from the asperity, fluid velocities throughout the domain are in good agreement with numerical solutions such as that of Pozrikidis for which the asperity's influence on the flow extends to infinity.

Table 5.3: Relative percentage error between the COMSOL solution (with $40a_a \times 20a_a \times 20a_a$ domain) and the numerical solution of Pozrikidis [Poz97] for the undisturbed hydrodynamic field around a single asperity on a flat surface. The errors are determined for the scaled fluid velocity in the $x-$ and $z-$ directions at three positions in the $x-z$ plane of the field.

$(x/a_p, z/a_p)$		**COMSOL Solution**	**Pozrikidis Solution**	**Relative % Error**
$(-2.0, +1.0)$	u_x^*	$+0.40982$	$+0.40787$	$+0.48$
	u_z^*	$+0.06026$	$+0.05954$	$+1.21$
$(-2.5, +1.5)$	u_x^*	$+0.98419$	$+0.97381$	$+1.07$
	u_z^*	$+0.13117$	$+0.12971$	$+1.13$
$(+2.0, +2.0)$	u_x^*	$+1.33385$	$+1.33233$	$+0.11$
	u_z^*	-0.24701	-0.24686	$+0.06$

5.3.2 Use of Trilinear Interpolation

A trilinear interpolation procedure [Tod03] is used to calculate the undisturbed fluid velocity $\mathbf{u}$ at any given location of the particle center within the computational sub-domain. With the undisturbed hydrodynamic field numerically determined using the finite element software, this field is then inserted into the PTM in the form of a three-dimensional Cartesian grid of a particular resolution that is equal in all three Cartesian directions. The largest resolution possible, $0.5a_p$ (half of the particle radius), was selected for the flow fields in this study in order to decrease the size of the flow field data files that are read into the PTM's FORTRAN code. This, in turn, reduces the time spent in the `HUNT` subroutine to identify adjacent nodes to the current particle position, and hence reduces the overall duration of simulation runs. This resolution also ensures that when the particle is nearly in contact with any surface, the undisturbed flow field at the center of the particle will always be based on grid nodes that are not on or within the substrate's surface, thereby avoiding zero velocities at no-slip boundaries or NaN (*i.e.*, Not a Number) values.

To validate this interpolation technique used by the PTM, the errors in

fluid velocity in all three Cartesian directions are compared against the infinity norm (*i.e.*, vector component with the highest value) of the scaled undisturbed fluid velocity vector $\mathbf{u}^*$ along a number of paths in a flow field generated by COMSOL. For scenarios in this study, the infinity norm is the $x-$ component of the fluid velocity vector, u_x^*, and this is confirmed by comparing the magnitudes of u_x^* and u_z^* throughout the flow field in Figures 5.1(a) and (b). For this validation – as depicted schematically in Figure 5.2 – the asperity-to-particle size ratio $\lambda = 5$ and Paths 1 to 7 originate in the center of the asperity, which is located at $(x/a_p, y/a_p, z/a_p) = (0.0, 0.0, 5.0)$ (*i.e.*, scaled radial position $r^* = 0$). These paths extend outward from the surface of the asperity (*i.e.*, $r^* = 5$) in the following directions: $1 = x-$ axis; $2 = xy-$ diagonal; $3 = y-$ axis; $4 = yz-$ diagonal; $5 = z-$ axis; $6 = xz-$ diagonal and $7 = xyz-$ diagonal.

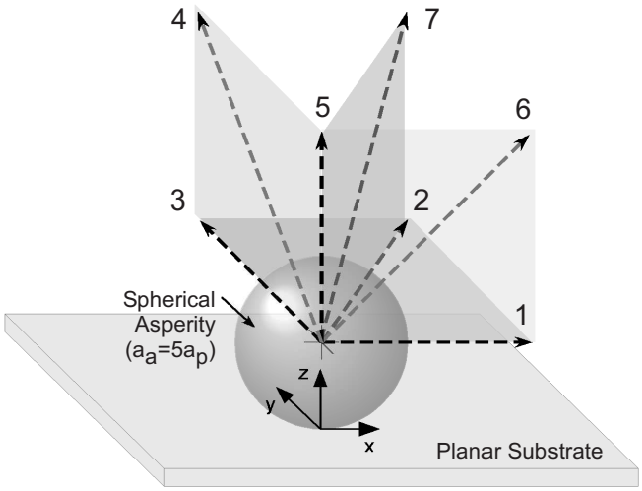

Figure 5.2: Schematic representation of Paths 1 to 7 along which the use of trilinear interpolation to determine undisturbed fluid velocity throughout the computational sub-domain is tested. Paths 1 to 7 extend from the center of a spherical asperity on a planar surface, and the asperity-to-particle size ratio λ $(= a_a/a_p)$ for this particular scenario is 5.

In parts (a) to (c) of Figure 5.3, the thick lines show how the fluid velocity

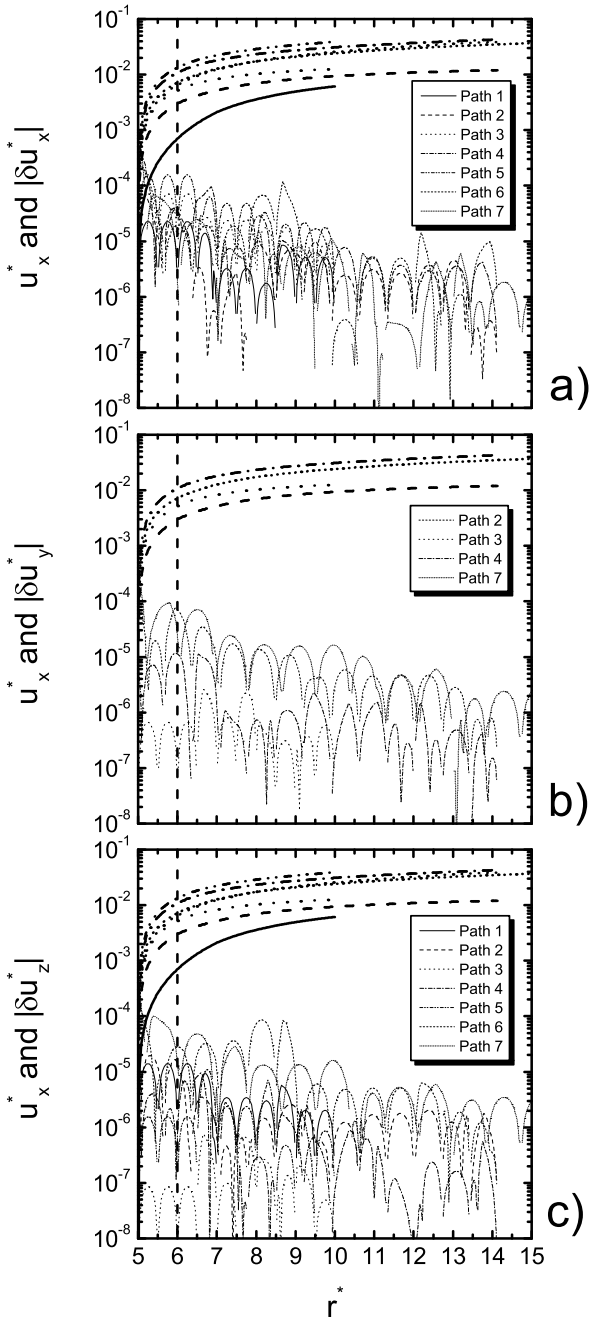

Figure 5.3: Scaled undisturbed fluid velocity in the prevailing direction of flow, u_x^*, and error in the scaled undisturbed fluid velocity in the (a) $x-$, (b) $y-$ and (c) $z-$ directions along Paths 1 to 7 in Figure 5.2. Paths 1, 5 and 6 are not included in (b) because they lie in the $x-z$ plane where $u_y^* = 0$ due to flow field symmetry, and therefore the error $|\delta u_y^*| = 0$ as well.

in the direction of prevailing flow, u_x^*, varies with the scaled radial position r^* along Paths 1 to 7. The lighter lines are for the absolute error in the respective component of $\mathbf{u}^*$ (*e.g.* $|\delta u_y^*|$ in the $y-$ direction), and this error is the difference between the value interpolated in the PTM and the value acquired from post-processing data in COMSOL. The parabolic curves that these absolute error lines take are due to the error approaching zero when the position along the given path coincides with a grid node in the computational sub-domain that the PTM uses. The vertical dashed line at $r^* = 6$ in Figures 5.3(a) to (c) indicates where the center of a particle would be when in contact with the asperity. Since the PTM calculates the deterministic particle velocity based on the undisturbed fluid velocity at the particle's center, the fluid velocities and their associated errors for $r^* \leq 6$ are of no concern in this validation.

It is evident from Figures 5.3(a) to (c) that for Paths 1 to 7, the errors in the fluid velocity in all three Cartesian directions, $|\delta u_x^*|$,$|\delta u_y^*|$ and $|\delta u_z^*|$, are always 2 to 4 orders of magnitude smaller than the infinity norm of the fluid velocity vector, u_x^*. Assuming that the error or uncertainty in $\mathbf{u}^*$ is attributed to interpolation errors in its Cartesian components, and that these errors are independent of each other, then the overall error in $\mathbf{u}^*$ is mainly due to the error in the $x-$ direction. Subsequently, one can conclude from Figure 5.3(a) that the error in undisturbed fluid velocity introduced by the trilinear interpolation procedure to the PTM simulations is less than 1%, and therefore, insignificant.

5.4 Brownian Motion

The strictly Lagrangian perspective of the particle's motion in the PTM must be reconciled with the Eulerian view of diffusion by Brownian motion. First consider the spread of a number of particles in the $x-$ direction of the bulk of a quiescent fluid (*i.e.*, no flow), which can be represented by the one-dimensional version of Fick's Second Law [RSS89, vdV89] (*i.e.*, the Convection-Diffusion equation with the convection term dropped out [MB06]),

$$\frac{\partial n}{\partial t} = D_\infty \frac{\partial^2 n}{\partial x^2}, \tag{5.1}$$

where $n(x,t)$ is the number of particles per unit volume at a distance x and time t, and D_∞ is the Stokes-Einstein diffusion coefficient. With the initial and boundary conditions – $t = 0$ for $|x| > 0$ and $x = \pm\infty$ at time t, respectively – all set at zero, the solution of Eq. (5.1) is the normal, or Gaussian distribution,

$$n(x,t) = \frac{N}{\sqrt{4\pi D_\infty t}} \exp\left(\frac{-x^2}{4D_\infty t}\right), \tag{5.2}$$

with N $(= \int_{-\infty}^{+\infty} n(x,t)\,dx)$ as the total number of particles released at $x = 0$ per unit cross-sectional area, and these particles exert no forces on each other. Viewed as a space summation, this solution means that at time t, a distribution of particles has been obtained, with the relative number of particles between the planes x and $x + dx$ given by $f(x,t)\,dx$. From the statistical mechanical perspective of a time summation, $n(x,t)$ represents the probability that a single particle in the space summation has been displaced to the region between x and $x+dx$. Observing the displacements that the particle undergoes over successive time intervals, the relative frequency of these displacements will match what is predicted by Eq. (5.2) for an indefinitely large number of observations (refer to Note 10 on page 99 of [F$\ddot{5}$6]). Since the particles in the space summation do not interact with each other, the number of observations can be increased not only by the total time elapsed but also by the number of particles observed.

In his landmark paper on Brownian motion, Einstein [Ein05] identified the mean-square displacement (MSD) of the particles as an observable quantity for this phenomenon, and in the $x-$ direction

$$MSD_x = \frac{1}{N}\int_{-\infty}^{+\infty} x^2\, n(x,t)\,dx = \frac{\int_{-\infty}^{+\infty} x^2\, n(x,t)\,dx}{\int_{-\infty}^{+\infty} n(x,t)\,dx}. \tag{5.3}$$

Substituting Eq. (5.2) into Eq. (5.3) results in,

$$MSD_x = 2D_\infty t, \tag{5.4}$$

which applies to the $y-$ and $z-$ directions as well. In the radial $r-$ direction, the mean-square displacement is the summation of the mean-square displacements in all three Cartesian directions over the same time interval [Ein05],

$$MSD_r = 6D_\infty t. \tag{5.5}$$

To demonstrate how the PTM effectively simulates diffusion in accordance with Fick's Second Law, a simple test has been performed, observing the Brownian displacements of a number of particles from an infinitely dilute suspension released in the bulk of a fluid undergoing no flow (*i.e.*, $\mathbf{u} = 0$). Each particle is released individually at time $t = 0$ with zero initial velocity from the origin of a Cartesian coordinate system that is situated far away from any surfaces or other particles. Since there are no particle-particle or particle-surface interactions under these conditions, there is no hydrodynamic retardation, so f_1 and f_4 (*i.e.*, the only UCFs involved in the PTM's simulation of Brownian displacement) are set to 1. The Brownian displacement of the particle in each of the Cartesian directions is calculated independently, with its position in the given direction recorded at the end of each time step. This position versus time information is compiled for all of the particles released in order to determine the mean-square displacements of the entire set of particles over time. Because there is no flow in this scenario, time must be scaled with respect to the diffusion time scale, a_p^2/D_∞; hence, scaled time $t^* = t(D_\infty/a_p^2)$. All displacements are scaled with respect to the characteristic length of the particle radius, a_p, and therefore the mean-square displacements are scaled by a_p^2.

Ideally, the relationship between their mean-square displacement in a given direction and total time elapsed should yield a slope that is a multiple of the Stokes-Einstein diffusion coefficient D_∞. After scaling Eqs. (5.4) and (5.5), the D_∞ factor cancels out, so the slope should be 2 in the individual $x-$, $y-$ and $z-$ directions (the scaled coefficient of Eq. 5.4) and 6 for the $r-$ direction (the scaled coefficient of Eq. 5.5). Both of these slopes are drawn as dashed lines in the graphs of Figure 5.4. Starting with only 10 particles in Figure 5.4(a), the scaled mean-square displacement (MSD^*) over the scaled time t^* only roughly follows the slope for each respective direction. However, as the number of particles N increases to 20 in Figure 5.4(b) and then 30 in Figure 5.4(c), one can see that the displacements are in greater agreement with the slopes. By extension, it is evident that as the total number of particles released in a PTM simulation is increased, the closer the PTM will emulate

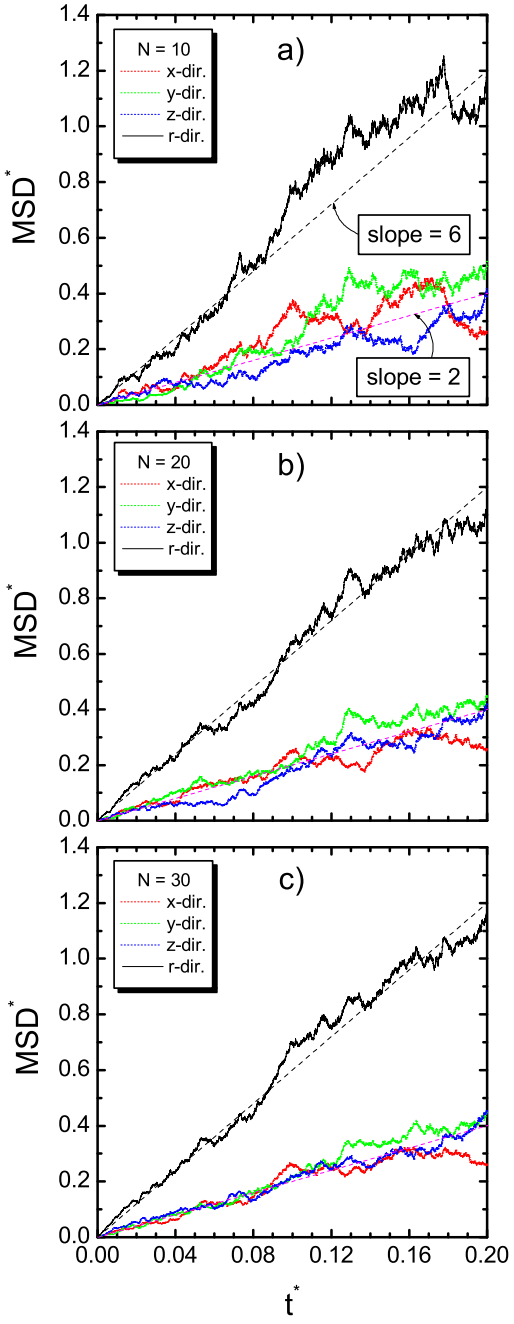

Figure 5.4: Scaled mean square displacement (MSD^*) over scaled time of (a) 10, (b) 20 and (c) 30 particles released in the bulk of a quiescent fluid, simulated using only the Brownian component of the PTM. The mean square displacements are shown in the $x-$, $y-$, $z-$ and $r-$ directions.

the diffusion mechanism of particle transport.

5.5 Hydrodynamic Interactions

In this section, the results of the PTM's approximate method for computing the hydrodynamic retardation on a particle's motion (using the UCFs with respect to the separation distance from the closest feature of the substrate) are compared against those of a numerical method based on the superposition of two linear velocity fields. The numerical solution methodology for obtaining this superposed solution is outlined in Appendix B.

5.5.1 Proximity Criteria - Transition Region

Before proceeding with the comparison, there is one issue to address regarding the proximity criterion of the PTM, as first described in Section 4.2.3. For the scenarios that the PTM is applied to in this study, the relative ($\mathbf{n}$,$\mathbf{t}$) coordinate system orients itself with respect to the portion of the substrate that the particle is closest to: an asperity (*i.e.*, PAP) or the flat surface (*i.e.*, PSP). With every asperity-to-particle size ratio λ, there are loci in the flow field where the particle is equidistant from both the asperity and the flat surface. These loci form a line of transition in the shape of a paraboloid that cradles the asperity, as depicted for $\lambda = 5$ in the $x - z$ plane by the dashed parabolic line in Figures 4.3(a) and (b). Figure 5.5 shows, also in the $x - z$ plane, these lines of transition between PAP and PSP for three different values of λ: 5, 1 and 0.2. The dashed circle represents the size of the asperity for $\lambda = 5$, the dotted circle indicates the asperity's size for $\lambda = 1$, and a solid dot is the asperity for $\lambda = 0.2$. For each of these lines, one particle position is shown with the directions of the unit normal vectors for PAP and PSP (*i.e.*, $\mathbf{n}_{PAP}$ and $\mathbf{n}_{PSP}$) included.

As with the case of particle position 1 for $\lambda = 5$ in Figure 5.5, a large change in the direction of the normal with respect to the distance of closest approach (90° between $\mathbf{n}_{PAP}$ and $\mathbf{n}_{PSP}$ for this position) may introduce some

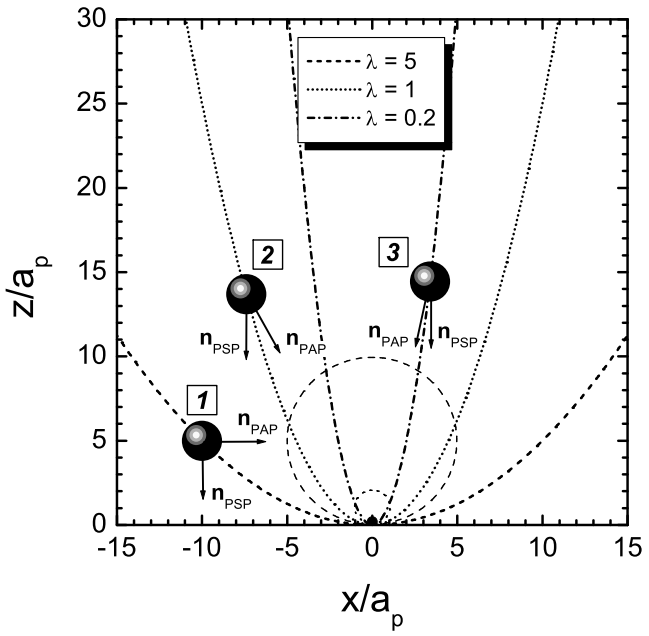

Figure 5.5: Schematic representation of the loci in the $x - z$ plane where the relative (**n**,**t**) coordinate system changes orientation between the surface normal of the flat portion of the substrate and that of the asperity (*i.e.*, between PSP and PAP; refer to Figure 4.3). Each parabola represents the loci where the particle is equidistant from the flat portion of the substrate and the asperity for a given asperity-to-particle size ratio λ (5, 1 and 0.2 in this figure) is (a) 1 and (b) 5.

error to the PTM's calculations for hydrodynamic retardation. However, when λ is reduced – as observed with $\lambda = 1$ at position 2 and $\lambda = 0.2$ at position 3, the angle between $\mathbf{n}_{PAP}$ and $\mathbf{n}_{PSP}$ is smaller over the corresponding transition line. Therefore, as $\lambda \to 0$, $\mathbf{n}_{PAP} \to \mathbf{n}_{PSP}$ for the entire flow field, approaching a sphere-plate interaction for which the UCFs were originally intended. The steric limit also eliminates the sections of the transition lines closest to the asperity since the particle can never reside there. One can conclude that the PTM's use of the UCFs is not expected to be a significant source of error in its calculation of a particle's hydrodynamic interactions with a physically heterogeneous surface when $\lambda < 1$. If $\lambda > 5$, the asperity would be large enough that the particle's hydrodynamic interactions with it would be like

those of a sphere and a flat plate. Again the PTM's use of the UCFs would be quite accurate in such scenarios, with the exception of the region adjacent to the asperity's contact point with the flat surface. This means that scenarios with a range of $1 \leq \lambda \leq 5$ are where one would find the greatest error in the PTM's calculation of hydrodynamic interactions.

5.5.2 Comparison of PTM with Numerical Method of Superposed Solutions

Figure 5.6 shows the relative percentage difference between the particle velocity components evaluated using the PTM and the numerical method of superposed solutions described in Appendix B. Only particle velocities in the $x-$ and $z-$ directions (v_x and v_z, respectively) are considered for this comparison, looking at the two asperity-to-particle size ratios where the greatest error may be found – $\lambda = 1$ (Figure 5.6a) and $\lambda = 5$ (Figure 5.6b) – with the numerical method regarded as the standard. For both the PTM and the numerical method, COMSOL has been used to solve for the corresponding fluid flow over the computational domain (half-field) for the appropriate system parameters and boundary conditions. In all of these scenarios, the size of the computational domain for $\lambda = 1$ is $40a_p \times 20a_p \times 20a_p$, and enlarged to $80a_p \times 40a_p \times 40a_p$ for $\lambda = 5$. The schematic insets in Figures 5.6(a) and (b) show the three lines (numbered 1 to 3) on the $x - z$ plane along which the particle's velocity components are studied in this comparison. Figure 5.6(a) does not include Line 1 due to steric constraints, as a particle centered on the midplane of an asperity of equal size and moving along the $x-$ axis would be in contact with the flat portion of the substrate, and therefore the particle's velocity would always be zero. The $z-$ component of the particle velocity is not analyzed for Line 2 in Figures 5.6(a) and (b) since the fluid velocities in the $z-$ direction along these lines are very close to zero. Values for v_z along Line 3 are also not shown in Figure 5.6(a) due to some anomalous results in one component of the numerical method when $H \leq 2.24$. Separation distances of $H < 0.5$ are not included here, as it was discovered that the errors in the

results of the numerical method start to become significant in that range of H. This is mainly because the numerical method in Appendix B, in its current form, does not account for the effects of particle rotation on the hydrodynamic interactions.

In Figures 5.6(a) and (b), a positive percentage difference indicates that the UCFs in the PTM have underestimated the hydrodynamic retardation effect for the scenario, while a negative percentage difference means that the UCFs overestimated the effect. For $\lambda = 1$ in Figure 5.6(a), the absolute percentage difference in v_x between the numerical solution and the approximate results of the PTM for $H_a \geq 1$ is about 1% or less for both Lines 2 and 3. This signifies that when the asperity and the particle are of equal size, the PTM accounts for hydrodynamic interactions very effectively in the far-field and down to $H_a = 1$. When $H_a = 0.5$, the difference becomes more substantial, reaching almost -5% on Line 2 and dropping to nearly -11% on the diagonal Line 3. However, these negative percentage differences show that the PTM imposes more hydrodynamic retardation on the particle than is required for $H_a \geq 0.5$. In other words, the PTM's depiction of hydrodynamic interactions for this value of λ would lead to slightly reduced probabilities in particle deposition on the surface. This is expected in the near-field, since the UCFs in the PTM are based on sphere-plate interactions, with the surface of an entire plate (instead of the smaller adjacent surface area of an equal-sized sphere) imparting hydrodynamic stress on the particle.

Looking at a larger asperity ($\lambda = 5$) in Figure 5.6(b), Line 1 starts with difference of about $+3\%$ at $H_a = 10$, then drops slightly until reaching $H_a = 4$ where the difference increases back to $+3\%$. At this separation distance, the relative $(\mathbf{n}, \mathbf{t})$ coordinate system changes orientation, with $\mathbf{n}$ pointing toward the asperity instead of the flat surface as depicted with particle position 1 in Figure 5.5. Despite the 90° change in the direction of $\mathbf{n}$, its effect on the accuracy of the PTM's calculation of v_x is minor. The insignificance of this effect is because hydrodynamic interactions are not prominent at this separation distance, and the UCFs employed to calculate v_x for PSP and

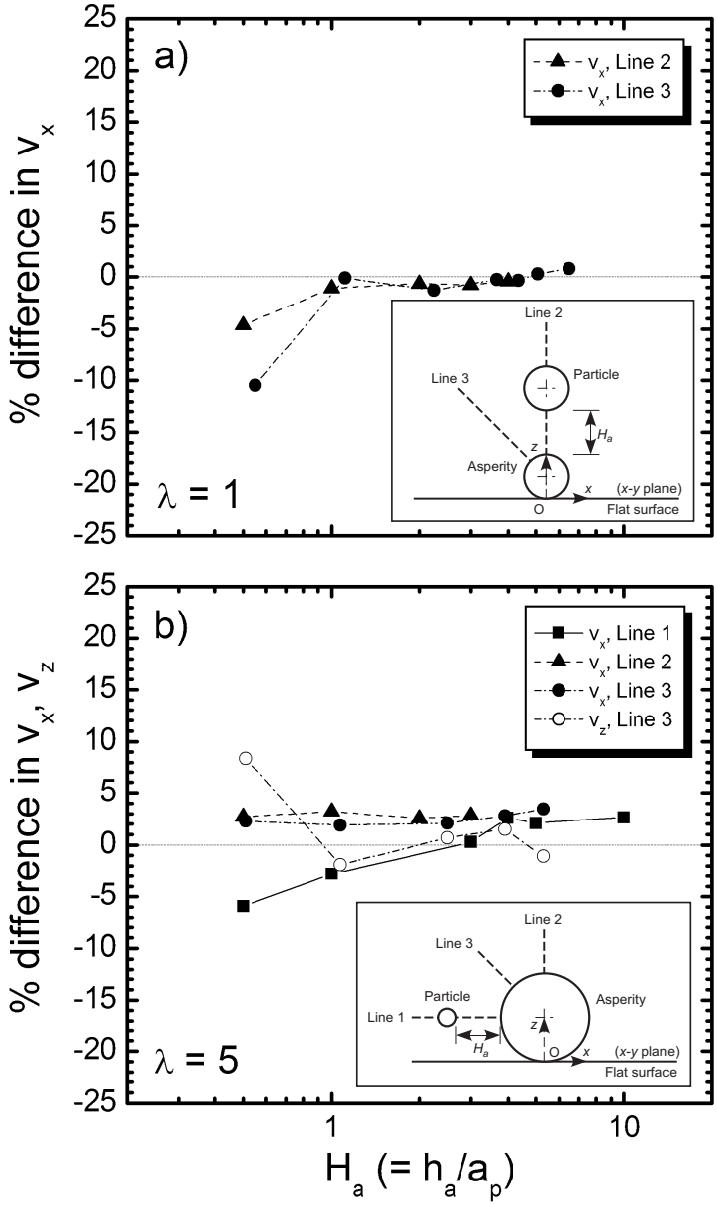

Figure 5.6: Validation of the use of UCFs in the Particle Tracking Model (PTM) to determine the hydrodynamic resistance (*i.e.*, retardation effect) on the particle when it is in close proximity to the spherical asperity when asperity-to-particle size ratio λ is (a) 1 and (b) 5. The percentage difference between the particle's velocity $\mathbf{v}$ (due to hydrodynamics only, in the $x-$ and $z-$ directions) as determined by the PTM and as determined by the numerical method described in Appendix B (*i.e.*, basis for comparison) is shown for several separation distances between the particle and the asperity along (a) two or (b) three lines in the $x - z$ plane (refer to the corresponding inset schematic for each subfigure).

PAP (refer to Figure 4.3 changes very little (*i.e.*, at $H = 4$: $f_3 = 0.9863$ for tangential to the flat surface; $f_1 f_2 = 0.9892$ for normal to the asperity). This transition becomes more seamless when the particle moves further away from the composite substrate. Further decreases in H_a lead to negative percentage differences in v_x, but with a difference of only -6% at $H_a = 0.5$. For v_x when the particle is situated Lines 2 and 3, the difference between the PTM and the numerical method in Appendix B remains around $+3\%$ for $0.5 \leq H_a \leq 5$. This signifies that the PTM underestimates the hydrodynamic retardation on v_x to a small extent for particle positions around the top-half of the asperity. Although the top half of this asperity is substantially disconnected from the flat portion of the substrate, the influence of the entire composite substrate on hydrodynamic interactions is slightly understated by the PTM, though still an acceptable approximation. For the vertical component of the particle velocity on Line 3, the difference in v_z remains within $\pm 2\%$ for $H_a \geq 1$ and only about $+8\%$ for $H_a = 0.5$.

It is anticipated that at very small separations between the particle and the asperity, some velocity components evaluated using the PTM's approximate methodology may exhibit a large error. However, for the parameters of this study, the colloidal and Brownian forces will have a dominant influence on the particle's displacement at such separations.

5.5.3 Angle between Fluid and Particle Velocity Vectors

Due to the linearity of the hydrodynamic field in Stokes flow, the hydrodynamic interactions between a spherical particle and another surface can be determined from the undisturbed fluid velocity at the center of the particle. Ideally, when the Stokes number for the particle is low enough ($St \leq 10^{-5}$) and regardless of the direction of flow, the particle's velocity would be in the same direction as the fluid but with a lower magnitude ($|\mathbf{v}| < |\mathbf{u}|$). For the scenarios in this study, however, the PTM sometimes underestimates or overestimates the effect of hydrodynamic retardation on the particle in the near-field, as

noted in the comparison of Figure 5.6. This may result in instances where the fluid and particle velocity vectors are not collinear. Similar to the DLVO force direction maps of Figures 3.11(b) and 3.12(b), Figure 5.7 is a map in the $x-z$ plane of the angular deviation between the undisturbed fluid velocity vector $\mathbf{u}$ and its associated particle velocity vector, $\mathbf{v}$, as determined by the PTM for the region near an asperity with an asperity-to-particle size ratio of $\lambda = 5$. In this figure, the asperity is shown with a dashed circle centered above the origin of the global Cartesian coordinate system. The dot product of the unit vectors for $\mathbf{u}$ and $\mathbf{v}$ (*i.e.*, $\mathbf{e}_u$ and $\mathbf{e}_v$, respectively; $\mathbf{e}_u = \mathbf{u}/|\mathbf{u}|$, for example) yields the cosine of the angle β between them (*i.e.*, $\mathbf{e}_u \cdot \mathbf{e}_v = \cos\beta$).

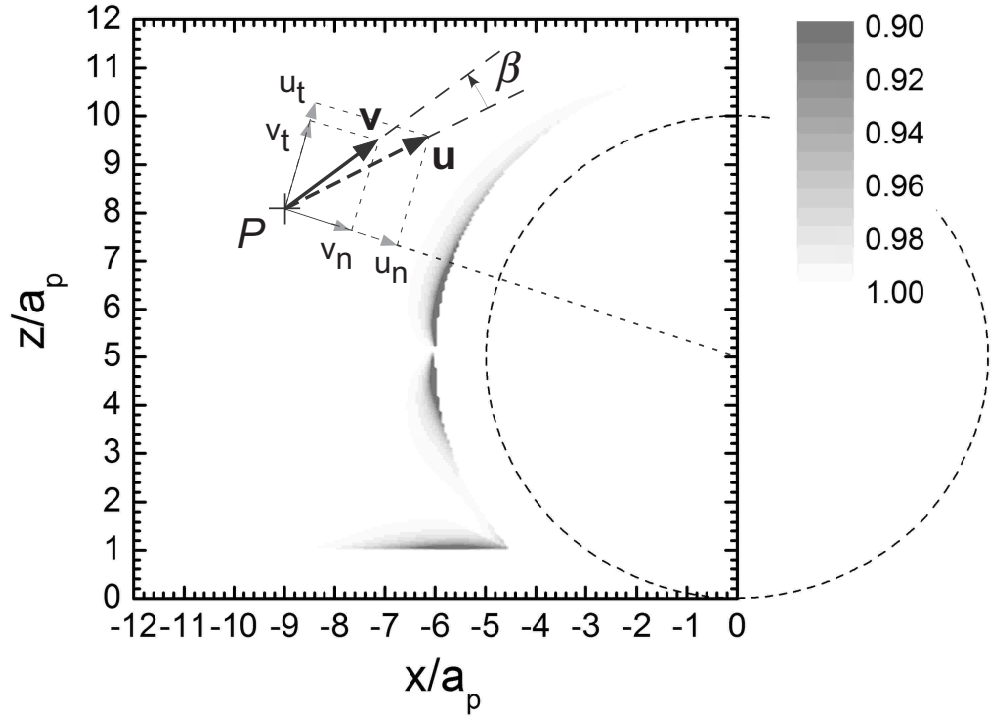

Figure 5.7: Angular deviation between the fluid and particle velocity vectors ($\mathbf{u}$ and $\mathbf{v}$ respectively) in the vicinity of a spherical asperity when the asperity-to-particle size ratio $\lambda = 5$. The shading scale is based on the dot product of the two vectors, yielding the cosine of the angle between them, β. A schematic depiction of the angle β is shown for an arbitrary point P in the flow field, including the normal and tangential components of the two vectors with respect to the point of closest approach with the substrate.

The shading scale for Figure 5.7 focuses on the range of $0.9 \leq \cos\ \beta \leq 1.0$, with all values below 0.9 displayed with the darkest shade. A value of 1.0 signifies that **u** and **v** are parallel and pointing in the same direction ($\beta = 0$), thereby indicating that the PTM is accurately accounting for hydrodynamic interactions between the particle and the composite substrate. As $\cos\beta$ decreases from 1.0, the angular deviation increases (*e.g.* $\cos\beta = 0.9$ represents an angle β of 25.8°) as depicted schematically in an exaggerated manner for the arbitrary position P near the asperity in Figure 5.7. In this schematic, it can be seen that the angular deviation arises when the magnitudes of the normal and tangential components of the particle velocity vector (v_n and v_t, respectively) are reduced more quickly than they should be when the PTM calculates the hydrodynamic interactions. In Figure 5.7, the regions where the highest angular deviation occur are along the surface of the asperity and on the flat surface neighbouring the asperity. An exception to this is the immediate vicinity of the front stagnation point of the asperity, $(x/a_p, y/a_p, z/a_p)$=$(-5.0, 0.0, 5.0)$ where **u** and **v** are essentially normal to the asperity's surface. Regions of angular deviation on the asperity's surface are expected since the PTM's use of the UCFs overestimates the hydrodynamic retardation effect on the particle by treating the asperity as a large flat plate. The angular deviation for the region on the flat surface occurs because the presence of the asperity further retards the tangential (with respect to the flat surface) component of the particle's velocity. This increased retardation is not accounted for by the PTM in this area, for which the UCFs are calculated solely on the basis of closest approach to the flat surface. Nonetheless, all of these regions of highest angular deviation are in the near-field (*i.e.*, at small separation distances, $H < 0.5$) of the composite substrate, where colloidal interactions and Brownian motion are typically the dominant transport mechanisms. It should also be noted from Figure 5.7 that there is little sign of angular deviation along the line of transition between PAP and PSP (refer to Figure 5.5, $\lambda = 5$).

The preceding comparisons show that the PTM's approximation technique provides a reasonable estimate of the hydrodynamic interactions for a particle

near a substrate with a complicated geometry. One of the goals of this study is to improve upon the velocity field used in conventional deposition models assuming a smooth substrate, so the simple methodology of the PTM, albeit approximate, constitutes a substantial improvement in how hydrodynamic retardation of a particle near a rough substrate is computed.

5.6 Happel Cell Model

As noted earlier, the PTM's approach to simulating particle trajectories is somewhat similar to that of the Lagrangian model described in a recent paper by Nelson and Ginn [NG05]. In their paper, the authors used their approach with the analytical Happel Sphere-in-Cell Model, which is commonly employed to simulate packed bed filtration and particle deposition in porous media [Hap58,SF73,EO90a,EO90b,TBW07]. For a range of particle sizes, they compared their results for the initial collection efficiency of a single spherical collector, η, with the established correlation equations of Rajagopalan and Tien [RT76, RTPT82, LJA+95] and Tufenkji and Elimelech [TE04]. The initial, single collector collection efficiency is defined as the ratio of the overall rate of deposition onto the collector to the convective flux of particles upstream from the collector over the projected area of the collector [TE04]. With this classic deposition model, the effectiveness of the PTM is demonstrated through the same comparison in Figure 5.8, also including the results of Nelson and Ginn [NG05] with the correlations previously mentioned.

The system parameters for this validation, as shown in Table 5.4, are identical to those of Table 3 in Nelson and Ginn [NG05] with the following exceptions: (i) gravity is not included, and (ii) the number of released particles for each simulation is 10000. No electrostatic interactions are included in any of these curves and results. For the PTM, each particle is released from a randomly-determined position on the surface of the Happel fluid shell upstream from the collector.

Figure 5.8 reveals that the results from the PTM simulations, including

Table 5.4: Parameters used in the Happel cell scenario, as listed in Table 3 of Nelson and Ginn [NG05].

Quantity	**Symbol**	**Value**	**Units**
Collector radius	a_c	163.5	μm
Porosity	χ	0.372	–
Approach velocity	U_∞	3.4375×10^{-4}	m/s
Fluid viscosity	μ	8.9×10^{-4}	Pa·s
Hamaker constant	A_H	10^{-20}	J
Particle density	ρ_p	1070	kg/m^3
Fluid density	ρ_f	997	kg/m^3
System temperature	T	298	K
Time step	Δt	1	μs
Number of released particles	N	6000	–

error bars [BHH78], follow the correlation curve of Rajagopalan and Tien throughout the entire range of particle sizes shown. In the interception-dominated regime (*i.e.*, large particles), PTM simulations are in good agreement with the predictions of both the Rajagopalan-Tien and Tufenkji-Elimelech correlations (with gravity excluded). In the strictly Brownian regime (*i.e.*, diffusion-dominated; $a_p \leq 1000$ nm), the analytical solution of the convection-diffusion equation yields the widely-recognized Levich approximation [Lev62, EGJW95]. For this regime, the collection efficiency of Brownian particles is proportional to $N_{Pe}^{-2/3}$, with N_{Pe} being the Peclet number. The curve of Rajagopalan and Tien [RT76,RTPT82,LJA$^+$95] has such a slope in the Brownian regime, and the results from the PTM also follow this slope in this regime. Earlier studies [NMB06b, NMB06a] have stated that the inclusion of gravity could lead to a deviation of the η vs. Pe curve in the Brownian deposition regime from the Levich solution. This deviation depends on the relative magnitudes of convective, diffusive and migrational forces. For instance, even for purely attractive colloidal interactions, one may observe no deposition if gravity opposes the colloidal interactions [NMB06b, NMB06a].

Despite the shared Lagrangian approach that this present study has with

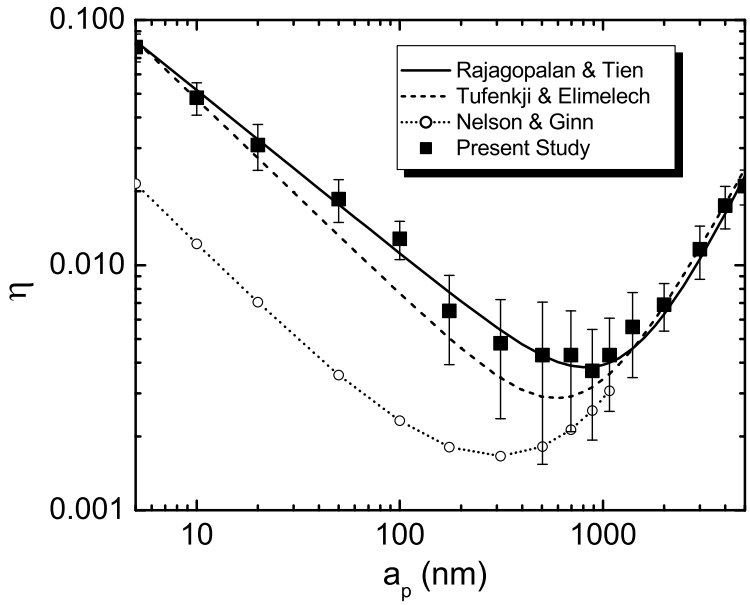

Figure 5.8: Variation of initial collection efficiency η with particle radius a_p for a single spherical collector using the Happel Sphere-in-Cell Model. The PTM simulations (present study) are performed under identical conditions as in Table 3 of Nelson and Ginn [NG05], but with gravity excluded. The results of the present study are shown with established correlation equations of Rajagopalan and Tien [RT76, RTPT82, LJA+95] (*solid line*) and Tufenkji and Elimelech [TE04] (*dashed line*), as well as the results of Nelson and Ginn [NG05] (*dotted line with hollow circles*).

that of Nelson and Ginn, there is a substantial difference between their results and those of the PTM in the Brownian regime. Considerable effort was applied to uncover the source of discrepancy between the two sets of the results, but to no avail thus far. Since the difference is mainly for Brownian particles and is more pronounced for smaller values of a_p, these factors point to the Brownian displacement term as a possible source. There is also a significant difference in how η is determined for the two approaches, but this possibility was not pursued in the present study. Further exploration is required to determine what causes this discrepancy. It is important to note that all of the lines in Figure 5.8 are from correlation equations (Rajagopalan and Tien, Tufenkji and Elimelech) or integrations over space of estimated probability functions

for particle collection (Nelson and Ginn). Consequently, these lines do not show the scatter of raw data as the results of the PTM simulations do.

5.7 Summary

Using several dimensionless numbers, the limits of the PTM's parameter space have been defined, relating particle size to the maximum average channel velocity U_{avg} that can be considered. For the undisturbed hydrodynamic field, the accuracy with which it is determined using finite element software and the effectiveness of trilinear interpolation in determining fluid velocity throughout the sub-domain grid has been confirmed. The approximate manner in which the PTM accounts for hydrodynamic interactions between a particle and a model rough surface has been shown to produce valid results in a range of interaction from the far-field to less than one particle radius, where colloidal interactions start to be more significant. Application of the PTM to determining the collection efficiency of an isolated spherical collector using the classic Happel cell model reveals good agreement with established, semi-empirical correlation equations. With the PTM validations complete, the following chapter begins the exploration of the parameter space to which the PTM can be applied for a substrate with a single spherical asperity on it.

Chapter 6

Particle Transport Near Surfaces with Spherical Asperities

6.1 Introduction

The PTM's parameter space is now defined and various aspects of the PTM's approach to simulating Brownian particle motion near heterogeneous substrates have been validated. In this chapter, the PTM is applied to a number of scenarios involving one or more spherical asperities protruding from a planar surface in the presence of a one-dimensional shear flow moving across it.[1] Modeling physical heterogeneity of a substrate using simple shapes such as spheres in ordered arrangements is certainly not an exact portrayal of a real, natural surface. Such models, however, add some sophistication to simulations of particle transport and deposition near collectors that would have features of heterogeneity, whether they are natural or artificial. Currently, there are efforts to manufacture substrates with ordered arrays of nanoscale asperities, as first mentioned in Section 2.3.3. In the course of analyzing the results of these scenarios, this chapter discusses (i) the importance of accurately depicting the undisturbed flow field near a rough surface, (ii) how the presence of surface roughness on a collector can modify near-field hydrodynamics and

[1]Some of the contents of this chapter have been published. Kemps and Bhattacharjee, 2009, *Langmuir*, 25(12):6887-6897.

ultimately affect the probability of particle deposition, and (iii) the effects of physical and/or chemical heterogeneity on deposit morphologies and other particle deposition phenomena.

6.2 Deposition in the Presence of a Single Asperity

Before embarking on investigations of systems with numerous asperities, an exploration of particle transport and deposition in the vicinity of a single spherical asperity is apropos. The objectives of this section are to demonstrate (i) how the presence of a single spherical asperity can modify the deposition behaviour on an otherwise smooth surface, (ii) the extent to which inclusion of hydrodynamic interactions can modify predictions of particle deposition, and (iii) how deterministic and Brownian forces interact with the asperity to yield variations in the deposition behaviour. From this point, all of the simulations in subsequent discussions use full, numerically-determined three-dimensional (and, for a few instances, two-dimensional) flow fields, as opposed to the analytical equations for the flow field used in Section 5.6.

6.2.1 Trajectory Analysis - Hydrodynamics Only

As a starting point, the influence of the deterministic forces on particle deposition is explored using PTM simulations that are performed while suppressing Brownian motion. Figures 6.1 and 6.2 depict the deterministic particle trajectories around a single asperity on an otherwise smooth planar surface, but in the absence of any colloidal (DLVO) forces. These simulations are performed using an asperity-to-particle size ratio (λ) of 5. With such a size ratio, the asperity protrudes a substantial distance into the fluid and the top half of the asperity is "more disconnected" from the flat portion of the substrate than with a lower value of λ. Consequently, fluid flow in the asperity's vicinity is significantly affected and the substrate's accessible surface area for particle deposition (when compared with a flat surface) is markedly increased. The

Peclet number (Pe) for these figures is arbitrary since the flow field is scaled with respect to the average fluid velocity in the channel U_{avg}, and only hydrodynamic interactions and drag in the Stokesian regime are accounted for.

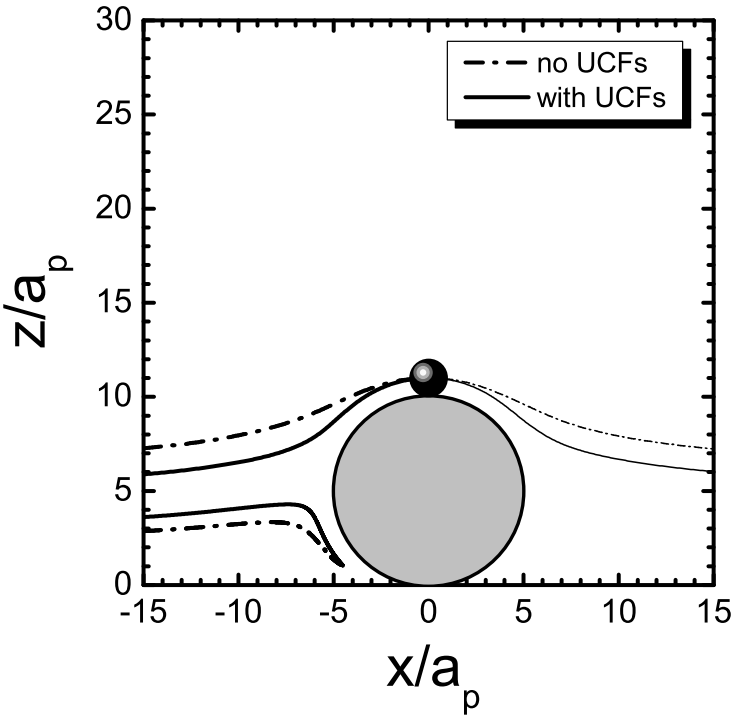

Figure 6.1: Comparison of particle trajectories in the $x - z$ plane (*i.e.*, $y/a_p = 0$) along the center of a spherical asperity with (solid lines) and without (dashed lines) hydrodynamic correction functions (UCFs). The endpoints of the limiting trajectories (thick lines) mark where the particles are intercepted by the asperity. The thinner pathlines extending downstream from the asperity are escape trajectories. Colloidal (DLVO) interactions are not included in these simulations, and the asperity-to-particle size ratio $\lambda = 5$.

In Figure 6.1, the trajectories are shown along the $x-z$ plane ($y = 0$, plane passing through the asperity center), and the particles are released from a position at a significant distance upstream from the asperity (*i.e.*, $x/a_p = -15$). The thick lines of Figure 6.1 represent the limiting trajectories that a particle would follow to be adsorbed onto the asperity. In particular, the discontinuous lines in this figure depict the upper and lower limiting trajectories for

the interception of the particle by the asperity when the hydrodynamic correction functions (f_1 to f_4) are not considered. The solid lines represent the corresponding limiting trajectories when the hydrodynamic interactions are considered. Particles released from heights between the upper and lower limiting trajectories will be intercepted by the asperity, and those released from positions above the upper limiting trajectory are not deposited anywhere, as shown by the thin lines in Figure 6.1. The limiting particle trajectories with the application of UCFs show a shorter range (compared to not using UCFs) of particle release heights from which they will be intercepted by the asperity.

When observed in three-dimensional space, Figure 6.2 reveals how the limiting trajectories for each case (*i.e.*, without UCFs and with UCFs) trace the perimeter of a nearly semi-circular area A_L in the $y-z$ plane at the position where the particles are released from, $x/a_p = -15$. This is the interception cross-section area for the top half of the asperity, and all particles released from within this area are intercepted by the asperity. The full interception cross-section area in the $y-z$ plane is not circular (instead, somewhat elliptical) due to the presence of the planar substrate. However, the lower half of the cross-section area is not a concern for this study since many particles released from there would be adsorbed on the flat portion of the substrate before having significant interactions with the asperity (refer to Appendix C for more details). It is evident from the limiting trajectories in Figure 6.2 that even in the purely convective limit, the particle deposition probability on the composite substrate containing a single asperity will be altered due to interception. It is also evident that the asperity primarily modifies the undisturbed flow field, which influences the deposition considerably. A comparison of the interception cross-section areas in Figures 6.2(a) and (b) shows that the inclusion of the UCFs will reduce the interception cross-section.

6.2.2 Trajectory Analysis - With Colloidal Interactions

Figures 6.3 and 6.4 depict the deterministic limiting trajectories in the presence of attractive (favourable) and repulsive (unfavourable) DLVO interactions, re-

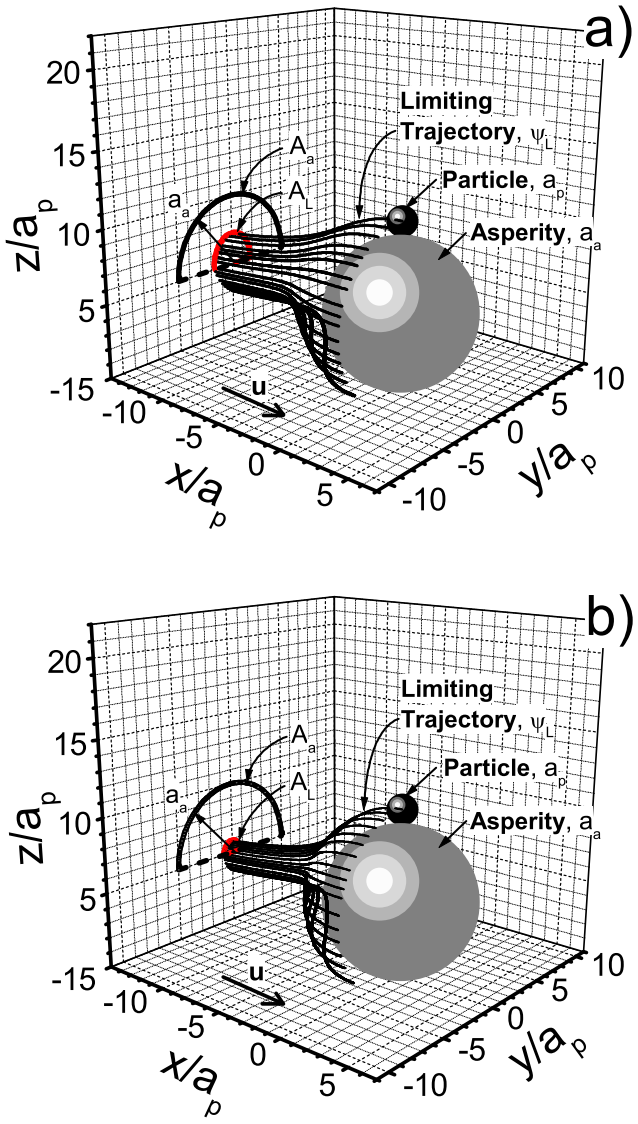

Figure 6.2: Comparison of limiting particle trajectories in three dimensions around a spherical asperity without (a) and with (b) hydrodynamic interactions included. Colloidal (DLVO) interactions are not included in these simulations. At $x/a_p = -15$ (where the particles are initially released), the area enclosed by the limiting trajectories (A_L) is found within the projected area of the top half of the asperity (A_a) in the $y - z$ plane.

spectively. For this part of the study, the electrostatic double layer interactions between the particle and the substrate are held constant, and favourable and unfavourable interactions are simulated by simply varying the magnitude of the Hamaker constant (pertinent interaction parameters given in Table 6.1). The parameters listed in Table 6.1 can be regarded as part of the basic system configuration for the PTM simulations, and all subsequent system configurations are derived from it, with one or more of these parameters modified to explore certain effects. The particle Peclet number is a function of shear rate $\dot{\gamma}$, which itself is a function of the average fluid velocity in the channel, U_{avg}, and the channel's half-height, b [EGJW95]:

$$Pe = \frac{\dot{\gamma} a_p^2}{D_\infty} = \frac{18\pi\mu a_p^2 U_{avg}}{k_B T}\left(\frac{a_p}{b}\right) \tag{6.1}$$

Table 6.1: Basic system configuration parameters used with the PTM simulations. Note that Case FF corresponds to when the entire composite substrate is fully favourable and Case UU to when it is fully unfavourable.

Quantity	**Symbol**	**Value**	**Units**
Particle radius	a_p	100	nm
Scaled asperity radius (a_a/a_p)	λ	5.0	–
Scaled Hamaker constant (Case UU)	$A_{H,pi}/(k_B T)$	1.0	–
Scaled Hamaker constant (Case FF)	$A_{H,pi}/(k_B T)$	5.0	–
Surface potential	ψ_p, ψ_i	-25	mV
Particle density	ρ_p	1000	kg/m^3
Fluid density	ρ_f	1000	kg/m^3
Fluid viscosity	μ	10^{-3}	Pa·s
System temperature	T	298.15	K
Permittivity of medium	ϵ	6.95×10^{-10}	C^2/N·m^2
Shear rate	$\dot{\gamma}$	3 to 3000	/s
Electrolyte (1:1) concentration	I	10^{-1}	M

Favourable Conditions to Deposition

The limiting trajectories along the $x-z$ plane for capture by the asperity ($\lambda = 5$) in the presence of attractive DLVO interactions between the particle and the

composite substrate (*i.e.*, favourable conditions to deposition, or Case FF) are presented in Figure 6.3. Under these conditions, both the spherical asperity and the flat portion of the substrate attract the particle. Figures 6.3(a) and (b) show the trajectories for two Peclet numbers, $Pe = 0.014$ and 1.4, respectively.

For favourable deposition, there are two limiting trajectories (shown as thick solid lines) that bound the release positions of particles leading to their capture by the asperity. The upper limiting trajectory terminates at the trailing edge of the asperity, while the lower limiting trajectory terminates somewhere on the asperity upstream from the upper limiting trajectory endpoint. Initial release heights of both these limiting trajectories are sufficiently distant from the planar substrate so that any particle-plate DLVO interactions are negligible relative to the flow intensity. For these limiting trajectories, the particle is convected with the flow, experiencing some hydrodynamic lift as it approaches the asperity, and only when it comes in close proximity to the asperity does the migrational DLVO force exert a measurable influence on its trajectory. Note that the interception zone subtended by these limiting trajectories is comparable to that obtained in Figure 6.1 when the UCFs were not considered (discontinuous lines). This indicates that the long-range van der Waals attraction and long-range hydrodynamic retardation effects approximately cancel each other.

For the low Peclet number of 0.014 in Figure 6.3(a), the relatively low convective forces allow the upper limiting trajectory to circle around the asperity and reach a position of 165° (close to the rear stagnation point) before making contact. The initial release height of this trajectory is approximately $11a_p$, which is higher than the asperity. At the higher Peclet number of 1.4, the upper limiting trajectory starts at a height of about $8a_p$ in Figure 6.3(b), and it terminates on the asperity at an angle of 145°. Therefore, increasing the flow intensity reduces the height of the upper limiting trajectory, and decreases the surface area of the asperity on which the particles can deposit. Furthermore, deposition does not occur at the rear stagnation point of the asperity for favourable conditions (based on the DLVO interaction parameters

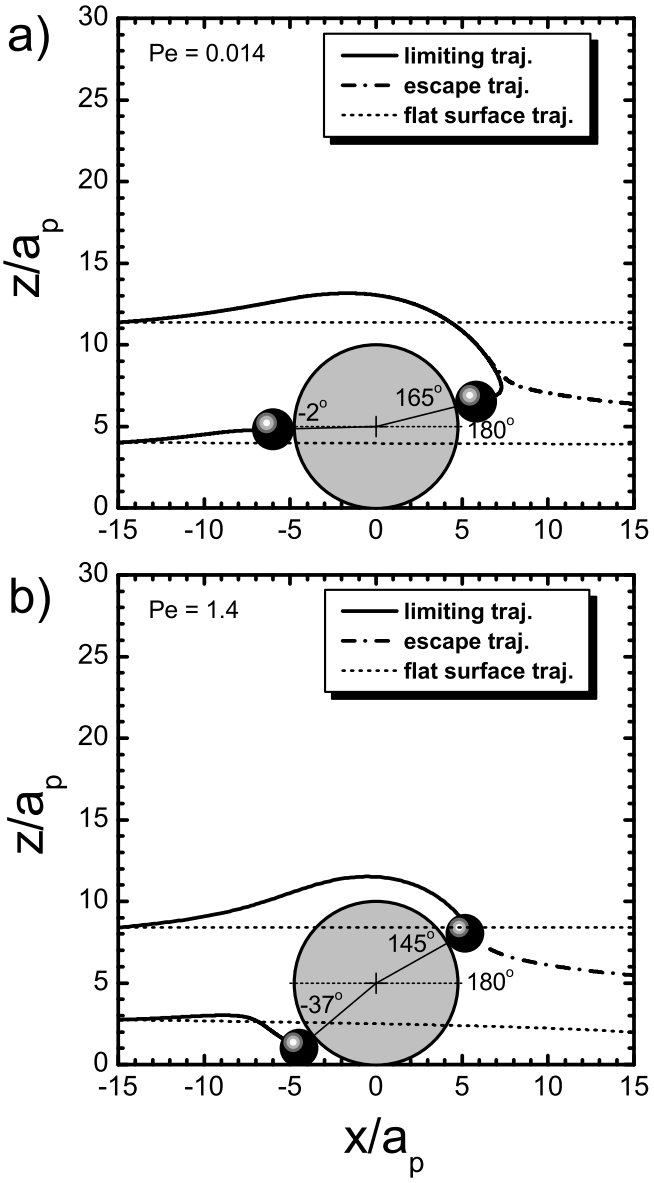

Figure 6.3: Limiting, escape and flat surface trajectories in the $x - z$ plane of particles under favourable conditions (Case FF) to deposition for the entire composite substrate (*i.e.*, single asperity with planar substrate). These trajectories are determined at two different particle Peclet numbers: (a) 0.014 and (b) 1.4. The parameters for these simulations can be found in Table 6.1.

in Table 6.1), as particles tend to deposit closer to the peak of the asperity.

The lower limiting trajectories of Figure 6.3 also show interesting dependence on the flow intensity. For $Pe = 0.014$, the initial height of the lower limiting trajectory is $4a_p$. Particles following this trajectory are lifted slightly higher as they approach the asperity, eventually depositing at a location slightly below the forward stagnation point (angular location $-2°$). In contrast, initial height of the lower limiting trajectory for $Pe = 1.4$ is about $3a_p$, in which case the trajectory leads to the particle being wedged between the asperity and the flat surface, at the $-42°$ position. Particles originating below this height deposit on the planar substrate before reaching the asperity.

If it is not intercepted by the asperity or depositing on the planar substrate, the particle will follow the escape trajectory, such as those shown by the dash-dot lines in Figures 6.3(a) and (b). These escape pathlines are obtained by releasing the particles at heights slightly above their associated limiting trajectories. Figure 6.3 also includes flat surface trajectories (dashed lines) depicting the paths that particles would travel when released from the same initial position as their associated limiting trajectories if the asperity was not present. When comparing the height of the escape trajectories with the flat surface trajectories at a point downstream from the asperity (*i.e.*, $x/a_p = +15$), it is apparent that the asperity exerts a net attraction on the moving particle, bringing it closer to the planar region of the collector at downstream locations.

Unfavourable Conditions to Deposition

The limiting trajectories in the presence of unfavourable DLVO interactions (*i.e.*, unfavourable conditions to deposition, or Case UU) are depicted in Figure 6.4 for the same Pe values and the same system as in Figure 6.3. Under these conditions, the system's Hamaker constant is relatively low, so there is a substantial repulsive EDL force barrier that prevents particle adsorption anywhere on the composite collector surface. Although the paths of the limiting trajectories for unfavourable conditions are comparable to those obtained with favourable conditions, they do not terminate in the same manner as in

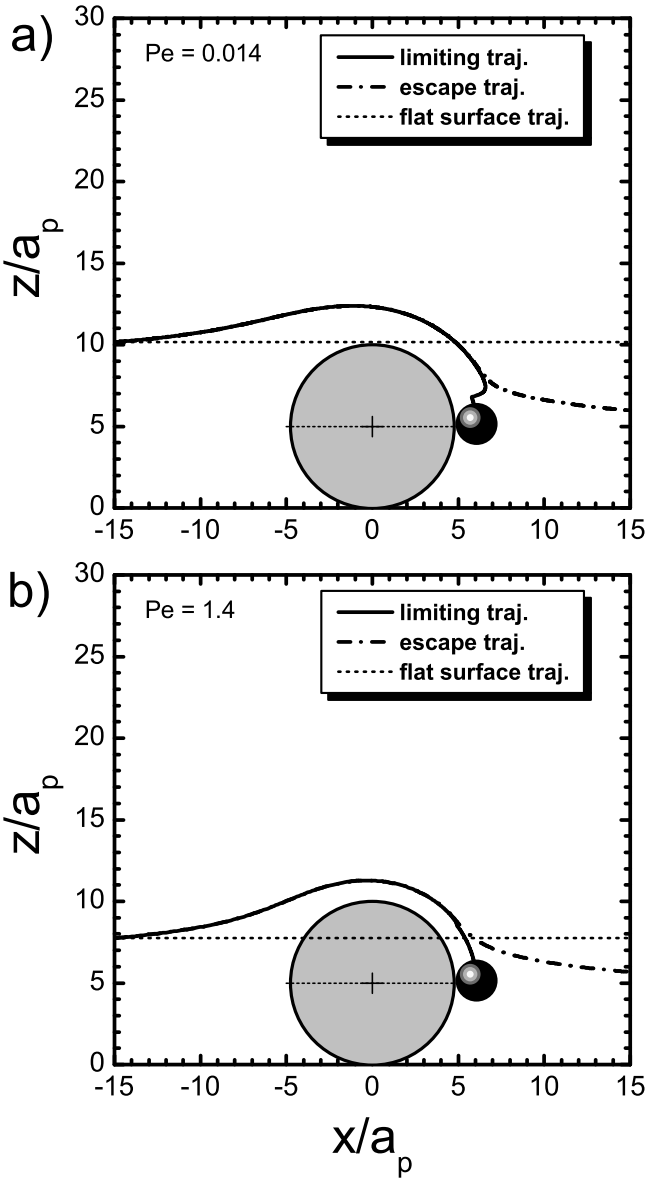

Figure 6.4: Limiting, escape and flat surface trajectories in the $x - z$ plane of particles under unfavourable conditions (Case UU) to deposition for the entire composite substrate (*i.e.*, single asperity with planar substrate). These trajectories are determined at two different particle Peclet numbers: (a) 0.014 and (b) 1.4. The parameters for these simulations can be found in Table 6.1.

the favourable case. For unfavourable interactions at both Peclet numbers (Figures 6.4a and b), the terminal position of the particle is the rear stagnation region of the spherical asperity (*i.e.*, 180° position with respect to the shear flow direction), at a finite separation from the asperity. In this region, there are no significant tangential (with respect to the asperity) forces acting on the particle. This separation distance is located just beyond the secondary DLVO minimum where, in the normal direction to the asperity, a small attractive colloidal force is balanced against a small outward fluid drag force. The force balance in the $x-$ direction can be seen in Figure 6.5, with the ratio F_x^{DLVO*}/F_x^{drag*} approaching -1.0 (*i.e.*, equal but opposite) as the particle rolls toward the rear stagnation point at $\theta = 180°$. With these deterministic forces canceling each other, a local "equilibrium" has been reached at which the particle can be trapped indefinitely.

The idea of colloidal particles being immobilized or trapped in the secondary energy minimum has been proposed in several recent studies [RWE04, HAO04, TE05b, KE07]. Experimental results from Kuznar and Elimelech showed 4.1 μm particles depositing in the rear stagnation points of spherical glass bead collectors despite conditions being unfavourable to deposition [KE07]. They concluded that once the particles reach the secondary minimum, they translated along the glass bead surface until they reached a region of stagnant flow. This explanation seems feasible based on the results of the PTM simulations shown in Figure 6.4. However, it should be noted that the particles used by Kuznar and Elimelech were much larger than those used in this study (*i.e.*, 100 nm), so the secondary minimum would be much deeper and particle trajectories would be predominantly deterministic for their experiments. The terminal points of these trajectories in Figure 6.4 do not represent a definitive contact with the asperity, but rather a "soft" immobilization based on virtually no observable displacement of the particle in a local deterministic force equilibrium. Such a scenario would change when Brownian motion is accounted for in the particle's transport.

The initial positions of the upper limiting trajectories in Figures 6.4(a)

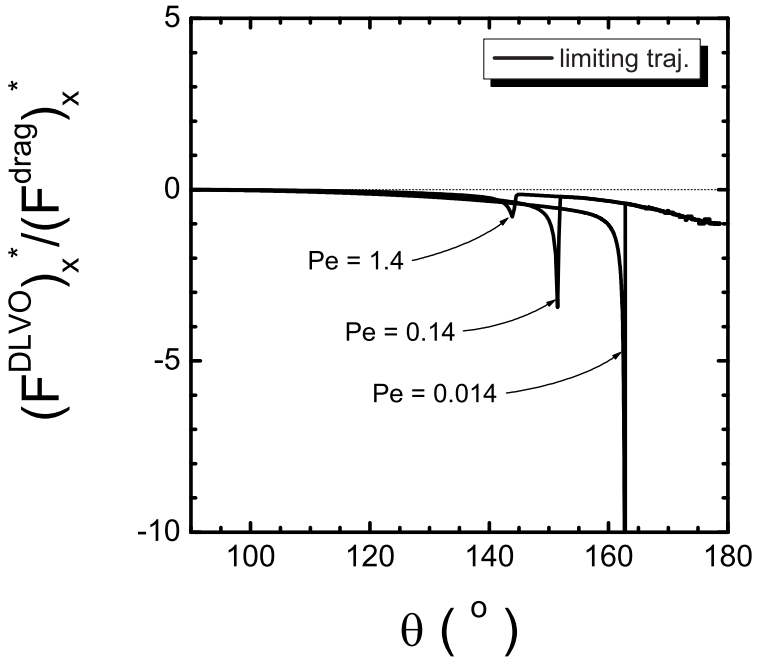

Figure 6.5: Ratio of scaled DLVO force over scaled drag force acting on the particle in the $x-$ direction as it travels along its limiting trajectory around a single spherical asperity (shown as angular position θ relative to the forward stagnation point) under unfavourable conditions (Case UU). Three values of Pe are shown here: 0.014, 0.14 and 1.4 (refer to Eq. 6.1).

and (b) are only slightly lower than the release points for the corresponding trajectories with favourable DLVO interactions (Figures 6.3a and b). Unlike for favourable conditions, lower limiting trajectories are not shown for the unfavourable case; each particle released below the upper limiting trajectory either finds its way to the equilibrium position where it is trapped, or it meanders through – and eventually exits – the computational domain. Figures 6.4(a) and (b) also show the escape trajectories of the particles as dash-dot lines extending downstream from the asperity, and the trajectories for a smooth flat plate (*i.e.*, in the absence of the spherical asperity) are shown as dashed lines. Again, a comparison of the flat surface trajectories with their associated escape trajectories reveals that the particle is brought closer to the flat substrate downstream from the asperity for unfavourable colloidal interac-

tions as well. This can be mainly attributed to the long-range van der Waals attraction between the particle and the asperity.

Figures 6.3 and 6.4 ultimately demonstrate the significance of depicting the hydrodynamic field around a rough surface as accurately as possible in order to model deposition phenomena with greater realism. Comparisons of all of the respective flat surface and escape trajectories indicate that particles tend to be attracted toward the composite substrate downstream from an asperity (*i.e.*, the dash-dot line falls below the dashed line), regardless of whether the short-range particle-asperity colloidal interactions are attractive or repulsive.

6.2.3 Deposition Probability - Deterministic Forces

Different approaches to modeling the deterministic forces (particularly hydrodynamics) can lead to variations in deposition probability for the spherical asperity. To demonstrate this, a number of simulations spanning the range of shear rates listed in Table 6.1 (and hence, Pe values, through Eq. 6.1) were performed for several scenarios. The first scenario represents the classical approach to studies of deposition, in which the collector is assumed to be a smooth, flat surface. Each subsequent scenario highlights one component of the PTM's approach to modeling particle transport and deposition onto heterogeneous surfaces. Comparisons of the results from these scenarios reveal how each component of the PTM plays a role in particle deposition on these physically heterogeneous surfaces.

For each simulation run, 1000 particles are released one at a time from random positions within a semi-circular window in the $y-z$ plane located at $x/a_p = -15$, as shown schematically in Figure 6.6. The semi-circular cross-section of the window is equal to the projected area of the upper half of the asperity. Only the top half of the asperity is considered to clearly isolate deposition onto the asperity. The time step used in these simulations, Δt, is 1 μs. The deposition probability on the asperity can be defined as

$$\phi_a = \frac{\text{Number of particles deposited on the asperity}}{\text{Number of particles released}}. \tag{6.2}$$

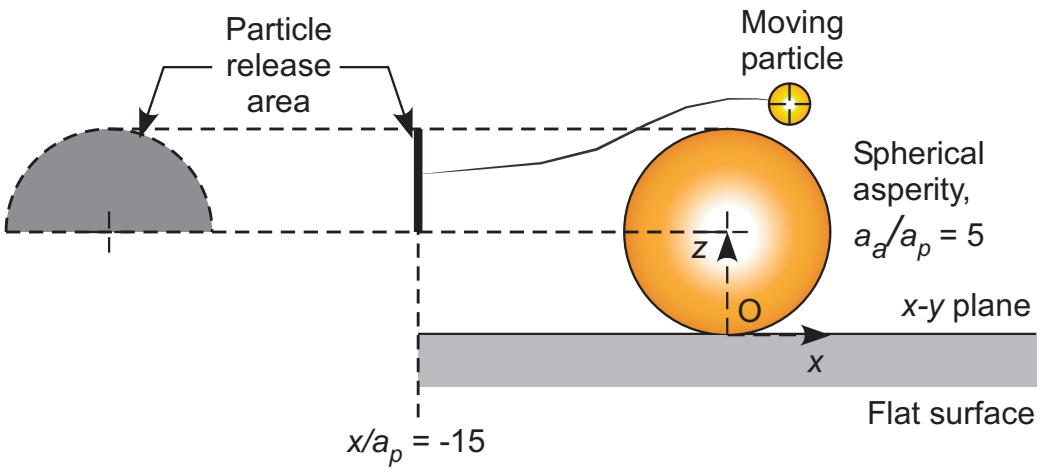

Figure 6.6: Deposition onto a planar substrate containing a single spherical asperity. Schematic showing the semi-circular area from which the particles are released randomly into the domain containing a single spherical asperity (*i.e.*, $a_a = 5a_p$).

Figure 6.7 compares the variation of ϕ_a with Pe as computed using different modeling approaches, considering only the deterministic forces. The first approach (*symbol:* asterisk) shown in Figure 6.7 employs the undisturbed velocity field near a flat surface (one-dimensional shear flow). The disturbance to the flow field due to the presence of the asperity is ignored. Also, the hydrodynamic universal correction functions (UCFs) are not used (*i.e.*, f_1 to $f_4 = 1$) and no DLVO interactions are considered in this scenario. In this case, the trajectory calculations lead to two trivial results. If the asperity is present (but not accounted for hydrodynamically), all of the particles released are intercepted by it (*i.e.*, $\phi_a = 1.0$), regardless of Pe. The other trivial result is that in the absence of the asperity, no particle released from this region will deposit on the planar substrate.

The second approach (*symbol:* hollow triangle) uses the detailed, undisturbed velocity field near the asperity (computed numerically). As with the first approach, neither the UCFs (*i.e.*, f_1 to $f_4 = 1$) nor the DLVO interactions are used in these simulations. In other words, although the hydrodynamic field modification due to the asperity is considered, higher order hydrodynamic and

colloidal interactions between the particle and the substrate are neglected. The deposition probability is markedly reduced to approximately 0.16 in this case, but it remains independent of Pe. This reduction occurs because inclusion of the detailed velocity field around the spherical asperity dramatically reduces the size of the interception cross-section area relative to the projected frontal area of the asperity (*i.e.*, A_L relative to A_a respectively in Figure 6.2a).

When the UCFs are applied to the particle's equations of motion (*symbol:* hollow circle), there is a further reduction in deposition probability, down to about 0.03. The increased hydrodynamic resistance between the particle and the asperity as they approach each other prevents nearly all particles from depositing on the asperity. The deposition probability in this case would be zero if contact was defined in the PTM as when the separation distance h is zero. For simulations in this study, contact occurs when $h = 0.3$ nm (see Section 4.3.8: Trajectory Termination Criteria), which accounts for Born repulsion (from overlapping electron clouds) and avoids divergence in the van der Waals force calculation. Consequently, a few particles are able to make contact with the asperity before the Stokes' lubrication force (*i.e.*, hydrodynamic interactions) can prevent it. Therefore, the inclusion of UCFs with the detailed velocity field further reduces the interception cross-section area A_L, which was demonstrated earlier in going from part (a) to (b) in Figure 6.2. In all the above situations, the mechanism of particle capture is purely interception, and the ϕ_a values simply reflect the reduction in the interception region compared to the projected asperity area in the presence of the detailed hydrodynamic field, and subsequently, the UCFs. None of the preceding cases included DLVO interactions, and deposition probability was always independent of Pe.

The resulting deposition probabilities with the preceding scenarios are somewhat analogous to the generally accepted definition of collection efficiency due to interception η_I [MB06] if applied to only the top half of the asperity. A rigorous expression for the collection efficiency due to interception under these circumstances is derived in Appendix C. Using the starting positions from the limiting trajectories in Figures 6.2(a) and (b), results from this expression for

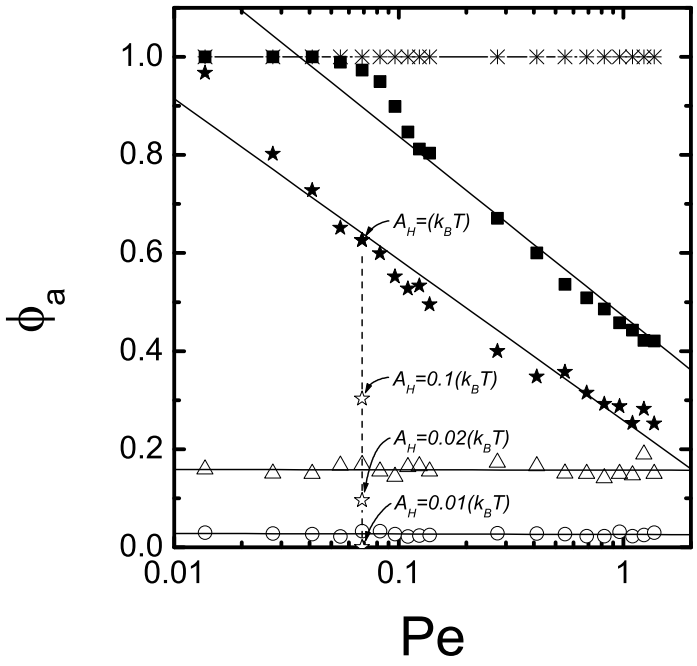

Figure 6.7: Variation of deposition probability ϕ_a with particle Peclet number, Pe, in the deterministic simulations. The results of four approaches to these simulations are shown with the following symbols: *asterisk* = one-dimensional shear flow on a planar surface (asperity not considered); *hollow triangle* = explicit, numerically-evaluated flow field around the composite substrate; *hollow circle* = UCFs included with explicit flow field; *filled square* = UCFs and favourable deposition conditions (FF) included with explicit flow field; *filled star* = UCFs and unfavourable deposition conditions (UU) included with explicit flow field. The parameters for these simulations are shown in Table 6.1.

η_I are compared with those of the average deposition probabilities ϕ_a for the hollow triangles (without UCFs) and hollow circles (with UCFs) in Figure 6.7. As Table C.1 reveals for both scenarios, there is good agreement between η_I and ϕ_a for the top half of the asperity.

The filled squares and stars in Figure 6.7 represent the deterministic simulations including attractive (favourable) and repulsive (unfavourable) DLVO interactions, respectively. With the introduction of the DLVO interactions, a relationship between ϕ_a and Pe can be observed as a general trend of de-

creased deposition probability as $Pe \rightarrow 1$. The simulations were conducted by considering the detailed flow field as well as higher order hydrodynamic interactions (UCFs). In the presence of both favourable and unfavourable DLVO interactions, a higher probability of deposition compared to $\phi_a \approx 0.03$ can be observed, which was obtained on the basis of hydrodynamic interactions alone. Under favourable conditions (Case FF, *symbol:* filled square), the deposition probability is 1.0 (all particles released are deposited on the asperity) until $Pe \approx 0.05$, and then falls to about 0.45 for $Pe = 1.0$. For unfavourable deposition (Case UU, *symbol:* filled star), ϕ_a decreases almost monotonically from about 1.0 at the lowest Peclet number to less than 0.3 for $Pe = 1.0$. With the unfavourable condition, the particles are not irreversibly captured as in favourable deposition, but are typically immobilized on the downstream side of the asperity near the rear stagnation point. Different modes of particle capture on these complex surfaces and their implications will be discussed later in this chapter.

The deposition probability in the presence of unfavourable colloidal interactions is higher than the corresponding values of ϕ_a in the absence of colloidal interactions. As mentioned earlier, this behaviour is attributed to the long-range van der Waals interactions, which effectively increase the interception cross-section area. The vertical dashed line in Figure 6.7 depicts the variations of the deposition probability as the van der Waals interactions are gradually reduced at a fixed $Pe \approx 0.07$. Along this line, a wide range of deposition probabilities are sampled ($0 < \phi_a < 0.6$) by varying the Hamaker constant between $0.01(k_BT)$ to (k_BT). Reducing the Hamaker constant in this manner yields an effect somewhat similar to altering the DLVO force by decreasing the solution ionic strength I. A decrease in either parameter leads to an increase in the repulsive EDL energy barrier height, and subsequently, a decrease in deposition probability. It is also true that, starting from $A_H = (k_BT)$ and $I = 10^{-1}$ M for this scenario, lowering the ionic strength to 10^{-3} M increases the thickness of the EDL barrier, extending it 10 times further ($U^{DLVO} \approx 10k_BT$ at $H_i = 0.22$) than with reducing the Hamaker constant to $0.01(k_BT)$ ($U^{DLVO} \approx 10k_BT$ at

$H_i = 0.023$). Nonetheless, all of this indicates that the far-field transport of particles to the asperity is largely dictated by a combination of hydrodynamic and van der Waals interactions, whereas the deposition behaviour near the collector surface is dictated by the repulsive or attractive EDL interactions. This behaviour is expected for the range of ionic strengths (10^{-3} to 10^{-1} M 1:1 electrolytes) commonly encountered in aquatic systems, which – for the particle size ($a_p = 100$ nm) used in the PTM simulations – renders $\kappa a_p > 10$ in all cases. Therefore, changing the Hamaker constant in these simulations reveals a measurable influence of the range of DLVO interactions on deposition behaviour. Consequently, variation of EDL interactions by changing ionic strengths is not explored in this part of the present study.

6.2.4 Deposition Probability - Deterministic and Brownian Forces

In this section, the effects of Brownian forces on the deposition probability ϕ_a are observed. Using the same approach as in Figure 6.6, 1000 particles are released in each run, with the time step, Δt, held at 100 ns. Figure 6.8 depicts the variation of the deposition probabilities with Peclet number.

With the undisturbed velocity field near the substrate represented as one-dimensional shear flow on a flat surface and ignoring any hydrodynamic or colloidal interactions, (*symbol:* asterisk), ϕ_a gradually increases toward the maximum of 1.0 as Pe increases. This is attributed to the convective forces becoming stronger than the Brownian force as Pe increases, so the probability of deposition converges to a state of pure interception like its counterpart in Figure 6.7. However, as noted earlier, this approach does not depict the hydrodynamic field around the asperity with any realism. When the correct undisturbed flow field around the asperity is provided (*symbol:* hollow triangle), the relationship between ϕ_a and Pe becomes parabolic as ϕ_a rises with Pe to a maximum where $Pe \approx 1.0$ and then falls gradually as Pe continues to increase. The same relationship is found when the UCFs are also applied (*symbol:* hollow circle), albeit at comparatively lower values of ϕ_a due to the

increased hydrodynamic resistance when the particles come near the asperity.

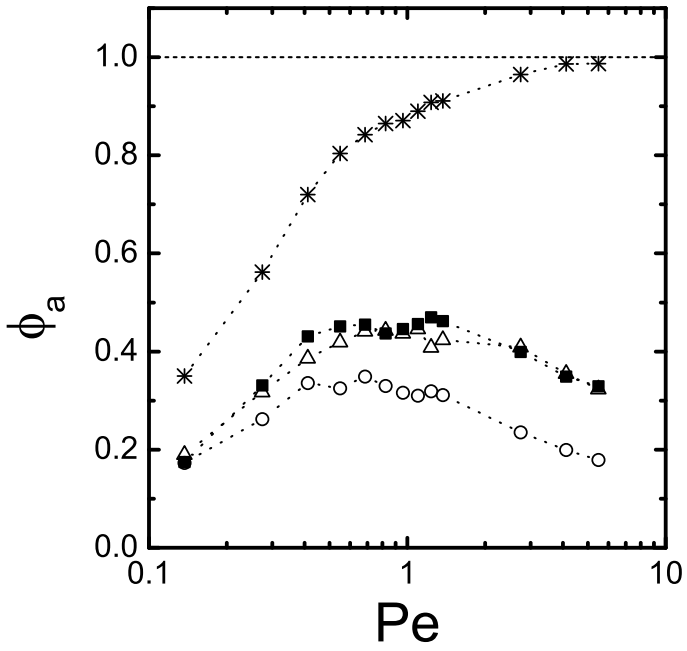

Figure 6.8: Variation of deposition probability ϕ_a with particle Peclet number, Pe, in the complete Brownian simulations. The simulations are performed under identical conditions as in Figure 6.7, with a stochastic (Brownian) displacement added to the deterministic motion. The results of five approaches to these simulations are shown with the following symbols: *asterisk* = one-dimensional shear flow on a planar surface (asperity not considered); *hollow triangle* = explicit, numerically-determined flow field around the composite substrate; *hollow circle* = UCFs included with explicit flow field; *filled square* = UCFs and favourable deposition conditions (FF) included with explicit flow field. The parameters for these simulations are shown in Table 6.1.

When the DLVO interactions are included for favourable (FF) conditions to deposition (*symbol:* filled square), the parabolic relationship is still evident. The comparatively higher values of ϕ_a are attributed to the strength of the attractive vdW interactions between the particle and the asperity. In this case, a maximum probability coincides with $Pe \approx 1.0$, which is also true when the DLVO interactions have not been included in the PTM. Under these conditions, it appears that with the hydrodynamic and Brownian forces roughly equal, the particles have the greatest chance of being adsorbed somewhere on

the surface of the asperity. Simulations under unfavourable (UU) conditions did not yield any deposited particles at any value of Pe for the parameters of this study, so these trivial results are not displayed in Figure 6.8. This absence of deposition is primarily due to the strength of the repulsive EDL barrier ($\approx 25 k_B T$). The barrier is sufficiently strong to prevent particles from penetrating it via Brownian motion to reach the primary DLVO interaction minimum.

6.2.5 Effects of Asperity-to-Particle Size Ratio

This part of the study investigates particle transport and deposition for a range of asperity-to-particle size ratios (*i.e.*, $0.5 \leq \lambda \leq 5$), approximately accounting for hydrodynamic interactions with the PTM in this scale of collector surface roughness. Figures 6.9, 6.10, and 6.11 show the trajectories of 100 nm ($= a_p$) particles traveling in the $x - z$ plane past a single asperity of varied size relative to the particles. Regardless of asperity size, the paths of all particles start at $x/a_p = -15$, and the remaining system parameters are in accordance with Table 6.1. For Figures 6.9 (Case FF) and 6.10 (Case UU), the Peclet number is 1.4 and parts (a), (b), (c) and (d) correspond to asperity-to-particle size ratios of $\lambda = 5$, 2, 1 and 0.5 respectively. In addition to the regular particle trajectories around each asperity, Figures 6.9 and 6.10 show limiting trajectories and their corresponding escape and flat surface trajectories in the same manner as Figures 6.3 and 6.4. To explore another aspect of particle transport near the asperity, Figure 6.11 displays only regular and escape trajectories for the size ratios of $\lambda = 5$ and $\lambda = 1$ respectively, but in the convection-dominated regime of $Pe = 14$ when the entire substrate is unfavourable to deposition (Case UU). For this scenario, the higher Peclet number is due to an increase in the average fluid velocity in the channel U_{avg}, which in turn increases the shear rate $\dot{\gamma}$ (refer to Eq. 6.1).

Figure 6.9 looks at the different size ratios under favourable conditions to deposition (Case FF). As expected, the release heights of the limiting trajectories are lower and closer together as the size ratio decreases, which suggests

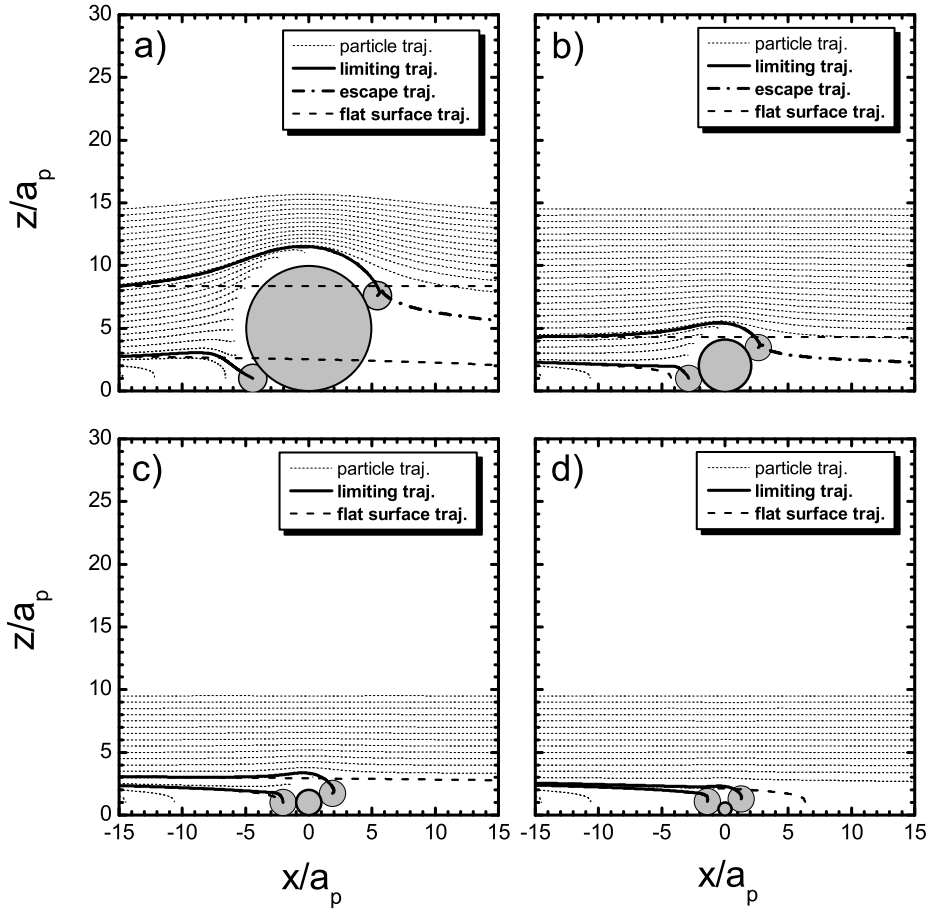

Figure 6.9: Limiting, escape and flat surface trajectories in the $x - z$ plane of particles under favourable conditions (Case FF) to deposition for the entire composite substrate (*i.e.*, single asperity with planar substrate) at various asperity-to-particle size ratios ($\lambda = a_a/a_p$). These trajectories are determined when the particle Peclet number is 1.4 for four size ratios: (a) $\lambda = 5$, (b) $\lambda = 2$, (c) $\lambda = 1$ and (d) $\lambda = 0.5$. The remaining parameters for these simulations can be found in Table 6.1.

there is a reduction in deposition probability for an individual asperity as it shrinks in size relative to the particle. For asperities that are larger than the particle (Figures 6.9a and b), the escape trajectories clearly indicate that the particle is brought closer to the composite substrate due to the presence of the asperity. With $\lambda = 5$, the escape trajectory has not dropped enough (*i.e.*, leaving the domain at a height of almost $6a_p$) for van der Waals interactions to be substantial enough to eventually pull the particle down to the substrate. However, the relentless attraction to the substrate starts to be seen in the escape trajectory of $\lambda = 2$ in Figure 6.9(b), where the particle leaves the domain at a height just over $2a_p$. Escape trajectories are not shown in Figures 6.9(c) and (d) as they are nearly indistinguishable from their respective upper limiting trajectories. Nevertheless, the upper limiting trajectories in these two figures also indicate the attractive influence of the asperities on the particles. It is also readily apparent from Figure 6.9 that as the size ratio decreases, the difference between a limiting trajectory (both upper and lower) and its associated flat surface trajectory diminishes. For these system parameters, a significant difference between the upper limiting and associated flat surface trajectories remains up to when the particle and asperity sizes are equal ($\lambda = 1$; Figure 6.9c). This alludes to the fact that even previously deposited Brownian particles can affect the deposition of subsequent Brownian particles via convective and migrational transport.

Figure 6.10 looks at the different size ratios under unfavourable conditions to deposition (Case UU). Even though irreversible adsorption is not possible under these conditions, the influence of the asperity on a particle's path is once again observable as in Figure 6.9, though to a lesser extent due to the reduced strength of the van der Waals interactions. An interesting aspect of Figure 6.10 is how the endpoint of the limiting trajectory – where the deterministic forces are balanced and the particle is immobilized – changes with size ratio. In Figure 6.10(a), the asperity appears to be large enough so that the endpoint of the limiting trajectory is situated at the rear stagnation point. This endpoint drops when $\lambda = 2$ in Figure 6.10(b) so that the particle rests in the wedge

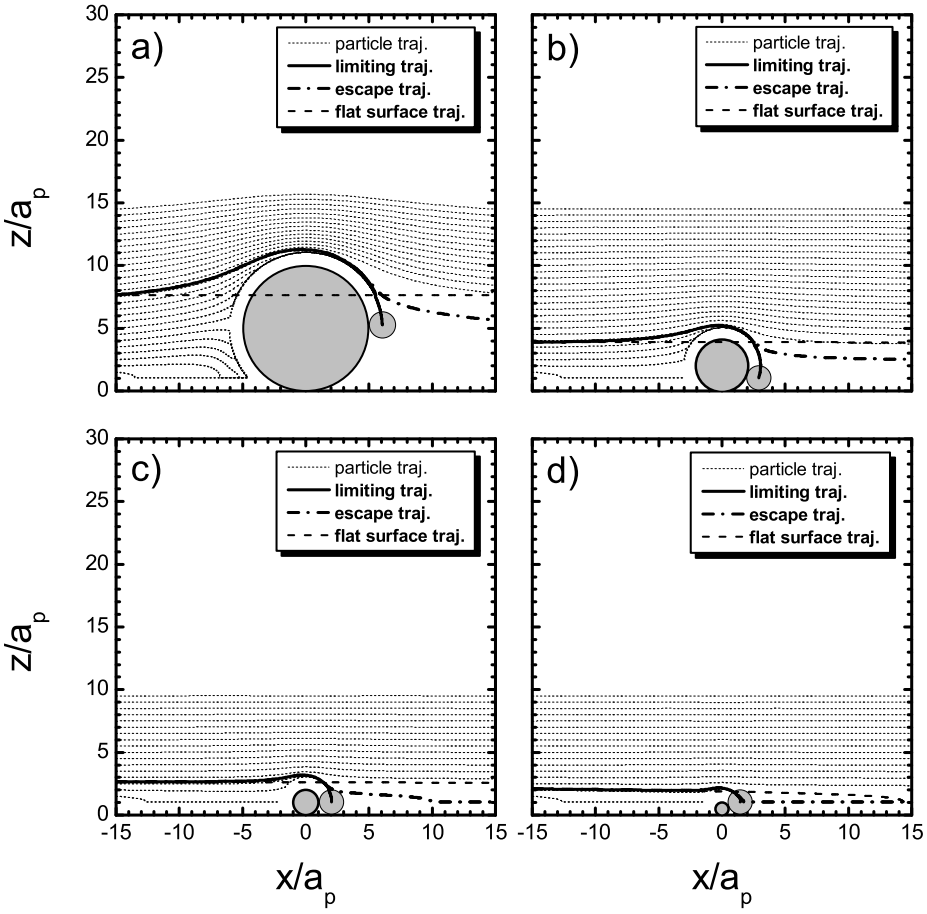

Figure 6.10: Limiting, escape and flat surface trajectories in the $x-z$ plane of particles under unfavourable conditions (Case UU) to deposition for the entire composite substrate (*i.e.*, single asperity with planar substrate) at various asperity-to-particle size ratios ($\lambda = a_a/a_p$). These trajectories are determined when the particle Peclet number is 1.4 for four size ratios: (a) $\lambda = 5$, (b) $\lambda = 2$, (c) $\lambda = 1$ and (d) $\lambda = 0.5$. The remaining parameters for these simulations can be found in Table 6.1.

region between the asperity and the flat portion of the substrate. When the size ratio is 1 and 0.5 (Figures 6.10c and d, respectively), the particle ends up directly behind the asperity as convective forces under these conditions are insufficient to dislodge it.

When $Pe = 14$ and conditions are still unfavourable to deposition, such as in Figure 6.11, there are no positions at which a 100 nm particle will be immobilized when its Brownian motion is suppressed. All particles escape the computational domain, though many of their paths are influenced by the asperity. In both parts of Figure 6.11, the hatched regions upstream from the asperity denote the trajectories for which the particles have the same escape trajectory downstream of the asperity. These particles experience varying amounts of lift depending on their release heights. When comparing the escape trajectories for $\lambda = 5$ at Peclet numbers of 1.4 and 14 (Figures 6.10a and 6.11a, respectively), they depart the computational domain at about the same height ($\approx 6a_p$), but their initial release heights are different ($\approx 7.5a_p$ for $Pe = 1.4$, between $\approx 4a_p$ and $6a_p$ for $Pe = 14$). A comparison of the same trajectories for $\lambda = 1$ at the two values of Pe (Figures 6.10c and 6.11b, respectively) reveal not only a difference in release heights but also in heights at which the trajectories leave the domain. For $Pe = 1.4$, the particle slides along the flat surface downstream from the asperity, while for $Pe = 14$, it maintains a height of $\approx 2a_p$.

The preceding observations reiterate the fact that convection is dominating particle transport near the asperity when $Pe = 14$, with the van der Waals component of the migrational transport less significant than when $Pe = 1.4$. The lift cannot be due to inertia for all scenarios in this study since the flow is Stokesian (*i.e.*, no fluid inertia) and the particles are small enough that their inertia can be neglected, as detailed in Section 4.2.3. Although both size ratios in Figure 6.11 exhibit some particle lift, the $\lambda = 5$ scenario imparts lift to particles traveling within a range of release heights more than 3 times greater than the $\lambda = 1$ scenario. This is anticipated since the larger the asperity, the greater the height above the flat surface to which the local undisturbed flow field is af-

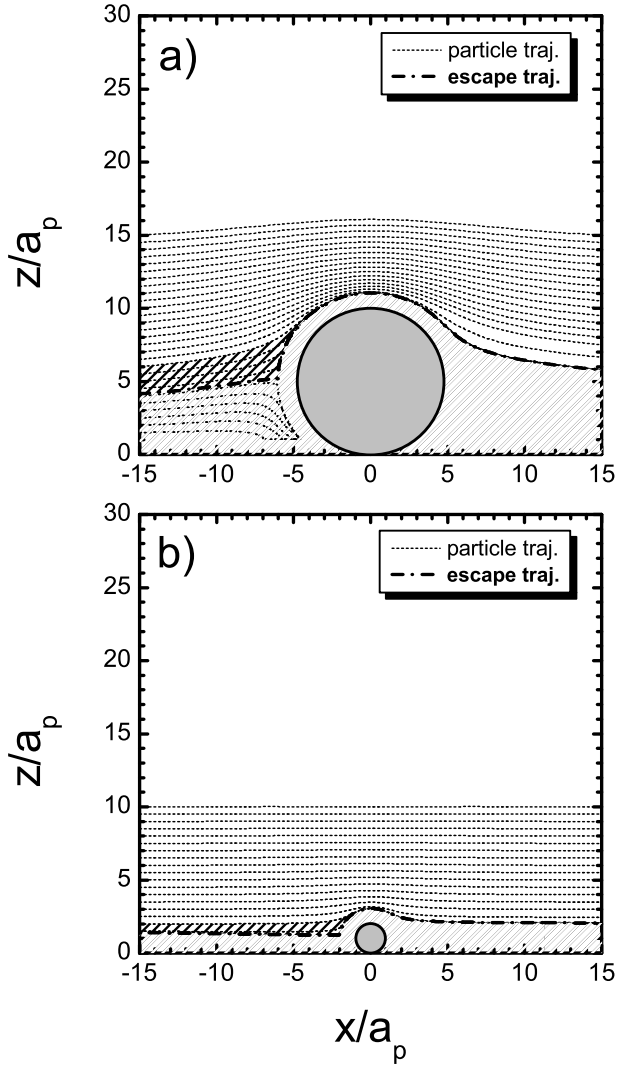

Figure 6.11: Presence of lift indicated with escape trajectories in the $x - z$ plane (highlighted with hatching) of particles under unfavourable conditions (Case UU) to deposition for the entire composite substrate (*i.e.*, single asperity with planar substrate). These trajectories are determined when the particle Peclet number is 14 for two size ratios: (a) $\lambda = 5$ and (b) $\lambda = 1$. The remaining parameters for these simulations can be found in Table 6.1.

fected by the presence of the asperity, which subsequently affects more particle trajectories near the substrate. The transport behavior depicted in Figure 6.11 is like "focusing", in which a number of trajectories at various starting heights end up with a common path downstream from the asperity. This behavior can be explained by the "shadow" effect [KE00, DKE08, vLKWP09], which occurs due to both hydrodynamic and colloidal interactions; the repulsive EDL (in these scenarios) and lubrication forces push the particles away while vdW forces pull them in, leading to focusing.

6.2.6 Effects of Particle Size

Using the same approach as what is depicted in Figure 6.6, 10000 particles are released from random positions within the semi-circular window at $x/a_p = -15$ for each Pe value. Both deterministic and Brownian forces are included in these simulations. Aside from particle size, the system parameters for the results in Figure 6.12(a) are identical to those for Case UU in Table 6.1, including $\lambda = 5$. Case UU is specifically defined as unfavourable conditions to deposition for 100 nm particles interacting with the substrate, with the height of the repulsive DLVO energy barrier at $\approx 25 k_B T$. In colloid science and related fields, it is commonly recognized that when the DLVO energy barrier is higher than $20 k_B T$, the stability of a colloidal dispersion is assured (*i.e.*, deposition cannot take place) [BBV+07]. However, the height of the barrier is dependent on the particle size, decreasing to $\approx 12 k_B T$ for 50 nm particles, $\approx 5 k_B T$ for 20 nm and $\approx 2 k_B T$ for 10 nm.

The 10 and 20 nm particles in Figure 6.12(a) clearly show the same parabolic relationships between deposition probability and particle Peclet number as those in Figure 6.8. The scatter of data points for $a_p = 50$ nm is due to the very low fraction of released particles that deposited; a parabolic relationship like that of the other two particle sizes would be seen if more particles had been released. Regardless of particle size, the peak values of ϕ_a in Figure 6.12(a) occur at $Pe \approx 0.5$, which indicates that maximum deposition occurs in the diffusion-dominated regime of particle transport. These maximum deposi-

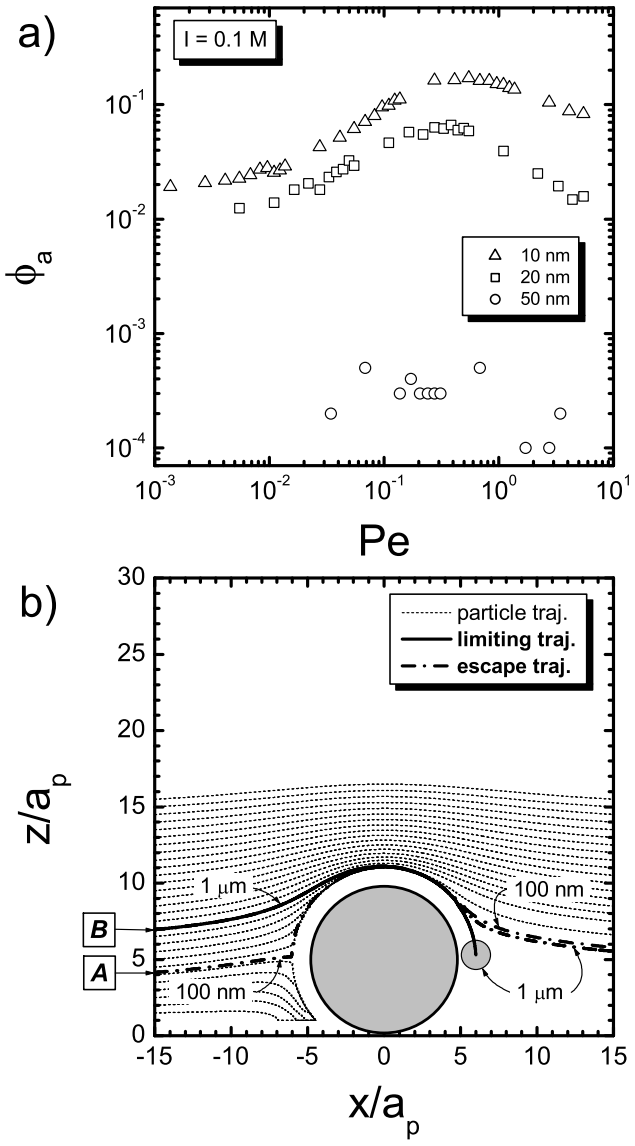

Figure 6.12: Effects of particle size on deposition when conditions for the entire composite substrate (*i.e.*, single asperity with planar substrate) are as described in Table 6.1 with a scaled Hamaker constant of 1.0. (a) Variation of deposition probability ϕ_a with particle Peclet number in the complete Brownian simulations for three particle radii: 10 nm (*hollow triangles*), 20 nm (*hollow squares*) and 50 nm (*hollow circles*). (b) Limiting and escape trajectories in the $x - z$ plane for 100 nm and 1 μm radius particles traveling across the composite substrate when the particle Peclet number is 14.

tion probabilities are ≈ 0.16 for 10 nm, ≈ 0.06 for 20 nm and < 0.001 for 50 nm. The large decline in ϕ_a for 50 nm signifies how the increased height of the repulsive barrier beyond just $10k_BT$ can influence deposition probability. When the system parameters are equal to those of Case FF in Table 6.1 (*i.e.*, scaled Hamaker constants increased from 1.0 to 5.0), the parabolic curves shift slightly upwards and to the right (toward higher Pe values) as a result of the increased strength of the attractive van der Waals interactions.

Particle transport around a single asperity under unfavourable conditions is also affected by particle size, and this can be seen with a simple trajectory analysis (*i.e.*, only deterministic forces considered). Particle Peclet number changes with particle size a_p, but the Pe value is held constant to compare trajectories for different particle sizes. According to Eq. (6.1), an increase in a_p by 10 times requires a decrease in shear rate $\dot{\gamma}$ (through U_{avg}) of 100 times. Continuing with the scenario represented in Figure 6.11(a) (*i.e.*, Case UU, $Pe = 14$), a 1 μm particle released at $x/a_p = -15$ at any height between the points labeled as A and B in Figure 6.12(b) is immobilized at the rear stagnation point of the asperity, unlike a 100 nm particle that always escapes the domain. These results indicate that a 1 μm particle can be immobilized at the asperity's rear stagnation point because it is large enough to have substantial van der Waals interactions with the asperity relative to the hydrodynamic drag forces acting on it (like what is depicted in Figure 6.5). Smaller particles ($a_p < 100$ nm) were not considered in this analysis since the van der Waals force acting on them would be too insubstantial to lead to immobilization in this convection-dominated regime. Therefore, both Figures 6.12(a) and (b) demonstrate that the effects of particle size on deposition are primarily due to the volume-based van der Waals interactions in migrational transport.

6.3 Deposition onto Arrays of Spherical Asperities

The single asperity model substrate investigated thus far can be regarded as a single unit of nanoscale roughness for a collector surface. The next step is to explore how a number of these units can influence particle transport and deposition. This includes: (i) discussions of the extent to which roughness can modify the undisturbed flow field, (ii) the effects of separation distance between asperities, and (iii) the analysis of results from simulations involving several configurations of substrate heterogeneity (physical and/or chemical) using arrays of spherical asperities. The presence of multiple asperities provides many possible system configurations for the simulation scenarios, especially when considering how the physical and chemical characteristics of each component of the substrate can be individually assigned with the PTM. A few simple situations are studied in the following sections.

6.3.1 Surface Roughness and the Undisturbed Flow Field

Before considering particle transport and deposition near arrays of asperities, the effects of roughness in the form of such arrays on the undisturbed flow field requires some discussion. Two types of roughness in the $x - z$ plane are investigated: cylindrical asperities of radius a_a (Figure 6.13a) and semi-circular corrugation with a half-amplitude of a_a (Figure 6.13b), both of which extend from $+\infty$ to $-\infty$ in the $y-$ direction. A one-dimensional (varying in the $z-$ direction), Stokesian shear flow field is applied at a substantial distance upstream, like with all systems investigated in the present study. All distances are scaled with respect to a_a, and fluid velocities are scaled with respect to the average fluid velocity in the channel U_{avg}. Figures 6.13(a) and (b) are schematic representations of the computational domains used, and therefore are not-to-scale. Nevertheless, the limits of these domains are far away from the features of heterogeneity that are centered around the origin of the Cartesian coordinate system, labeled as point O in parts (a) and (b).

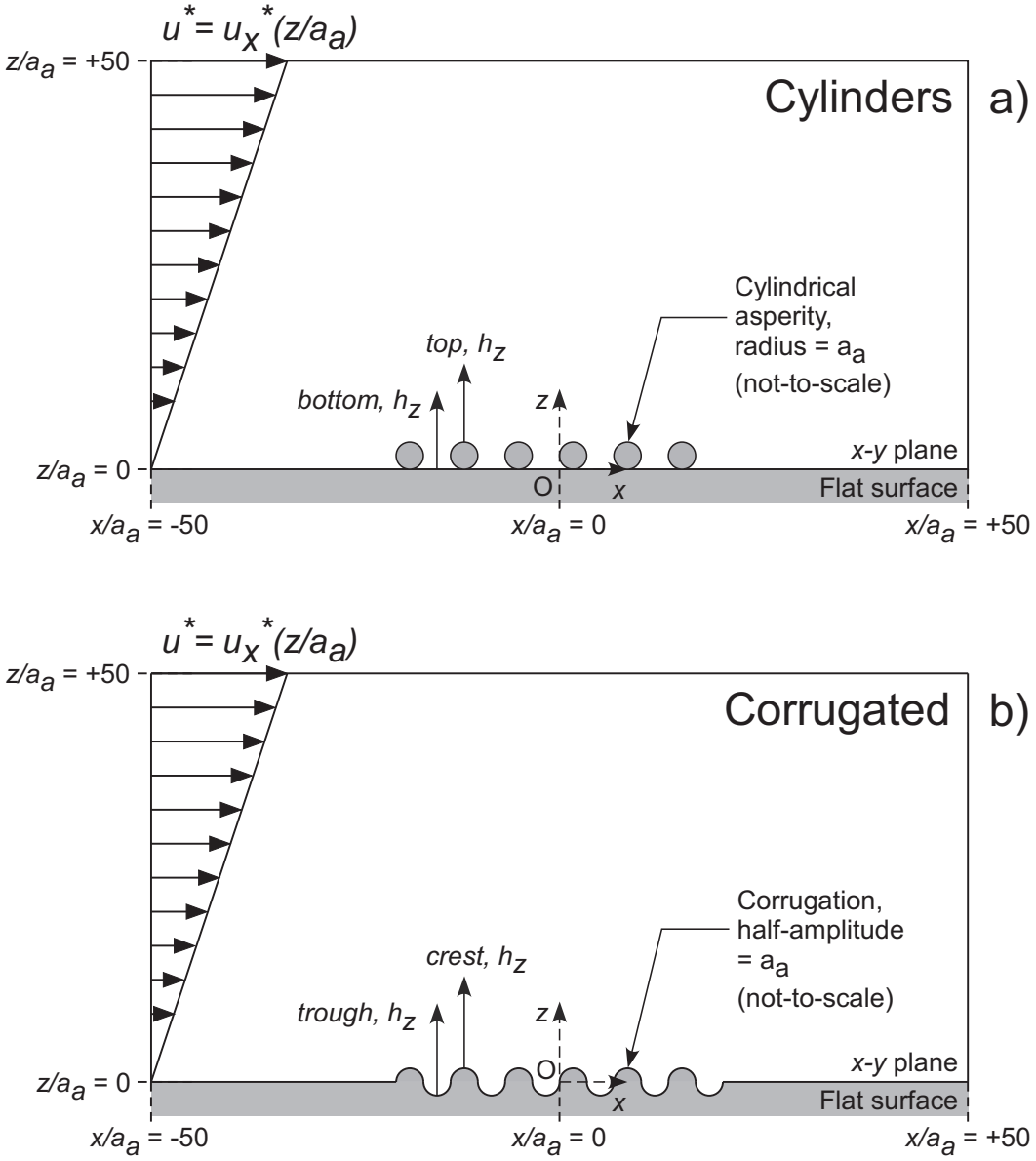

Figure 6.13: Schematics of two-dimensional computational domains in the $x - z$ plane for numerically determining the undisturbed fluid velocity fields across arrays of roughness features aligned along the $x-$ axis. Two types of roughness features, extending to $\pm\infty$ in the $y-$ direction (*i.e.*, into/out of the page) are depicted: (a) cylindrical asperities with radius a_a and (b) corrugation with half-amplitude of a_a. A one-dimensional shear flow is applied to the domain at a substantial distance upstream from the leftmost asperity. Note that these schematics are not-to-scale.

The inlet, outlet and surface boundary conditions for these simulations are identical to those described in Section 4.2.2, with the no-slip condition applied everywhere on the surface. These scenarios have only periodic arrangements of roughness features of constant height.

As Figure 2.2 portrays, the presence of asperities can modify the local undisturbed flow field from the analytical expression for one-dimensional shear flow over a smooth, flat surface, which a collector is often assumed to be. Figures 6.14(a) and (b) reveal how the (numerically-determined) scaled undisturbed fluid velocity in the $x-$ direction (u_x^*) is altered from what it would be for a flat surface ($u_{x,flat}^*$) by cylindrical asperities and corrugation, respectively. Each of the lines represents what the ratio $u_x^*/u_{x,flat}^*$ is along the $x-$ direction and at a particular height from the $x-y$ plane in the region directly above the roughness features. The ratio is always between 0 and 1, with 0 indicating the greatest modification to the flow and 1 signifying no modification (*i.e.*, the presence of the asperities does not affect the undisturbed flow). For both types of roughness studied in Figure 6.14, their effect on the flow becomes insignificant (*i.e.*, $u_x^*/u_{x,flat}^* > 0.95$) at heights of 10 times or greater than the characteristic length of the roughness ($z/a_a \geq 10.0$).

The thick solid lines in Figures 6.14(a) and (b) represent the height above the $x-y$ plane (z/a_a) that intermittently makes contact with the tops ($z/a_a = 2.0$ in part a) or crests ($z/a_a = 1.0$ in part b) of the roughness features. Both of these heights correspond to a scaled, vertical (*i.e.*, $z-$ direction) separation distance of $h_z = 2.0$ above the substrate, which is indicated with a thin, dashed line in Figure 6.15. In between the tops and crests of the features at this height, the fluid velocity is reduced from what it would be for a flat plate at the same height. This can be seen in how $u_x^*/u_{x,flat}^*$ varies with h_z along the thick dashed (bottoms of cylindrical asperities) and dash-dotted (troughs of corrugation) lines in Figure 6.15. Clearly, both types of roughness show substantial variations in fluid velocities near the surface when compared with those observed for a flat plate, and this agrees with the findings of Higdon [Hig85] and of Pozrikidis [Poz97,Poz99]. Particles that are small enough to move near, and

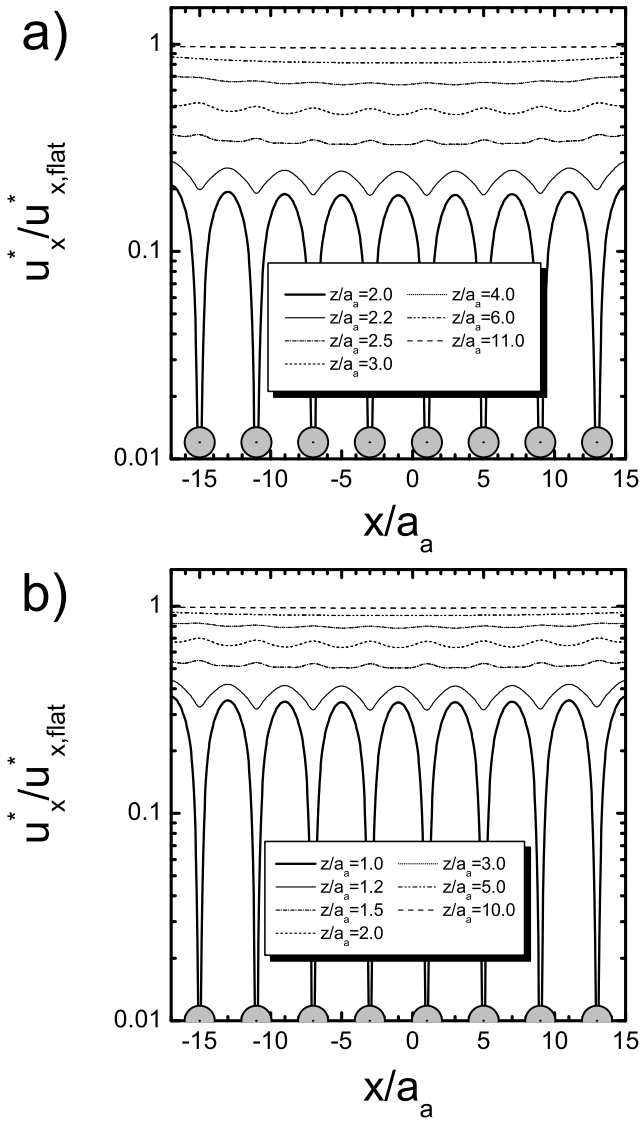

Figure 6.14: Variation in ratio of (numerically-determined) rough surface to (analytically-determined) flat surface values of the undisturbed fluid velocity in the $x-$ direction ($u_x^*/u_{x,flat}^*$) with $x-$ position for roughness features in the form of (a) cylindrical asperities and (b) corrugation. The ratios are taken at several scaled heights above the $x-y$ plane (z/a_a). The asperities themselves are shown as grey shapes or contours at the bottom of each respective figure.

perhaps between, these roughness features will have their convective transport significantly affected by the modifications to the undisturbed fluid flow caused by those features. These results reinforce the need for an accurate depiction of the undisturbed flow field near a physically heterogeneous substrate when studying particle transport and deposition for it.

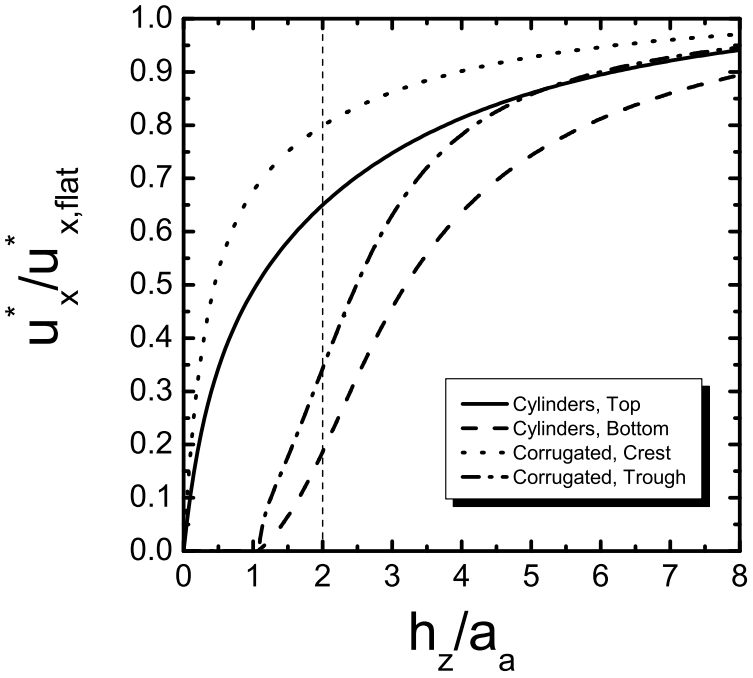

Figure 6.15: Variation in ratio of (numerically-determined) rough surface to (analytically-determined) flat surface values of the undisturbed fluid velocity in the $x-$ direction ($u_x^*/u_{x,flat}^*$) with scaled vertical separation distance from the surface (h_z/a_a). Vertical separation distances are taken from the tops and bottoms of cylindrical asperities and the crest and troughs of corrugation. The thin dashed line represents the vertical separation distance at which the top (or crest) is above the bottom (or trough) of the roughness features (= 2).

6.3.2 Trajectory Analysis - Separation between Two Asperities

The presence of more than one asperity results in some changes to particle transport and deposition on the substrate from what is observed with a single

asperity. This is primarily attributed to the modification of the local undisturbed flow field with the addition of each asperity to the substrate. A trajectory analysis is employed to demonstrate this, suppressing Brownian motion and observing the deterministic motion of particles past a pair of asperities. Like the trajectory analyses performed with the single asperity models earlier in this chapter, 100 nm particles are released from various heights in the $x-z$ plane above the flat surface at a distance of one asperity diameter ($= 2a_a$) upstream from the first asperity. The remaining system parameters are the same as those listed in Table 6.1, with the entire composite substrate being favourable to deposition (Case FF). The two asperities ($\lambda = 5$) are positioned along the $x-$ axis and therefore parallel to the direction of prevailing fluid flow. The surface-to-surface separation distance between the asperities (s) is gradually increased in Figure 6.16, with $s = 2a_a$ in part (a), $s = 4a_a$ in part (b) and $s = 6a_a$ in part (c). Once again, the particle Peclet number for all of these scenarios is 1.4.

The gap between the limiting trajectories (solid lines) for the two asperities indicates the range of heights from which a 100 nm particle can be released and subsequently deposited on the second (downstream) asperity. This gap is rather narrow for all three spacings, equal to less than one particle radius. From within gap, there are intermediate trajectories (dashed lines) along which a particle travels very close to the first asperity but escapes its pull and continues on to be deposited on the second asperity. Therefore, considering only deterministic forces, Figure 6.16 reveals that a small increase in the particle's release height can lead to markedly different locations for deposition on such a physically heterogeneous substrate. As the asperities are placed further apart, the minimum height reached by the intermediate trajectory drops lower from $z/a_p \approx 7.5$ for $s = 2a_a$ (Figure 6.16a) to $z/a_p \approx 5.5$ for $s = 6a_a$ (Figure 6.16c). Simulations involving greater separation of the asperities ($s > 6a_a$) were performed but yielded no significant change in the local minimum for the intermediate trajectory. This implies that particles cannot deposit on the flat surface between the two asperities in this arrangement without Brownian mo-

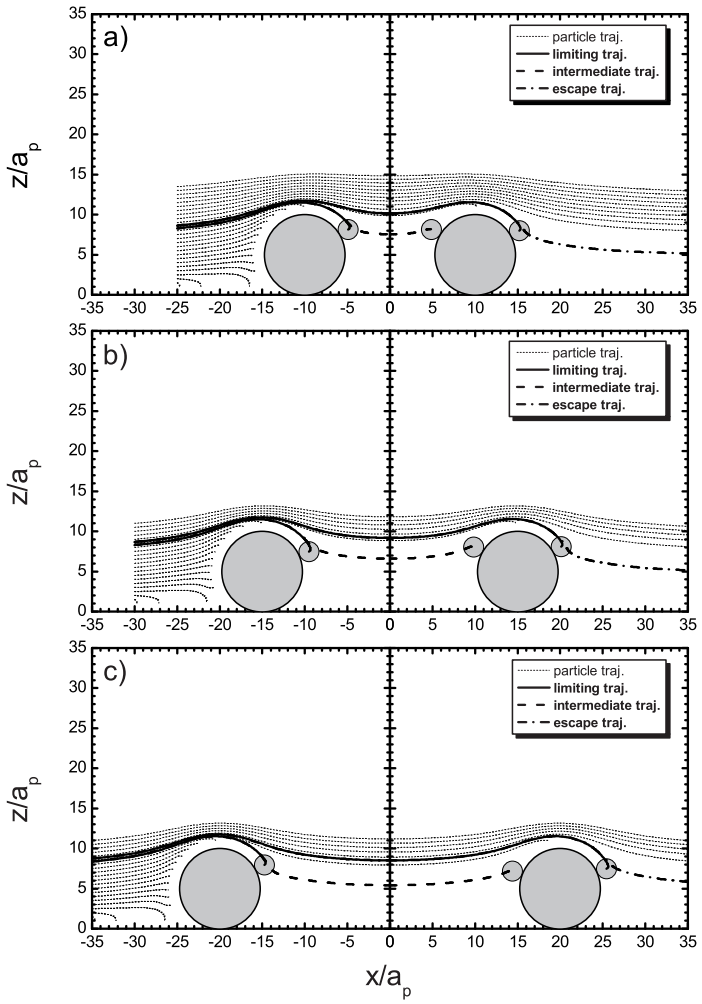

Figure 6.16: Limiting, intermediate and escape trajectories in the $x-z$ plane of particles under favourable conditions (Case FF) to deposition for the entire composite substrate (*i.e.*, two asperities with planar substrate) at various separation distances between asperities. These trajectories are determined when the particle Peclet number is 1.4 and size ratio $\lambda = 5$ for three separation distances: (a) $s = 2a_a$, (b) $s = 4a_a$ and (c) $s = 6a_a$. The remaining parameters for these simulations can be found in Table 6.1.

tion. Lowering the particle Peclet number by reducing the shear rate (*i.e.*, less contribution of convection to particle motion) would enable particles to reach this region.

Since the asperities have the same height and shape in these scenarios, the upstream asperity blocks the downstream one. Without migrational transport via DLVO interactions, the blocking would be complete (*i.e.*, no interception of particles by the downstream asperity). The van der Waals interactions make it possible for a particle to deposit on the second asperity, with the first asperity attracting it closer to the composite substrate. It is reasonable to assume that with each asperity added downstream along the $x-$ axis from this pair, the height of the gap between the limiting trajectories for the first and last asperities would increase as well, thereby pulling more particles down to deposit on the substrate. The increase in height would depend on the strength of the van der Waals interactions (*i.e.*, Hamaker constant for this model) and the particle Peclet number (*i.e.*, shear rate).

6.3.3 Arrays of Asperities - Chemically-Uniform Substrate

This section explores the deposition of spherical, Brownian particles suspended in a Stokesian fluid undergoing simple shear flow onto a model substrate that is chemically-uniform but physically heterogeneous. The model substrate is designed as a planar base with a periodic array of spherical protrusions (asperities) extending into the fluid. Two arrangements of the asperities are investigated: in-line and staggered arrays relative to the direction of the shear flow in the $x-$ direction. The entire composite substrate is favourable to deposition (Case FF) and all other physical and chemical conditions are as described in Table 6.1. In this section and for the remaining simulations in this chapter, the asperities are spaced apart a distance of $s = 2a_a$ from each other. This separation distance is sufficient so that particle-substrate hydrodynamic interactions are clearly dictated by the nearest feature of the substrate to the particle at a given position. Such spacing also permits a substantial number of

asperities (12 to 16) to be placed within the computational domain that was chosen for this part of the study.

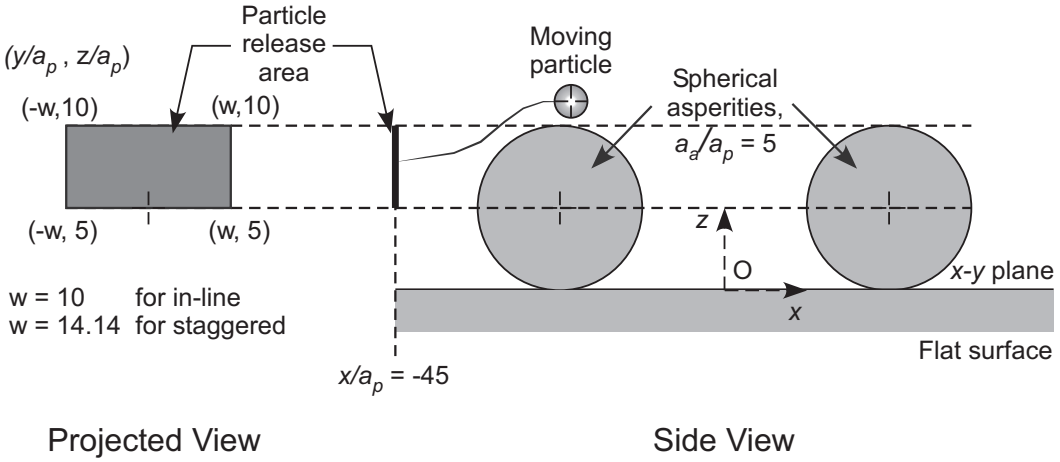

Figure 6.17: Deposition onto a planar substrate containing an array of spherical asperities. Schematic showing the rectangular window from which the particles are released randomly into the domain containing an array of spherical asperities (*i.e.*, $a_a = 5a_p$, or $\lambda = 5$).

Figure 6.17 describes some aspects of the model substrates, and Figures 6.18 and 6.19 show the results of some simulations of particles flowing through both types of arrays of asperities. In each simulation, N particles are released one at a time from random positions within a rectangular window in the $y - z$ plane located at $x/a_p = -45$, shown schematically in Figure 6.17. The particles are released into a domain measuring $80a_p \times 80a_p \times 20a_p$ containing an array of spherical asperities ($\lambda = 5$). This domain has a one-dimensional shear flow across it, moving from left to right in the positive $x-$ direction. From the top view of the substrate, the in-line and staggered array configurations are shown in Figures 6.18(a) and (b), respectively. The staggered array is essentially the in-line array rotated 45° in the $x - y$ plane with respect to the shear flow. For each array, the width of the sub-domain spanned by the window described in Figure 6.17 is periodic in the $y-$ direction, and is indicated by the corresponding transparently-shaded region. To have the same particle flux through this window for both types of arrays, the total number of particles released is varied: for the in-line array, $N = 1000$; for the staggered

array, $N = 1414$. The rectangular sub-domain is also one asperity radius in height and its base is situated one asperity radius above the planar substrate. In all of these simulations, colloidal, hydrodynamic and Brownian forces are considered simultaneously.

Figures 6.18(a) and (b) depict the endpoints of particles that have been adsorbed within the domain when the particle Peclet number is 1.4. For both configurations of asperities in Figures 6.18(a) and (b), the majority of the particles that come to rest within the domain deposit on the asperities. Particle attachment is quite deterministic and mainly clustered within the transparently-shaded, particle release sub-domain due to the dominance of the attractive migration forces. At first glance, an interesting observation from these figures is the tendency of particles to deposit on the "peaks" or upper hemispherical regions of the asperities as opposed to the planar portion of the composite substrate. For the staggered array (Figure 6.18b), a large proportion of the particles deposit on the peaks of the two central asperities (*i.e.*, on the $x-$ axis). This is primarily due to their location in the domain, essentially blocking the shear flow so that many of the released particles travel within their vicinity. These central asperities have approximately the same number of particle endpoints (and hence, roughly equal deposition probabilities), even though the downstream asperity is blocked by the upstream one. This can be explained by the attractive migration forces in this scenario, which pull the particles closer to the substrate as they flow through the domain, sometimes depositing further downstream on the planar regions as well as the asperities.

Much like Figure 6.8, Figure 6.19(a) looks at the relationship between the deposition probability of all of the asperities within the domain, ϕ_a, and the particle Peclet number Pe. For both configurations, ϕ_a starts from a plateau, with the in-line arrangement (*symbol:* filled square) at 0.45, which is slightly higher than for the staggered arrangement (*symbol:* hollow square). However, as Pe increases, the two curves converge, following a downward trend as convective forces dominate. Therefore, there is nothing to distinguish the deposition probability of one configuration from the other when hydrodynamic

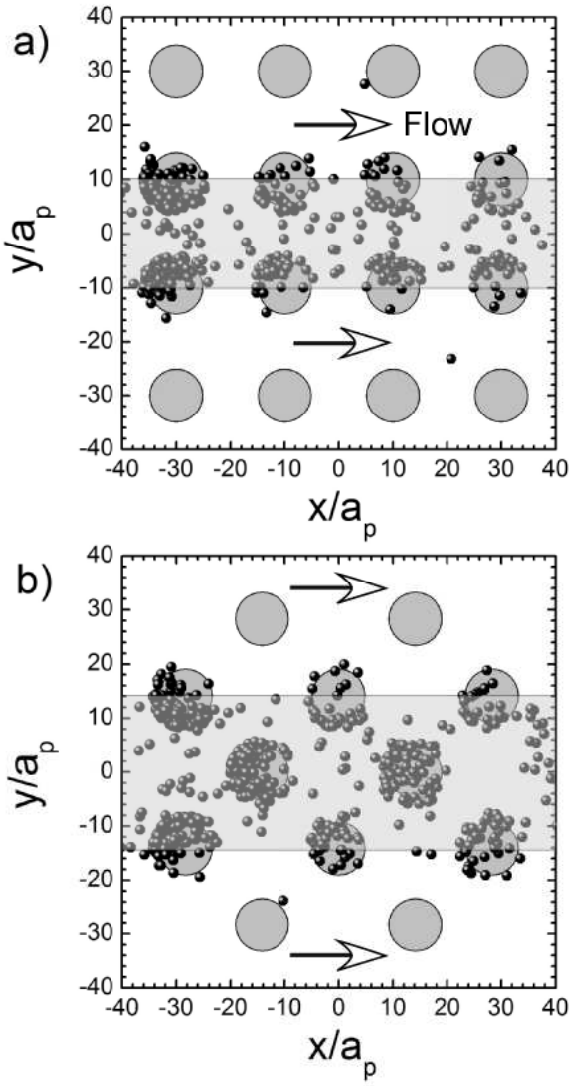

Figure 6.18: Deposition onto a planar substrate containing an array of spherical asperities aligned parallel to the shear flow (in-line) and at an angle of 45° (staggered) relative to the shear flow. Trajectories are computed employing the complete Brownian simulations in the presence of favourable (FF) conditions. (a) and (b): Top views of the substrate, showing capture locations (trajectory endpoints shown as small, dark spheres) for the in-line and staggered arrays, respectively, of the asperities (large gray circles) when the particle Peclet number is 1.4. The arrows in each graph indicate the flow direction, and the rectangular, transparently-shaded region indicates the width of the particle release window. All other parameters are as shown in Table 6.1.

interactions become substantial.

Since the vast majority of studies of deposition phenomena have involved smooth surfaces, it would be appropriate to compare the deposition probabilities of rough surfaces with those of smooth, flat surfaces using the PTM. For an equal comparison at all values of Pe, 1000 particles are released from within the same window as with the rough substrate bearing the in-line array of asperities. The total deposition probability for the rough and flat versions of the substrate are defined respectively as

$$\phi_T = \frac{\text{Number of particles deposited on rough substrate}}{\text{Number of particles released}} \tag{6.3}$$

$$\phi_{flat} = \frac{\text{Number of particles deposited on flat substrate}}{\text{Number of particles released}} \tag{6.4}$$

The ratio ϕ_T/ϕ_{flat} provides a means of comparing the particle deposition probability of a section of a surface when it is rough (*i.e.*, with spherical asperities, in this study) to when it is smooth and flat. This ratio is always greater than 1.0 since the rough versions of the domain in this study have larger available surface areas for deposition than the flat version.

For the range of Pe values shown in Figure 6.19(b), ϕ_T/ϕ_{flat} follows the same trend for both the in-line and staggered configurations of asperities, slowly increasing from about 1.2 at $Pe = 0.14$ to nearly 8.0 at $Pe = 5.6$. First of all, this signifies that models using flat surfaces underestimate the deposition probability of real surfaces. The presence of asperities enhances deposition probability, and this enhancement increases as convective forces come to dominate. It also reveals that the orientation of an ordered array of asperities with respect to the direction of prevailing hydrodynamic flow is not necessarily a factor to consider for encouraging or discouraging Brownian particle deposition on a rough surface.

6.3.4 Arrays of Asperities - Chemical Heterogeneity Through van der Waals Interactions

Thus far, the composite substrate has been physically heterogeneous but chemically-uniform. One way to introduce chemical heterogeneity into the model sub-

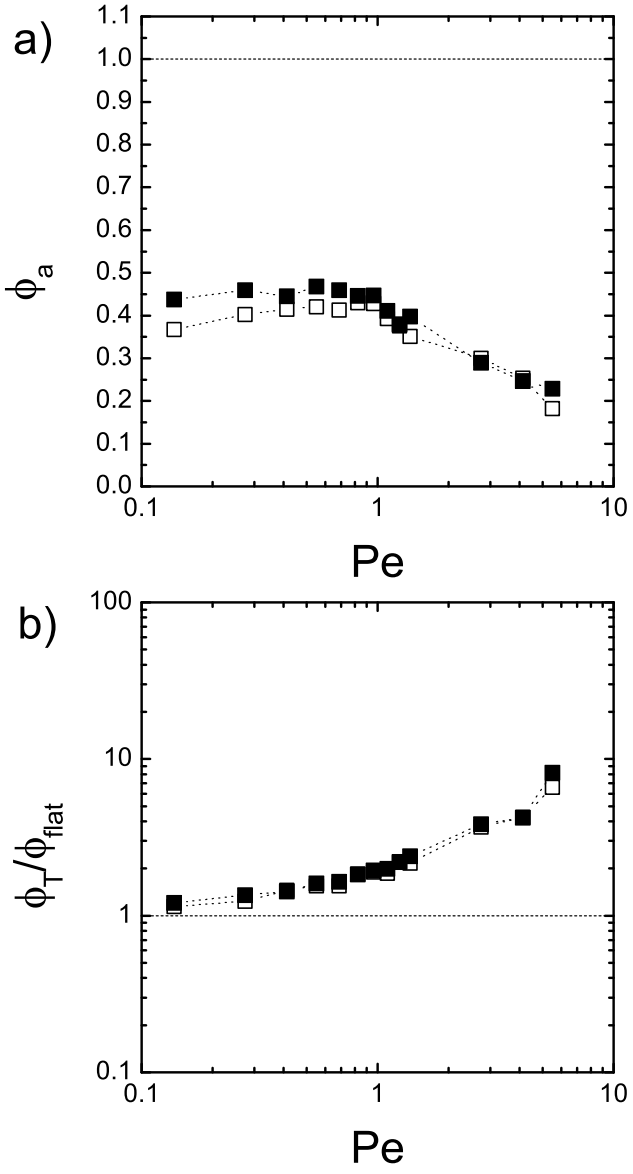

Figure 6.19: Deposition probabilities for a planar substrate containing an array of spherical asperities aligned parallel to the shear flow (in-line) and at an angle of 45° (staggered) relative to the shear flow. Complete Brownian simulations in presence of favourable (FF) conditions are performed for the two configurations of asperities, and the results are shown with the following symbols: *filled square* = in-line array; *hollow square* = staggered array. (a) Variation of deposition probability on the asperities ϕ_a with particle Peclet number. (b) Variation of the deposition probability ratio ϕ_T/ϕ_{flat} (surface with asperities vs. flat surface) with particle Peclet number. All parameters are as shown in Table 6.1.

strate is to vary its chemical composition by assigning individual Hamaker constants to each component of the substrate. In this study, only two values of Hamaker constant are used, with one for the asperities and the other for the flat surface. Using the basic system configuration parameters in Table 6.1 as the standard, Table 6.2 shows the scaled Hamaker constants for three scenarios that are investigated: Cases #1, #2 and #3. With these cases, the particle's surface potential has been changed to −50 mV, and the higher scaled Hamaker constant of 5.0 indicates favourable conditions to deposition according to DLVO theory.

Table 6.2: System parameters altered from those of the basic system configuration listed in Table 6.1 and used with the PTM simulations for Cases #1 to #12. The electrolyte concentration for all cases listed is 10^{-1} M, except for Cases #10 and #11 for which it is 10^{-3} M.

Case	**Scaled Hamaker constant**		**Surface potential**		
	Particle-Asperity	**Particle-Flat surface**	**Particle**	**Asperities**	**Flat surface**
	$A_{H,pa}/(k_BT)$	$A_{H,ps}/(k_BT)$	ψ_p	ψ_a	ψ_s
	–	–	**mV**	**mV**	**mV**
#1	1.0	5.0	−50	−25	−25
#2	5.0	1.0	−50	−25	−25
#3	5.0	5.0	−50	−25	−25
#4	1.0	1.0	−25	−25	+50
#5	1.0	1.0	−25	+25	−50
#6	1.0	1.0	−25	−50	+25
#7	1.0	1.0	−25	+50	−25
#8	1.0	1.0	−75	−25	+25
#9	1.0	1.0	−75	+25	−25
#10	1.0	1.0	−75	−25	+25
#11	1.0	1.0	−75	+25	−25
#12	1.0	1.0	−25	+25	−75

Figures 6.20 and 6.21 display the results of simulations of particles flowing through past a substrate with the in-line array of asperities for the three cases described above. The dimensions of the domain and the application

of a one-dimensional shear flow (moving left to right, in the positive $x-$ direction) upstream from the asperities are identical to that of the scenario in Figure 6.18(a). In each simulation (*i.e.*, for each Pe value for each case), 10000 particles are released one at a time from random positions within a rectangular window in the $y-z$ plane located at $x/a_p = -45$, as previously described for the in-line arrangement of asperities in Figure 6.17. Colloidal, hydrodynamic and Brownian forces are included in all of these simulations.

Figure 6.20 shows the endpoints of particle trajectories from top views of the substrate at three different Pe values for Cases #1 (parts a, b and c) and #2 (parts d, e and f). The particle Peclet values included are 0.14 (parts a and d), 1.4 (parts b and e) and 5.6 (parts c and f). Of course, Figure 6.20 simply depicts that the regions where the particles tend to deposit depends on which portion of the composite substrate is favourable to deposition. However, these pictures provide information about particle transport near these asperities under these chemically heterogeneous conditions. At $Pe = 0.14$ in both cases, diffusion-dominated particle transport carries many particles to regions beyond the dimensions of the release window in the $y-$ direction ($y/a_p = \pm 10$, shown by the transparently-shaded sub-domain in Figure 6.18a). Specifically in Case #2 (Figure 6.20d), peripheral asperities centered at $y/a_p = \pm 30$ have several particles deposited on them, mainly situated at mid-height of the asperities (*i.e.*, mid-plane of the roughness; $z/a_p = 5$ in these scenarios). As the shear rate increases for this case (Figures 6.20e and f), particles are less likely to deposit on the peaks of the central asperities and the peripheral asperities all-together. The particles experience greater increases in fluid drag as their height above the flat surface increases, overwhelming migrational (primarily van der Waals) forces around the peak of asperities. They also pass more directly through the domain, with less excursions to peripheral regions via Brownian motion, making it more difficult for particles to deposit.

It may appear from Figure 6.20 that more particles deposit on the flat surface than on the asperities for all Pe values. It is important to point out that these top views of the substrate are probability maps, indicating

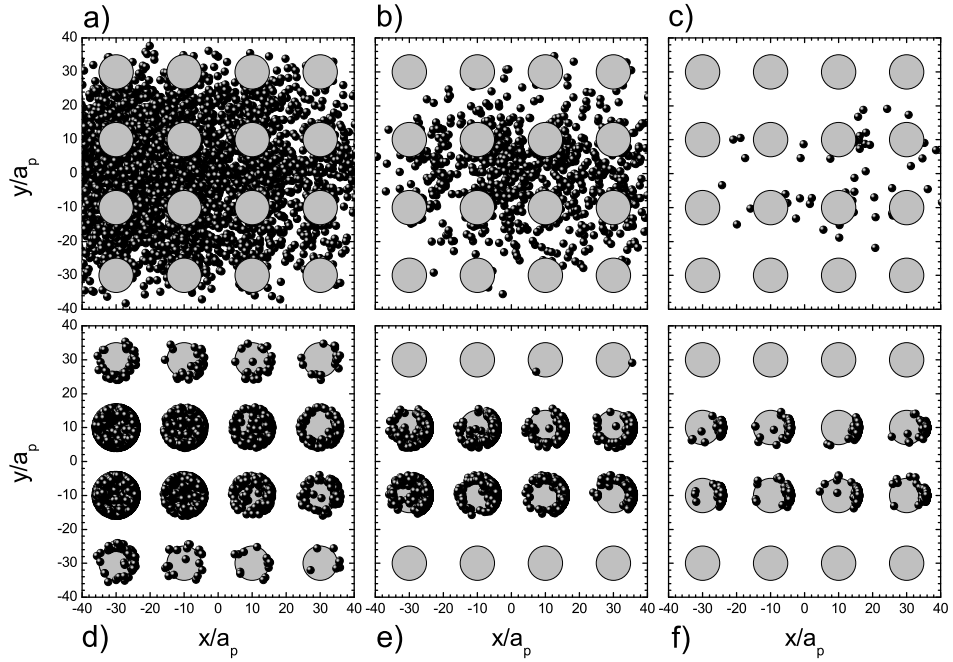

Figure 6.20: Deposition onto a planar substrate containing an in-line array of spherical asperities (large gray circles) with chemical heterogeneity through van der Waals interactions (*i.e.*, scaled Hamaker constants). Trajectories are computed employing the complete Brownian simulations for two scenarios described in Table 6.2: Cases #1 (a, b and c) and #2 (d, e and f). Top views of the substrate, showing capture locations (trajectory endpoints shown as small, dark spheres) when the particle Peclet number is 0.14 (a and d), 1.4 (b and e) and 5.6 (c and f). All other parameters are as shown in Table 6.1.

where particles will most likely deposit. With Case #1, the asperities promote hydrodynamic dispersion, scattering the particles across most of the substrate in the computational domain, as Figures 6.20(a), (b) and (c) depict. On the other hand, Case #2 promotes accretion and order, as diffusion (Figure 6.20d) and convection (Figures 6.20e and f) bring particles close to the asperities where van der Waals interactions can draw them in to deposit there.

In Figure 6.21(a), the total deposition probability of the composite substrate ϕ_T is lower when the flat surface is favourable than when the asperities are. For Case #1, ϕ_T starts at ≈ 0.36 for $Pe = 0.14$ and falls to almost zero when Pe reaches 14, but for Case #2, it starts at ≈ 0.62 and drops to ≈ 0.12.

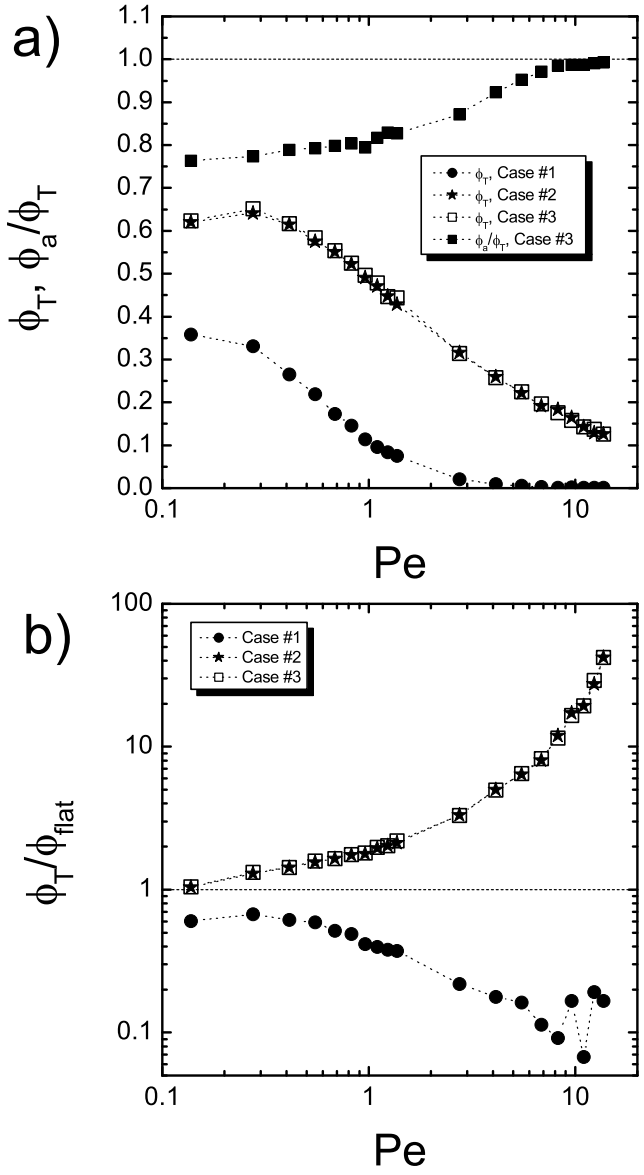

Figure 6.21: Deposition probabilities for a planar substrate containing an in-line array of spherical asperities with chemical heterogeneity through van der Waals interactions. Complete Brownian simulations are performed for three scenarios described in Table 6.2: Cases #1 (*filled circles*), #2 (*filled stars*) and #3 (*hollow and filled squares*). (a) Variation of total deposition probability for the entire composite substrate ϕ_T (and asperities-to-total probability ratio ϕ_a/ϕ_T) with particle Peclet number. (b) Variation of the deposition probability ratio ϕ_T/ϕ_{flat} (surface with asperities vs. flat surface) with particle Peclet number. All other parameters are as shown in Table 6.1.

Lower probabilities can be expected for Case #1 since the release window for the particles is situated at the same range of heights as the top halves of the asperities; the particle trajectories start at a substantial distance above the flat surface. However, as Pe increases within the range tested, the exchange between diffusion-dominated and convection-dominated transport makes virtually no difference in ϕ_T for Cases #2 (filled stars) and #3 (hollow squares). This is quite remarkable when considering how much the ratio ϕ_a/ϕ_T (*i.e.*, deposition probability for the asperities over that of the total substrate) changes for Case #3, which shown with filled squares in Figure 6.21(a). Starting at ≈ 0.75 for $Pe = 0.14$, ϕ_a/ϕ_T rises to almost 1.0 at $Pe = 14$ for this chemically-uniform substrate. This occurs because at low Pe values (< 1), the particles deposit wherever it is favourable, led mostly by Brownian motion. As Pe increases into the convection-dominated regime, the particles deposit on the closest substrate features in their travels, which are the asperities.

Deposition probabilities for the rough substrate (ϕ_T) are compared with that of a flat substrate (ϕ_{flat}) of equal size and chemical characteristics in Figure 6.21(b). Similar to results shown in Figure 6.19(b), the ratio ϕ_T/ϕ_{flat} increases gradually with Pe (from ≈ 1 at $Pe = 0.14$ to ≈ 45 at $Pe = 14$) for Cases #2 and #3. This reiterates the earlier assertion that roughness in the form of favourable asperities increases the chances of particles depositing on the substrate. To the contrary, Case 1 has a decline in ϕ_T/ϕ_{flat} from 0.6 down to ≈ 0.1. Under these circumstances, the particles have a higher likelihood of depositing on the flat substrate than the rough one. In this case, the unfavourable asperities are preventing some of the substrate's surface area from being available for deposition.

6.3.5 Arrays of Asperities - Chemical Heterogeneity Through EDL Interactions

Two system parameters in this study that can be manipulated and measured to some extent in experimental settings are surface potential and electrolyte concentration (*i.e.*, solution ionic strength). Surface modification by applying

coatings of functionalized molecules (*e.g.* alkanethiols and silanes) can alter surface potentials in a somewhat controlled manner (*i.e.*, positive charge versus negative charge), and adjusting solution ionic strength of a test fluid such as water is a routine laboratory task. These two EDL interaction parameters help to determine if a surface is favourable or unfavourable to deposition, so it is appropriate to explore the effects of changing these parameters on deposition probabilities for a composite substrate with several spherical asperities.

From the perspective of EDL interactions, chemical heterogeneity in the model substrate is achieved through variations in surface potential (or charge, though it is not explicitly considered in the present study) for the different substrate components (*i.e.*, the asperities and the flat surface). Table 6.2 lists the surface potentials and other parameters altered from those of Table 6.1 for all of the scenarios considered in this analysis: Cases #4 to #12. However, unlike with Cases #1 to #3 in Table 6.2 and Section 6.3.4, a portion of the substrate is regarded as favourable to deposition if its surface potential is of opposite sign to that of the particle. The scaled Hamaker constant for the entire substrate is kept constant at 1.0, and the solution ionic strength is 10^{-1} M for all but Cases #10 and #11, for which it is 10^{-3} M. The domain size, substrate configuration (in-line array of asperities) and particle release window are the same as with Section 6.3.4. For a range of 19 Pe values with each scenario, each simulation involves the release of 10000, 100 nm particles, one at a time, with both deterministic and Brownian motion included.

Figure 6.22 displays top views of the composite substrate with particle trajectory endpoints for the same Pe values (0.14, 1.4 and 5.6) as in Figure 6.20 for Cases #8 (parts a, b and c) and #9 (parts d, e and f). In this example, the surface potentials of the asperities and the flat surface are equal (25 mV) but opposite in sign from each other. A comparison of Figures 6.20 and 6.22 shows that they are qualitatively very similar, with both clearly distinguishing deposition on the flat surface from that on the asperities. Minor differences in distributions of endpoints between these two figures can be attributed to how the corresponding DLVO energy curves (for the favourable regions) reach

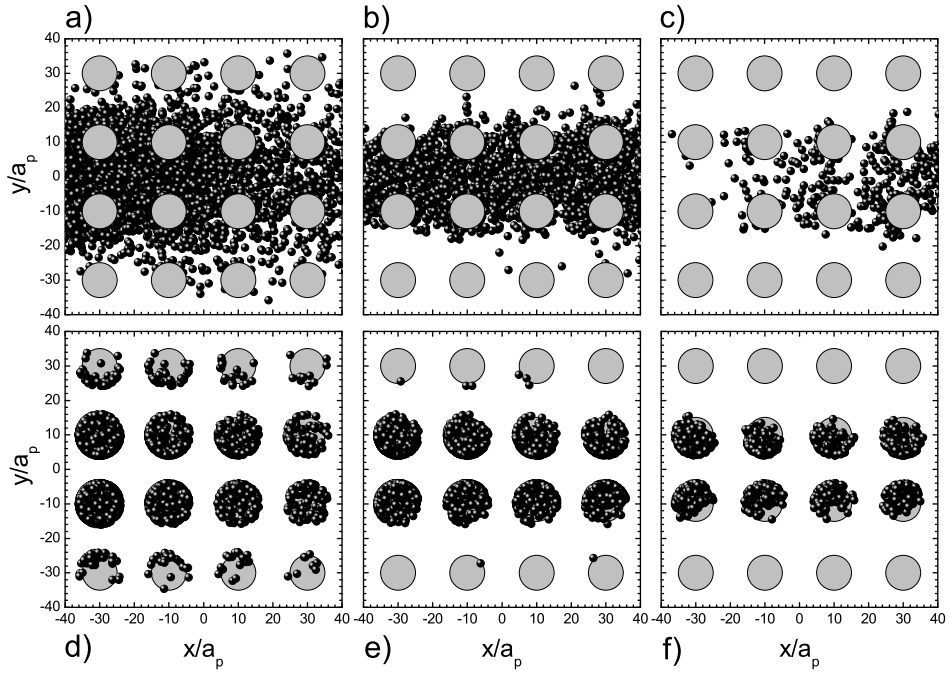

Figure 6.22: Deposition onto a planar substrate containing an in-line array of spherical asperities (large gray circles) with chemical heterogeneity through EDL interactions (*i.e.*, surface potentials). Trajectories are computed employing the complete Brownian simulations for two scenarios described in Table 6.2: Cases #8 (a, b and c) and #9 (d, e and f). Top views of the substrate, showing capture locations (trajectory endpoints shown as small, dark spheres) when the particle Peclet number is 0.14 (a and d), 1.4 (b and e) and 5.6 (c and f). All other parameters are as shown in Table 6.1.

their primary minimums as the scaled separation distance H decreases.

Holding the solution ionic strength of the system constant at 10^{-1} M, Figure 6.23 depicts the variations in total deposition probability ϕ_T with Pe for Cases #4 to #9 inclusive. Table 6.2 defines the surface potentials of the substrate components for these cases, with ψ_a and ψ_s between -50 mV and $+50$ mV. However, this range can be expanded to ± 75 mV with the inclusion of Cases #8 and #9; it can be seen from Eq. (4.34) that the EDL force remains the same if surface potential magnitudes are switched between those of the particle and, for instance, the flat surface (*i.e.*, Case #9 = Case #12).

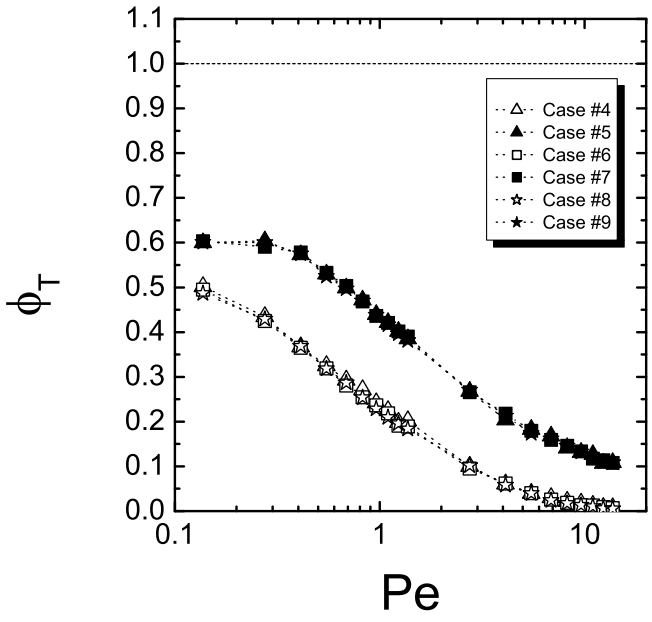

Figure 6.23: Deposition probabilities for a planar substrate containing an in-line array of spherical asperities with chemical heterogeneity through EDL interactions (*i.e.*, surface potentials). Complete Brownian simulations are performed for six scenarios described in Table 6.2: Cases #4 (*hollow triangles*), #5 (*filled triangles*), #6 (*hollow squares*), #7 (*filled squares*), #8 (*hollow stars*) and #9 (*filled stars*). Variation of total deposition probability for the entire composite substrate ϕ_T with particle Peclet number. All other parameters are as shown in Table 6.1.

These six scenarios are divided into two groups in Figure 6.23: those with the flat surface favourable to deposition (*i.e.*, hollow triangles, squares and stars) and those with favourable asperities, (*i.e.*, filled triangles, squares and stars). For each group, the data points for three different configurations of surface potentials on the composite substrate essentially lie on top of each other. This signifies that when particular regions of the substrate are favourable to deposition, the surface potential of those regions has no bearing on the deposition probability. This remains true when the ionic strength is reduced to 10^{-3} M, but these results are not included in Figure 6.23 for the sake of clarity.

The effects of changing solution ionic strength on deposition probability are

shown with Cases #8 to #11 (refer to Table 6.2) in Figure 6.24. With system parameters the same as those in Table 6.1, the solution ionic strength is tested at two levels: 10^{-1} M (Cases #8 and #9) and 10^{-3} M (Cases #10 and #11). On the basis of DLVO theory, a diminished ionic strength extends the length of significant EDL interaction (*i.e.*, inverse Debye length), therefore attracting or repelling particles at a greater separation distance from the substrate. When the asperities are favourable, ϕ_T is increased by 0.05 to 0.10 for the range of Pe values tested as the ionic strength is reduced (from filled stars to filled circles in Figure 6.24a). This agrees with what is expected from DLVO theory. Contrary to this, there is a small decrease in ϕ_T (of 0.02 to 0.04) when the flat surface is favourable over the same Pe range as ionic strength is reduced (from hollow stars to hollow circles in Figure 6.24a). This small decrease in ϕ_T occurs because the unfavourable asperities are, to some extent, impeding the transport of particles to the flat surface. The lower ionic strength not only increases the range of attraction to the flat surface, but the range of repulsion from the asperities as well. Consequently, the increased range of repulsion also reduces the area available for particle deposition on the flat surface, as Figure 6.25 (part a = Case #8; part b = Case #10) demonstrates at $Pe = 1.4$. In both parts of this figure, the large, thin circles represent the "shadows" of the spherical asperities on the flat surface. With high ionic strength making the inverse Debye length very thin, Figure 6.25(a) has particles depositing within these circles, indicating that they are located in the wedge region where the spherical asperity contacts the flat surface. In Figure 6.25(b), no particles deposit in positions overlapping the shadow regions because of the increased thickness of the repulsive EDL barrier around the asperities.

As Figure 6.24(b) shows, the ratio ϕ_T/ϕ_{flat} increases with Pe when the asperities are favourable (filled symbols; Cases #9 and #11) in a similar manner as with both array configurations in Figure 6.19(b) and Cases #2 and #3 in Figure 6.21(b). When the flat surface is favourable to deposition (hollow symbols; Cases #8 and #10), the increase in ϕ_T/ϕ_{flat} is much smaller, rising from ≈ 0.80 at $Pe = 0.14$ to ≈ 4 at $Pe = 14$. Under these conditions, the

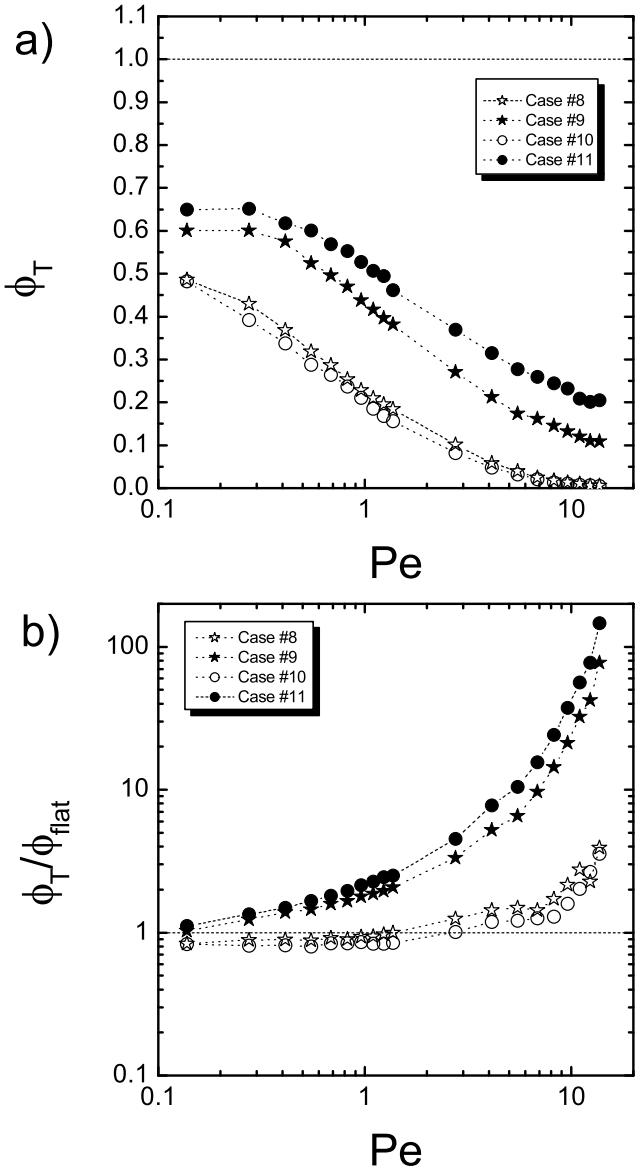

Figure 6.24: Deposition probabilities varying with solution ionic strength for a planar substrate containing an in-line array of spherical asperities with chemical heterogeneity through EDL interactions. Complete Brownian simulations are performed for four scenarios described in Table 6.2: Cases #8 (*hollow stars*), #9 (*filled stars*), #10 (*hollow circles*) and #11 (*filled circles*). (a) Variation of total deposition probability for the entire composite substrate ϕ_T with particle Peclet number. (b) Variation of the deposition probability ratio ϕ_T/ϕ_{flat} (surface with asperities vs. flat surface) with particle Peclet number. All other parameters are as shown in Table 6.1.

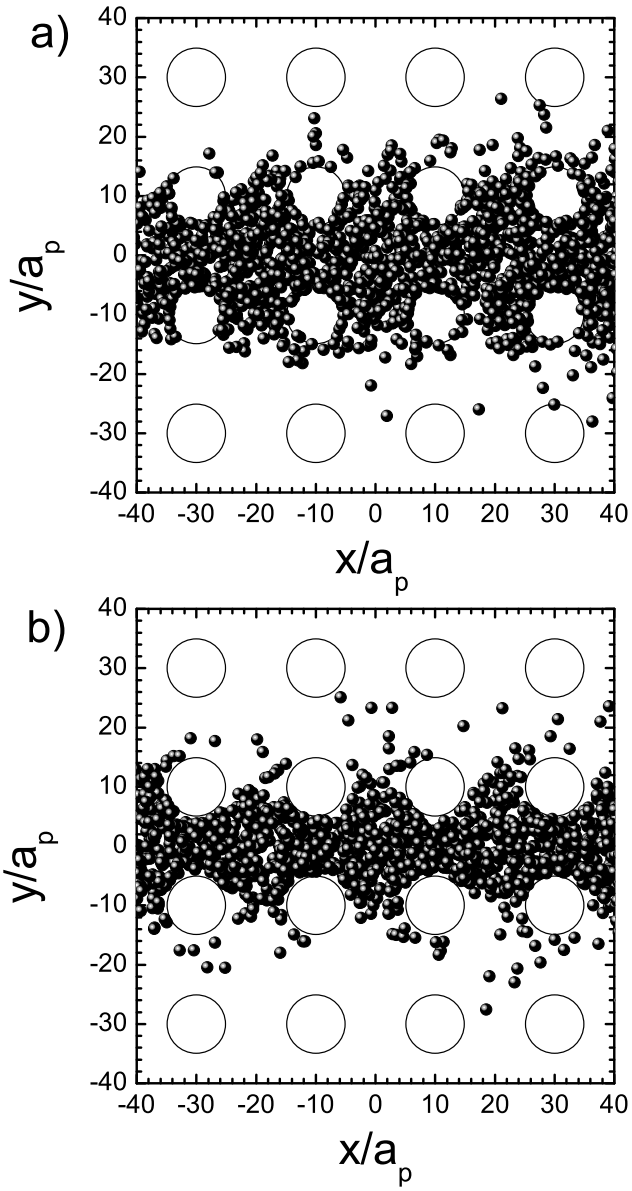

Figure 6.25: Deposition onto a planar substrate containing an in-line array of spherical asperities (large hollow circles) with chemical heterogeneity through EDL interactions (*i.e.*, surface potentials). Trajectories are computed employing the complete Brownian simulations for two scenarios described in Table 6.2: Cases #9 (a) and #11 (b), with solution ionic strengths of 10^{-1} M and 10^{-3} M, respectively. Top views of the substrate, showing capture locations (trajectory endpoints shown as small, dark spheres) when the particle Peclet number is 1.4. All other parameters are as shown in Table 6.1.

flat surface has higher probability for deposition in the diffusion-dominated regime, but in the convection-dominated regime, the rough surface is higher. This draws attention to how the presence of both physical and chemical heterogeneity can make substrates more or less likely to have particles deposit on them, depending on the interplay between convective, diffusional and migrational transport mechanisms.

For any charged solid surface, the measured value of its surface potential represents the average electrokinetic charge of the entire surface [ENKR00]. This average value does not explicitly account for the presence of local charge heterogeneity, so it can be somewhat misleading when interpreting the results of deposition experiments in the context of DLVO theory. Table 6.3 includes two cases of local surface charge (and hence, potential) heterogeneity on the model substrate depicted in the top views of Figure 6.22. The average surface potential ψ_{avg} for each case is determined using surface area weighting of the asperities and the flat surface within the limits of the computational domain. For $\lambda = 5$ in these scenarios, this results in

$$\psi_{avg} = (0.44)\psi_a + (0.56)\psi_s. \tag{6.5}$$

Using a scaled Hamaker constant of 1.0 for the entire substrate and the remaining system parameters from Table 6.1, Cases #9 and #12 have identical DLVO force curves for the particle approaching either part of the substrate. Using the corresponding average surface potential in each scenario (-3 mV for Case #9; $\psi_{avg} = -31$ mV for Case #12) and assuming the surface to be flat, this "smeared out" perspective of the substrate's surface properties leads to different expectations on the basis of DLVO theory. For the averaged version of Case #9, the lack of a repulsive barrier would lead one to expect unhindered deposition across the entire substrate, which is not the case for the flat surface in the same figures. Conversely for the averaged version of Case #12, there is a repulsive DLVO energy barrier of $\approx 43 k_B T$, to which an observer would conclude there should be no deposited particles [BBV+07], even though Figures 6.22(d), (e) and (f) reveal this to be a false assertion. These findings agree

Table 6.3: Average surface potential of composite substrate (based on surface area weighting) for Cases #9 and #12. For the cases listed here, the scaled Hamaker constant for the entire composite substrate is 1.0, and the remaining system parameters are listed in Table 6.1. Note that a portion of the substrate is deemed to be favourable to deposition if its surface potential is opposite in sign to that of the particle.

Case	**Surface potential**			
	Particle	**Asperities**	**Flat surface**	**Substrate average**
	ψ_p **mV**	ψ_a **mV**	ψ_s **mV**	ψ_{avg} **mV**
#9	-75	$+25$	-25	-3
#12	-25	$+25$	-75	-31

with the conclusions of previous studies [ENKR00,BJC06,NMB06a,DKDS09], in that averaged or mean-field surface properties can lead to erroneous assumptions concerning colloidal interactions and probabilities of particle deposition on real surfaces. Therefore, it would be preferable to account for surface charge (potential) heterogeneity, as well as any physical heterogeneity, when analyzing deposition kinetics for a given experimental system.

6.4 Summary

The above simulations demonstrate the ability of geometrically uniform asperities on a planar surface to create variations in deposit morphologies. Although the simulations in this study span a very small parametric phase space, they provide confidence regarding the ability of the developed model (PTM) to simulate deposition phenomena onto surfaces with micro- or nanoscale roughness. Further extensive simulations based on this model, though time consuming and computationally demanding, may elucidate the influence of physical heterogeneity of surfaces on particle deposition dynamics and deposit morphologies. The model also incorporates the effects of chemical heterogeneity within the framework of the pairwise additivity assumption, enabling simultaneous exploration of physico-chemical surface heterogeneity on particle deposition. Using

the PTM, considerable attention has been devoted to the limiting case when a single spherical asperity is present on a planar substrate. Following this, simulations of particle deposition onto a planar substrate containing a regular array of spherical asperities have been performed and analyzed. Through the use of the PTM with several substrate configurations, it is apparent that the presence of both physical and chemical heterogeneity can significantly influence particle transport (convection, diffusion and migration) and deposition for such substrates.

Chapter 7

Conclusion and Future Work

7.1 Overview

The primary aim of this research was to investigate how substrate heterogeneity can affect particle transport and deposition onto it. An extensive review of earlier deposition studies has revealed an intermediate realm that has not been fully explored in which the features of physical and/or chemical heterogeneity are of similar sizes to the particles. Even for Brownian particles, physical heterogeneity at comparable scales modifies an idealized, analytical fluid velocity profile for a flat plate into a more complex, numerically-determined one, which changes how particles can be transported to the surface by just fluid motion. There is also a question of how the surface roughness of a substrate affects its hydrodynamic interactions with an approaching particle. To seek answers to these and other related questions, the present study has proposed a general approach to particle transport and deposition on such physically and chemically heterogeneous substrates. This approach depicts a heterogeneous substrate as an assemblage of subunits. Since the physical and chemical properties of these subunits can be individually assigned, this provided a means to simulate the heterogeneity of a substrate using simple shapes. For this study, the model substrate was comprised of one or more spherical asperities attached to a planar surface, or a planar surface divided into spherical subunits when looking at only colloidal interactions. The simulation tool created from this approach includes convective, diffusional and migrational (due to colloidal interactions

only in this study) transport in a Stokesian fluid, all of which are retarded using an approximate technique to account for hydrodynamic interactions as the spherical particle approaches the heterogeneous substrate. This tool was employed to simulate the trajectories of many particles released individually near the model substrate in a variety of configurations of physical and/or chemical heterogeneity. The results of these simulations were evaluated in terms of deposition probabilities and spatial distribution maps of trajectory endpoints.

7.2 Concluding Remarks

The first objective of this thesis is centered around the effects of substrate heterogeneity on migrational particle transport (*i.e.*, colloidal interactions). The major conclusions arrived at in pursuing this objective are summarized below:

1. In the near-field of rough surfaces where colloidal forces are typically dominant (*i.e.*, stronger than the Brownian force), the net DLVO force on a particle is directed along the distance of closest approach to the substrate (normal to the surface). Physical heterogeneity by itself does not lead to significant forces acting laterally (tangentially) to the region of closest approach.

2. When the substrate is chemically heterogeneous, the lateral component of the colloidal (DLVO) force can become substantial, exceeding the strength of the normal component at close, near-field separations corresponding to the secondary minimum of the DLVO interaction potential. Generally ignored in most deposition studies involving DLVO theory, these lateral forces indicate the presence of chemical heterogeneity on the substrate near the region of the particle's closest approach, regardless of substrate topography. For high electrolyte concentrations (*e.g.* 10^{-1} M, as found in many biological systems), the most significant lateral forces occur in regions near the edges of heterogeneous patches. Under these conditions, the particle can also reach a local equilibrium position where

the net DLVO force (both lateral and normal components) acting on it approaches zero. This location does not necessarily coincide with where the particle's minimum interaction energy state is.

Shifting from migrational forces to those of convection, the second objective of this thesis is concerned with the undisturbed hydrodynamic field near a surface with features of roughness on a similar scale to the particle size. Conclusions related to this objective are based on validations as well as subsequent simulations:

1. When the asperity-to-particle size ratio is greater than 1 (*i.e.*, $\lambda > 1$), the modification of the local flow field near a spherical asperity can dramatically alter deterministic particle trajectories from what they would be with flat plates, and therefore, the locations of their deposition onto the composite substrate. This indicates that physical substrate heterogeneity on a scale greater than the particle size has a far reaching influence on particle deposition from a predominantly hydrodynamic standpoint.

2. It is important to accurately determine the flow field near roughness features in colloid deposition models to predict deposition probabilities or deposit morphologies with any degree of realism. A comparison of fluid velocities over rough substrates with those over a smooth, flat one shows that the roughness significantly modifies ($> 5\%$) the flow field up to heights (above the midplane) of about 10 times the characteristic length of the roughness features. Assuming perfectly smooth collectors to compute the flow field can lead to substantial errors in predicting deposition phenomena for non-ideal and physically heterogeneous collectors.

In the course of meeting the third and fourth objectives, simulations using one form of the simulation tool devised in this study – the Particle Tracking Model (PTM) – have led to the following conclusions about particle transport and deposition on physically and chemically heterogeneous substrates:

1. When they are favourable to deposition, asperities protruding from the planar surface can act as additional collectors, increasing the available substrate surface area onto which particles can deposit. If convective particle transport is not clearly dominant ($Pe \leq 1.4$) under such conditions, particles can deposit on the "peaks" of the favourable asperities.

2. At low to moderate particle Peclet numbers (*e.g.* $Pe \leq 1.4$), asperities act as attractive "beacons" for particles, pulling them closer to the composite substrate at downstream locations. For high particle Peclet numbers, asperities can provide lift for particles traveling at heights between the centers and the tops of the asperities.

3. Solution ionic strength (*i.e.*, electrolyte concentration) has some influence on deposition probability for a heterogeneous substrate. When the asperities are favourable and the flat surface is unfavourable, a reduction in ionic strength from 10^{-1} M to 10^{-3} M leads to increases in deposition probability of up to 10%. When conditions are reversed, the unfavourable asperities block some particles from depositing on the lower planar surface, resulting in a slight decrease in deposition probability with decreased ionic strength.

4. Surface potential has little influence on deposition probability for a heterogeneous substrate. Furthermore, using mean-field (averaged) values of the surface potential of a substrate can also be very misleading in determining if the entire substrate is favourable or unfavourable to deposition. Favourability of a given region of a substrate is based on colloidal interactions at the distance of particle's closest approach. Therefore, finding particles deposited on surfaces that are expected to be unfavourable on the basis of average surface potential and the DLVO theory is a clear indication of the presence of chemical heterogeneity.

5. The simulation tool described in this study (*i.e.*, HIM and PTM) can serve as a design tool to study particle deposition onto nanotextured

surfaces containing geometrically well-defined surface features.

7.3 Future Work

The research described in this thesis can be considered as an initial step to simulating how substrate heterogeneity on a similar scale to the approaching particles can affect particle deposition. Out of the numerous improvements and potential applications of the PTM simulation tool that could be undertaken, three prominent examples are listed below:

1. In its current form, the PTM uses an undisturbed hydrodynamic field that is based on the initial or "clean" state of the substrate. However, with each particle that is irreversibly adsorbed over time, the surface becomes more physically (and perhaps chemically) heterogeneous, thereby altering the flow field and affecting subsequent particle transport and deposition. To observe long term deposition behaviour for a given model substrate using the PTM, the flow field would need to be updated with each particle deposited within the field. The approach presented here would demonstrate the effects of dynamic heterogeneity on the formation of particle monolayers and could shed light on possible methods for producing artificial thin films and the mechanisms involved in the growth of biofilms on surfaces. Results of the PTM simulations could also be compared with those of previous studies that used some form of random sequential adsorption (RSA) in their models.

2. The simulation tool can be used for detailed studies of slip length, relating surface heterogeneity to the presence of slip at solid-fluid interfaces. In addition to the hydrophilic, fully-wetted surfaces of the present study, portions of the model substrate could be rendered hydrophobic by changing boundary conditions for the numerical flow field solution and/or through appropriate specifications of surface chemistry. Instantaneous velocities of many particles could be monitored as they travel very close to the heterogeneous model substrates. These simulations would

be compared with the findings of experimental studies of slip length for particular surfaces. As mentioned earlier in this thesis, insights into slip length could lead to the design of surfaces with reduced friction for fluid flows, thereby saving power.

3. Applications of the simulation tool described in this study can be extended by combining features of the Heterogeneous Interaction Model (HIM) and the Particle Tracking Model (PTM). By varying the sizes of the subunits (as well as their chemical properties), these building blocks can create substrates of arbitrary topography and therefore, more accurate renderings of real surfaces can be achieved. With such flexibility in depicting the characteristics of the substrate, a potential avenue of research for such a simulation tool is the transport of particles in confined spaces of micro- and nanoscale dimensions. It is currently a topic of interest, with applications including water filtration membranes (*i.e.*, pore transport), lab-on-chip designs, and microcirculation in tumors. The general approach with this simulation tool would account for hydrodynamic interactions, albeit approximately, in scenarios of hindered convection and diffusion such as the entrance to a cylindrical pore. Simulation results would be compared with other methods proposed to model hindered transport in these particular environments.

Bibliography

[AB06] Samartha G. Anekal and Michael A. Bevan, *Self-diffusion in submonolayer colloidal fluids near a wall*, J. Chem. Phys. **125** (2006), no. 3.

[Ada03] Z. Adamczyk, *Particle adsorption and deposition: role of electrostatic interactions*, Adv. Colloid Interface Sci. **100** (2003), no. Sp. Iss. SI, 267–347.

[Ada06] ———, *Particles at Interfaces: Interactions, Deposition, Structure; Interface and Science Technology, Vol. 9*, 1st ed., Academic Press, Amsterdam, 2006.

[ADK09] Sabine Attinger, Jiva Dimitrova, and Wolfgang Kinzelbach, *Homogenization of the transport behavior of nonlinearly adsorbing pollutants in physically and chemically heterogeneous aquifers*, Adv. Water Resour. **32** (2009), no. 5, Sp. Iss. SI, 767–777.

[AO54] S. Asakura and F. Oosawa, *On Interaction between Two Bodies Immersed in a Solution of Macromolecules*, J. Chem. Phys. **22** (1954), no. 7, 1255–1256.

[AQMB08] Noor Al Quddus, Walied A. Moussa, and Subir Bhattacharjee, *Motion of a spherical particle in a cylindrical channel using arbitrary Lagrangian-Eulerian method*, J. Colloid Interface Sci. **317** (2008), no. 2, 620–630.

[ASC95] A. Abdel-Salam and C. V. Chrysikopoulos, *Modeling of colloid and colloid-facilitated contaminant transport in a 2-dimensional fracture with spatially-variable aperture*, Transp. Porous Media **20** (1995), no. 3, 197–221.

[AvdV81] Z. Adamczyk and Theo G. M. van de Ven, *Deposition of particles under external forces in laminar-flow through parallel-plate and cylindrical channels*, J. Colloid Interface Sci. **80** (1981), no. 2, 340–356.

[AZSC86] Z. Adamczyk, M. Zembala, B. Siwek, and J. Czarnecki, *Kinetics of Latex Particle Deposition from Flowing Suspensions*, J. Colloid Interface Sci. **110** (1986), no. 1, 188–200.

[BB88] J. F. Brady and G. Bossis, *Stokesian Dynamics*, Annu. Rev. Fluid Mech. **20** (1988), 111–157.

[BBV+07] K. Boussu, A. Belpaire, A. Volodin, C. Van Haesendonck, P. Van der Meeren, C. Vandecasteele, and B. Van der Bruggen, *Influence of membrane and colloid characteristics on fouling of nanofiltration membranes*, J. Membr. Sci. **289** (2007), no. 1-2, 220–230.

[BE79] B. D. Bowen and N. Epstein, *Fine particle deposition in smooth parallel-plate channels*, J. Colloid Interface Sci. **72** (1979), no. 1, 81–97.

[BE97] S. Bhattacharjee and M. Elimelech, *Surface element integration: A novel technique for evaluation of DLVO interaction between a particle and a flat plate*, J. Colloid Interface Sci. **193** (1997), no. 2, 273–285.

[BHH78] George E. P. Box, William G. Hunter, and J. Stuart Hunter, *Statistics for Experimenters: An Introduction to Design, Data Analysis and Model Building*, 1st ed., John Wiley and Sons, New York, 1978.

[BJC06] J. A. Brant, K. M. Johnson, and A. E. Childress, *Characterizing NF and RO membrane surface heterogeneity using chemical force microscopy*, Colloid Surf. A-Physicochem. Eng. Asp. **280** (2006), no. 1-3, 45–57.

[BKE98] Subir Bhattacharjee, Chun-Han Ko, and Menachem Elimelech, *DLVO interaction between rough surfaces*, Langmuir **14** (1998), no. 12, 3365–3375.

[BKE99] S. Bhattacharjee, A. S. Kim, and M. Elimelech, *Concentration polarization of interacting solute particles in cross-flow membrane filtration*, J. Colloid Interface Sci. **212** (1999), no. 1, 81–99.

[BLE76] B. D. Bowen, S. Levine, and N. Epstein, *Fine particle deposition in laminar flow through parallel-plate and cylindrical channels*, J. Colloid Interface Sci. **54** (1976), no. 3, 375–390.

[BPB98] H. J. Busscher, A. T. Poortinga, and R. Bos, *Lateral and perpendicular interaction forces involved in mobile and immobile adhesion of microorganism on model solid surfaces*, Curr. Microbiol. **37** (1998), no. 5, 319–323.

[Bre61] Howard Brenner, *The slow motion of a sphere through a viscous fluid towards a plane surface*, Chem. Eng. Sci. **16** (1961), no. 3-4, 242–251.

[Bri47] H. C. Brinkman, *A calculation of the viscous force exerted by a flowing fluid on a dense swarm of particles*, Appl. Sci. Res., Section A **1** (1947), no. 1, 27–34.

[BS06] P. J. Bond and M. S. P. Sansom, *Insertion and assembly of membrane proteins via simulation*, J. Am. Chem. Soc. **128** (2006), no. 8, 2697–2704.

[BSB+05] S. A. Bradford, J. Simunek, M. Bettahar, Y.F. Tadassa, M. T. van Genuchten, and S. R. Yates, *Straining of colloids at textural interfaces*, Water Res. **41** (2005), no. 10.

[BSVS93] J. Bafaluy, B. Senger, J. C. Voegel, and P. Schaaf, *Effect Of Hydrodynamic Interactions On The Distribution Of Adhering Brownian Particles*, Phys. Rev. Lett. **70** (1993), no. 5, 623–626.

[BT00] R. B. Bai and C. Tien, *Transient behavior of particle deposition in granular media under various surface interactions*, Colloid Surf. A-Physicochem. Eng. Asp. **165** (2000), no. 1-3, 95–114.

[BT07] S. A. Bradford and N. Toride, *A stochastic model for colloid transport and deposition*, J. Environ. Qual. **36** (2007), no. 5, 1346–1356.

[BTW07] S. A. Bradford, S. Torkzaban, and S. L. Walker, *Coupling of physical and chemical mechanisms of colloid straining in saturated porous media*, Water Res. **41** (2007), no. 13, 3012–3024.

[Bur05] John Burkhardt, *Source Codes in Fortran90*, Website, 2005, `http://people.sc.fsu.edu/~burkardt/f_src/timestamp/timestamp.f90`.

[BWN01] M. Bostrom, D. R. M. Williams, and B. W. Ninham, *Specific ion effects: Why DLVO theory fails for biology and colloid systems*, Phys. Rev. Lett. **8716** (2001), no. 16.

[CAS97] C. V. Chrysikopoulos and A. Abdel-Salam, *Modeling colloid transport and deposition in saturated fractures*, Colloid Surf. A-Physicochem. Eng. Asp. **121** (1997), no. 2-3, 189–202.

[CC83] B. K. C. Chan and D. Y. C. Chan, *Electrical double-layer interaction between spherical colloidal particles - an exact solution*, J. Colloid Interface Sci. **92** (1983), no. 1, 281–283.

[CCC08] You-Im Chang, Yu-Sheng Chen, and Wei-You Cheng, *The deposition morphology of Brownian/non-Brownian particles within a constricted tube*, J. Chin. Inst. Chem. Eng. **39** (2008), no. 1, 85–100.

[CCL03] Y. I. Chang, S. C. Chen, and E. Lee, *Prediction of Brownian particle deposition in porous media using the constricted tube model*, J. Colloid Interface Sci. **266** (2003), no. 1, 48–59.

[CD80] J. Czarnecki and T. Dąbroś, *Attenuation of the van der Waals Attraction Energy in the Particle/ Semi-Infinite Medium System Due to the Roughness of the Particle Surface*, J. Colloid Interface Sci. **78** (1980), no. 1, 25–30.

[CDC07] Suman Chakraborty, Tamal Das, and Shubhasish Chattoraj, *A generalized model for probing frictional characteristics of pressure-driven liquid microflows*, J. Appl. Phys. **102** (2007), no. 10, 1–11.

[CDCC04] Y. I. Chang, C. L. Du, S. W. Chen, and S. C. Chen, *Effect of the energy barrier of DLVO theory on the deposition of Brownian particles in porous media using the constricted tube model*, J. Chin. Inst. Chem. Eng. **35** (2004), no. 1, 65–76.

[CDS09] Jaime Castillo, Maria Dimaki, and Winnie Edith Svendsen, *Manipulation of biological samples using micro and nano techniques*, Integr. Biol. **1** (2009), no. 1, 30–42.

[CHG03] K. Y. Chun, Y. W. Huang, and V. K. Gupta, *Polymer adsorption on nanoheterogeneous surfaces: Impact of size and density of heterogeneous sites*, J. Chem. Phys. **118** (2003), no. 7, 3252–3257.

[CK06] Chang-Hwan Choi and Chang-Jin Kim, *Large slip of aqueous liquid flow over a nanoengineered superhydrophobic surface*, Phys. Rev. Lett. **96** (2006), no. 6, 1–4.

[CL98] R. S. Cushing and D. F. Lawler, *Depth filtration: Fundamental investigation through three dimensional trajectory analysis*, Environ. Sci. Technol. **32** (1998), no. 23, 3793–3801.

[CL06] R. A. Curtis and L. Lue, *A molecular approach to bioseparations: Protein-protein and protein-salt interactions*, Chem. Eng. Sci. **61** (2006), no. 3, 907–923.

[CR85a] K. Chari and R. Rajagopalan, *Deposition of Colloidal Particles in Stagnation-Point Flow*, J. Chem. Soc., Faraday Trans. II **81** (1985), no. Sep, 1345–1366.

[CR85b] ———, *Transport of Colloidal Particles over Energy Barriers*, J. Colloid Interface Sci. **107** (1985), no. 1, 278–282.

[CUK+06] Chang-Hwan Choi, Umberto Ulmanella, Joonwon Kim, Chih-Ming Ho, and Chang-Jin Kim, *Effective slip and friction re-*

duction in nanograted superhydrophobic microchannels, Phys. Fluids **18** (2006), no. 8, 1–8.

[CW75] Allen T. Chwang and T. Yao-Tsu Wu, *Hydromechanics of Low-Reynolds Number Flow .2. Singularity Method for Stokes Flows*, J. Fluid Mech. **67** (1975), no. Feb 25, 787–815.

[CW87] J. Czarnecki and P. Warsynski, *The evaluation of tangential forces due to surface inhomogeneities in the particle deposition process*, Colloids Surf. **22** (1987), no. 2-4, 207–214.

[Cza86] J. Czarnecki, *The effects of surface inhomogeneities on the interactions in colloidal systems and colloid stability*, Adv. Colloid Interface Sci. **24** (1986), no. 4, 283–319.

[DA79] T. Dąbroś and Z. Adamczyk, *Noninertial Particle Transfer to the Rotating-Disk Under an External Force-Field (Laminar-Flow)*, Chem. Eng. Sci. **34** (1979), no. 8, 1041–1049.

[DAD05] F. Delay, P. Ackerer, and C. Danquigny, *Simulating solute transport in porous or fractured formations using random walk particle tracking: A review*, Vadose Zone J. **4** (2005), no. 2, 360–379.

[Dah74] B. Dahneke, *Diffusional deposition of particles*, J. Colloid Interface Sci. **48** (1974), no. 3, 520–522.

[DB05] P. K. Das and S. Bhattacharjee, *Electrostatic double layer force between a sphere and a planar substrate in the presence of previously deposited spherical particles*, Langmuir **21** (2005), no. 10, 4755–4764.

[DBB87] L. Durlofsky, J. F. Brady, and G. Bossis, *Dynamic Simulation of Hydrodynamically Interacting Particles*, J. Fluid Mech. **180** (1987), 21–49.

[DBFG08] Loredana S. Dorobantu, Subir Bhattacharjee, Julia M. Foght, and Murray R. Gray, *Atomic force microscopy measurement of heterogeneity in bacterial surface hydrophobicity*, Langmuir **24** (2008), no. 9, 4944–4951.

[D§9] T. Dąbroś, *Interparticle hydrodynamic interactions in deposition processes*, Colloids Surf. **39** (1989), no. 1-3, 127–141.

[DD07] Ranojoy D. Duffadar and Jeffrey M. Davis, *Interaction of micrometer-scale particles with nanotextured surfaces in shear flow*, J. Colloid Interface Sci. **308** (2007), no. 1, 20–29.

[DD08] ———, *Dynamic adhesion behavior of micrometer-scale particles flowing over patchy surfaces with nanoscale electrostatic heterogeneity*, J. Colloid Interface Sci. **326** (2008), no. 1, 18–27.

[Der34] B. V. Derjaguin, *Friction and adhesion IV. The theory of adhesion of small particles*, Kolloid Z. **69** (1934), 155–164.

[Dho96] Jan K. G. Dhont, *An Introduction to Dynamics of Colloids: Studies in Interface Science, Vol. 2*, 1st ed., Elsevier Science, Amsterdam, 1996.

[DKDS09] Ranojoy Duffadar, Surachate Kalasin, Jeffrey M. Davis, and Maria M. Santore, *The impact of nanoscale chemical features on micron-scale adhesion: Crossover from heterogeneity-dominated to mean-field behavior*, J. Colloid Interface Sci. **337** (2009), no. 2, 396–407.

[DKE08] Alexis J. De Kerchove and Menachem Elimelech, *Bacterial swimming motility enhances cell deposition and surface coverage*, Environ. Sci. Technol. **42** (2008), no. 12, 4371–4377.

[DL41] B. V. Derjaguin and L. Landau, *Theory of the stability of strongly charged lyophobic sols and of the adhesion of strongly charged particles in solutions of electrolytes*, Acta Physicochim., URSS **14** (1941), 633–662.

[DLvL04] J. F. L. Duval, F. A. M. Leermakers, and H. P. van Leeuwen, *Electrostatic interactions between double layers: Influence of surface roughness, regulation, and chemical heterogeneities*, Langmuir **20** (2004), no. 12, 5052–5065.

[Don02] H. L. Dong, *Significance of electrophoretic mobility distribution to bacterial transport in granular porous media*, J. Microbiol. Methods **51** (2002), no. 1, 83–93.

[DvdV83] T. Dąbroś and T. G. M. van de Ven, *A Direct Method for Studying Particle Deposition Onto Solid Surfaces*, Colloid Polym. Sci. **261** (1983), no. 8, 694–707.

[DvdV87] ———, *Deposition of Latex Particles on Glass Surfaces in an Impinging Jet*, Physicochem. Hydrodyn. **8** (1987), no. 2, 161–172.

[DvdV92] ———, *Hydrodynamic interactions between two spheres near a solid plane*, Int. J. Multiph. Flow **18** (1992), no. 5, 751–764.

[ECK03] M. Elimelech, J. Y. Chen, and Z. A. Kuznar, *Particle deposition onto solid surfaces with micropatterned charge heterogeneity: The "hydrodynamic bump" effect*, Langmuir **19** (2003), no. 17, 6594–6597.

[EGJW95] Menachem Elimelech, John Gregory, Xiaodong Jia, and Richard A. Williams, *Particle Deposition and Aggregation: Measurement, Modeling and Simulation*, 1st ed., Butterworth-Heinemann, Woburn, MA, 1995.

[Ein05] A. Einstein, *The motion of elements suspended in static liquids as claimed in the molecular kinetic theory of heat*, Ann. Phys. - Berlin **17** (1905), no. 8, 549–560.

[EM78] D. L. Ermak and J. A. McCammon, *Brownian dynamics with hydrodynamic interactions*, J. Chem. Phys. **69** (1978), no. 4, 1352–1360.

[ENKR00] M. Elimelech, M. Nagai, C.-H. Ko, and J. N. Ryan, *Relative insignificance of mineral grain zeta potential to colloid transport in geochemically heterogeneous porous media*, Environ. Sci. Technol. **34** (2000), no. 11, 2143–2148.

[EO90a] M. Elimelech and C. R. O'Melia, *Effect of particle-size on collision efficiency in the deposition of Brownian particles with*

electrostatic energy barriers, Langmuir **6** (1990), no. 6, 1153–1163.

[EO90b] ———, *Kinetics of deposition of colloidal particles in porous-media*, Environ. Sci. Technol. **24** (1990), no. 10, 1528–1536.

[F$\ddot{5}$6] R. Fürth (ed.), *Investigations on the theory of Brownian movement by Albert Einstein, Ph.D.*, 1st ed., Dover Publications, New York, 1956.

[Fed80] J. Feder, *Random Sequential Adsorption*, J. Theor. Biol. **87** (1980), no. 2, 237–254.

[GCB67a] A. J. Goldman, R. G. Cox, and H. Brenner, *Slow viscous motion of a sphere parallel to a plane wall .1. Motion through a quiescent fluid*, Chem. Eng. Sci. **22** (1967), no. 4, 637–651.

[GCB67b] ———, *Slow viscous motion of a sphere parallel to a plane wall .2. Couette flow*, Chem. Eng. Sci. **22** (1967), no. 4, 653–660.

[GO71] S. L. Goren and M. E. O'Neill, *Hydrodynamic resistance to a particle of a dilute suspension when in neighbourhood of a large obstacle*, Chem. Eng. Sci. **26** (1971), no. 3, 325–338.

[HA06] E. M. V. Hoek and G. K. Agarwal, *Extended DLVO interactions between spherical particles and rough surfaces*, J. Colloid Interface Sci. **298** (2006), no. 1, 50–58.

[Ham37] H. C. Hamaker, *The London - Van Der Waals attraction between spherical particles*, Physica **4** (1937), 1058–1072.

[HAO04] M. W. Hahn, D. Abadzic, and C. R. O'Melia, *Aquasols: On the role of secondary minima*, Environ. Sci. Technol. **38** (2004), no. 22, 5915–5924.

[Hap58] J. Happel, *Viscous flow in multiparticle systems - Slow motion of fluids relative to beds of spherical particles*, AIChE J. **4** (1958), no. 2, 197–201.

[HBE03] E. M. V. Hoek, S. Bhattacharjee, and M. Elimelech, *Effect of membrane surface roughness on colloid-membrane DLVO interactions*, Langmuir **19** (2003), no. 11, 4836–4847.

[HC97] W. J. C. Holt and D. Y. C. Chan, *Pair interactions between heterogeneous spheres*, Langmuir **13** (1997), no. 6, 1577–1586.

[HHF66] R. Hogg, T. W. Healy, and D. W. Fuerstenau, *Mutual coagulation of colloidal dispersions*, Trans. Faraday Soc. **62** (1966), no. 522P, 1638–1651.

[Hig85] J. J. L. Higdon, *Stokes-flow in arbitrary two-dimensional domains - Shear-flow over ridges and cavities*, J. Fluid Mech. **159** (1985), no. Oct, 195–226.

[HLZ81] T. J. R. Hughes, W. K. Liu, and T. K. Zimmermann, *Lagrangian-Eulerian finite-element formulation for incompressible viscous flows*, Comput. Meth. Appl. Mech. Eng. **29** (1981), no. 3, 329–349.

[HP90] M. C. Herman and K. D. Papadopoulos, *Effects of asperities on the vanderWaals and electric double-layer interactions of 2 parallel flat plates*, J. Colloid Interface Sci. **136** (1990), no. 2, 385–392.

[HP91] ———, *A method for modeling the interactions of parallel flat-plate systems with surface-features*, J. Colloid Interface Sci. **142** (1991), no. 2, 331–342.

[Hu96] H. H. Hu, *Direct simulation of flows of solid-liquid mixtures*, Int. J. Multiph. Flow **22** (1996), no. 2, 335–352.

[Hun01] R. J. Hunter, *Foundations of Colloid Science*, 2nd ed., Oxford University Press, New York, 2001.

[Isr92] Jacob Israelachvili, *Intermolecular and Surface Forces*, 2nd ed., Academic Press, New York, 1992.

[IW96] J. Israelachvili and H. Wennerström, *Role of hydration and water structure in biological and colloidal interactions*, Nature **379** (1996), no. 6562, 219–225.

[JLY07] W. P. Johnson, Xiqing Li, and Gozde Yal, *Colloid retention in porous media: Mechanistic confirmation of wedging and retention in zones of flow stagnation*, Environ. Sci. Technol. **41** (2007), no. 4, 1279–1287.

[JO84] D. J. Jeffrey and Y. Onishi, *Calculation of the Resistance and Mobility Functions for Two Unequal Rigid Spheres in Low Reynolds Number Flow*, J. Fluid Mech. **139** (1984), no. Feb, 261–290.

[JWH80] B. Jonsson, H. Wennerström, and B. Halle, *Ion distributions in lamellar liquid-crystals - A comparison between results from Monte-Carlo simulations and solutions of the Poisson-Boltzmann equation*, J. Phys. Chem. **84** (1980), no. 17, 2179–2185.

[Kad00] Leo P. Kadanoff, *Statistical Physics: Statics, Dynamics, and Renormalization*, 1st ed., World Scientific, Singapore, 2000.

[KB05] Jeffrey A. L. Kemps and Subir Bhattacharjee, *Interactions between a solid spherical particle and a chemically heterogeneous planar substrate*, Langmuir **21** (2005), no. 25, 11710–11721.

[KB09] ———, *Particle Tracking Model for Colloid Transport near Planar Surfaces Covered with Spherical Asperities*, Langmuir **25** (2009), no. 12, 6887–6897.

[KBB+00] F. Kuhnen, K. Barmettler, S. Bhattacharjee, M. Elimelech, and R. Kretzschmar, *Transport of iron oxide colloids in packed quartz sand media: Monolayer and multilayer deposition*, J. Colloid Interface Sci. **231** (2000), no. 1, 32–41.

[KBE00] Chun-Han Ko, Subir Bhattacharjee, and Menachem Elimelech, *Coupled influence of colloidal and hydrodynamic interactions on the RSA dynamic blocking function for particle deposition onto packed spherical collectors*, J. Colloid Interface Sci. **229** (2000), no. 2, 554–567.

[KCW08] Timothy R. Kline, Gexin Chen, and Sharon L. Walker, *Colloidal deposition on remotely controlled charged micropatterned surfaces in a parallel-plate flow chamber*, Langmuir **24** (2008), no. 17, 9381–9385.

[KE00] C.-H. Ko and M. Elimelech, *The "shadow effect" in colloid transport and deposition dynamics in granular porous media: Measurements and mechanisms*, Environ. Sci. Technol. **34** (2000), no. 17, 3681–3689.

[KE07] Zachary A. Kuznar and Menachem Elimelech, *Direct microscopic observation of particle deposition in porous media: Role of the secondary energy minimum*, Colloid Surf. A - Physicochem. Eng. Asp. **294** (2007), no. 1-3, 156–162.

[KET83] C. Kanaoka, H. Emi, and W. Tanthapanichakoon, *Convective diffusional deposition and collection efficiency of aerosol on a dust-loaded fiber*, AIChE J. **29** (1983), no. 6, 895–902.

[KFT08] Milos Kojic, Nenad Filipovic, and Akira Tsuda, *A mesoscopic bridging scale method for fluids and coupling dissipative particle dynamics with continuum finite element method*, Comput. Meth. Appl. Mech. Eng. **197** (2008), no. 6-8, 821–833.

[KH02] A. S. Kim and E. M. V. Hoek, *Cake structure in dead-end membrane filtration: Monte Carlo simulations*, Environ. Eng. Sci. **19** (2002), no. 6, 373–386.

[KK05] Sangtae Kim and Seppo J. Karrila, *Microhydrodynamics: Principles and Selected Applications*, 1st ed., Dover Publications, Mineola, NY, 2005.

[KN01] P. A. Kralchevsky and K. Nagayama, *Particles at Fluid Interfaces and Membranes: Attachment of Colloid Particles and Proteins to Interfaces and Formation of Two-Dimensional Arrays*, 1st ed., Elsevier, Amsterdam, 2001.

[KS08] S. Kalasin and M. M. Santore, *Hydrodynamic crossover in dynamic microparticle adhesion on surfaces of controlled*

nanoscale heterogeneity, Langmuir **24** (2008), no. 9, 4435–4438.

[Kuw59] S. Kuwabara, *The forces experienced by randomly distributed parallel circular cylinders or spheres in a viscous flow at small Reynolds numbers*, J. Phys. Soc. Jpn. **14** (1959), no. 4, 527–532.

[LBRE03] J. P. Loveland, S. Bhattacharjee, J. N. Ryan, and M. Elimelech, *Colloid transport in a geochemically heterogeneous porous medium: aquifer tank experiment and modeling*, J. Contam. Hydrol. **65** (2003), no. 3-4, 161–182.

[Len94] A. M. Lenhoff, *Contributions of surface-features to the electrostatic properties of rough colloidal particles*, Colloid Surf. A - Physicochem. Eng. Asp. **87** (1994), no. 1, 49–59.

[Lev62] Veniamin G. Levich, *Physicochemical Hydrodynamics*, 2nd ed., Prentice-Hall, Englewood Cliffs, NJ, 1962.

[LH09] Wei Long and Markus Hilpert, *A Correlation for the Collector Efficiency of Brownian Particles in Clean-Bed Filtration in Sphere Packings by a Lattice-Boltzmann Method*, Environ. Sci. Technol. **43** (2009), no. 12, 4419–4424.

[LHLS07] Yuncheng Liang, Nidal Hilal, Paul Langston, and Victor Starov, *Interaction forces between colloidal particles in liquid: Theory and experiment*, Adv. Colloid Interface Sci. **134-35** (2007), 151–166.

[LJA+95] B. E. Logan, D. G. Jewett, R. G. Arnold, E. J. Bouwer, and C. R. O'Melia, *Clarification of Clean-Bed Filtration Models*, J. Environ. Eng. - ASCE **121** (1995), no. 12, 869–873.

[LZLJ05] X. Q. Li, P. F. Zhang, C. L. Lin, and W. P. Johnson, *Role of hydrodynamic drag on microsphere deposition and reentrainment in porous media under unfavorable conditions*, Environ. Sci. Technol. **39** (2005), no. 11, 4012–4020.

[MB06] Jacob H. Masliyah and Subir Bhattacharjee, *Electrokinetic and Colloid Transport Phenomena*, 1st ed., John Wiley and Sons, Hoboken, NJ, 2006.

[MCM+08] E. Martines, L. Csaderova, H. Morgan, A. S. G. Curtis, and M. O. Riehle, *DLVO interaction energy between a sphere and a nano-patterned plate*, Colloid Surf. A-Physicochem. Eng. Asp. **318** (2008), no. 1-3, 45–52.

[MCWH94] S. J. Miklavic, D. Y. C. Chan, L. R. White, and T. W. Healy, *Double-layer forces between heterogeneous charged surfaces*, J. Phys. Chem. **98** (1994), no. 36, 9022–9032.

[MDvdV86] K. Malysa, T. Dąbroś, and T. G. M. van de Ven, *The sedimentation of one sphere past a 2nd attached to a wall*, J. Fluid Mech. **162** (1986), 157–170.

[MN76] J. Mahanty and B. W. Ninham, *Dispersion Forces*, 1st ed., Academic Press, London, 1976.

[MPFJ09] Huilian Ma, Julien Pedel, Paul Fife, and William P. Johnson, *Hemispheres-in-Cell Geometry to Predict Colloid Deposition in Porous Media*, Environ. Sci. Technol. **43** (2009), no. 22, 8573–8579.

[MR76] S. Marčelja and N. Radić, *Repulsion of Interfaces due to Boundary Water*, Chem. Phys. Lett. **42** (1976), no. 1, 129–130.

[MR04] M. Manciu and E. Ruckenstein, *The polarization model for hydration/double layer interactions: the role of the electrolyte ions*, Adv. Colloid Interface Sci. **112** (2004), no. 1-3, 109–128.

[MSH+07] Liang-Chieh Ma, Ramkumar Subramanian, Hong-Wen Huang, Vishva Ray, Choong-Un Kim, and Seong Jin Koh, *Electrostatic funneling for precise nanoparticle placement: A route to wafer-scale integration*, Nano Lett. **7** (2007), no. 2, 439–445.

[Nel04] K. E. Nelson, *A Lagrangian Method for Investigating Bacterial Transport and Attachment in the Colloid Filtration Theory*, PhD in Civil and Environmental Engineering, University of California, Davis, Department of Civil and Environmental Engineering, 2004.

[NG05] K. E. Nelson and T. R. Ginn, *Colloid filtration theory and the Happel sphere-in-cell model revisited with direct numerical simulation of colloids*, Langmuir **21** (2005), no. 6, 2173–2184.

[Nin99] B. W. Ninham, *On progress in forces since the DLVO theory*, Adv. Colloid Interface Sci. **83** (1999), no. 1-3, 1–17.

[NLSK04] S. O. Nielsen, C. F. Lopez, G. Srinivas, and M. L. Klein, *Coarse grain models and the computer simulation of soft materials*, J. Phys.-Condes. Matter **16** (2004), no. 15, R481–R512.

[NMB06a] Neda Nazemifard, Jacob H. Masliyah, and Subir Bhattacharjee, *Particle deposition onto charge heterogeneous surfaces: Convection-diffusion-migration model*, Langmuir **22** (2006), no. 24, 9879–9893.

[NMB06b] ———, *Particle deposition onto micropatterned charge heterogeneous substrates: Trajectory analysis*, J. Colloid Interface Sci. **293** (2006), no. 1, 1–15.

[PBBK08] Chan-Hee Park, Christof Beyer, Sebastian Bauer, and Olaf Kolditz, *A study of preferential flow in heterogeneous media using random walk particle tracking*, Geosci. J. **12** (2008), no. 3, 285–297.

[Phi95] R. J. Phillips, *Calculation of multisphere linearlized Poisson-Boltzmann interactions near cylindrical fibers and planar surfaces*, J. Colloid Interface Sci. **175** (1995), no. 2, 386–399.

[PL80] D. C. Prieve and M. M. J. Lin, *Adsorption of Brownian hydrosols onto a rotating disk aided by a uniform applied force*, J. Colloid Interface Sci. **76** (1980), no. 1, 32–47.

[PMM08] Christopher J. Pipe, Trushant S. Majmudar, and Gareth H. McKinley, *High shear rate viscometry*, Rheol. Acta. **47** (2008), no. 5-6, 621–642.

[Poz94] C. Pozrikidis, *The motion of particles in the Hele-Shaw cell*, J. Fluid Mech. **261** (1994), 199–222.

[Poz97] ———, *Shear flow over a protuberance on a plane wall*, J. Eng. Math. **31** (1997), no. 1, 29–42.

[Poz99] ———, *Little Book of Streamlines*, 1st ed., Academic Press, San Diego, CA, 1999.

[Pro03] Ronald F. Probstein, *Physicochemical Hydrodynamics*, 2nd ed., John Wiley and Sons, Hoboken, NJ, 2003.

[PRT74] A. C. Payatakes, R. Rajagopalan, and C. Tien, *Use of Happel's Model for filtration studies*, J. Colloid Interface Sci. **49** (1974), no. 2, 321–325.

[PTVF92] William H. Press, Saul A. Teukolsky, William T. Vetterling, and Brian P. Flannery, *Numerical Recipes in FORTRAN 77: The Art of Scientific Computing*, 2nd ed., Cambridge University Press, Cambridge, MA, 1992.

[RB07] Tania Rizwan and Subir Bhattacharjee, *Initial deposition of colloidal particles on a rough nanofiltration membrane*, Can. J. Chem. Eng. **85** (2007), no. 5, 570–579.

[RB09] ———, *Particle Deposition onto Charge-Heterogeneous Substrates*, Langmuir **25** (2009), no. 9, 4907–4918.

[RK02] U. Raviv and J. Klein, *Fluidity of bound hydration layers*, Science **297** (2002), no. 5586, 1540–1543.

[RPCPB06] S. Rentsch, R. Pericet-Camara, G. Papastavrou, and M. Borkovec, *Probing the validity of the Derjaguin approximation for heterogeneous colloidal particles*, Phys. Chem. Chem. Phys. **8** (2006), no. 21, 2531–2538.

[RPW01] J. H. Ren, A. I. Packman, and C. Welty, *Analysis of an observed relationship between colloid collision efficiency and mean collector grain size*, Colloid Surf. A-Physicochem. Eng. Asp. **191** (2001), no. 1-2, Sp. Iss. SI, 133–144.

[RSS89] W. B. Russel, D. A. Saville, and W. R. Schowalter, *Colloidal Dispersions*, 1st ed., Cambridge University Press, Cambridge, MA, 1989.

[RT76] R. Rajagopalan and C. Tien, *Trajectory analysis of deep-bed filtration with sphere-in-cell porous-media model*, AIChE J. **22** (1976), no. 3, 523–533.

[RT05] ———, *Comment on "Correlation equation for predicting single-collector efficiency in physicochemical filtration in saturated porous media"*, Environ. Sci. Technol. **39** (2005), no. 14, 5494–5495.

[RTPT82] R. Rajagopalan, C. Tien, R. Pfeffer, and G. Tardos, *Letter to the editor*, AIChE J. **28** (1982), no. 5, 871–872.

[RWE04] J. A. Redman, S. L. Walker, and M. Elimelech, *Bacterial adhesion and transport in porous media: Role of the secondary energy minimum*, Environ. Sci. Technol. **38** (2004), no. 6, 1777–1785.

[SB89] J. Sjollema and H. J. Busscher, *Deposition of polystyrene latex-particles toward polymethylmethacrylate in a parallel plate flow cell*, J. Colloid Interface Sci. **132** (1989), no. 2, 382–394.

[SB90] ———, *Deposition of polystyrene particles in a parallel plate flow cell .1. The influence of collector surface properties on the experimental deposition rate*, Colloids Surf. **47** (1990), 323–336.

[SC99] J. Stankovich and S. L. Carnie, *Interactions between two spherical particles with nonuniform surface potentials: The linearized Poisson-Boltzmann theory*, J. Colloid Interface Sci. **216** (1999), no. 2, 329–347.

[SESR01] N. Sun, M. Elimelech, N. Z. Sun, and J. N. Ryan, *A novel two-dimensional model for colloid transport in physically and geochemically heterogeneous porous media*, J. Contam. Hydrol. **49** (2001), no. 3-4, 173–199.

[SF73] L. A. Spielman and J. A. Fitzpatrick, *Theory for particle collection under London and gravity forces*, J. Colloid Interface Sci. **42** (1973), no. 3, 607–623.

[SFGGH06] Peter Salamon, Daniel Fernandez-Garcia, and J. Jaime Gomez-Hernandez, *A review and numerical assessment of the random walk particle tracking method*, J. Contam. Hydrol. **87** (2006), no. 3-4, 277–305.

[SK07] Maria M. Santore and Natalia Kozlova, *Micrometer scale adhesion on nanometer-scale patchy surfaces: Adhesion rates, adhesion thresholds, and curvature-based selectivity*, Langmuir **23** (2007), no. 9, 4782–4791.

[SS66] L. J. Snyder and W. E. Stewart, *Velocity and pressure profiles for Newtonian creeping flow in regular packed beds of spheres*, AIChE J. **12** (1966), no. 1, 167–173.

[ST89] P. Schaaf and J. Talbot, *Kinetics Of Random Sequential Adsorption*, Phys. Rev. Lett. **62** (1989), no. 2, 175–178.

[SW96] L. Suresh and J. Y. Walz, *Effect of surface roughness on the interaction energy between a colloidal sphere and a flat plate*, J. Colloid Interface Sci. **183** (1996), no. 1, 199–213.

[SZ01] M. Souli and J. P. Zolesio, *Arbitrary Lagrangian-Eulerian and free surface methods in fluid mechanics*, Comput. Meth. Appl. Mech. Eng. **191** (2001), no. 3-5, 451–466.

[SZSR09] Maria M. Santore, Jun Zhang, Sudhanshu Srivastava, and Vincent M. Rotello, *Beyond Molecular Recognition: Using a Repulsive Field to Tune Interfacial Valency and Binding Specificity between Adhesive Surfaces*, Langmuir **25** (2009), no. 1, 84–96.

[Tad01] R. Tadmor, *The London-van der Waals interaction energy between objects of various geometries*, J. Phys. - Condens. Matter **13** (2001), no. 9, L195–L202.

[TBW07] Saeed Torkzaban, Scott A. Bradford, and Sharon L. Walker, *Resolving the coupled effects of hydrodynamics and DLVO forces on colloid attachment in porous media*, Langmuir **23** (2007), no. 19, 9652–9660.

[TE04] N. Tufenkji and M. Elimelech, *Correlation equation for predicting single-collector efficiency in physicochemical filtration in saturated porous media*, Environ. Sci. Technol. **38** (2004), no. 2, 529–536.

[TE05a] ———, *Response to comment on "Correlation equation for predicting single-collector efficiency in physicochemical filtration in saturated porous media"*, Environ. Sci. Technol. **39** (2005), no. 14, 5496–5497.

[TE05b] ———, *Spatial distributions of Cryptosporidium oocysts in porous media: Evidence for dual mode deposition*, Environ. Sci. Technol. **39** (2005), no. 10, 3620–3629.

[TJ06] Meiping Tong and William P. Johnson, *Excess colloid retention in porous media as a function of colloid size, fluid velocity, and grain angularity*, Environ. Sci. Technol. **40** (2006), no. 24, 7725–7731.

[Tod03] Don Todd, *B4WIND User's Guide: Trilinear Interpolation*, Website, 2003, `http://www.grc.nasa.gov/WWW/winddocs/utilities/b4wind_guide/trilinear.html`.

[TSHM08] Esben Thormann, Adam C. Simonsen, Per L. Hansen, and Ole G. Mouritsen, *Interactions between a polystyrene particle and hydrophilic and hydrophobic surfaces in aqueous solutions*, Langmuir **24** (2008), no. 14, 7278–7284.

[TSVYT05] P. Taboada-Serrano, V. Vithayaveroj, S. Yiacoumi, and C. Tsouris, *Surface charge heterogeneities measured hy*

atomic force microscopy, Environ. Sci. Technol. **39** (2005), no. 17, 6352–6360.

[TV79] G. M. Torrie and J. P. Valleau, *Monte-Carlo study of an electrical double-layer*, Chem. Phys. Lett. **65** (1979), no. 2, 343–346.

[TV80] ———, *Electrical double-layers .1. Monte-Carlo study of a uniformly charged surface*, J. Chem. Phys. **73** (1980), no. 11, 5807–5816.

[VDMBGG+05] J. J. Valle-Delgado, J. A. Molina-Bolivar, F. Galisteo-Gonzalez, M. J. Galvez-Ruiz, A. Feiler, and M. W. Rutland, *Hydration forces between silica surfaces: Experimental data and predictions from different theories*, J. Chem. Phys. **123** (2005), no. 3.

[vdV89] Theo G. M. van de Ven, *Colloidal Hydrodynamics*, 1st ed., Academic Press, San Diego, CA, 1989.

[VHRMC07] Darrell Velegol, Gretchen L. Holtzer, Aleksandar F. Radovic-Moreno, and Joshua D. Cuppett, *Force measurements between sub-100 nm colloidal particles*, Langmuir **23** (2007), no. 3, 1275–1280.

[vLKWP09] Marijn T. J. van Loenhout, E. Stefan Kooij, Herbert Wormeester, and Bene Poelsema, *Hydrodynamic flow induced anisotropy in colloid adsorption*, Colloid Surf. A-Physicochem. Eng. Asp. **342** (2009), no. 1-3, 46–52.

[VO48] E. J. W. Verwey and J. Th. G. Overbeek, *Theory of the Stability of Lyophobic Colloids*, 1st ed., Elsevier, Amsterdam, 1948.

[vOG04] C. J. van Oss and R. F. Giese, *Role of the properties and structure of liquid water in colloidal and interfacial systems*, J. Dispersion Sci. Technol. **25** (2004), no. 5, Sp. Iss. SI, 631–655.

[VP92] V. Vlachy and J. M. Prausnitz, *Donnan equilibrium - Hypernetted-chain study of one-component and multicomponent models for aqueous polyelectrolyte solutions*, J. Phys. Chem. **96** (1992), no. 15, 6465–6469.

[VT01] D. Velegol and P. K. Thwar, *Analytical model for the effect of surface charge nonuniformity on colloidal interactions*, Langmuir **17** (2001), no. 24, 7687–7693.

[Wal98] J. Y. Walz, *The effect of surface heterogeneities on colloidal forces*, Adv. Colloid Interface Sci. **74** (1998), 119–168.

[Whi83] L. R. White, *On the Deryaguin Approximation for the Interaction of Macrobodies*, J. Colloid Interface Sci. **95** (1983), no. 1, 286–288.

[WK96] X. H. Wen and C. S. Kung, *Implementation of the constant displacement scheme in random walk*, Comput. Geosci. **22** (1996), no. 4, 369–377.

[WRE04] S. L. Walker, J. A. Redman, and M. Elimelech, *Role of cell surface lipopolysaccharides in Escherichia coli K12 adhesion and transport*, Langmuir **20** (2004), no. 18, 7736–7746.

[WS94] J. Y. Walz and A. Sharma, *Effect of Long Range Interactions on the Depletion Force between Colloidal Particles*, J. Colloid Interface Sci. **168** (1994), no. 2, 485–496.

[WUU99] K. Watanabe, Y. Udagawa, and H. Udagawa, *Drag reduction of Newtonian fluid in a circular pipe with a highly water-repellent wall*, J. Fluid Mech. **381** (1999), 225–238.

[YHO71] K. M. Yao, M. M. Habibian, and C. R. O'Melia, *Water and waste water filtration - Concepts and applications*, Environ. Sci. Technol. **5** (1971), no. 11, 1105–1112.

[Yip05] S. Yip (ed.), *Handbook of Materials Modeling, Vols. 1 and 2*, 1st ed., Springer, Berlin, 2005.

[ZBC+08] Hongying Zhao, Subir Bhattacharjee, Ross Chow, Dean Wallace, Jacob H. Masliyah, and Zhenghe Xu, *Probing Surface*

Charge Potentials of Clay Basal Planes and Edges by Direct Force Measurements, Langmuir **24** (2008), no. 22, 12899–12910.

Appendix A

Procedure for Creating Undisturbed Hydrodynamic Fields near Model Substrates

A.1 Introduction

The entire numerical solution methodology for the undisturbed hydrodynamic field near a rough substrate is centered around using commercially-available finite element software. However, information from this solution needs to be transformed into something that is readily usable for the PTM. This appendix provides details of the procedure employed in this study to create the data files containing the hydrodynamic field information, using the configuration of the computational domain and its associated boundary conditions as described in Section 4.2.2.

A.2 Solution of the Hydrodynamic Field Using Finite Element Software

An important part of the PTM's (Particle Tracking Model's) simulation of hydrodynamics is the undisturbed hydrodynamic field in the vicinity of the physically heterogeneous substrate. In this study, this field is obtained using the finite element software COMSOL Multiphysics 3.3 (Comsol Inc.; Burlington, MA), which numerically solves the Stokes equations for steady state, sim-

ple shear flow across the field's computational domain. In COMSOL, three-dimensional, steady state, Stokesian flow fields are solved in the Incompressible Navier-Stokes (chns) Module using a stationary solver. All governing equations, boundary conditions and relevant parameters are non-dimensionalized. Despite the linearity, the finite element matrices for the flow fields in this research are non-symmetric and somewhat sparse, so the iterative linear system solver GMRES (Generalized Minimum RESidual method) is employed with the incomplete LU matrix preconditioner (drop tolerance set at 0.01). Although COMSOL 3.3 has several linear system solvers, only this solver and preconditioner would generate solutions without run-time errors or premature termination of the solver's function.

The computational domain is partitioned into tetrahedral mesh elements using an automatic mesh generator. Prismatic and hexahedral elements were tested, but the tetrahedral elements were found to perform better in both computational effort and level of accuracy. Unstructured (referred to as "free" in COMSOL) mesh networks are used since they have no restrictions on the distribution of elements. For the single asperity scenarios such as those in Section 5.3.1, a computational (half-field) domain measuring $40a_p \times 20a_p \times 20a_p$ (a_p is the particle radius) is rendered with a free mesh of 170603 degrees of freedom and 36674 tetrahedral Lagrange elements. For the multiple, in-line asperity scenarios, the half-field domain is enlarged to $300a_p \times 100a_p \times 100a_p$, with 219761 degrees of freedom and 59099 tetrahedral Lagrange elements. In all scenarios, the mesh starts at its finest resolution (*i.e.*, Predefined mesh size: Finer) on the surfaces of the asperities. Having the smallest mesh elements on the asperities' surfaces provides a better representation of these curved boundaries while conforming to the tetrahedral meshes, and results in more accurate integrations of stress tensors to determine net force values. The characteristic lengths of the elements grow by 40% per layer as the mesh extends into the fluid from those surfaces. All calculations for solving these fields were performed on a 2 GHz AMD Athlon 64 X2 Dual Core Processor 3800+ personal computer with 2 GB of RAM.

A.3 Creation of Hydrodynamic Field Data Files

After COMSOL has numerically solved the hydrodynamic field over the entire computational domain for the given system, the corresponding field data files used by the PTM in the sub-domain can be generated. Since the sub-domain grid's Cartesian architecture is superimposed on a substrate with regions of curvature, it is important to ensure that none of the eight grid nodes used for flow velocity interpolation (see Section 4.3.4) reside within the composite substrate. This is achieved by setting the grid resolution to one-half of the particle's radius (*i.e.*, `RES` $= 0.5a_p$). In doing so, interpolating for $\mathbf{u}$ at the position of the particle's center will always involve finite, non-zero values in the adjacent nodes. This can be seen schematically in Figure 4.5(b), as all of the nodes are a substantial distance ($> 0.5a_p$) away from the outer surface of the particle.

The process of generating these hydrodynamic field data files involves the following steps:

1. Produce a grid data file for the current system configuration (called `GRID.dat`, as an example), listing the Cartesian coordinates of each grid node with the chosen computational sub-domain.

   For this study, this grid data file was produced with a FORTRAN program, which inputs a separate data file listing the coordinates of the centers of all asperities within the computational sub-domain. A number of parameters for the computational sub-domain must be specified in this program, all of which are listed in Table A.1. At this stage, only the half-field of the sub-domain is considered for each system.

2. Import the grid data file `GRID.dat` into COMSOL.

   In COMSOL 3.3, this can be found by the path *File/Export/Post processing Data*, and then under the tab labeled "Subdomain", the filename is entered in the blank beside "Location: Coordinates from File:".

Table A.1: Parameters required for post-processing the hydrodynamic field data within the computational sub-domain (half-field) for each configuration of physical heterogeneity investigated with the PTM in this study. In all configurations, the asperity-to-particle size ratio λ is 5, dimensions are scaled with respect to particle size a_p, and the grid resolution of $0.5a_p$ applies to all three directions.

Parameter	**Variable**	**Substrate Configuration**		
		Single Asperity	**Two Asperities**	**Multiple Asperities**
Min. $x-$ position	`XMIN`	-40	-50	-50
Max. $y-$ position	`YMAX`	$+20$	$+20$	$+40$
Max. $z-$ position	`ZMAX`	$+20$	$+20$	$+20$
No. of grid nodes, $x-$	`NX`	161	201	201
No. of grid nodes, $y-$	`NY`	41	41	81
No. of grid nodes, $z-$	`NZ`	41	41	41
No. of asperities	`NSA`	1	2	8 (in-line) 7 (staggered)

3. Export the $x-$, $y-$ and $z-$ fluid velocity data (*i.e.*, u, v and w respectively in COMSOL) into temporary data files (called `temp_u.txt`, `temp_v.txt` and `temp_w.txt` in this example), one at a time.

   This can be found by the same path in COMSOL under the tab labeled "General", with the filename entered in the blank beside "Export to file:". The data is exported from Subdomains and the format of exported data should be set at *Coordinates, data*.

4. Immediately after creating these temporary files, remove the first line (*i.e.*, column titles) and replace all NaNs (*i.e.*, Not a Number) with zeroes for each of them.

   Depending on the configuration of the asperities in the computational sub-domain, the solution of the hydrodynamic field may produce NaNs at some mesh nodes near the substrate's surface. These NaNs will appear in the data files exported from COMSOL, and as long as they are a short

distance from the substrate's surface ($\ll 0.5a_p$), they can be replaced with zeroes.

5. Using another FORTRAN program, convert the temporary files exported from COMSOL into the undisturbed hydrodynamic field data files in full field form with the appropriate format (*i.e.*, preferably binary to reduce file length) to be read by the PTM simulation program. In this example, `temp_u.txt` becomes `outputbinary_u.dat`, and similarly for the other two velocity components.

   It is very important to confirm that the parameters used in this step agree with those used in step 1. In this step, the nodes located within the asperities are assigned zeroes so that the final data files can be read as complete arrays by the PTM's `main` program. The full field form of each hydrodynamic field data file is determined by a reflection of its respective half-field data about the $y-$ axis. Consequently, the values of `NY` and `NSA` used in the PTM differ from those listed in Table A.1, and they are shown in Table A.2.

Table A.2: Parameters to be used with the full field versions of hydrodynamic field data files for each configuration of physical heterogeneity investigated with the PTM in this study. In all configurations, the asperity-to-particle size ratio λ is 5.

Parameter	**Variable**	**Substrate Configuration**		
		Single Asperity	**Two Asperities**	**Multiple Asperities**
No. of grid nodes, $y-$	`NY`	81	81	161
No. of asperities	`NSA`	1	2	16 (in-line) 12 (staggered)

Appendix B

Numerical Method for Validation of the PTM

In this Appendix, the following is a description of the method that was devised to validate a key element of the Particle Tracking Model (PTM): the use of Universal Correction Functions (UCFs) to approximate the hydrodynamic retardation effect when a moving particle approaches a spherical asperity attached to a planar substrate. The UCFs were originally formulated for sphere-wall interactions, and they have been employed in countless studies with such simple geometries since they were first proposed. These functions were essentially derived from ratios of the actual hydrodynamic drag over the Stokes drag on a particle moving in a fluid. It is commonly known that the actual hydrodynamic drag on the particle depends on the local geometry of the surface it is approaching, and the PTM seeks to approximate this.

The method, first referred to as the numerical method of superposed solutions in Chapter 5, begins with a force balance at the particle's surface. The hydrodynamic force exerted by the surrounding fluid on the particle is

$$\mathbf{F}^{hyd} = \iint_p d\mathbf{S} \cdot \sigma, \tag{B.1}$$

in which σ is the pressure – or hydrodynamic stress, shown in scaled form in Eq. (4.8) – tensor for an incompressible fluid, and $d\mathbf{S}$ is a directed element of the particle's surface area pointing into the fluid. Linearity in Stokesian flow fields allows the solutions for the continuity and Stokes equations, as

well as the hydrodynamic stress and force on the particle, to be expressed as the sum of their translational (t), rotational (r) and shear (sh) contributions [GCB67a, GCB67b]. For a non-accelerating particle that is neutrally buoyant, the total stress and force are equal to zero:

$$\sigma = \sigma^{\mathbf{t}} + \sigma^{\mathbf{r}} + \sigma^{\mathbf{sh}} = 0 \tag{B.2}$$

$$\mathbf{F}^{hyd} = \mathbf{F}^{\mathbf{t}} + \mathbf{F}^{\mathbf{r}} + \mathbf{F}^{\mathbf{sh}} = 0 \tag{B.3}$$

(The sum is zero because $\mathbf{F}^{\mathbf{t}}$ and $\mathbf{F}^{\mathbf{r}}$ together represent the total force acting on the fluid due to the particle's movement, which is balanced by $\mathbf{F}^{\mathbf{sh}}$, the force acting on the particle due to the fluid's motion.) Even though the particle undergoes rotation and experiences torques under these circumstances, the rotational contribution is neglected here since its effects on the hydrodynamic force are not significant until the particle reaches very close separation distances with some point on the surface of the composite substrate. The focus in this study is on the forces and translational velocities of the particle, and consequently, Eq. (B.3) is reduced to

$$\mathbf{F}^{\mathbf{t}} + \mathbf{F}^{\mathbf{sh}} = 0. \tag{B.4}$$

The translational and shear forces can be determined independently from solutions of two separate problems, which will be discussed shortly. These forces are then scaled with respect to their corresponding Stokes drag, that is, the drag force on the particle in an unbounded fluid. For instance, the components of the translational and the shear forces in the $x-$ direction will be

$$F_x^{t*} = F_x^t/(6\pi\mu a_p v_x) \qquad \text{and} \qquad F_x^{sh*} = F_x^{sh}/(6\pi\mu a_p u_x) \tag{B.5}$$

with v_x as the particle's velocity and u_x as the fluid velocity at a given position in the undisturbed flow field. This yields, after substitution into Eq. (B.3),

$$\left(\frac{v_x}{u_x}\right) = \frac{-F_x^{sh*}}{F_x^{t*}}. \tag{B.6}$$

Since u_x is previously solved for, the particle's velocity can be easily calculated after the translation and shear contributions to the hydrodynamic force have been numerically determined.

The translation and shear contributions are solved for as two distinct problems using the software COMSOL. The translation problem involves solving for the total drag force on the particle for the case when the particle has a uniform velocity $\mathbf{u}$ while it is near the composite substrate. The velocity $\mathbf{u}$ applied to the particle is the local undisturbed fluid velocity at the location of the particle center (which was computed as described in Section 2.1). The Stokes equation is numerically solved for this case employing the boundary conditions (as in Figure 4.2)

$$\begin{aligned} \mathbf{u_a}, \mathbf{u_s} &= 0 \quad \text{on} \quad \Gamma_a, \Gamma_s \\ \mathbf{u_p} &= \mathbf{u} \quad \text{on} \quad \Gamma_p \\ \sigma^{\mathbf{t}} \cdot \mathbf{n} &= 0 \quad \text{on} \quad \Gamma_{in}, \Gamma_{out}, \end{aligned} \tag{B.7}$$

where the subscripts a, s, and p refer to the asperity, the planar surface, and the particle, respectively. The boundary Γ_p refers to the particle surface. The last boundary condition (*i.e.*, Γ_{in},Γ_{out}) pertains to a neutral (*i.e.*, no normal fluid stress) outer boundary. In scaled form, the solution of the governing equations using the above boundary conditions, followed by calculation of the surface integral of the total translational stress on the particle (σ^{t*}), yields the translational force, $\mathbf{F^{t*}}$.

The calculation of the shear component of the force can be ideally performed by imposing a shear flow in the computational domain while keeping the particle and the substrate stationary [AQMB08]. However, for numerical calculations with a finite computational domain, the inlet flow boundary condition cannot be defined accurately, since the undisturbed shear flow is applicable only at an infinite distance. To circumvent this problem, the shear component is solved for by imposing the shear flow as a boundary condition on the particle and the asperity. This provides a more accurate numerical estimate – and additive inverse – of the shear force on the particle. Therefore,

the boundary conditions for this problem become

$$\begin{aligned} \mathbf{u_s} &= 0 \quad \text{on} \quad \Gamma_s \\ \mathbf{u_a}, \mathbf{u_p} &= \dot{\gamma} z \quad \text{on} \quad \Gamma_a, \Gamma_p \\ \sigma^{\mathbf{sh}} \cdot \mathbf{n} &= 0 \quad \text{on} \quad \Gamma_{in}, \Gamma_{out} \end{aligned} \tag{B.8}$$

Like with the translation component, the scaled shear force on the particle, $\mathbf{F^{sh*}}$, is obtained by integrating the total scaled shear stress σ^{sh*} over the particle's surface.

This numerical method of superposed solutions has been found to be most effective in determining the force components and particle velocity in the direction of the prevailing flow, which is in the $x-$ direction for the present study. The translational and shear contributions to the scaled hydrodynamic force in the $x-$ direction are,

$$F_x^{t*} = \left(\iint_p d\mathbf{S}^* \cdot \sigma^{\mathbf{t}*} \right) \cdot \mathbf{i}, \tag{B.9}$$

$$F_x^{sh*} = \left(- \iint_p d\mathbf{S}^* \cdot \sigma^{\mathbf{sh}*} \right) \cdot \mathbf{i}. \tag{B.10}$$

These results can then be substituted into Eq. (B.6), together with the $x-$ component of $\mathbf{u}$, to obtain the particle's velocity in the $x-$ direction, v_x, thereby accounting for the hydrodynamic retardation effect on the particle for this substrate geometry. The same procedure can be applied for the velocity components in the $y-$ and $z-$ directions, which includes simply replacing the unit vector $\mathbf{i}$ with $\mathbf{j}$ or $\mathbf{k}$, respectively, in Eqs. (B.9) and (B.10).

The results of this numerical approach were compared with those of Goldman, Cox and Brenner [GCB67b] (*i.e.*, to evaluate the universal correction function f_3) for sphere-flat plate interactions, and they were found to have a difference of less than 0.5% for scaled separation distances down to H =0.5431, and a maximum difference of about 4% at $H = 0.0453$.

Appendix C

Calculation of Capture Efficiency due to Interception

Although the Eulerian (flux-oriented) and Lagrangian (particle-oriented) approaches are markedly different in many respects, this study has uncovered a common factor between them when observing particles being captured by a single asperity on an otherwise planar substrate. Beginning with Figure 6.2, a number of particles are released in a simple shear flow field from the semi-circular window A_a at a substantial distance upstream from a single spherical asperity (in this case, at $x/a_p = -15$, with an asperity-to-particle size ratio of $\lambda = 5$). Since the approach velocity of the fluid U_∞ varies with height ($= \dot{\gamma} z$), the particle flux for a differential element dN at a given height in the semi-circular window A_a (depicted in Figure C.1) is given by

$$\begin{aligned} dN &= n_\infty U_\infty \, dA_a \\ &= n_\infty \dot{\gamma} z \times 2\sqrt{a_a^2 - (z - a_a)^2} \, dz \\ &= 2\dot{\gamma} n_\infty \times z\sqrt{2a_a z - z^2} \, dz \end{aligned} \tag{C.1}$$

Therefore, the total flux of particles released from the window A_a is determined by integrating Eq. (C.1) once with respect to height z, resulting in

$$N = 2\dot{\gamma} n_\infty \int_{a_a}^{2a_a} z\sqrt{2a_a z - z^2} \, dz. \tag{C.2}$$

The capture (or collection) efficiency due to interception for the asperity (η_I) is defined as the ratio of two fluxes [vdV89,MB06]: the actual flux (number

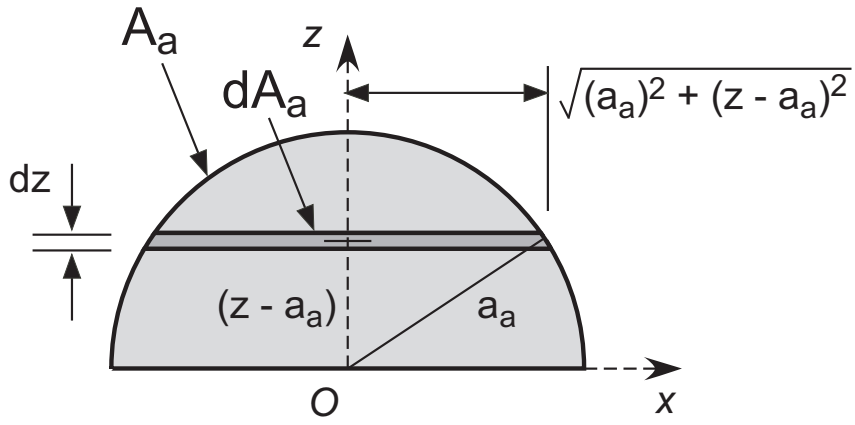

Figure C.1: Schematic showing how the non-uniform particle flux through the upstream release area A_a is determined by dividing the area into differential elements.

of captures per second) relative to a reference flux, usually the flux when hydrodynamic and colloidal forces are neglected and particle trajectories are rectilinear (*i.e.*, ignoring the effect of the asperity on the undisturbed fluid flow). From the Lagrangian perspective with the PTM, this reference flux translates into a deposition probability of 1.0 (refer to asterix data points in Figure 6.7), meaning that all particles released from area A_a will be captured by the asperity.

In general for the single asperity scenario, this ratio is

$$\eta_I = \frac{N_L}{2\dot{\gamma} n_\infty \int_{a_a}^{2a_a} z\sqrt{2a_a z - z^2}\, dz}, \tag{C.3}$$

where N_L is the actual flux based on the area enclosed by the limiting trajectories shown in Figure 6.2. The calculation of the release area for particles captured by the asperity for a given scenario (A_L, in both parts of Figure 6.2) is not perfectly circular due to the influence of the flat surface on the undisturbed fluid flow. Nonetheless, the local flux at any differential area element dA_L is

$$\begin{aligned} dN_L &= n_\infty U_\infty\, dA_L \\ &= n_\infty \dot{\gamma} z\, dA_L \end{aligned} \tag{C.4}$$

Table C.1: Comparison of capture (collection) efficiency due to interception η_I with deposition probability ϕ_a for a single asperity attached to a flat surface with a shear fluid flow across it, with and without hydrodynamic interactions (UCFs) accounted for in the motion of the particles.

	Eulerian Approach	**Lagrangian (PTM) Approach**
	η_I	ϕ_a
Without UCFs	0.1342	≈ 0.16
With UCFs	0.0202	≈ 0.03

and so the total flux through A_L is

$$N_L = \dot{\gamma} n_\infty \int_{A_L} z \, dA_L. \tag{C.5}$$

Substituting Eq. (C.5) into Eq. (C.3) then yields

$$\eta_I = \frac{\int_{A_L} z \, dA_L}{2 \int_{a_a}^{2a_a} z\sqrt{2a_a z - z^2} \, dz}, \tag{C.6}$$

providing a rigorous definition of η_I based on a non-uniform particle flux. The numerator of Eq. (C.6) must be solved for numerically (with Simpson's rule integration) using the starting points of the limiting trajectories calculated with the PTM (refer to Figure 6.2), while its denominator has an analytical solution. An interesting observation from Eq. (C.6) is that η_I is independent of $\dot{\gamma}$, and hence Pe as well. This is also true for the two cases in Figure 6.7 shown with hollow triangles and circles. The hollow triangles represent the results for deposition probability on the asperity ϕ_a for the scenario with the numerically-determined flow field around the asperity but hydrodynamic interactions are neglected (*i.e.*, without UCFs; limiting trajectories drawn in Figure 6.2a). The hollow circles are for the same scenario with hydrodynamic interactions included (*i.e.*, with UCFs; limiting trajectories drawn in Figure 6.2b). Based on the comparison of η_I to ϕ_a in Table C.1, the definition of deposition probability in Eq. (6.2) corresponds qualitatively to the capture efficiency of the asperity due to interception in both cases. It should be emphasized that this

similarity between η_I and ϕ_a for these deterministic transport cases only applies for particles released in the projected area of the top half of the asperity. Particles released in the projected area of the lower half of the asperity are expected to differ considerably, as the undisturbed flow field in this region is significantly modified by the presence of the planar surface. Such a flow field differs greatly from the flow field around an isolated spherical collector, which the Eulerian approach discussed here is based upon.